Technische Universität München

Lehrstuhl für Anorganische Chemie mit Schwerpunkt Neue Materialien

Synthesis and Characterization of Phosphidotetrelate and Phosphide-Based Solid-State Ion Conductors

Henrik Eickhoff

Vollständiger Abdruck der von der Fakultät für Chemie der Technischen Universität München zur Erlangung des akademischen Grades eines

Doktors der Naturwissenschaften (Dr. rer. nat.)

genehmigten Dissertation

Vorsitzende(r): Prof. Dr. Tom Nilges

Prüfer der Dissertation:

1. Prof. Dr. Thomas F. Fässler
2. Prof. Dr. Hubert A. Gasteiger

Die Dissertation wurde am 09.07.2019 bei der Technischen Universität München eingereicht und durch die Fakultät für Chemie am 12.08.2019 angenommen.

"The fact that we live at the bottom of a deep gravity well, on the surface of a gas covered planet going around a nuclear fireball 90 million miles away and think this to be normal is obviously some indication of how skewed our perspective tends to be."

Douglas Adams, The Salmon of Doubt: Hitchhiking the Galaxy One Last Time

Danksagung

Besonders bedanke ich mich bei meinem Doktorvater

Prof. Dr. Thomas F. Fässler

Für die Aufnahme in die Arbeitsgruppe und der Möglichkeit an seinem Lehrstuhl promovieren zu können. Vielen Dank auch für das sehr interessante Forschungsthema an dem wir konstruktiv zusammen arbeiteten und ich mit großer Freiheit eigene Ideen umsetzen konnte.

Diese Arbeit wäre auch ohne die vielen Menschen mit denen ich im Verlauf der Promotion zusammenarbeiten durfte nicht möglich gewesen. Diesen möchte ich hier ebenfalls Danken.

Dank geht an die Mitarbeiter des ASSB Bayern Projekts, welches durch das ZAE Bayern koordiniert und durch das Bayrische Staatsministerium für Wirtschaft, Landesentwicklung und Energie finanziert wird.

Ein besonderer Dank geht an Manuela Donaubauer, auf deren Unterstützung und Hilfe ich in Bezug auf organisatorische Angelegenheiten jederzeit zählen konnte und ohne deren Geduld und Organisationstalent am Lehrstuhl vieles nicht so reibungslos ablaufen würde.

Auch bei Wilhelm Klein möchte ich mich bedanken, der mir mit seinen Ratschlägen zu Veröffentlichungen und für die Laborarbeit und deren Auswertung, besonders in Bezug auf die Röntgenstrukturanalyse, immer eine große Hilfe war. Auch sein Einsatz beim Lösen von kristallografischen Fragestellungen und sein humorvoller Umgang mit Problemen hat die Zeit am Lehrstuhl bereichert.

Des Weiteren möchte ich mich bei Viktor Hlukhyy, Maria Müller und Ingrid Werner für ihren Einsatz um ein angenehmes und erfolgreiches Arbeiten am Lehrstuhl zu ermöglichen danken.

Ein besonderer Dank gilt hier auch Lorenzo Toffoletti, der mich in bemerkenswerte Weise an das Projekt herangeführt und mich dafür begeistert hat. Ohne seine großartige Vorarbeit wäre die weiterführende Arbeit nicht annähernd so erfolgreich gewesen. Umso mehr freut es mich, dass dieses Projekt fortgeführt wird und gleich drei weitere Doktoranden, Tassilo Restle, Stefan Strangmüller und David Müller, mit denen ich sehr gerne zusammengearbeitet habe, sich damit beschäftigen.

Neben den bereits genannten Personen möchte ich auch allen anderen Kollegen am Lehrstuhl für die großartige Arbeitsatmosphäre und die schöne Zeit während der Promotion danken. Ich danke Andrea, Volodymyr, Iryna, Thomas H., Carina, Herta, Manuel, Lavinia, Kerstin, Christina, Sebastian, Felix, Sabine, Michael, Marina, Jasmin, Benedikt, Lorenz, Thomas W., Thomas B., Christoph, Kevin und Frau Schier, sowie allen Masteranden, Bacheloranden, Forschungspraktikanten, Auszubildenden und Hilfswissenschaftlern.

Auch Prof. Dr. Tom Nilges und seiner Gruppe möchte ich für die schönen gemeinsamen Events und die angenehme Zusammenarbeit danken.

Prof. Dr. Hubert A. Gasteiger und seiner Gruppe, besonders Johannes Landesfeind, Christian Sedlmeier, Tanja Zünd und Benjamin Strehle, danke ich für die erfolgreiche gemeinsame Arbeit und viele erhellende Diskussionen.

Prof. Dr. Leo van Wüllen und Holger Kirchhain danke ich für Temperaturabhängige NMR Messungen zur Bestimmung der Aktivierungsenergie und den interessanten interdisziplinären Austausch.

Wolfgang G. Zeier und seiner Gruppe, speziell Christian Dietrich, danke ich ebenfalls für viele aufschlussreiche Anregungen und Einsichten in die Untersuchung von festen Elektrolyten.

Danke an Dr. Gabriele Raudaschl-Sieber für MAS NMR Messungen und die angenehmen Gespräche.

Anatoliy Senyshyn und Volker L. Deringer danke ich ebenfalls für ihre Beiträge.

Auch meinen Praktikanten, Lukas Niederegger, Yixia Zhu, Degenhart Hochfilzer, Maximilan Graf, Alexander Mutschke, Ludwig Petters, Patrick Mollik, sowie den Auszubildenden, Anja Lechner, Lukas Erdelt, Celina Rippel und Juliane Roder möchte ich für die Unterstützung im Labor und das Interesse an meinem Projekt danken. Ich hoffe, dass alle so viel Spaß an der gemeinsamen Zeit hatten wie ich.

Vielen Dank an meine Freunde, die immer zu mir gehalten haben und mit denen ich viele schöne Stunden abseits der Chemie verbringen konnte.

Meiner Familie, besonders meinen Eltern und Brüdern, danke ich für ihre Unterstützung. Dafür, dass sie mir das alles ermöglicht und mich jederzeit mit meinen Entscheidungen gefördert haben.

Mein größter Dank geht an meine Partnerin, die mein Leben immer wieder bereichert und mich regelmäßig zu Höchstleistungen motiviert. Auch ihrer Familie möchte ich für die Unterstützung danken.

Zusammenfassung

Die fortschreitende Veränderung der weltweiten Produktion und Nachfrage elektrischer Energie führt zu immer größeren Ansprüchen an Energiespeicher. Besonders im Bereich der Batterie führt das zu rasanten Entwicklungen neuer, immer leistungsfähigerer Systeme. Um Energiedichte, Leistungsdichte, Zuverlässigkeit und Kosten zu optimieren, werden sowohl bekannte Materialien weiterentwickelt, als auch neue Konzepte entworfen. Ein hohes Potential für Batterien der nächsten Generation versprechen Festkörperbatterien, für deren erfolgreiche Umsetzung feste Elektrolyte mit hohen ionischen Leifähigkeiten nötig sind. Die bekanntesten Vertreter dieser Materialgruppe sind Schwefel- und Sauerstoff-basierte Verbindungen, welche bereits umfassend untersucht wurden. Eine neue Klasse von Ionenleitern bilden Phosphor-basierte Systeme, zu denen auch Lithiumphosphidosilikate gehören. Diese wurden in dieser Arbeit erstmals systematisch untersucht.

Durch Variation der Zusammensetzung und Synthesebedingungen wurden neue Lithiumphosphidosilikate synthetisiert. Die Verbindungen $Li_3Si_3P_7$, $Li_{10}Si_2P_6$ und $Li_{14}SiP_6$ zeigen für das Li/Si/P System neue Strukturmotive. $Li_3Si_3P_7$ kristallisiert in einem neuen Strukturtyp mit Doppelschichten aus eckenverknüpften SiP_4 Tetraedern, deren beiden Hälften über eine P-Kette miteinander verknüpft sind. $Li_{10}Si_2P_6$ beinhaltet $[Si_2P_6]^{10-}$-Einheiten aus zwei verknüpften Tetraedern, welche auch in $Na_{10}Si_2P_6$ auftreten. Im Gegensatz dazu werden in $Li_{14}SiP_6$ sowohl SiP_4 Tetraeder als auch P^{3-} Einheiten realisiert. Bemerkenswerterweise weist diese Verbindung fehlgeordnete Li und Si Atome, sowie eine große Anzahl mobiler Li^+ auf. Elektrische Untersuchung der Ladungsträgermobilität zeigen eine ionische Leitfähigkeit von 1 mS cm^{-1}.

Der Transfer der Erkenntnisse von Lithiumphosphidosilikaten zu Lithiumphosphidogermanaten ermöglicht die Untersuchung des Einflusses der Anionengröße auf die Leitfähigkeit. Die Erforschung des Li/Ge/P Phasensystems führte zur Darstellung von α-Li_8GeP_4 und β-Li_8GeP_4 als auch zu Li_2GeP_2 und $LiGe_3P_3$. α-Li_8GeP_4 und β-Li_8GeP_4 weisen beide isolierte GeP_4 Tetraeder auf, wobei α-Li_8GeP_4 isotyp zu Li_8SiP_4 und β-Li_8GeP_4 verwandt mit Li_8SnP_4 ist. Die beiden Lithiumorthophosphidogermanate α- und β-Li_8GeP_4 sowie das Lithiumorthophosphidosilikat Li_8SiP_4 zeigen vergleichbare Werte für ionische Leitfähigkeiten von 10^{-5} S cm^{-1} bis 10^{-4} S cm^{-1}, aber eine deutlich höhere elektronische Leitfähigkeit für die germaniumhaltigen Verbindungen. Li_2GeP_2 bildet 3D-Netzwerke aus eckenverknüpften Tetraedern und zeigt mit 1.6×10^{-7} S cm^{-1} etwas niedrigere Leitfähigkeiten wie isotypes Li_2SiP_2 (4×10^{-7} S cm^{-1}). $LiGe_3P_3$ hingegen besteht aus Schichten von kondensierten GeP_4 und $Ge(P_3Ge)$ Tetraedern (Ge-Ge Hanteln) und zeigt keine Mobilität der Li-Ionen, aber eine bemerkenswerte Stabilität gegen Luft und Feuchtigkeit.

Untersuchung der P-armen und *Tt*-reichen (*Tt* = Si, Ge) Abschnitte der beiden ternären Phasensysteme führt zu den Verbindungen $Li_{10.68(8)}Si_5P$ und $Li_{10.1(2)}Ge_5P$. Beide Verbindungen sind aus aromatischen, planaren Tt_5-Ringen und isolierten P^{3-} Atomen aufgebaut. Trotz starker Fehlordnung der Li Atome in diesen Verbindungen kann lediglich eine elektronische Leitfähigkeit nachgewiesen werden.

Der Transfer der Informationen von Li-basierten Systemen auf Na-enthaltende Systeme führt zu einer genaueren Betrachtung von Na_3P. Für diese Verbindung wird eine Überstruktur, die auf eine Auslenkung der Na Untergitter basiert, gefunden. Elektrische Messungen zeigen hauptsächlich elektronische Leitfähigkeit.

Des Weiteren wurden bei der Untersuchung des Na/Ge/P Phasensystems die Verbindungen $Na_2Ge_3P_3$ und $Na_5Ge_7P_5$ gefunden, welche aus Röhren von 9 atomigen Käfigen aufgebaut sind. Diese Baueinheiten sind wiederkehrende Motive in verwandten Phasensystemen.

Abstract

The ongoing change in the electric energy production and demand leads to increasing requirements in energy storage. Especially, in the battery sector, this leads to a fast evolution of new, increasingly efficient systems. To optimize energy density, power density, reliability and costs, known materials are improved and new concepts are designed. A highly promising candidate for next generation batteries are all solid state batteries, which rely on solid electrolytes with high ionic conductivities. The most popular representatives of this material group are sulfur- and oxygen-based compounds, which are investigated extensively. A new class of ion conductors is represented by phosphides, which comprise lithium phosphidosilicates. These are investigated systematically within this work for the first time.

By variation of composition and synthesis conditions, new lithium phosphidosilicates are prepared. The compounds $Li_3Si_3P_7$, $Li_{10}Si_2P_6$ and $Li_{14}SiP_6$ show new structural motives in the Li/Si/P phase system. $Li_3Si_3P_7$ crystallizes with a new structure type entailing of double layers of corner sharing SiP_4 tetrahedra. The two layers are connected via a P chain. $Li_{10}Si_2P_6$ consists of $[Si_2P_6]^{10-}$ units of two condensed tetrahedra, which also occur in $Na_{10}Si_2P_6$. By contrast, in $Li_{14}SiP_6$ SiP_4 tetrahedra are realized beside P^{3-} units. Remarkably this compound exhibits disordered Li and Si atoms as well as a large number of mobile Li^+ ions. Investigations of the charge carrier mobility showed an ionic conductivity of 1 mS cm^{-1}.

The transfer of the knowledge gained from lithium phosphidosilicates to lithium phosphidogermanates enables the investigation of the effect of anion size on conductivity. The exploration of the Li/Ge/P phase system leads to the synthesis of α-Li_8GeP_4 and β-Li_8GeP_4 as well as Li_2GeP_2 and $LiGe_3P_3$. α-Li_8GeP_4 and β-Li_8GeP_4 both exhibit isolated GeP_4 tetrahedra, whereby α-Li_8GeP_4 is isotypic to Li_8SiP_4 and β-Li_8GeP_4 related to Li_8SnP_4. Both lithium phosphidogermanates α- and β-Li_8GeP_4 and the lithium phosphidosilicate Li_8SiP_4 show comparable ionic conductivities ranging from 10^{-5} S cm^{-1} to 10^{-4} S cm^{-1}, but a distinctly higher electronic conductivity for the Ge containing compounds. Li_2GeP_2 forms 3D networks of corner sharing tetrahedra and shows with 1.6×10^{-7} S cm^{-1} conductivities that are slightly lower compared to the isotypic Li_2SiP_2 (4×10^{-7} S cm^{-1}). $LiGe_3P_3$ on the other hand consists of slabs of condensed GeP_4 and $Ge(P_3Ge)$ tetrahedra (Ge-Ge dumbbells) and does not show any mobility of Li ions but a remarkably stability versus air and moisture.

Investigation of the P poor and *Tt* rich (*Tt* = Si, Ge) sections of the two ternary phase systems leads to the compounds $Li_{10.68(8)}Si_5P$ und $Li_{10.1(2)}Ge_5P$. Both compounds are built from aromatic, planar Tt_5 rings and P^{3-} units. Despite a pronounced disorder of the Li atoms in these compounds only electronic conductivity could be determined.

The transfer of knowledge from Li based systems to Na containing systems leads to a revision of Na_3P. For this compound a superstructure is found, that is caused by a dislocation of Na sublattices. Electric measurements yielded a mainly electronic conduction.

Further, during the investigation of the Na/Ge/P phase system the compounds $Na_2Ge_3P_3$ and $Na_5Ge_7P_5$ are found, which consist of tubess of 9 atom cages of Ge and P. These building blocks are recurring motives found in related systems.

List of Abbreviations

0b	zero bonded
1b	one bonded
2b	two bonded
3b	three bonded
4b	four bonded
A	alkali metal atom
AE	alkaline earth metal atom
ASSB	all solid state battery
bcc	body centered cube
ccp	cubic closed pack
CEI	cathode electrolyte interface
c-SiP	cubic silicon phosphide
DFT	density functional theory
DSC	differential scanning calorimetry
E	element atom
EIS	electrochemical impedance spectroscopy
EV	electronic vehicles
hcp	hexagonal close pack
LFP	lithium iron phosphate
LIB	lithium-ion battery
MAS	magic angle spinning
MD	molecular dynamics
MEM	maximum entropy method
NCA	$LiAl_{1-x-y}Co_xNi_yO_2$
NMC	$LiMn_{1-x-y}Co_xNi_yO_2$
NMR	nuclear magnetic resonance
O_h	oktahedron
o-SiP	orthorhombic silicon phosphide
Pn	pnictide atom
PND	powder neutron diffraction
PXRD	powder X-ray diffraction
SC-XRD	single crystal X-ray diffraction
SE	solid electrolyte

SEI	solid electrolyte interphase
S.O.F	site occupation factor
T_d	tetrahedron
Tt	tetrel atom
X	halide atom

Table of Content

Declaration

This dissertation is composed as a publication-based thesis. Articles published in peer reviewed journals and manuscripts prepared for publication are included in this work. The articles are compiled in Chapter 5. All peer reviewed articles and their bibliographic data are listed in Chapter 6. The relevance of this work as well as a review of significant literature is given in Chapter 1. An overview about experimental synthetic and characterization procedures and contributions of coauthors is presented in Chapter 2. In Chapter 3 a summary of the most intriguing features discussed for every embedded article is stated. A conclusion and potential impact on future work is presented in Chapter 4.

1 Introduction

1.1 Electric Energy Storage

Within the past decades, various countries have declared intentions, which will lead to a strongly increased demand for electric energy storage media in the coming years. [1-5] Driven by air pollution concerns and climate change, the energy transition will be further realized. Fossil fuel and nuclear fission based power plants are planned to be stepwise replaced by renewable energy plants.[6,7] Some of those newly installed systems, especially solar and wind based plants, show a strongly varying energy output that needs to be buffered.[8-11] Secondly, in the transportation sector, the share of combustion engines based vehicles is going to be reduced and substituted by electronic vehicles (EV).[12-14] And thirdly, the digital transformation, which goes along with more portable and wireless electronics, will be further expedited.[15,16]

The buffering of power plant output is currently dominated by pumped-storage hydroelectricity with estimated 4.5 of 4.7 TWh in 2017.[17] In a smaller scale, also molten salt thermal storage, compressed air storage, flywheels and electrochemical storage media, like lead acid, vanadium flow, lithium-ion and sodium based batteries, are in use.[17-19] However, due to changing demands coming along with an increasing share of renewables, the amount of non-pumped-storage hydroelectricity is expected to strongly increase. Additionally, in the transportation sector and for mobile electronics, almost exclusively lithium-ion batteries are applied due to their high specific energy density. The worldwide annual production of energy storage capacity is therefore expected to increase from 120 GWh to more than 500 GWh until 2025.[17,20,21]

1.2 Batteries

Batteries belong to the electrochemical storage devices and can be categorized into various types. While primary cells tend to exhibit high energy densities but are not rechargeable, secondary cells are rechargeable, which makes them favorable candidates for long term application with high energy flux as addressed in chapter 1.1. The secondary cells can be further subdivided in different forms that differ in cell voltage, specific capacity and cost and are named after the materials used, as lead-acid, lithium-ion, nickel-cadmium, nickel metal hydride, sodium-sulfur, vanadium flow batteries and many more. Since lead-acid and lithium-ion batteries are the most common ones, these will be described here in more detail.[22,23]

In general, batteries are utilizing compounds with different chemical potentials and their redox reactions to store and release electric energy. Therefore, the main parts of a battery are redox active

materials in a positive and a negative electrode. In batteries, they are usually referred to as cathode and anode, respectively. Furthermore, an electrolyte is necessary. For practical and structural purposes, also a casing, separator and current collectors are necessary. The electrodes attached to current collectors are placed in the electrolyte and are electronically separated within the cell by the separator. During discharging in the negative electrode, an oxidation reaction takes place, while the positive electrode gets reduced and an ion exchange takes place via the electrolyte. Electrons cannot pass the electronical insulating electrolyte or separator and can be used via an external circuit to power consumer load. During charging, an external power source is applied that inverts the redox reaction within the cell, the negative electrode becomes reduced and the positive one oxidized, again accompanied by ion exchange via the electrolyte.[22,23] For lead-acid batteries, the negative electrode is Pb metal, the positive electrode PbO_2, and the electrolyte H_2SO_{4aq}. In the discharge process, formally Pb is oxidized to $Pb(II)SO_4$ and $Pb(IV)O_2$ is reduced to $Pb(II)SO_4$ at the same time. As mentioned before, this reaction is inverted during charging.[22-24] While in the described lead-acid battery the electrochemistry is based on a dissolution and precipitation of Sulfate, in lithium-ion batteries a migration of Li between the electrodes is used. Typical materials which can be applied as negative electrode are C/LiC_6 (graphite/lithium graphite) on a copper current collector, $LiCoO_2/CoO_2$ on an aluminum current collector as positive electrode, and $LiPF_6$ in ethylene carbonate as an electrolyte. At discharging, Li deintercalates from the lithium graphite, dissolves in the electrolyte as Li^+, while Li^+ reacts with CoO_2 to form $LiCoO_2$. The formal oxidation of Li to Li^+ is accompanied by a reduction of Co^{4+} to Co^{3+} (Fig. 1.1).[23,25-28]

These differences in materials and cell chemistry have a huge impact on the macroscopic properties of the cells. For example, the number of charge carriers accessible per weight unit gives a specific capacity, which is an important indicator for the use in EVs and portable electronics. The maximum achievable specific capacity for the previous described electrode combinations of 158 mAh g^{-1} for Li-ion and 83 mAh g^{-1} for lead acid illustrate why Li-ion systems are used in that field of application. Additionally, the chemical potential of the materials defines the cell voltage and affects the specific energy, which is again superior in Li based systems. They exhibit theoretical and practical specific energies of ~550 Wh kg^{-1} and ~150 Wh kg^{-1}, respectively, compared to 170 Wh kg^{-1} and ~35 Wh kg^{-1} for lead-acid batteries.[22,23] High cell voltages go also along with a necessary replacement of the electrolyte. As water decomposes at a voltage larger than 1.5 V (1.23 V plus overpotential)[22,29], for higher chemical potential differences organic electrolytes like ethylene carbonate or propylene carbonate are used.[26,30,31] Approaching their electrochemical stability window edges, also these liquids react on the electrode surface and form

solid/cathode electrolyte interphase (SEI/CEI), which lead to a capacity drop but are necessary for the safe operation of the cell.[28,32,33]

Driven by the high demand and changing requirements, battery systems undergo a continuous optimization process. Batteries combining high energy density for long operation times, high power density for a good peak performance and, at the same time, good safety performance, low production costs and abundant raw materials are desirable. In Li based systems currently different electrode materials, such as lithium titanate or silicon based anodes, and on the cathode side lithium iron phosphate (LFP) or mixed metal oxides like $LiMn_{1-x-y}Co_xNi_yO_2$ (NMC), $LiAl_{1-x-y}Co_xNi_yO_2$ (NCA), are used or are in development.[34-37] Parallel to this continuous ongoing improvements, new concepts for next generation lithium batteries are investigated like lithium sulfur, lithium air or all solid state batteries which promise different advantages compared to state of the art Li-ion technology.[36-39] These developments are supported by research on different types of batteries such as Na based batteries for stationary devices due to cost and abundance reasons.[40,41]

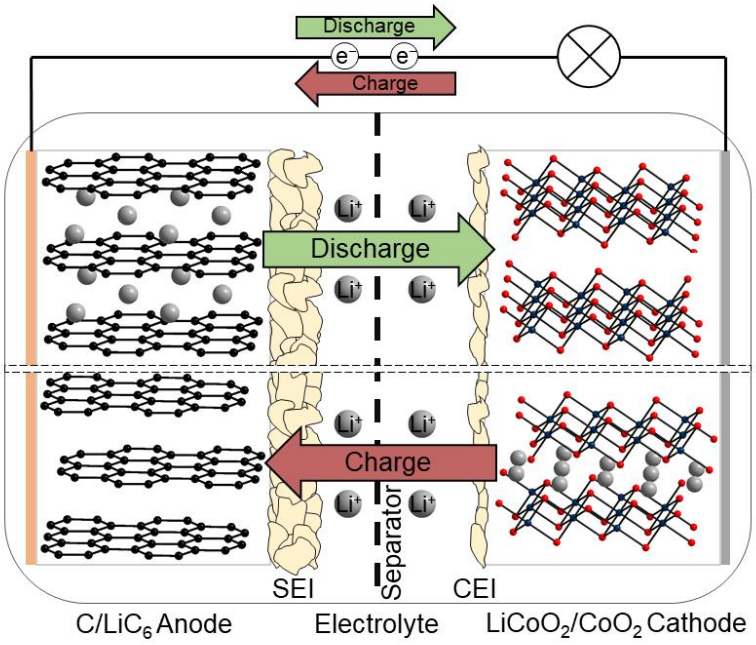

Figure 1.1: Sketch of a battery cell on the basis of a lithium-ion cell with a C/LiC_6 anode on a Cu current collector and a $LiCoO_2/CoO_2$ cathode on an Al current collector. Charge carrier movement during charging (red) and discharging (green) is indicated by arrows.

1.3 All Solid State Batteries

One of the most promising candidates for next generation Li batteries are all solid state batteries (ASSB).[20,39,42] In these batteries, the liquid electrolyte is replaced by a solid inorganic, crystalline or glassy material or an organic polymer. This exchange is expected to come along with a variety of advantages. A main point discussed in literature is the increasing safety. The usually flammable and toxic liquid is substituted by a solid which is resistant to thermal decomposition, mechanic damage and leakage. The inability of leakage also enables savings concerning inactive parts of the cell such as casing leading, to a lower mass and higher specific energy.[43,44] In addition, taking into account electrochemical and mechanical properties of the solid electrolyte (SE), utilization of Li metal anodes is conceivable. This anode type promises high energy densities due to its low weight and high Li content. In combination with liquid electrolytes, Li anodes tend to form dendrites upon cycling and rapidly lead to short circuits. In ASSBs, this mechanism of short circuit formation could be blocked due to the mechanical strength of SEs.[45,46] By introducing a SE, also capacity fading induced by transfer of soluble species from one electrode to the other can be suppressed.[47] Further, in liquid electrolytes, beside Li^+ also anions move within the electric field. Thus, they also contribute to the measured ionic conductivity and form concentration gradients resulting in reduced power densities. The share of the electrochemical active species in the total ion mobility μ is represented by the transference number t_{Li}:

$$t_{Li} = \frac{\mu_{Li}}{\sum_i \mu_i} \tag{1}$$

In liquid-based systems, t_{Li} between 0.2 and 0.4 are realized. In SE, the anion framework is static leading to transference numbers close to unity and therefore facilitate higher power densities.[48] Despite these numerous potential advantages of SEs, a simple replacement of the liquid electrolyte does not lead to optimal results. The SEs should exhibit different properties dependent on the part in the cell they are used for. A pure electrolyte should exhibit high ionic but no electronic conductivity, while for an SE used in composite electrodes high ionic and electronic conductivities as well as stability against the active material are desirable. These properties support ion transfer into the electrode similar to a liquid electrolyte filled pore in a conventional cell's electrode as well as electron transfer between grains and to the current collector (Fig. 1.2). Nevertheless, a key feature of solid electrolytes is still their lithium ion conductivity. While a lot of materials have been found to show mobile Li^+, only few exhibit ionic conductivities similar or exceeding the ones of liquid electrolytes of ~10^{-2} S cm^{-1}. The highest conductivities so far are measured for inorganic,

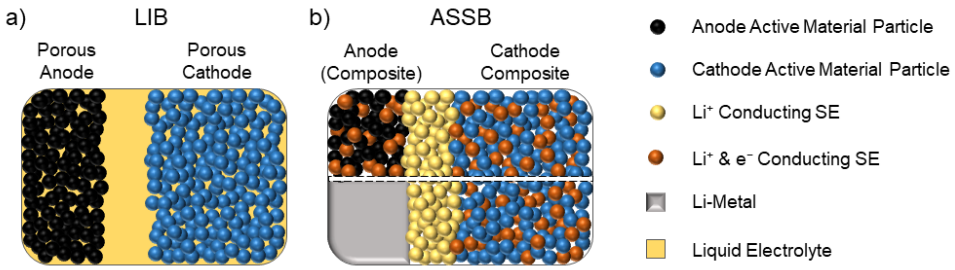

Figure 1.2: Comparison of cell architecture of LIB and potential designs of ASSB. a) Porous electrodes in LIBs are filled with the liquid electrolyte. b) In ASSB Li^+ conduction into the electrodes can be supported with a mixed conducting SE (top). Corresponding cell design with a Li metal anode (bottom).

crystalline materials. Polymer based materials in general show lower conductivities. Since they also feature different conduction mechanisms and difficulties to overcome, the following discussion will focus on inorganic polycrystalline materials. [39,49,50]

The ionic resistance of a pure, polycrystalline material arises from at least two components, the bulk or intragrain resistance and the grain boundary or intergrain resistance. The latter originates from the transfer of Li^+ from one grain to another and is usually strongly affected by the contact area, while the bulk resistance is an intrinsic property of the material and depends on the crystal structure.[44,51] On a microscopic level, Li^+ hops from its original position to a neighboring vacant site within an immobile framework of anions. In this process, it is passing an unfavorable transition state defining the activation energy.[52] For a slow ionic motion, independent hops into defect positions or interstitial sites are proposed. With increasing ionic conductivity also concerted mechanisms including many Li^+ at the same time appear conceivable.[53,54] Beside various approaches that have been developed to improve the ionic conductivity in certain inorganic, crystalline systems, information on the fundamental mechanism of conduction are scarce and prediction of promising ionic conductors is difficult. To increase the conductivity, one approach includes the variation of the particle size and the shape or the contact between grains. As the resistance of a polycrystalline material consists of a bulk and grain boundary contribution, changing the surface to volume ratio or contact surface leads to altering shares in the materials resistance. Nevertheless, much larger changes are observed via approaches focusing on the crystal structure and composition. As can be seen in formula 2, the ionic conductivity σ can be increased via two methods: increasing the number of mobile species n, Li^+ or voids, or increasing the mobility μ of existing ions, which is in general realized by lowering the energy barrier E_A for ion hopping.[48,55]

$$\sigma = \sum_{i} \mu_i n_i Z_i e \tag{2}$$

$$\mu \propto e^{-\frac{E_A}{kT}} \tag{3}$$

Whereas Z is the charge of the ion, e is the unit charge of electrons, k the Boltzmann constant and T the temperature. By practical means, the introduction of defects by e.g. introducing mechanical stress or doping can be used to adjust the concentration of Li^+ and vacant sites. Another method is the partial aliovalent ion substitution on the (poly-) anion side. An often observed statistical mixing of those anions leads to a mixed anion effect additionally reducing the activation energy.[53,56] As a further method, increasing the ion softness, for example by isovalent substitution with heavier homologues, strongly decreases the activation barrier.[57,58]

Within the past decades, different classes of crystalline, solid electrolytes for Li batteries have been found and investigated. The largest groups represent oxide and sulfide based systems, but also halide,[59] and nitride[60] systems exhibit intriguing properties.[49,61] Detailed studies of these different groups show different advantages and disadvantages also with respect to the general benefits expected from SEs. Oxide ion conductors can be subdivided into their most important classes: garnets (e.g. $Li_7La_3Zr_2O_{12}$),[62] LiSICON (e.g. $Li_{14}ZnGe_4O_{16}$),[63] NaSICON type (e.g. $Li_{1.3}Ti_{1.7}Al_{0.3}(PO_4)_3$),[64] perovskites (e.g. $Li_{3x}La_{2/3-x}\square_{1/3-2x}TiO_3$)[65] and antiperovskites (e.g. Li_3OCl).[66] In general, oxides show the expected good chemical and electrochemical stability against air and various electrode materials. However, in air carbonate formation, is observed at the surface leading to additional resistances[67] and, in combination with Li anodes, only few materials, such as the garnet $Li_7La_3Zr_2O_{12}$, are stable.[68,69] Also, their conductivity is relatively low and compounds like $Li_{6.55}La_3Zr_2Ga_{0.15}O_{12}$ (1.3×10^{-3} S cm^{-1})[70] that exceed 10^{-3} S cm^{-1} are rare. Sulfide based materials represent a possible solution to the low conductivity of the SE. The compound classes of Thio-LiSICON (e.g. $Li_{3.25}Ge_{0.25}P_{0.75}S_4$)[71], LGPS type (e.g. $Li_{10}GeP_2S_{12}$)[72] and argyrodites (e.g. Li_6PS_5Br),[73] show, in general, higher conductivities compared to oxides (Fig. 1.3a) and, to date, the LGPS type compound $Li_{9.54}Si_{1.74}P_{1.44}S_{11.7}Cl_{0.3}$ shows the highest Li^+ conductivity at room temperature with 2.5×10^{-2} S cm^{-1}.[74] LGPS type materials are, like Thio-LiSICONs, composed of ES_4-tetrahedra (E = P, Si, Ge, Sn), which are more polarizable than the EO_4-tetrahedra found in LiSICON and NaSICON type materials. Within the fastest Li^+ conductors, these centered tetrahedra are arranged in a manner that forms interconnected 1D channels for Li^+ movement. In the last-mentioned sulfide based class of Li argyrodites, the tetrahedra form a cubic close pack (*ccp*). In this lattice, additional S^{2-} and X^- (X = Cl, Br, I) occupy the octahedral and half of the tetrahedral voids. Li^+ moves in the vicinity of the isolated S^{2-} and X^- (Fig. 1.3b). Additionally to their high conductivity, sulfide materials are soft and can be easily

pressed into dense films.[39] On the other hand, they show small electrochemical stability windows and are often sensitive to air and moisture. To apply these materials in ASSB, protection strategies have to be implemented to avoid reactions in contact with electrodes.[68,75]

To overcome the described drawbacks, new materials with alternating properties are desirable and in development. Recently, a novel class of ion conductors has been reported, which can be derived from cubic closed packs of P atoms as found in Li_3P ($\sigma(Li_3P) = 10^{-4}$ S cm^{-1}).[76,77] Further, by introducing Si, which occupies tetrahedral voids in the P lattice, SiP_4 units are formed. These structural elements are comparable to EO_4 and ES_4 tetrahedra (E = P, Si, Ge) found in many good Li^+ conductors [63,71-74]. The resulting lithium phosphidosilicates have been shown to exhibit ionic conductivities of up to 6×10^{-6} S cm^{-1} at room temperature.[78,79] The high concentration of Li^+ in these compounds, which result from the substitution of chalcogenides with phosphides, is expected to lead to further compounds with high Li^+ conductivities.

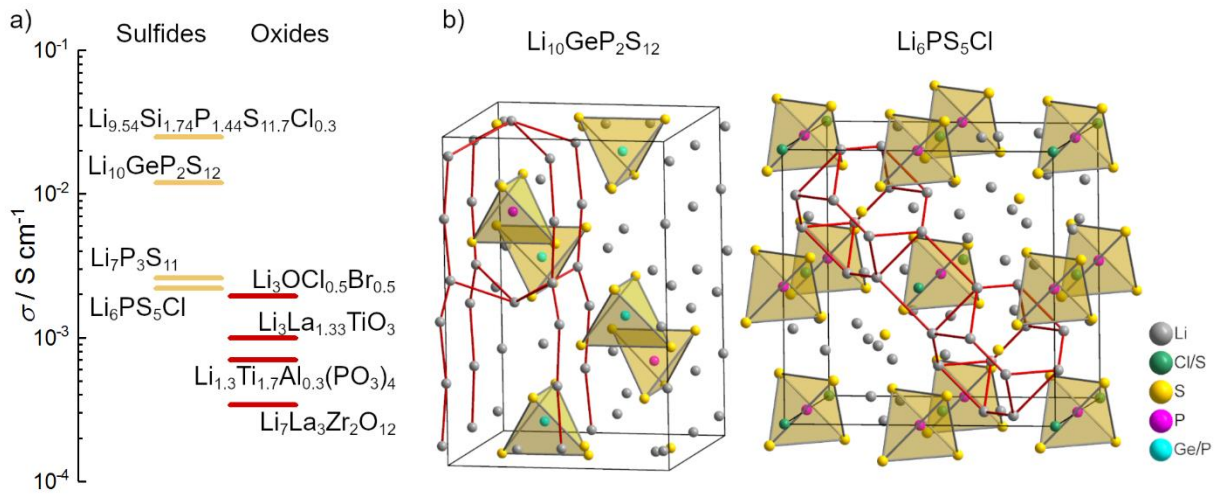

Figure 1.3: a) Ionic conductivity σ of selected sulfidic (yellow) and oxidic (red) Li-ion conductors. b) Crystal structures of Li^+ conductors $Li_{10}GeP_2S_{12}$ (LGPS) and Li_6PS_5Cl (Li-argyrodite). Yellow tetrahedra depict PS_4 and GeS_4 building blocks and red lines visualize selected Li hopping pathways.

1.4 The Ternary Li/Si/P Phase System

The recently reinvestigated lithium phosphidosilicates showed high ionic conductivities and an intriguing structural chemistry. To get insight into realized and possible structures in the ternary Li/Si/P system, properties of the constituents will be discussed. Lithium is the lightest alkali metal and crystallizes with a body centered cubic (*bcc*) structure. It tends to form ionic or polar compounds, in the formal oxidation state of 0 or +1. On the other hand, silicon is a semiconductor with diamond-like structure and has a high tendency to form homoatomic Si-Si and heteroatomic bonds. As a tetrel element, up to four bonds and oxidation states of −4 to +4 are possible. Phosphorus is a non-metal and owns a large number of different allotropes such as the very reactive white phosphorus, comprising P_4 tetrahedra, the thermodynamic stable, sheet like black

phosphorus, the amorphous red phosphorus, violet or *Hittdorf*'s phosphorus, consisting of P-strands, and many more. In these allotropes, phosphorus forms three bonds but in compounds also phosphonium or phosphate like building units with four bonds are observed and formal oxidation states ranging from −3 to +5 are possible.[80]

Binary compounds in the Li/P and Li/Si system play an important role in high capacity anodes of Si and P, respectively. Compared to graphite based anodes with a theoretic capacity of 372 mAh g^{-1}, these alloying or conversion anodes exhibit capacities of up to 3572 mAh g^{-1},[81] but high volume changes during lithiation and delithiation, and following strong capacity losses impede their application.[82] The binary Li/P and Li/Si compounds belong to the *Zintl* phases, polar intermetallic phases that follow the 8-N electron rule. Hence, these phases are semiconductors with diamagnetic behavior and show higher melting points compared to their elemental constituents. They consist of main group elements from both sides of the *Zintl* line between main group 13 and 14. As in *Zintl* phases a complete electron transfer from the alkali or alkaline earth element to the more electronegative p-block element is formulated, lithium formally transfers its single 2s electron to P and Si.[83,84] For the lithium richest lithium phosphide Li_3P this results in P^{3-} anions.[85] With decreasing Li content more covalent bonds between the P atoms emerge, and chains (LiP)[86], cages (Li_3P_7)[87] or networks (LiP_5, LiP_7)[88,89] are formed. In the Li/Si phase system also compounds with alternating properties such as high electric conductivity and paramagnetic behavior exist. These "metallic *Zintl* phases" or polar intermetallics such as $Li_{17}Si_4$,[90] $Li_{15}Si_4$,[91,92] $Li_{13}Si_4$,[93] Li_7Si_3[94] and $Li_{12}Si_7$[95] comprise unpaired electrons, which cause these different characteristics. $Li_{17}Si_4$ and $Li_{15}Si_4$, for example, are built from unbound Si units, which are expected to have a formal charge of 4−. However, in $Li_{17}Si_4$, one excessive electron per formula unit is provided by lithium, while $Li_{15}Si_4$ "lacks" one electron, leading to the description of $(Li^+)_{17}$ $(Si^{4-})_4$ e^- and $(Li^+)_{15}$ $(Si^{4-})_4$ h^+, respectively. Despite the alternating properties in these phases, also more condensed Si subunits occur with decreasing Li content. In $Li_{13}Si_4$ and Li_7Si_3 Si_2 dumbbells and in Li_7Si_3 planar, pentagonal Si_5 rings and trigonal Si_4 stars are found.

Contrary to the clearly ionic Li/P and Li/Si structures, binary Si/P compounds have a higher tendency to form polar covalent networks. Nevertheless, cubic SiP_2 (*c*-SiP_2), which crystallizes in the pyrite structure type, can be described ionically as P_2^{4-} dumbbells in a *bcc* of Si^{4+}, leading to octahedral SiP_6 and tetrahedral $P(Si_3P)$ units.[96] On the other hand, orthorhombic SiP_2 (*o*-SiP_2) forms covalent Si-P tubes connected to 2D slabs. Within the tubes, armchair-like 6-membered rings and 5-membered rings are formed, resulting in local atomic environments of SiP_4 tetrahedra

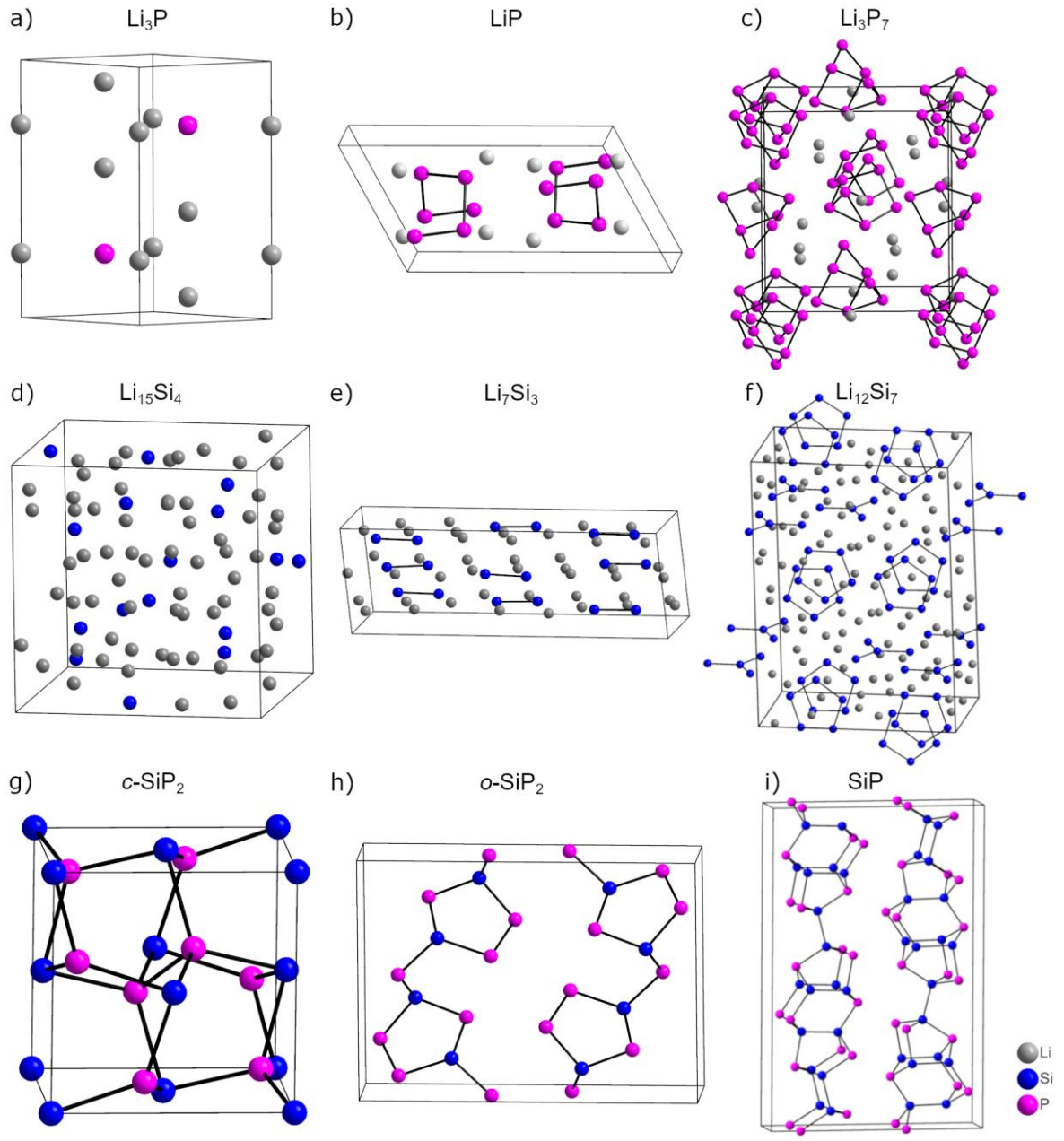

Figure 1.4: Structures of selected binary compounds in the Li/Si/P phase system with different anionic building blocks a) Li_3P, b) LiP c) Li_3P_7, d) $Li_{15}Si_4$, e) Li_7P_3, f) $Li_{13}Si_7$, g) *c*-SiP_2, h) *o*-SiP_2 and i) SiP.

as well as PSi_3 and $P(SiP_2)$ trigonal pyramids.[97] A related structure to *o*-SiP_2 is realized in SiP. Here, also covalently bound slabs are formed from tubes with an alternative Si and P distribution. A different connectivity of these tubes leads solely to $Si(P_3Si)$ tetrahedra and PSi_3 pyramids as building blocks (Fig. 1.4).[98]

Introducing an electropositive metal as third element in these Si-P structures leads to phosphidosilicates or phosphosilicides. These compounds follow the construction principles of *Zintl* phases and comprise metal cations and reduced covalently bound Si-P units. In most cases, tetrahedral and trigonal pyramidal building blocks, of which SiP_4 is the most prominent one, are retained. Reported transition metal phosphidosilicates, such as $ZnSiP_2$, AuSiP, Ag_2SiP_2 and

$IrSi_3P_3$, exhibit highly condensed 3D frameworks of centered Si-P tetrahedra and trigonal pyramids.[99-104] The compound $ZnSiP_2$[99] realizes a network of corner-sharing SiP_4 tetrahedra and shows, in accordance to its non-centrosymmetric space group, good properties for application as non-linear optical material. For alkaline earth metals, additionally to highly condensed frameworks, also compounds with a lower dimensionality, degree of condensation and increased network charge of Si-P subunits are found reaching their maximum with AE_4SiP_4 (*AE* = Sr, Ba)[105] comprising $[SiP_4]^{8-}$ building blocks.[106-109] Alkali metal phosphidosilicates behave similar. Frameworks built from corner-sharing SiP_4 tetrahedra, forming supertetrahedra in $LiSi_2P_3$, Li_2SiP_2, $NaSi_2P_3$, $Na_{19}Si_{13}P_{25}$ and many more[78,79,110], layers (KSi_2P_3),[111] chains (K_2SiP_2),[112] dimeric edge-sharing $Si_2P_6^{10-}$ units in $Na_{10}Si_2P_6$[113] and isolated tetrahedra in Li_8SiP_4,[78] but also more exotic units like carbonate like SiP_3^{5-} in Cs_5SiP_3 are realized.[114] Focusing on the Li/Si/P ternary system, one finds all known compounds on a pseudo binary line between Li_3P and the yet unknown "Si_3P_4". By formal addition of Li_3P to $LiSi_2P_3$, it can be transformed first to Li_2SiP_2 and finally to Li_8SiP_4. On this line, more or less condensed Si-P subunits with solely heteroatomic bonds are present (Fig. 1.5). Beside that line it is conceivable to find more compounds with Si-Si or even P-P bonds, which are also present in the binaries SiP and *o*-SiP_2.

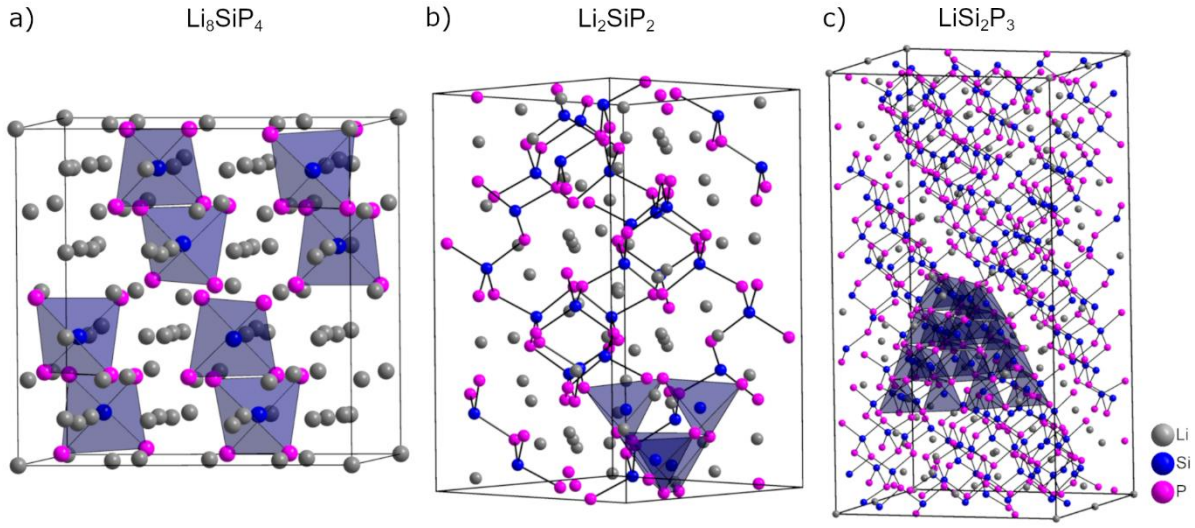

Figure 1.5: Crystal structures of the lithium phosphidosilicates a) Li_8SiP_4, b) Li_2SiP_2 and c) $LiSi_2P_3$. All compounds are built from SiP_4 tetrahedra (examples highlighted blue). With reduced Li content they are condensed to supertetrahedra.

1.5 Scope and Outline

The goal of this work is the synthesis and characterization of novel phosphide based Li^+ conductors for potential application as SEs in ASSBs. These materials are expected to exhibit high ionic conductivities, due to high lithium concentration caused by the charge of anionic phosphorus and fast ion hopping resulting from its anion softness. The recently electronically investigated lithium phosphidosilicates Li_8SiP_4 and Li_2SiP_2 exhibit up to 6×10^{-6} S cm^{-1} for Li_8SiP_4.[78] Beside the ionic conductivity, these materials entail low material density and abundant constituents.

In order to get a better understanding of the chemistry taking place in the Li/Si/P phase system, alternative compositions and new synthetic approaches leading to higher purity or new materials are investigated. Two compounds with intriguing structural features, $Li_3Si_3P_7$ and $Li_{10}Si_2P_6$, are presented in chapter 3.1. Their structure is characterized via single crystal X-ray diffraction (SC-XRD). The purity of the powder samples from optimized syntheses are investigated with powder X-ray diffraction (PXRD) and magic angle spinning nuclear magnetic resonance (MAS NMR) spectroscopy.

Experiments to increase the Li^+ content and, therefore, the charge carrier concentration on the pseudo binary Li_3P-"Si_3P_4" line result in $Li_{14}SiP_6$ (chapter 3.2). The structure is characterized via powder neutron diffraction (PND), PXRD, SC-XRD and MAS NMR spectroscopy and the ionic mobility and conduction mechanism are investigated via impedance spectroscopy, T-dependent static NMR spectroscopy, PND and density functional theory (DFT) calculations.

The results from the Li/Si/P system are transferred to the Li/Ge/P system to investigate the effect of ion size in this compound class. In chapter 3.3, the synthesis of previously described Li_8SiP_4 is improved and translated to the Ge analogues. Single crystals and powders are investigated with diffraction techniques and impedance spectroscopy and T-dependent static NMR spectroscopy are used to analyze Li ion motion. Additionally, the lithium poorer compounds Li_2GeP_2 and $LiGe_3P_3$ are introduced.

Resulting from the search of alternative structural features in Li/*Tt*/P phase systems (*Tt* = Si, Ge), investigation of the *Tt* (*Tt* = Si, Ge) rich compositions yields the compounds $Li_{10.68(8)}Si_5P$ and $Li_{10.1(2)}Ge_5P$. These materials are characterized with SC-XRD, PXRD and MAS NMR spectroscopy.

First experiments to transfer the results from phosphide based Li^+ conductors to Na^+ containing systems showed discrepancies for the structure of Na_3P to its published structure. Its structure was redetermined on the basis of SC-XRD (chapter 3.5). Additionally, the thermal and electronic behavior was investigated with differential scanning calorimetry (DSC) and impedance spectroscopy.

Further, in the ternary Na/Ge/P system, the compounds $Na_2Ge_3P_3$ and $Na_5Ge_7P_5$ have been found. These compounds are characterized via X-ray diffraction techniques and compared to related structures.

References

[1] UNFCCC. Conference of the Parties (COP), *Report of the Conference of the Parties on its twentyfirst session, held in Paris from 30 November to 13 December 2015. Addendum. Part two: Action taken by the Conference of the Parties*, Paris Climate Change Conference, Paris, France, United Nations Office at Geneva, Geneva, Switzerland, **2015**.

[2] United Nations, *Status of Treaties, Paris Agreement*, United Nations Treaty Collection, https://treaties.un.org/pages/ViewDetails.aspx?src=TREATY&mtdsg_no=XXVII-7-d&chapter=27&clang=_en, **2016**, 20.03.2019.

[3] UNECE, *Gothenburg Protocol*, United Nations Economic Commission for Europe, http://www.unece.org/environmental-policy/conventions/air/guidance-documents-and-other-methodological-materials/gothenburg-protocol.html, **1999**, 20.03.2019.

[4] United Nations Environment Programme, *Towards a Pollution-Free Planet Background Report*, United Nations Environment Programme, Nairobi, Kenya, **2017**.

[5] European Environment Agency, *Improving Europe's air quality – measures reported by countries*, European Environment Agency, https://www.eea.europa.eu/themes/air/improving-europe-s-air-quality, **2018**, 21.03.2019.

[6] European Union, *DIRECTIVE 2009/28/EC OF THE EUROPEAN PARLIAMENT AND OF THE COUNCIL of 23 April 2009 on the promotion of the use of energy from renewable sources and amending and subsequently repealing Directives 2001/77/EC and 2003/30/EC*, EUR-Lex, https://eur-lex.europa.eu/legal-content/EN/ALL/?uri=CELEX:32009L0028, **2009**, 21.03.2019.

[7] REN21, *Renewables 2018 Global Status Report*, REN21 Secretariat, Paris, France, **2018**.

[8] M. Kaltschmitt, W. Streicher, A. Wiese, *Erneuerbare Energien. Systemtechnik, Wirtschaftlichkeit, Umweltaspekte*. Springer, Berlin/Heidelberg, Germany, **2013**.

[9] EWEA, *Wind Energy - The Facts - an Analysis of Wind Energy in the EU-25*, European Wind Energy Association, Brussels, Belgium, **2007**.

[10] S. L. Piano, K. Mayumi, *Appl. Energy* **2017**, 186, 167-176.

[11] X. Li, D. Hui, X. Lai, *IEEE T. Sustain. Energ.* **2013**, 4, 464-473.

[12] IEA, *Global EV Outlook 2017 - two million and counting*, International Energy Agency, https://www.iea.org/publications/freepublications/publication/GlobalEVOutlook2017.pdf, **2017**, 05.04.2019.

[13] DERA, *Verfügbarkeit von Kobalt bis 2026 -Monitoring für eine sichere Rohstoffversorgung*, Batterieforum Deutschland 2019, Berlin Germany, **2019**.

[14] Blomberg – New Energy Finance, *Electric Vehicle Outlook 2018*, Blomberg, https://bnef.turtl.co/story/evo2018?teaser=true, **2018**, 05.04.2019.

[15] European Union, *Watify – Boosting Technological Tranformation*, European Commission, https://ec.europa.eu/growth/tools-databases/dem/watify/, **2017**, 05.04.2019.

[16] World Economic Forum, *Digital Transformation*, World Economic Forum, http://reports.weforum.org/digital-transformation/wp-content/blogs.dir/94/mp/files/pages/files/dti-executive-summary-20180510.pdf, **2018,** 05.04.2019.
[17] IRENA, *Electricity Storage and Renewables: Costs and Markets to 2030*, International Renewable Energy Agency, Abu Dhabi, United Arab Emirate, **2017**.
[18] IEA, *Technology Roadmap Energy Storage*, International Energy Agency, Paris, France, **2014**.
[19] ICEF, *Energy Storage Roadmap – Technology and Institution*, Innovation for Cool Earth Forum, https://www.icef-forum.org/pdf2018/roadmap/Energy_Storage_Roadmap_ICEF2017.pdf, **2017**, 08.04.2019.
[20] European Union, *Commission Staff Working Document - Report on Raw Materials for Battery Applications*, European Commission, Brussels, Belgium, **2018**.
[21] BNEF, *Lithium-ion Battery Costs and Market*, Bloomberg – New Energy Finance, https://data.bloomberglp.com/bnef/sites/14/2017/07/BNEF-Lithium-ion-battery-costs-and-market.pdf, **2017**, 08.04.2019
[22] C. H. Hamann, A. Hamnett, W. Vielstich, *Electrochemistry*, 2nd Edition, Wiley-VHC, Weinheim, Germany, **1998**.
[23] C. Daniel, J. O. Besenhard, *Handbook of Battery Materials*, Volume 1, Wiley-VHC, Weinheim, Germany, **2012**.
[24] G. J. May, A. Davidson, B. Monahow, *J. Energy Storage* **2018**, 15, 145-157.
[25] K. Ozawa, *Solid State Ionics* **1994**, 69, 212-221.
[26] M. Winter, B. Barnett, K. Xu, *Chem. Rev.* **2018**, 118, 11433-11456.
[27] V. Etacheri, R. Marom, R. Elazari, G. Salitra, D. Aurbach, *Energ. Environ. Sci.* **2011**, 4, 3243-3262.
[28] J. B. Goodenough, K.-S. Park, *J. Am. Chem. Soc.* **2013**, 135, 1167-1176.
[29] K. Mizushima, P. C. Jones, P. J. Wiseman, J. B. Goodenough, *Mater. Res. Bull.* **1980**, 15, 783-789.
[30] W. S. Harris, *Electrochemical Studies in Cyclic Esters*; Dissertation submitted to University of California, Berkeley, USA, **1958**.
[31] D. Guyomard, J. M. Tarascon, *J. Electrochem. Soc.* **1992**, 139, 937-948.
[32] P. Verma, P. Maire, P. Novák, *Electrochim. Acta* **2010**, 55, 6332-6341.
[33] K. Edström, T. Gustafsson, J. O. Thomas, *Electrochim. Acta* **2004**, 50, 397-403.
[34] G. E. Bomgren, *J. Electrochem. Soc.* **2017**, 164, A5019-A5025.
[35] N. Nitta, F. Wu, J. T. Lee, G. Yushin, *Mater. Today* **2015**, 18, 252-264.
[36] D. Deng, *Energy Sci. Eng.* **2015**, 3, 385-418.
[37] M. Li, J. Lu, Z. Chen, K. Amine, *Adv. Mater.* **2018**, 30, 1800561.
[38] X. Shen, H. Liu, X.-B. Cheng, C. Yan, J.-Q. Huang, *Energy Storage Mater.* **2018**, 12, 161-175.
[39] J. Janek, W. G. Zeier, *Nat. Energy* **2016**, 1, 1-4.
[40] K. Chayambuka, G. Mulder, D. L. Danilov, P. H. L. Notten, *Adv. Energy Mater.* **2018**, 8, 1800079.
[41] Y. Fang, L. Xiao, Z. Chen, X. Ai, Y. Cao, H. Yang, *Electrochemical Energy Reviews* **2018**, 1, 294-323.
[42] Z. Gao, H. Sun, L. Fu, F. Ye, Y. Zhang, W. Luo, Y. Huang, *Adv. Mater.* **2018**, 30, 1705702.

[43] J. B. Goodenough, *J. Solid State Electrochem.* **2012**, 16, 2019-2029.
[44] P. Knauth, H. L. Tuller, *J. Am. Ceram. Soc.* **2002**, 85, 1654-1680.
[45] D. Lin, Y. Liu, Y. Cui, *Nat. Nanotech.* **2017**, 12, 194-206.
[46] C. Yang, K. Fu, Y. Zhang, E. Hitz, L. Hu, *Adv. Mater*. **2017**, 29, 1701169.
[47] Y. V. Mikhaylik, J. R. Akridge, *J. Electrochem. Soc.* **2004**, 151, A1969-A1967.
[48] K. Xu, *Chem. Rev.* **2004**, 104, 4303-4417.
[49] Z. Zhang, Y. Shao, B. Lotsch, Y.-S. Hu, H. Li, J. Janek, L. F. Nazar, C.-W. Nan, J. Maier, M. Armand, L. Chen, *Energy Environ. Sci.* **2018**, 11, 1945-1976.
[50] J. G. Kim, B. Son, S. Mukherjee, N. Schuppert, A. Bates, O. Kwon, M. J. Choi, H. Y. Chung, S. Park, *J. Power Sources* **2015**, 282, 299-322.
[51] J. T. S. Irvine, D. C. Sinclair, A. R. West, *Adv. Mater.* **1990**, 2, 132-138.
[52] Y. Wang, W. D. Richards, S. P. Ong, L. J. Miara, J. C. Kim, Y. Mo, G. Ceder, *Nat. Mater.* **2015**, 14, 1026-1032.
[53] Y. Deng, C. Eames, B. Fleutot, R. David, J.-N. Chotard, E. Suard, C. Masquelier, M. S. Islam, ACS Appl. Mater. Interfaces **2017**, 9, 7050-7058.
[54] X. He, Y. Zhu, Y. Mo, *Nat. Commun.* **2017**, 8, 15893.
[55] A. R. West, *Solid State Chemistry and its Applications*, 2nd Edition, Student Edition, Wiley, West Sussex, United Kingdom, **2014**.
[56] B. Carette, M. Ribes, J. L. Souquet, *Solid State Ionics* **1983**, 9, 735-737.
[57] M. A. Kraft, S. P. Culver, M. Calderon, F. Böcher, T. Krauskopf, A. Senyshyn, C. Dietrich, A. Zevalkink, J. Janek, W. G. Zeier, *J. Am. Chem. Soc.* **2017**, 139, 10909-10918.
[58] T. Krauskopf, C. Pompe, M. A. Kraft, W. G. Zeier, *Chem. Mater.* **2017**, 29, 8859-8869.
[59] T. Asano, A. Sakai, S. Ouchi, M. Sakaida, A. Miyazaki, S. Hasegawa, *Adv. Mater.* **2018**, 30, 1803075.
[60] A. G. Belous, G. N. Novitskaya, S. V. Polyanetskaya and Y. I. Gornikov, *Russ. J. Inorg. Chem.* **1987**, 32, 156–157.
[61] J. C. Bachmann, S. Muy, A. Grimaud, H.-H. Chang, N. Pour, S. F. Lux, O. Paschos, F. Maglia, S. Lupart, P. Lamp, L. Giordano, Y. Shao-Horn, *Chem. Rev.* **2016**, 116, 140-162.
[62] V. Thangadurai, S. Narayanan, D. Pinzaru, *Chem. Soc. Rev.* **2014**, 43, 4714-4727.
[63] H. Y.-P. Hong, *Mater. Res. Bull.* **1978**, 13, 117-124.
[64] M. Monchak, T. Hupfer, A. Senyshyn, H. Boysen, D. Chernyshov, T. Hansen, K. G. Schell, E. C. Bucharsky, M. J. Hoffmann, H. Ehrenberg, *Inorg. Chem.* **2016**, 55, 2941-2945.
[65] G. Adachi, N. Imanaka, S. Tamura, *Chem. Rev.* **2002**, 102, 2405-2430.
[66] M. H. Braga, J. A. Ferreira, V. Stockhausen, J. E. Oliveira, A. El-Azab, *J. Mater. Chem. A* **2014**, 2, 5470-5480.
[67] L. Cheng, E. J. Crumin, W. Chen, R. Qiao, H. Hou, S. F. Lux, V. Zorba, R. Russo, R. Kostecki, Z. Liu, K. Persson, W. Yang, J. Cabana, T. Richardson, G. Chen, M. Doeff, *Phys. Chem. Phys.* **2014**, 16, 18294-18300.
[68] Y. Zhu, X. He, Y. Mo, *ACS Appl. Mater. Interfaces* **2015**, 7, 23685-23693.
[69] V. Thangadurai, W. Weppner, *Adv. Funct. Mater.* **2005**, 15, 107-112.
[70] C. Bernuy-Lopez, W. Manalastas, Jr., J. M. Lopez de Amo, A. Aguadero, F. Aguesse, J. A. Kilner, *Chem. Mater.* **2014**, 26, 3610-3617.

[71] R. Kanno, M. Murayama, *J. Electrochem. Soc.* **2001**, 148, A742-A746.
[72] N. Kamaya, K. Homma, Y. Yamakawa, M. Hirayama, R. Kanno, M. Yonemura, T. Kamiyama, Y. Kato, S. Hama, K. Kawamoto, A. Mitsui, *Nat. Mater.* **2011**, 10, 682-686.
[73] H.-J. Deiseroth, S.-T. Kong, H. Eckert, J. Vannahme, C. Reiner, T. Zaiß and M. Schlosser, *Angew. Chem.* **2008**, 120, 767-770; Angew. *Chem. Int. Ed.* **2008**, 47, 755-758.
[74] Y. Kato, S. Hori, T. Saito, K. Suzuki, M. Hirayama, A. Mitsui, M. Yonemura, H. Iba, R. Kanno, *Nat. Energy* **2016**, 1, 16030.
[75] W. Zhang, D. A. Weber, H. Weigand, T. Arlt, I. Manke, D. Schröder, R. Koerver, T. Leichtweiss, P. Hartmann, W. G. Zeier, J. Janek, *ACS Appl. Mater. Interfaces* **2017**, 9, 17835-17845.
[76] G. A. Nazri, *Solid State Ionics* **1989**, 34, 97-102.
[77] G. A. Nazri, R. A. Conell, C. Julien, *Solid State Ionics* **1996**, 86-88, 99-105.
[78] L. Toffoletti, H. Kirchhain, J. Landesfeind, W. Klein, L. van Wüllen, H. A. Gasteiger, T. F. Fässler, *Chem. Eur. J.* **2016**, 22, 17635-17645.
[79] A. Haffner, T. Bräuniger, D. Johrendt, *Angew. Chem.* **2016**, 128, 13783-13786; *Angew. Chem. Int. Ed.* **2016**, 55, 13585-13588.
[80] N. Wiberg, E. Wiberg, A. F. Hollemann, *Lehrbuch für Anorganische Chemie*, 102 Auflage, Walter de Gruyter, Berlin, **2007**.
[81] B. Key, R. Bhattacharyya, M. Morcrette, V. Seznéc, J.-M. Tarascon, C. P. Grey, *J. Am. Chem. Soc.* **2009**, 131, 9239-9249.
[82] U. Kasavajjula, C. Wang, A. J. Appleby, *J. Power Sources* **2007**, 163, 1003-1039.
[83] T. F. Fässler, *Zintl Phases – Principles and recent developments*, Structure and Bonding Vol. 139, Springer-Verlag, Heidelberg, Germany, **2011**.
[84] U. Müller, *Inorganic Structural Chemistry*, Second Ed., John Wiley & Sons, Ltd, West Sussex, England, **2006**.
[85] Y. Dong, F. J. DiSalvo, *Acta Cryst. E* **2007**, 63, i97-i98.
[86] W. Hönle, H. G. von Schnering, *Z. Kristallogr.* **1981**, 155, 307-314.
[87] V. Manriquez, W. Hönle, H. G. von Schnering, *Z. Anorg. Allg. Chem.* **1986**, 539, 95-109.
[88] J. Schmedt auf der Günne, S. Kaczmarek, L. van Wüllen, H. Eckert, D. Paschke, A. J. Foecker, W. Jeitschko, *J. Solid State Chem.* **1999**, 147, 341-349.
[89] H. G. von Schnering, W. Wichelhaus, *Naturwissenschaften* **1972**, 59, 78-79.
[90] M. Zeilinger, D. Benson, U. Häussermann, T. F. Fässler, *Chem. Mater.* **2013**, 25, 1960-1967.
[91] M. N. Obrovac, L. Christensen, *Electrochem. Solid St.* **2004**, 7, A93-A96.
[92] T. D. Hatchard, J. R. Dahn, *J. Electrochem. Soc.* **2004**, 151, A838-A842.
[93] U. Frank, W. Müller, H. Schäfer, *Z. Naturforsch.* **1975**, 30b, 10-13.
[94] H. G. von Schnering, R. Nesper, J. Curda, K.-F. Tebbe, *Angew. Chem.* **1980**, 92, 1070.
[95] H. G. von Schnering, R. Nesper, K.-F. Tebbe, J. Curda, *Z. Metallkd.* **1980**, 71, 357-363.
[96] J. Osugi, R. Namikawa, Y. Tanaka, *Rev. Phys. Chem. Jpn.* **1966**, 36, 35-43.
[97] A. J. SpringThorpe, *Mater. Res. Bull.* **1969**, 4, 125-128.
[98] T. Wadsten, *Chem. Commun.* **1973**, 7, 1-4.
[99] S. A. Mughal, A. J. Payne, B. Ray, *J. Mater. Sci.* **1969**, 4, 895-901.
[100] P. Kaiser, W. Jeitschko, *Z. Naturforsch. B* **1997**, 52, 462-468.
[101] M. Kirschen, H. Vincent, C. Perrier, P. Chaudouët, B. Chenevier, R. Madar, *Mater. Res. Bull.* **1995**, 30, 507-513.

[102] P. Kaiser, W. Jeitschko, *Z. Anorg. Allg. Chem.* **1996**, 622, 53-56.
[103] H. Vincent, J. Kreisel, C. Perrier, O. Chaix-Pluchery, P. Chaudouët, R. Madar, *J. Solid State Chem.* **1996**, 124, 366-373.
[104] C. Perrier, H. Vincent, P. Chaudouët, B. Chenevier, R. Madar, *Mater. Res. Bull.* **1995**, 30, 357-364.
[105] B. Eisenmann, H. Jordan, H. Schäfer, *Mater. Res. Bull.* **1982**, 17, 95-99.
[106] X. Zhang, T. Yu, C. Li, S. Wang, X. Tao, *Z. Anorg. Allg. Chem.* **2015**, 641, 1545-1549.
[107] B. Eisenmann, H. Jordan, H. Schäfer, *Z. Naturforsch. B* **1984**, 39, 864-867.
[108] A. Haffner, D. Johrendt, *Z. Anorg. Allg. Chem.* **2017**, 643, 1717-1720.
[109] J. Mark, J.-A. Dolyniuk, N. Tran, K. Kovnir, *Z. Anorg. Allg. Chem.* **2019**, 645, 242-247.
[110] A. Haffner, A.-K. Hatz, I. Moudrakovski, B. V. Lotsch, D. Johrendt, *Angew. Chem.* **2018**, 130, 6263-6268; *Angew. Chem. Int. Ed.* **2018**, 57, 6155-6160.
[111] K. Feng, L. Kang, W. Yin, W. Hao, Z. Lin, J. Yao, Y. Wu, *J. Solid State Chem.* **2013**, 205, 129-133.
[112] B. Eisenmann, M. Somer, *Z. Naturforsch.* **1984**, 39b, 736-738.
[113] B. Eisenmann, M. Somer, *Z. Naturforsch.* **1985**, 40b, 886-890.
[114] B. Eisenmann, J. Klein, M. Somer, *Angew. Chem.* **1990**, 102, 92-93.

2 Experimental Section

2.1 Synthesis

To avoid contaminations and reactions with air and moisture, all starting materials and reaction products are carefully handled and stored under inert gas atmosphere in glove boxes (MBraun) or sealed vessels with oxygen and water levels below 1 ppm. Argon (Westfalen, purity grade 4.8) is used as inert gas and dried over P_2O_5 and molecular sieve prior to usage.

2.1.1 Starting Materials

All materials are prepared directly or via a precursor from pure elements listed in Tab. 2.1. Alkali metal and tetrel elements are processed before usage. Lithium and sodium are stripped from their passivation layer of lithium oxide and lithium nitride and sodium oxide, respectively, by cutting with a knife. Chunks of silicon and germanium are ground to powders with a ball mill. Per batch roughly 30 g tetrel element are processed with 150 rpm for 2 h in an 80 mL WC milling jar with 25×10 mm balls.

Table 2.1: List of elements used for synthesis.

Element	Shape	Supplier	Purity / %
Li	Rods	Rockwood Lithium	99
Na	Rods	Chempur	99
Si	Granules	Wacker	99.9
P_{red}	Powder	Sigma-Aldrich	97
P_{red}	Pieces	Chempur	99.999
Ge	Pieces	Evochem	99.999

2.1.2 Mechanical Alloying

To ensure a complete reaction, certain element mixtures are preprocessed by mechanical alloying in a planetary ball mill (Retsch, PM100). This treatment improves the distribution of the constituents and bypasses the very different thermal properties and reactivities by formation of precursor compounds. Ternary reactive mixtures are prepared in a 50 mL milling jar with 3×15 mm balls in batches of 1.5 g to 5 g. The reactants Si, P_{red} and Ge are filled in as powders and Li is cut into small pieces (< 3 mm). For the chosen conditions, a milling program with a revolution

rate of 350 rpm, 36 h milling time, 10 min interval and 3 min break turned out to result in well homogenized samples of precursors and low amounts of abrasion.

2.1.3 High Temperature Treatment

Sample processing at elevated temperatures is used to induce a reaction to binary or ternary phases as well as affecting order on an atomic scale and improving crystallinity. The samples are sealed in Nb, Ta or carbon-coated silica glass ampoules. Nb and Ta ampoules are chosen for reactions containing elemental Li or Na, since these react with silica glass and also the carbon coating. For reaction mixtures containing large amounts of elemental P_{red}, these metals tend to the formation of NbP and TaP at elevated temperatures. Thus, for those samples, the carbon coated silica glass ampoules are selected. Additionally, elemental alkali metals need to be transferred in a less reactive precursor form of binary lithium phosphides or reactive mixtures from the ball mill.

Preparation of Nb and Ta ampoules is done by cutting the corresponding tube (10 mm outer diameter, 0.5 mm wall thickness) into 3 cm to 5 cm long pieces, which are closed on one side with a fitting cap by arc welding (MAM-1, Johanna Otto). These ampoules are cleaned by sonication in acetic acid, deionized water and acetone for 15 min each and dried for > 12 h at 120 °C. After transferring the ampoules into the glove box they are loaded with reactants. Ductile metals are filled in as cut pieces and brittle compounds are mixed and ground in advance. The ampoules are sealed by arc welding, while cooling the bottom of the ampoule containing the educts in a water-cooled copper block. To avoid reactions of the ampoule material with air, the metal ampoules are placed in an evacuated silica glass tube (ilmasil PN, Qsil) for reaction in tubular vertical furnaces (Loba-1200-40-600, HTM Reetz) or sealed in an evacuated silica glass ampoule (outer diameter = 18 mm, wall thickness = 1 mm) for reactions in muffle furnaces (Li5/11/P330, Nabertherm).

For silica glass ampoules, tubes (ilmasil PN, Qsil) with outer diameters of 10 mm, 15 mm and 18 mm (1 mm to 2.5 mm wall thickness) are cut and welded with a H_2/O_2 torch into 30 cm long, semi-closed raw ampoules. Some drops of acetone are filled into the raw ampoules and heated with the torch until evaporation. Further heating of the semi-closed raw ampoule leads to decomposition and formation of the black carbon layer on the glass. The reaction is continued until ca. 5 cm of the ampoule are covered with a dense film. After cooling, the ampoule is cleaned with isopropanol and dried for > 12 h at 120 °C. In the glove box, sample mixtures are ground and pressed to pellets before loading into the ampoule. A cap is attached to the silica raw ampoule via a silicone gasket to provide an airtight seal, before transferring the ampoule outside of the glove

box. The ampoule is evacuated with a *Schlenk* line via a valve integrated in the attached cap and sealed by welding with a H_2/O_2 torch.

All reactions in ampoules are conducted in tubular vertical and muffle furnaces, which allow temperature programs with set heating and cooling rates. Fast cooling is performed by quenching the hot metal or silica glass ampoule in water. To avoid side reactions with the ampoule material, for all ampoule materials a maximum reaction temperature of 800 °C is not exceeded.

2.1.4 Experimental Contributions of Coauthors

Table 2.2 List of coauthors with experimental contributions to the publications.

Author affiliation	Publication (Chapter no.)	Contribution
Volodymyr Baran	$Li_{14}SiP_6$ (3.2)	Neutron powder diffraction
Volker L. Deringer	$Li_{14}SiP_6$ (3.2)	DFT calculations
Christian Dietrich	Li_2GeP_2 & $LiGe_3P_3$ (3.3) Na_3P (3.5)	Impedance spectroscopy
Holger Kirchhain	$Li_{14}SiP_6$ (3.2) α/β-Li_8GeP_4 (3.3)	Static T-dependent NMR spectroscopy
Gabriele Raudaschl-Sieber	$Li_{10}Si_2P_6$ & $Li_3Si_3P_7$ (3.1) $Li_{14}SiP_6$ (3.2) Li_2GeP_2 & $LiGe_3P_3$ (3.3) $Li_{10.68(8)}Si_5P$ & $Li_{10.1(2)}Ge_5P$ (3.4)	MAS NMR spectroscopy
Christian Sedlmeier	$Li_{14}SiP_6$ (3.2) Li_2GeP_2 & $LiGe_3P_3$ (3.3)	Impedance spectroscopy
Anatoliy Senyshyn	$Li_{14}SiP_6$ (3.2)	Neutron powder diffraction
Stefan Strangmüller	$Li_{14}SiP_6$ (3.2) α/β-Li_8GeP_4 (3.3)	Synthesis of $Li_{14}SiP_6$ Synthesis of α/β-Li_8GeP_4
Lorenzo Toffoletti	$Li_{10}Si_2P_6$ & $Li_3Si_3P_7$ (3.1) $Li_{10.68(8)}Si_5P$ & $Li_{10.1(2)}Ge_5P$ (3.4)	Synthesis of $Li_{10}Si_2P_6$ Synthesis of $Li_{10.68(8)}Si_5P$

2.2 Characterization

2.2.1 Single Crystal X-ray Diffraction

Single crystal X-ray diffraction (SC-XRD) is a powerful tool to determine the crystal structure of crystalline solid materials. It provides information about composition and atomic environment. Suitable crystals are selected and separated from the sample under a microscope in a glove box. The crystals are cleaned with perfluorinated ether and transferred into a glass capillary with a glass needle. The capillary is sealed with a hot tungsten wire and mounted on a single crystal X-ray diffractometer. All three used diffractometers, an Xcalibur3 (Oxford Diffraction), a D8 Kappa Apex II (Bruker AXS) and a StadiVari (STOE & Cie) device, use Mo K_α radiation (λ = 0.71073 Å) and allow active sample cooling with an N_2 gas jet.

The Xcalibur3 (Oxford Diffraction) is equipped with a fine focused radiation source, a graphite monochromator and a Sapphire 3 CCD detector. Data processing was carried out with the CrysalisRed[1] software.

Data collection on the D8 Kappa Apex II (Bruker AXS), equipped with a FR591 rotating anode and an Apex II detector, is done with the Bruker Apex software package,[2] containing the program Saint[3] for data integration and reduction and Sadabs[4] for absorption corrections.

The StadiVari (STOE & Cie) is equipped with a fine focused radiation source and a Dectris Pilatus 300 K detector.

Structures were solved with direct methods with the ShelXS software and refined with full-matrix least squares on F^2 with the program ShelXL.[5] Graphical illustration of crystal structures is done with the Diamond 3[6] and Vesta[7] software.

2.2.2 Powder X-Ray Diffraction

To determine the purity of crystalline samples as well as phase fractions of the constituents, powder X-ray diffraction (PXRD) is used. For measurements in transmission or *Debye-Scherrer* geometry, samples are ground and sealed in capillaries with a diameter of 0.3 mm. Two diffractometers with Cu $K_{\alpha1}$ (λ = 1.54056 Å) and Mo $K_{\alpha1}$ radiation (λ = 0.71073 Å), respectively, each equipped with a Ge(111) monochromator and a Dectris Mythen 1K detector, are available for sample measurements. The samples are mounted on the diffractometer and measured for 15 minutes for qualitative and > 12 h for quantitative analysis. Data are calibrated with an internal or external Si standard and processed with the WinXPow[8] software package and Jana2006[9] or FullProf[10] software packages for *Rietveld* refinements yielding quantitative data and structure refinements.

2.2.3 Powder Neutron Diffraction

Powder neutron diffraction (PND) allows, similar to PXRD, phase analysis on crystalline samples. However, due to larger contrast in neutron scattering lengths compared to X-ray form factors and an independence of scattering lengths of the scattering angle, more precise data especially on light elements like Li can be collected.

PND experiments are performed by Anatoliy Senyshyn and Volodimyr Baran on the high-resolution powder diffractometer SPODI at the research reactor FRM II. Measurements are performed in *Debye-Scherrer* geometry with a wave length of $\lambda = 1.5482$ Å. The device is equipped with a Ge (551) monochromator and a detector consisting of 80 ^{3}He tubes with 1 inch in diameter covering an angular range of 160°. The sample (ca. 2 cm^3) is loaded into a niobium ampoule (outer diameter 10 mm, 0.5 mm wall thickness). The welded ampoule is mounted on the device. Sample heating and cooling is possible with a refrigerator and vacuum furnace sample holder using ^{4}He as heat transmitter.

Rietveld refinement on obtained neutron diffraction data as well for simultaneous refinement of neutron and X-ray data is performed with FullProf.[10] Neutron diffraction data at 1024 K are used as basis for maximum entropy method (MEM) calculations yielding Li migration paths.

2.2.4 Energy Dispersive X-Ray Spectroscopy

Energy dispersive X-ray spectroscopy (EDX) yields element types and composition of examined particles. Single crystals of selected compounds are isolated from the samples and placed on a cylindrical aluminum sample holder with a graphite tape. The samples are analyzed with JEOL JSM-5900 LV (20 kV) and Hitachi TM-1000 Table Top (15 kV) scanning electron microscopes.

2.2.5 Nuclear Magnetic Resonance Spectroscopy

Nuclear magnetic resonance (NMR) spectroscopy experiments gives information about the chemical environment as well as dynamic and static disorder of certain species.

Magic angle spinning (MAS) NMR spectroscopy experiments on ^{6}Li, ^{7}Li, ^{29}Si and ^{31}P nuclei are conducted by Gabriele Raudaschl-Sieber on an Avance 300 spectrometer (Bruker) operating at 7.04 T. The samples are packed in ZrO_2 MAS NMR probes with diameter of 4 mm or 7 mm and rotated with revolution frequencies from 5 kHz to 15 kHz. All spectra were referenced to 1 mol L^{-1} LiCl (0.0 ppm) solution, solid LiCl (1.15 ppm), $Si(Si(CH_3)_3)_4$ (−9.8 ppm) and $(NH_4)H_2PO_3$ (1.11 ppm).

Static NMR spectroscopy experiments on ^{7}Li and ^{31}P nuclei are performed by Holger Kirchhain and Leo van Wüllen on an Avance III spectrometer (Bruker) operating at 7 T employing a WVT

MAS probe with a diameter of 4 mm accessing temperature range of 150 K to 300 K. The samples are sealed in silica glass ampoules with a diameter of 3.7 mm to avoid leaking during temperature changes. The spectra were referenced to 9.7 mol L^{-1} LiCl solution and concentrated H_3PO_4. Calibration for measurements with changing temperature is performed using the temperature dependent ^{207}Pb NMR shift of $Pb(NO_3)_2$.

2.2.6 Infrared Spectroscopy

IR spectra are recorded on a Spectrum Two ATR-FTIR device (Perkin-Elmer) including a diamond ATR crystal and resolution of 4 cm^{-1}.

2.2.7 Raman Spectroscopy

Raman spectroscopy is recorded by Sebastian Geier using a Renishaw In Via Raman Microscope RE04 (λ = 532 nm). The device includes a nitrogen cooled CCD (charge coupled device) detector and the measurement was performed at room temperature. Data evaluation is executed with the program WiRE.[11]

2.2.8 Elemental Analysis

To determine the exact composition of samples, elemental analysis is performed by the microanalytical laboratory at the department of chemistry of the Technische Universität München. The amount of Li is analyzed via atomic absorption spectroscopy using a 280FS AA spectrometer (Agilent Technologies), Si and P are assigned photometrically via molybdate and vanadate methods using a Cary UV-Vis spectrometer (Agilent Technologies).

2.2.9 Differential Scanning Calorimetry

Differential scanning calorimetry (DSC) to determine the thermal behavior and to identify phase transitions is performed by Lavinia Scherf and Tassilo Restle on a DSC 404 Pegasus (Netzsch) or by Maximilian Baumgartner and Patrick Walke on a DSC 200 F3 Maia (Netzsch).

To detect thermal events in the temperature range of 200 °C to 1000 °C the DSC 404 Peagasus is used. Samples (50 mg to 100 mg) are loaded into a custom built Nb ampoule and sealed via arc welding. During the measurement heating and cooling rates of 10 K min^{-1} are applied with an Ar flow of 75 mL min^{-1}.

In temperature range of −150 °C to 600 °C the DSC 200 F3 Maia is used. Samples (ca. 10 mg) are sealed in an aluminum crucible by cold welding.

2.2.10 Electric Conduction Measurements

Determination of the lithium ion and electronic is performed by comparison of electrochemical impedance spectroscopy (EIS) data with dc polarization measurements. Christian Dietrich and Wolfgang Zeier or Christian Sedlmeier and Hubert A. Gasteiger conducted these measurements. Different custom built cells are used by both groups.

C. Dietrich and W. G. Zeier loaded 50 mg to 100 mg sample into a cell with an inner diameter of 10 mm. The powder is pressed with stainless steel pistons at 3 tons for 2 min. EIS measurements were conducted in a temperature range of 25 °C to 150 °C in a frequency range of 7 MHz to 10 Hz with an amplitude of ±20 mV. Polarization measurements within the same cell are carried out applying a voltage of 0.3 V to 2.0 V for 10 h each. For impedance measurements at higher temperatures up to 300 °C, a hot press setup is used.[12] The sample is pressed at 150 °C with 2 t pressure between steel dies (ø 12 mm). Data collection is performed in a frequency range of 1 MHz to 10 Hz with an amplitude of ±20 mV.

For measurements conducted by C. Sedlmeier and H. A. Gasteiger, 100 mg to 500 mg sample were loaded in a cell with steel dies and an inner diameter of 8 mm. The cell is closed and compacted by fastening 6 screws with a torque of 30 Nm. EIS measurements are conducted at room temperature or in a temperature range from 0 °C to 80 °C in a climate cabinet with a frequency ranging from 3 MHz to 50 mHz with an excitation of ±50 mV. Polarization measurements were recorded applying voltages of 50 mV, 100 mV and 150 mV for 16 h, each.

For all three impedance measurement setups, the pellet height is extrapolated at room temperature after hot pressing.

2.2.11 Density Functional Theory Simulations

Density functional theory (DFT) total energy computations using Castep[13] and DFT-based molecular dynamics (MD) simulations using cp2k[14] are carried out by Volker L. Deringer. For disordered crystal structures an ordered expansion of the conventional unit cell is used.

References

[1] *Crysalis Red, Version 1.171.33.34d*, Oxford Diffraction, Abingdon, UK, **2009**.
[2] *Apex Suite of Crystallographic Software*, Bruker AXS Inc., Madison, WI, USA, **2008**.
[3] *Saint*, Bruker AXS Inc., Madison, WI, USA, **2001**.
[4] *Sadabs*, Bruker AXS Inc., Madision, WI, USA, **2001**.
[5] G. M. Sheldrick, *Acta Crystallogr., Sect. A: Found. Adv.* **2015**, 71,3-8.
[6] *Diamond*, K. Brandenburg, Crystal Impact GbR, Bonn, Germany, **2014**.
[7] K. Momma, F. Izumi, *J. Appl. Crystallogr.* **2011,** 44**,** 1272-1276.
[8] WinXPow, STOE & Cie GmbH, Darmstadt, Germany, **2003**.
[9] V. Petříček, M. Dušek, L. Palatinus, *Z. Kristallogr. - Cryst. Mater.* **2014**, 229, 345-352.
[10] J. Rodriguez-Carvajal, J. Gonzales-Platas, *FullProf Suite 2. 05*, Institute Laue-Langevin Grenoble: France, **2011**.
[11] *WiRE 4.2 build 5037*, Renishaw plc, Gloucestershire, UK, **2002**.
[12] M. R. Busche, D. A. Weber, Y. Schneider, C. Dietrich, S. Wenzel, T. Leichtweiss, D. Schröder, W. Zhang, H. Weigand, D. Walter, S. J. Sedlmaier, D. Houtarde, L. F. Nazar, J. Janek, *Chem. Mater.* 2016, 28, 6152-6165.
[13] S. J. Clark, M. D. Segall, C. J. Pickard, P. J. Hasnip, M. J. Probert, K. Refson, M. C. Payne, *Z. Kristallogr.* **2005**, 220, 567-570.
[14] J. VandeVondele, M. Krack, F. Mohamed, M. Parrinello, T. Chassaing, J. Hutter, *Comput. Phys. Commun.* **2005**, 167, 103-128.

3 Result and Discussion

3.1 Synthesis and Characterization of Lithium Phosphidosilicates and Phosphidogermanates

See Chapter 5.1 Synthesis and Characterization of the Lithium-Rich Phosphidosilicates $Li_{10}Si_2P_6$ and $Li_3Si_3P_7$
H. Eickhoff, L. Toffoletti, W. Klein, G. Raudaschl-Sieber, T. F. Fässler, *Inorg. Chem.* 2017, 56, 6688-6694.

See Chapter 5.2 Fast Ionic Conductivity in the Lithium-Rich Phosphidosilicate $Li_{14}SiP_6$
S. Strangmüller, H. Eickhoff, D. Müller, W. Klein, G. Raudaschl-Sieber, H. Kirchhain, C. Sedlmeier, V. Baran, A. Senyshyn, V. L. Deringer, L. van Wüllen, H. A. Gasteiger, T. F. Fässler, manuscript for publication.

See Chapter 5.3 Lithium Phosphidogermanates α- and β-Li_8GeP_4 - A Novel Compound Class with Mixed Li^+ Ionic and Electronic Conductivity
H. Eickhoff, S. Strangmüller, W. Klein, H. Kirchhain, C. Dietrich, W. G. Zeier, L. van Wüllen, T. F. Fässler, *Chem. Mater.* 2018, 30, 6440-6448.

See Chapter 5.4 Polyanionic Frameworks in the Lithium Phosphidogermanates Li_2GeP_2 and $LiGe_3P_3$
H. Eickhoff, C. Sedlmeier, W. Klein, G. Raudaschl-Sieber, H. A. Gasteiger, T. F. Fässler, manuscript for publication

See Chapter 5.5 Planar Tetrelide Pentagons and Isolated Phosphide Anions in Lithium Phosphotetrelides $Li_{10.68(8)}Si_5P$ and $Li_{10.1(2)}Ge_5P$
H. Eickhoff, L. Toffoletti, W. Klein, G. Raudaschl-Sieber, T. F. Fässler, manuscript for publication

The recent investigation of the Li/Si/P phase system showed a variety of compounds with potential to conduct Li^+ and intriguing structural features. As described in chapter 1.4, these compounds include Li_8SiP_4, Li_2SiP_2 and $LiSi_2P_3$,[1,2] which are built from unbound or corner sharing SiP_4 tetrahedra. Contrary to ion conductors based on sulfides or oxides, these phosphide based materials can exhibit high degrees of condensation and at the same time a high Li content, potentially providing alternating mechanical properties and chemical stability. Due to the large variety of different structure types and connectivity patterns found for metal phosphidosilicates and silicon phosphides the Li/Si/P phase system is further explored for new compounds. Within this work the known phases in this phase system are extended by $Li_{10}Si_2P_6$, $Li_3Si_3P_7$, $Li_{14}SiP_6$ and $Li_{10.68(8)}Si_5P$ (Fig. 3.1).

While already several compounds are known in the Li/Si/P phase system the Li/Ge/P system is largely uncharted. The only compound reported is Li_5GeP_3,[3] which realizes a structure with mixed positions for Ge and Li, related to CaF_2 and $Li_{14}SiP_6$. However, knowledge from the lithium

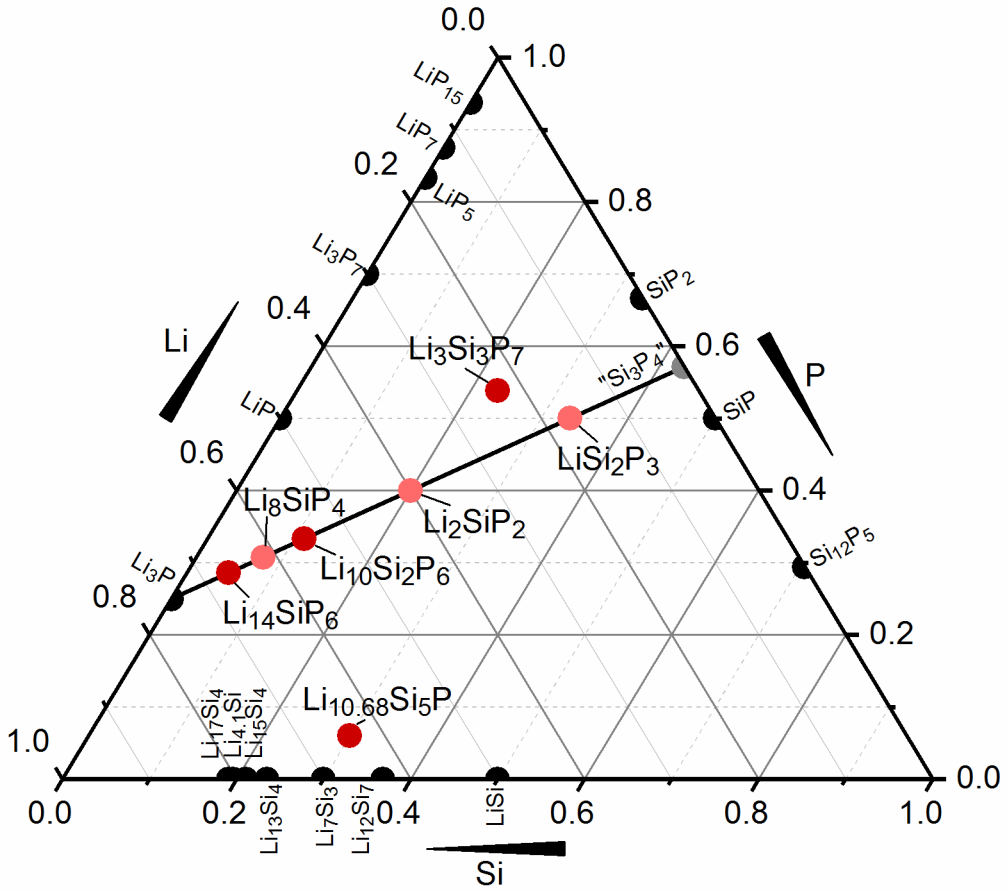

Figure 3.1: Gibbs diagram of the ternary Li/Si/P phase system. Ternary compounds presented in this work are highlighted red and previously reported compounds light red. The majority of the compounds are situated on a pseudo binary line Li_3P-"Si_3P_4". Ternary compounds above that line comprise P-P and compounds below the line Si-Si bonds. Binary compounds are black and the hypothetical compound "Si_3P_4" gray.

phosphidosilicates being fast ionic conductors makes the lithium phosphidogermanates interesting for further research. By substitution of an element by its heavier homologue often similar structures occur, while the properties alter. For example, crystalline Li^+ conductors show a strong variation of Li^+ conductivity depending on the anion size. The LGPS type family shows for $Li_{10}SiP_2S_{12}$, $Li_{10}GeP_2S_{12}$ and $Li_{10}SnP_2S_{12}$ conductivities of 2.3×10^{-3} S cm^{-1}, 1.2×10^{-2} S cm^{-1} and 4.0×10^{-3} S cm^{-1}, respectively.[4,5] These differences are caused by variations in ion softness, bottleneck sizes as well as hopping distances. To evaluate this effect in the Li/Si/P and Li/Ge/P phase system, the latter is explored for isotypic and new compounds. Following this approach, the new compounds α-Li_8GeP_4 as well as β-Li_8GeP_4 and, focusing on the Li or P poorer sections of the phase system, Li_2GeP_2, $LiGe_3P_3$ and $Li_{10.1(2)}Ge_5P$ are found (Fig. 3.2).

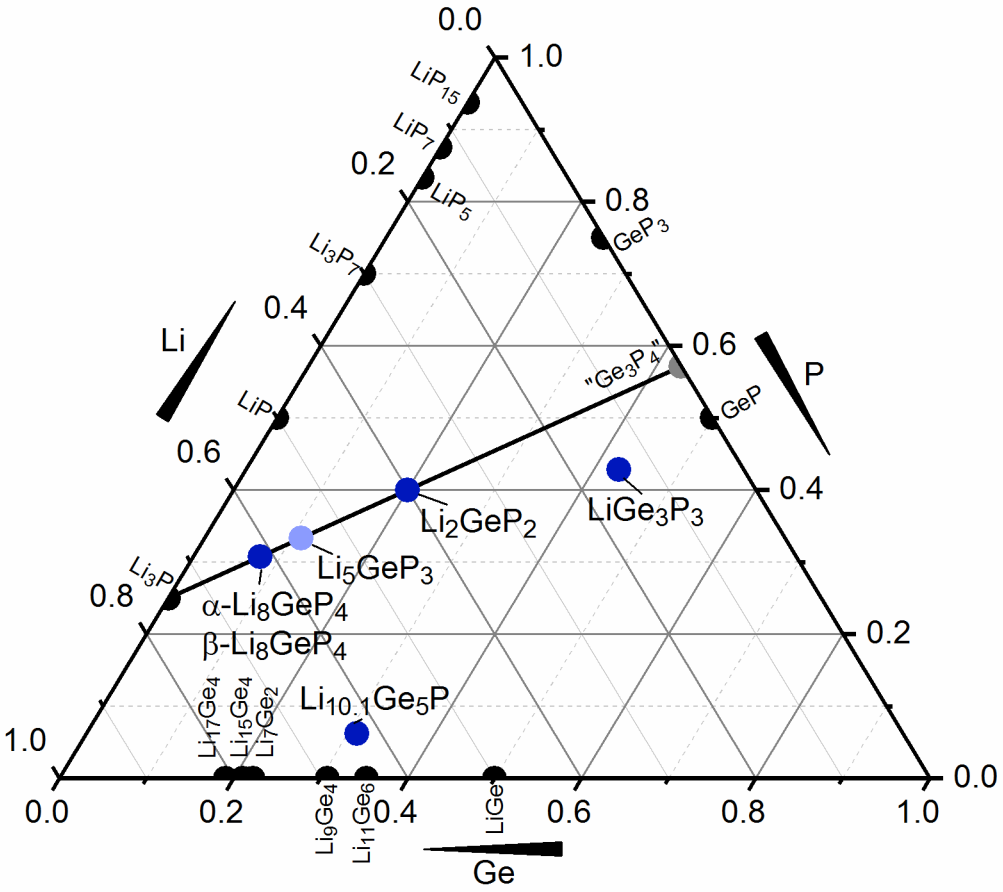

Figure 3.2: Gibbs diagram of the ternary Li/Ge/P phase system. Ternary compounds presented in this work are highlighted blue and previously reported compounds light blue. The majority of the compounds are situated on a pseudo binary line Li_3P-"Ge_3P_4". Ternary compounds below the line comprise Ge-Ge bonds. Binary compounds are black and the hypothetical compound "Ge_3P_4" gray.

3.1.1 Crystal Structures

In the Li/Si/P and Li/Ge/P phase systems the majority of compounds are built from tetrahedral building blocks, namely Li_8SiP_4,[1] Li_2SiP_2,[1] $LiSi_2P_3$,[2] $Li_{10}Si_2P_6$, $Li_3Si_3P_7$, $Li_{14}SiP_6$, Li_5GeP_3,[3] α-Li_8GeP_4, β-Li_8GeP_4, Li_2GeP_2 and $LiGe_3P_3$. Only in $Li_{10.68(8)}Si_5P$ and $Li_{10.1(2)}Ge_5P$ different structural motives are realized. Within the tetrahedral building blocks the tetrel element (Si, Ge) is situated in the center and is coordinated by four P atoms leading to the compositions of SiP_4 and GeP_4. These units can occur as isolated $[TtP_4]^{8-}$ (*Tt* = Si, Ge) or can be condensed to larger units or frameworks by reducing the charge and changing the ratio of *Tt* to P. This connection of the TtP_4 (*Tt* = Si, Ge) tetrahedra to larger units can be realized via different patterns. While for the Li/*Tt*/P phase systems centered tetrahedra connections via shared vertices are reported in advance to this work, also P-P bonds between the tetrahedra are conceivable. Additionally, by alternating TtP_4 tetrahedra to $Tt(P_3Tt)$ tetrahedra, *Tt*-*Tt* bonds can be realized. Regarding the Gibbs diagrams the different bonding refers to different sections. Compounds, in which tetrahedra are solely connected via shared P vertices are found on a line between Li_3P and the hypothetical compounds "Tt_3P_4". This is the case for Li_8SiP_4, Li_2SiP_2, $LiSi_2P_3$ and Li_5GeP_3, but also for $Li_{10}Si_2P_6$, $Li_{14}SiP_6$, α-Li_8GeP_4, β-Li_8GeP_4 and Li_2GeP_2 and therefore the majority of the compounds. Compounds aside of that line, shifted towards elemental P, like $Li_3Si_3P_7$, or elemental *Tt*, like $LiGe_3P_3$, contain P-P bonds or *Tt*-*Tt* bonds, respectively. Considering this, the compound lithium orthophosphidosilicate Li_8SiP_4, which contains the isolated $[SiP_4]^{8-}$ units counterbalanced by 8 Li, can be regarded as a prototype to derive further structures. Moreover, the $[SiP_4]^{8-}$ building block is known from Ca_4SiP_4, Sr_4SiP_4 and Ba_4SiP_4.[6] With heavier homologues of Si and P also Ba_4GeP_4, Li_8SnP_4, Na_8SnSb_4 and K_8SnSb_4 are reported.[6-9] Despite the similar composition, cubic unit cell and the *ccp* P sublattice, the tetrahedra within these compounds are arranged in a different manner compared to Li_8SiP_4. Within the unit cell of the lithium phosphidosilicate the tetrahedra span a rhombohedron, while in Ca_4SiP_4, Sr_4SiP_4, Ba_4SiP_4, Ba_4GeP_4 and Li_8SnP_4 the tetrahedra are arranged in a manner representing an A15 structure type (Cr_3Si type). In Na_8SnSb_4 and K_8SnSb_4 a diamond-like arrangement is formed by the centered tetrahedra.[10] This leads to the space groups $Pa\bar{3}$, $P\bar{4}3n$ and $Fd\bar{3}m$, respectively.

Derived from the isolated $[SiP_4]^{8-}$, frameworks of supertetrahedra of corner-sharing SiP_4 units are formed in Li_2SiP_2 and $LiSi_2P_3$ S. Due to the higher Li content in Li_2SiP_2 smaller supertetrahedra with two SiP_4 units per edge, compared to four and five condensed units in $LiSi_2P_3$, are realized.[1,2]

3.1.1.1 $Li_{10}Si_2P_6$

The compound $Li_{10}Si_2P_6$, which was investigated in close collaboration with L. Toffoletti,[11] fills the gap between Li_8SiP_4 and Li_2SiP_2 on the line between Li_3P and the hypothetical compound "Si_3P_4". However, contrary to its neighbors it cannot be described as a *ccp* of P atoms with a certain occupation of tetrahedral voids. The compound is isotypic to $Na_{10}Si_2P_6$, $Na_{10}Ge_2P_6$ and $Na_{10}Sn_2P_6$[12,13] and consists of $[Si_2P_6]^{10-}$ units surrounded by Li^+. These units are formed by two SiP_4 tetrahedra sharing one edge (Fig. 3.3). Structurally this unit can be regarded as a section from the structure of SiS_2 or K_2SiP_2.[14,15] The stress induced by formed $[Si_2P_2]$ rings is depicted by the structural chemistry of the heavy homologues. While the atom ratio of 5:1:3 is a recurrent one for this material class the dimeric units are only realized in $Li_{10}Si_2P_6$ and $Na_{10}Tt_2Pn_6$ (*Tt* = Si, Ge, Sn; *Pn* = P, As).[12,13,16,17] An increased anion size for example found in Na_5SnSb_3 leads to 1-dimensional $^1_\infty[SnSb_3]$ chains.[8] Increasing the cation size on the other hand to Rb^+ or Cs^+ leads to a cleavage of the tetrahedral units and the formation of carbonate like $[TtPn_3]^{5-}$ units (*Tt* = Si, Ge; *Pn* = P, As).[18,19]

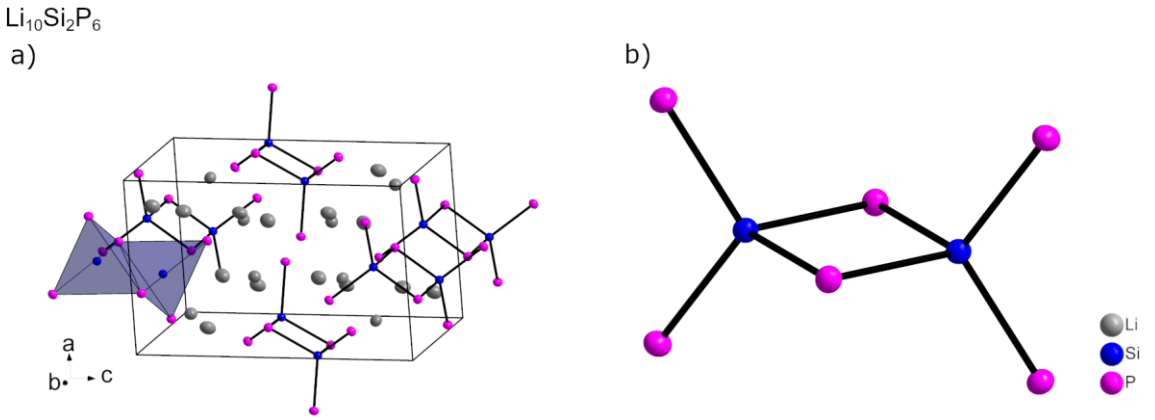

Figure 3.3: Crystal structure of $Li_{10}Si_2P_6$. a) Unit cell and b) $[Si_2P_6]^{10-}$ unit of two edge-sharing SiP_4 tetrahedra.

3.1.1.2 $Li_{14}SiP_6$

The compound $Li_{14}SiP_6$, which is also found on the line Li_3P and the hypothetical compound "Si_3P_4", unites the structural features of its neighbors, Li_3P[20] and Li_8SiP_4. The crystal structure of $Li_{14}SiP_6$ can be derived from the CaF_2 or Li_3Bi structure type.[21] The new lithium phosphidosilicate comprises a *ccp* of P atoms and disordered Si and Li positions. All Si atoms are distributed statistically over all tetrahedral voids. Li fills the remaining tetrahedral voids representing 11 Li atoms per formula unit. Further 3 Li atoms are distributed over the octahedral voids filling them half. On a local scale this results in $[SiP_4]^{8-}$ and twice as much P^{3-}. Remarkably, despite the different bonding situation of Si and Li in a P environment, no sign of the formation of an ordered structure is observed (Fig. 3.4). Additionally, it is worth mentioning that the presence

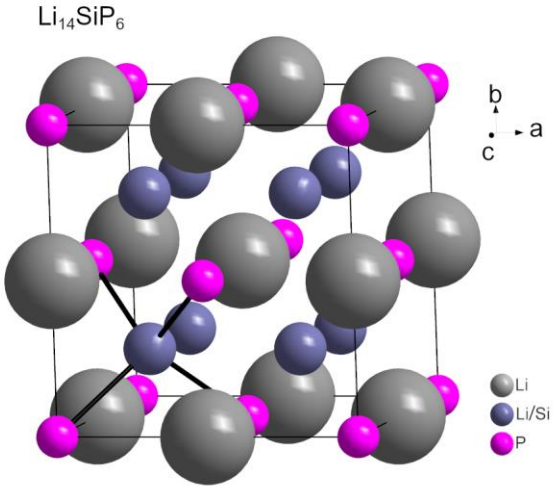

Figure 3.4: a) Crystal structure of $Li_{14}SiP_6$ containing disordered Li/Si sites.

of Si stabilizes the cubic form of Li_3Pn (*Pn* = P, As, Sb, Bi), which is for binaries only observed for Sb and Bi. Li_3P crystallizes in a hexagonal unit cell derived from a *hcp* (hexagonal close pack) of P.[20-22]

3.1.1.3 $Li_3Si_3P_7$

$Li_3Si_3P_7$ is the first compound in the Li/Si/P phase system comprising P-P bonds. The crystal structure built from slabs of Si and P separated by Li. These slabs consist of two layers of parallel aligned, corner sharing SiP_4 tetrahedra. Since single SiP units are missing, the layers are not dense and Li also occupies octahedral voids within the layers. P-P bonds between the tips of the tetrahedra of the two layers connect the halves of the slabs and result in the formation of P chains. Atypical for polyphosphide P^- chains, this specimen can be derived from an armchair-like conformation of hexagonal rings or section of the gray arsenic structure, while related P-structures exhibit a helical structure or can be derived from a boat-like configuration of hexagonal rings (Fig. 3.5).[23,24]

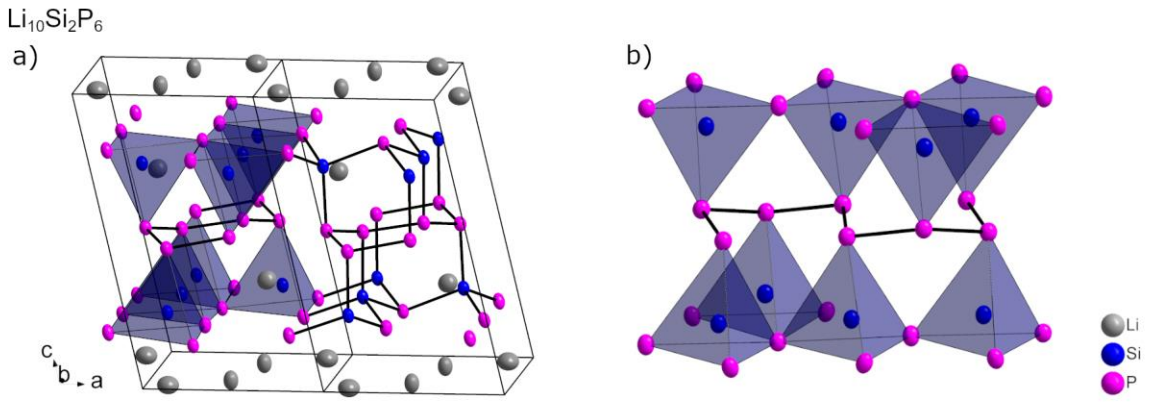

Figure 3.5: Crystal structure of $Li_3Si_3P_7$. a) Unit cell with selected SiP_4 tetrahedra highlighted blue. b) Polyphosphide chain with connectivity to SiP_4 tetrahedra.

3.1.1.4 α-Li_8GeP_4 and β-Li_8GeP_4

The composition Li_8GeP_4 represents the heavier homologue to Li_8SiP_4 in the Li/Ge/P phase system. With this composition two polymorphs, α-Li_8GeP_4 and β-Li_8GeP_4 are found (Fig. 3.6). Both polymorphs crystallize in cubic space groups with similar cell parameters and comprise a *ccp* of P atoms leading to $[GeP_4]^{8-}$ tetrahedra separated by Li^+. α-Li_8GeP_4 is isotypic to Li_8SiP_4[1] and crystallizes in space group $Pa\bar{3}$ with cell parameters of a = 11.80203(7) Å (T = 293 K). Within this cell GeP_4 tetrahedra span a rhombohedron. On the other hand, β-Li_8GeP_4 is isotypic to Li_8SnP_4[7] and crystallizes in space group $P\bar{4}3n$ with cell parameters of a = 11.77294(6) Å (T = 293). The arrangement of tetrahedra in this cell, a *bcc* with two units on each face, resembles the Cr_3Si[10] structure type, wherein both positions, Cr and Si, are occupied by GeP_4 tetrahedra. As indicated by the similar unit cell and pack of P atoms both structures are closely related via a CaF_2 or Li_3Bi-like aristotype. Regarding the Li positions different distributions are found. While in both compounds the remaining tetrahedral voids of the P *ccp* are filled with lithium, in α-Li_8GeP_4 1/4 of the octahedral voids is fully occupied and in β-Li_8GeP_4 3/4 of the octahedral voids are partially occupied. Additionally, in β-Li_8GeP_4 also certain tetrahedral coordinated Li positions are not fully occupied (Tab. 3.1). The occupation also varies for the related phases Li_8SiP_4 and Li_8SnP_4.

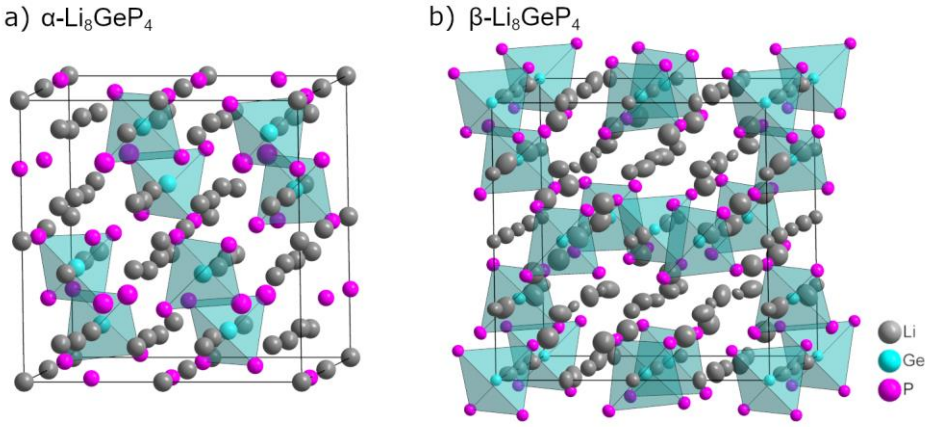

Figure 3.6: Crystal structure of a) α-Li_8GeP_4 and b) β-Li_8GeP_4.

Table 3.1: Comparison of the site occupation factor (S.O.F) and Wyckoff positions (Wyck.) of tetrahedral (T_d) and octahedral (O_h) voids in the *ccp* of P within the compounds Li_8SiP_4, α-Li_8GeP_4, β-Li_8GeP_4 and Li_8SnP_4.

Atom	Void	Wyck.	S.O.F ($Pa\bar{3}$)		Wyck.	S.O.F ($P\bar{4}3n$)	
			Li_8SiP_4[1]	α-Li_8GeP_4		β-Li_8GeP_4	Li_8SnP_4[7]
P		8c	1	1	8e	1	1
P		24d	1	1	24i	1	1
Tt	T_d	8c	1	1	2a	1	1
Tt	T_d	-	-	-	6c	1	1
Li	T_d	8c	1	1	6b	0.78	1
Li	T_d	24d	1	1	6d	1	0
Li	T_d	24d	1	1	8e	1	1
Li	T_d	-	-	-	12f	1	1
Li	T_d	-	-	-	24i	0.887	1
Li	O_h	4a	1	1	8e	-	1
Li	O_h	4b	0	1	24i	0.502	0.25
Li	O_h	24d	0.167	0	-	-	-

3.1.1.5 Li_2GeP_2

The crystal structure of Li_2GeP_2 is isotypic to Li_2SiP_2[1] and consists of a network of GeP_4 supertetrahedra. Each supertetrahedron consists of four GeP_4 tetrahedra and shares corners with four neighboring supertetrahedra, forming a diamond-like, 3-dimensional network. A second identical network occupies the voids of the first and is separated by Li^+ (Fig. 3.7). Between these two frameworks large channels along the [111] direction filled with lithium, imply the possibility of Li^+ migration. Despite the increase in cell parameters compared to Li_2SiP_2, in Li_2GeP_2 the channels are smaller, caused by a rotation and warping of the supertetrahedra. For compounds with heavier homologues of alkali metals, K_2SiP_2 and Cs_2SiP_2, different structures motives are realized, namely 1-dimensional chains of edge-sharing tetrahedra.[15,25]

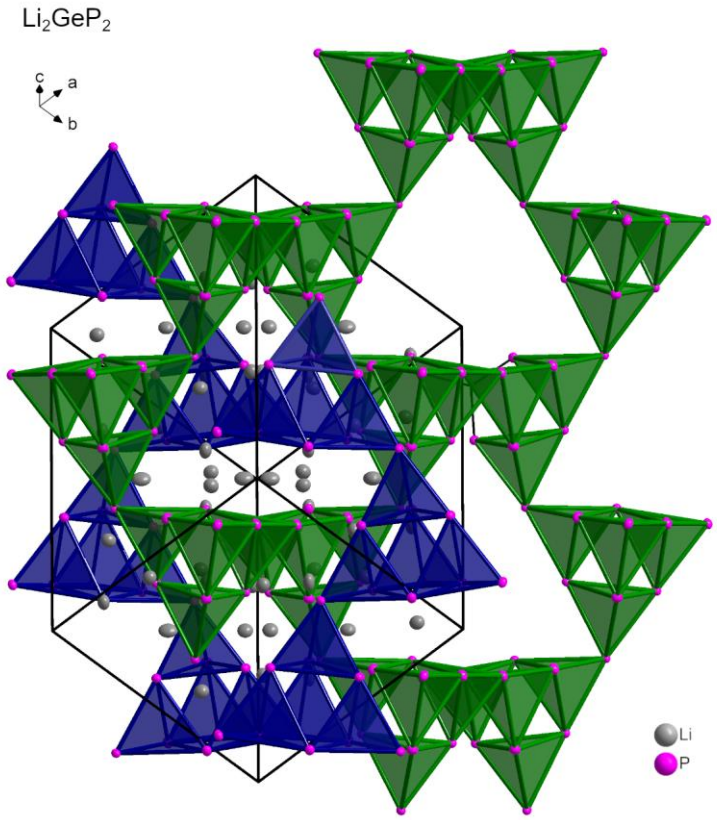

Figure 3.7: Unit cell of Li_2GeP_2. The two unconnected, interpenetrating networks of GeP_4 tetrahedra are depicted with blue and green color. Ge atoms are not shown for clarity.

3.1.1.6 $LiGe_3P_3$

The crystal structure of $LiGe_3P_3$ is composed of slabs of Ge-P tubes. These tubes are built from chains of corner sharing GeP_4 tetrahedra and Ge-Ge dumbbells, bridging the two remaining corners of each tetrahedron with those of the neighboring unit. With further bonds between Ge and P these tubes are connected to slabs, separated by Li^+ atoms. The complete slab can be described as consisting of two different kinds of centered tetrahedra, GeP_4 and $Ge(P_3Ge)$. These tetrahedra are connected via common corners and bonds between Ge and P corners (Fig. 3.8). According to the *Zintl Klemm* concept the anion can be described as $[Ge_3P_3]^{1-}$ with a formal negative charge at the three bonded Ge atom. Despite that, these structural motives are not known for ternary phases in Li/*Tt*/P (*Tt* = Si, Ge, Sn, Pb) systems, they occur frequently in other phosphides and heavier pnictides.[26-28] $LiGe_3P_3$ is isotypic to $Li_{0.9}Ge_{2.9}As_{3.1}$[28] and similar layers with different stacking are with other heavier pnictides and $NaGe_3P_3$.[26] Related structures are also realized in GeP, SiP and *o*-SiP_2 that differ in connectivity or atom distribution within the tubes.[29,30]

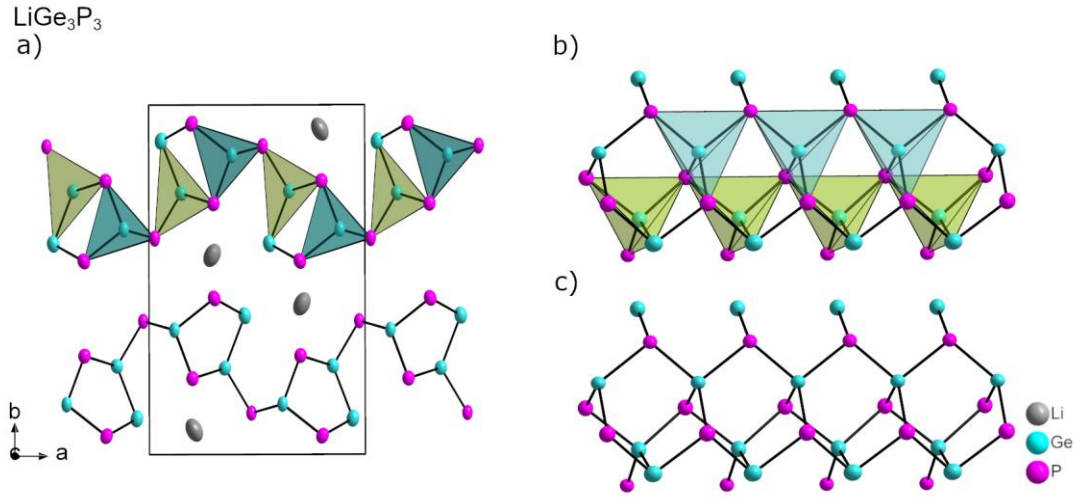

Figure 3.8: a) Unit cell of $LiGe_3P_3$ with slabs consisting of GeP_4 tetrahedra (light blue) and $Ge(P_3Ge)$ (green, containing Ge_2 dumbbells). Enlarged section with highlighted tetrahedra b) and without tetrahedra c).

By comparison of all lithium phosphidosilicates and phosphidogermanates intriguing trends and special cases can be derived (Tab. 3.2). In case of the Si-P bonds for most compounds a range between 2.2 Å and 2.3 Å is found, which represents also the range of Si-P bonds in literature. For $Li_{14}SiP_6$ a bond length of 2.562 Å is found, visualizing its uncommon structure. As Si and Li share the same crystallographic position an intermediate distance is found in the averaged crystal structure, which is dominated by the Li-P interaction. In general for Li/Si/P compounds a decreasing Si-P bond length is found with increasing degree of condensation. The longest Si-P bonds are found for Li_8SiP_4 (2.242 – 2.298 Å)[1] and the shortest for $LiSi_2P_3$ (2.232 – 2.268 Å)[2] and $Li_3Si_3P_7$ (2.210 – 2.297 Å). This illustrates the decreasing formal charge, going along with a decreasing ion radius of the P atoms in the respective compounds. Relatively wide ranges of bond length are found in $Li_3Si_3P_7$ (2.210 – 2.297 Å) and $Li_{10}Si_2P_6$ (2.224 – 2.307 Å) and can be attributed to tensions within the structure. In $Li_3Si_3P_7$ a large number of different vertices is present, while in $Li_{10}Si_2P_6$ the longest bond is found in the tetragonal Si_2P_2 ring. These tensions are also represented by the P-Si-P angle within the SiP_4 tetrahedra. In $Li_{14}SiP_6$ the angles are the ideal tetrahedral angle (109.47°) due to the high symmetry of the system. In Li_8SiP_4 already slight deviations are observed, which are further increasing with increasing degree of condensation. A notable special case is again is $Li_{10}Si_2P_6$ with a minimum angle of 96.75° in the Si_2P_2 ring. However, it is slightly larger than the one of related compounds with 95.63° and 93.63° for K_2SiP_2 and $Na_{10}Si_2P_6$, respectively.[12,15] Also substituting Si by Ge or Sn in $Na_{10}Ge_2P_6$ and $Na_{10}Sn_2P_6$ does not change the angle significantly (93.80° and 96.29°, respectively).[12,13]

Similar effects as for the Li/Si/P system are found in the Li/Ge/P system. The average Ge-P bond length lies between 2.3 Å and 2.4 Å. However, the largest bond length are found for Li_5GeP_3,

which exhibits, similar to $Li_{14}SiP_6$, solely mixed occupied Ge and Li positions. From the Li_8GeP_4 polymorphs to Li_2GeP_2 the bond length are decreasing and the variation of the bond angles are increasing. The long bond length found in $LiGe_3P_3$ can be explained by the presence of $Ge(P_3Ge)$ tetrahedra, which show a relatively strong distortion. Compared to $NaGe_3P_3$, $LiGe_3P_3$ shows a very similar structure, but also a decreased Ge-Ge bond length.[26]

Regarding the Li-Li and Li-P interactions for both phase systems, also clear trends are observed. With decreasing Li content the Li-Li distance increases and the Li-P distance decreases, due to decreasing P radii. Only the compounds $Li_{14}SiP_6$, Li_5GeP_3 and $LiGe_3P_3$ do not follow this trend due to their outstanding structural motives.

Table 3.2: Comparison of selected bond length and angles of lithium phosphidosilicates and phosphidogermanates. For covalent bonds the shortest (min) and longest (max) parameters are given, while for non-covalent interactions only the shortest distance is listed.

Compound	Si-P / Å		P-Si-P / °		P-P / Å		Li-P / Å	Li-Li / Å
	min	max	min	max	min	max	min	min
Li_8SiP_4[1]	2.242	2.298	107.81	111.09	-	-	2.51	2.38
$Li_{10}Si_2P_6$	2.224	2.307	96.75	115.33	-	-	2.48	2.72
Li_2SiP_2[1]	2.233	2.271	101.09	114.28	-	-	2.44	2.91
$LiSi_2P_3$[2]	2.232	2.268	99.29	122.17	-	-	2.40	3.19
$Li_{14}SiP_6$	2.562	2.562	109.47	109.47	-	-	2.56	2.56
$Li_3Si_3P_7$	2.210	2.297	106.28	112.40	2.202	2.215	2.54	2.96
	Ge-P / Å		P-Ge-P / °		Ge-Ge / Å		Li-P / Å	Li-Li / Å
	min	max	min	max	min	max	min	min
α-Li_8GeP_4	2.381	3.396	109.30	109.64	-	-	2.47	2.33
β-Li_8GeP_4	2.369	2.378	108.20	112.04	-	-	2.50	2.49
Li_5GeP_3[3]	2.550	2.550	109.47	109.47	-	-	2.55	2.95
Li_2GeP_2	2.315	2.345	104.07	114.79	-	-	2.46	2.94
$LiGe_3P_3$	2.314	2.405	96.90	112.13	2.539	2.539	2.94	3.60

3.1.1.7 $Li_{10.68(8)}Si_5P$

The compounds $Li_{10.68(8)}Si_5P$ and $Li_{10.1(2)}Ge_5P$ are the first compounds in the Li/*Tt*/P (*Tt* = Si, Ge) phase system, which are not built from TtP_4 tetrahedra. Instead they comprise pentagonal, planar and aromatic Tt_5 (*Tt* = Si, Ge) rings and unbound P^{3-} units surrounded by Li^+ (Fig. 3.9). The pentagonal rings form with lithium stacks along the *b*-axis. One lithium atom is sandwiched between two adjacent tetrel units. Surrounding the $^1_\infty[LiTt_5]$ stack five Li atoms per aromatic ring

form further pentagonal rings, extending the building block to $^{1}_{\infty}[Li_6 Tt_5]$. The sandwich stacks are separated by P^{3-} units. These isolated anions are surrounded by a disordered set of lithium atoms suggesting the presence of different local environments.

Multidecker-π-complexes of Tt_5 (*Tt* = Si, Ge, Sn, Pb) rings are also reported in $Li_{12}Si_7$, Li_8MgSi_6, Li_8MgGe_6, Na_8BaSn_6, Na_8EuSn_6 and Na_8BaPb_6.[31-33] In all compounds two different types of anions exist. These comprise Si_5 rings and Si_4 trigonal stars in $Li_{12}Si_7$ or Tt_5 and isolated *Tt* in all alkaline earth and Eu containing compounds. While $Li_{10.68(8)}Si_5P$ and $Li_{10.1(2)}Ge_5P$ are also built from two anionic species, they are the first compounds comprising two different elements within the anions, including Tt_5 rings. Further, when assigning charges to the anions ($[Tt_5]^{6-}$, $[Si_4]^{8-}$, Tt^{4-} and P^{3-}), most compounds are electron precise and can be described with solely positively charged Li^+, AE^{2+} and Eu^{2+}. However, the compounds $Li_{12}Si_7$, $Li_{10.68(8)}Si_5P$ and $Li_{10.1(2)}Ge_5P$ are not electron precise and formal excessive electrons (resulting in formal Li^0) is necessary for the description of these compounds, explaining their metallic appearance.

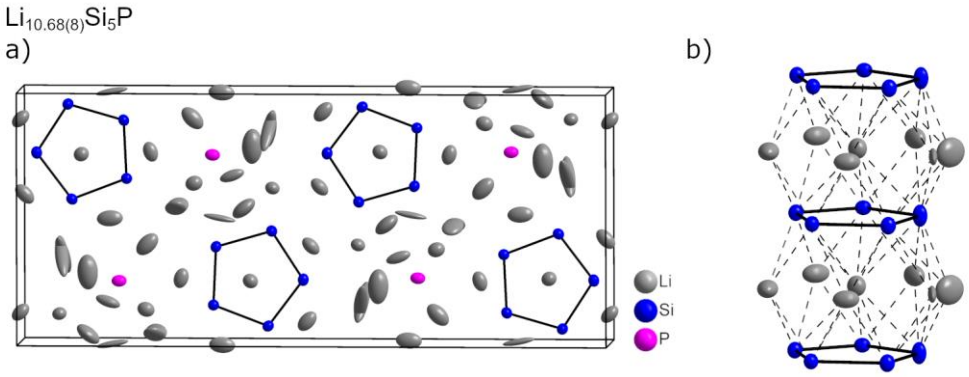

Figure 3.9: a) Crystal structure of $Li_{10.68(8)}Si_5P$ and b) Multidecker-π-complexe $^{1}_{\infty}[Li_6 Tt_5]$.

3.1.2 MAS NMR Spectroscopy

The characterization of the compounds in the Li/Si/P and Li/Ge/P phase system via solid state MAS NMR spectroscopy provides further insight into the structural chemistry. Especially the data from ^{31}P MAS NMR spectroscopy enables the assignment of P to certain local environments, depending on the chemical shift (Tab. 3.3). For phases in the Li/Si/P system, $Li_{14}SiP_6$ and $Li_{10.68(8)}Si_5P$, isolated P^{3-} are found in a range of -316.8 to −272.1 ppm, which is in good agreement with the chemical shift of Li_3P (−278 ppm).[34] ^{31}P MAS NMR spectroscopy on P^{3-} in the Li/Ge/P system ($Li_{10.1}Ge_5P$) shows a slight downfield shift to −280.9 and to −265.9 ppm. For P moieties covalently bound to *Tt* atoms the differences become larger. P^{2-} bound to one Si atom occurs in a shift range of −226.9 to −188.4 ppm, P^- bound to two Si atoms in a range from −241.5 to −124.1 ppm and P^0 bound to three Si atoms at −121.1 ppm. A single example of a P^0 moiety bound to one Si and two P is found at a chemical shift of −77.4 ppm. For P atoms bound to Ge atoms the

Table 3.3: Comparison of ^{31}P MAS NMR shifts (δ / ppm) of compounds in the Li/Si/P and Li/Ge/P phase system. The different P moieties (bold) are assigned to different groups dependent on the bonding situation (number of bonds #b and type of neighbor) and formal charge. In case more than one well resolved signal is present, the relative intensity is listed in brackets.

Compound	**(0b-P^{3-})**	**(1b-P^{2-})**-*Tt*	**(2b-P^{-})**-*Tt*$_2$	**(3b-P)**-*Tt*$_3$	**(3b-P)**-*Tt*P$_2$
Li_3P[34]	−278				
Li_8SiP_4[1]		−225.3 (1); −251.3 (3)			
$Li_{10}Si_2P_6$		−188.4 (1); −199.5 (1)	−124.1 (1)		
Li_2SiP_2[1]			−129.1 (1); −241.5 (3)		
$Li_{14}SiP_6$	−316.8 (1) (broad)	−226.9 (2) (broad)			
$Li_3Si_3P_7$			−178.7 (1); −168.8 (2)	−121.1 (1)	−77.4 (3)
$Li_{10.68(8)}Si_5P$	−272.1; −283.4; −294.9				
β-Li_8GeP_4[35]		−185.4 (1); −191.9 (3)			
Li_2GeP_2			−59.9 (1); −164.8 (1); −178.4 (2)		
$LiGe_3P_3$				−59.5 (1); −119.4 (1); −126.3 (1)	
$Li_{10.1(2)}Ge_5P$	−265.9; −271.8; −280.9				

signal is shifted downfield. Chemical shifts of P^{2-} bound to one Ge atom ranges from −185.4 to −191.9 ppm,[35] for P^- bound to two Ge atoms and P^0 bound to three Ge atoms are found to be −178.4 to −59.9 ppm and −126.3 to −59.6 ppm, respectively. These values are in good agreement with the expected trend, according to which the chemical shift of P atoms should move downfield with decreasing negative charge. Despite a certain overlap of the ranges of certain moieties, this chart enables a rough distinction of P species on the basis of ^{31}P MAS NMR spectroscopy. For $Li_{14}SiP_6$ the chemical shift of the P atoms was used to identify the occurring $[SiP_4]^{8-}$ and P^{3-} units. Despite the broad range of shifts in ^{31}P MAS NMR spectra, different groups show almost identical chemical shifts in ^{6}Li, ^{7}Li and ^{29}Si MAS NMR spectra (Tab. 3.4). In ^{6}Li and ^{7}Li NMR spectra all compounds containing tetrahedral building units (SiP_4 and GeP_4), which are electron precise, show one to two signals with a chemical shift between 2.1 and 5.4 ppm. Only the compounds $Li_{10.68(8)}Si_5P$ and $Li_{10.1(2)}Ge_5P$, which are not electron precise, show a large number of overlapping peaks in a range from −19.4 to 38.7 ppm and the influence of ring currents in aromatic *Tt*$_5$ rings must be considered.[36-38] The ^{29}Si MAS NMR spectra show similar trends. Compounds built from SiP_4 tetrahedra show shifts between −14.8 and 11.5 ppm, while $Li_{10.68(8)}Si_5P$ exhibits signals between 272 and 370 ppm. Compared to the 31P NMR spectrum, these two techniques are less sensitive to the connectivity of building blocks, but more sensitive to the nature of the building block.

Table 3.4: Chemical shifts of compounds in the Li/Si/P and Li/Ge/P phase system in ^{6}Li and ^{7}Li MAS NMR as well as ^{29}Si MAS NMR spectroscopy.

	^{7}Li (^{6}Li) MAS NMR δ / ppm	^{29}Si MAS NMR δ / ppm
Li_8SiP_4[1]	3.3	11.5
$Li_{10}Si_2P_6$	2.1	
Li_2SiP_2[1]	2.1	−14.8
$LiSi_2P_3$[2]	2.7	
$Li_{14}SiP_6$	5.4 (^{6}Li)	10.4
$Li_3Si_3P_7$	3.0	−3.3; −11.4
$Li_{10.68(8)}Si_5P$	38.7; 30.0; 3.2; −19.4	370; 295; 272
β-Li_8GeP_4[35]	3.4 (^{6}Li)	
Li_2GeP_2	2.4 (^{6}Li)	
$LiGe_3P_3$	3.6; 2.4 (^{6}Li)	
$Li_{10.1(2)}Ge_5P$	34.6; 31.3; 28.6; 22.3; 5.0; −7.0; −16.76	

3.1.3 Li^+ Ion Mobility

To determine the Li^+ motion within the compounds electrochemical impedance spectroscopy (EIS) measurements and static ^7Li NMR spectroscopy experiments are conducted. The impedance spectroscopy is used to determine the ionic conductivity σ and from temperature dependent experiments the activation energy E_A^{EIS} can be derived. From temperature dependent static ^7Li NMR spectroscopy measurements also activation energies E_A^{NMR} are deduced (Tab. 3.5). Therefore, the peak width as a function of the temperature is analyzed. From these experiments, materials with mobile Li^+ ions, are identified. All compounds described here are solely built from TtP_4 tetrahedra, while compounds with *Tt-Tt* bonds, such as $Li_{10.68(8)}Si_5P$ and $LiGe_3P_3$ show dominant electron conducting behavior. The Li^+ conducting compounds show conductivities in a range from 1.6×10^{-7} to 1.1×10^{-3} S cm^{-1} at 25 °C (Fig. 3.10). While the Si and Ge homologues only differ slightly in conductivity, strongly increasing mobility is observed with an increasing Li^+ content, finding a maximum of 1.1×10^{-3} S cm^{-1} at 25 °C in $Li_{14}SiP_6$. Compared to established Li^+ conducting materials this value is close to the highest values found for oxide based materials (e.g. $Li_{6.55}La_3Zr_2Ga_{0.15}O_{12}$: 1.3×10^{-3} S cm^{-1})[39], but still more than one order of magnitude lower than values found for fast conducting sulfides (>10^{-2} S cm^{-1}).[40] However, the evolution of ion conductivity in lithium phosphidotetrelates, starting from the first reports in 2016 with conductivities of 4×10^{-7} S cm^{-1} to 1.1×10^{-3} S cm^{-1} (25 °C) in this work, promises a further increase within the next years. This is supported by the fact that in conventional fast ion conductors usually four to five different elements are present, introducing mixed atom sites and defects, lowering the activation barrier and increasing conductivity. For lithium phosphidotetrelates so far only ternary compounds have been investigated, of which the compound $Li_{14}SiP_6$ already shows intrinsic disorder. By introducing further elements, for example by mixing SiP_4 and GeP_4 tetrahedra, the ion conduction may be further increased.

Table 3.5: List of ion conductivities σ and activation energies E_A for different lithium phosphidotetrelates.

Compound	σ / S cm^{-1} (25 °C)	E_A^{EIS} / kJ mol^{-1}	E_A^{NMR} / kJ mol^{-1}
Li_8SiP_4	4.5×10^{-5}	39	36[1]
Li_2SiP_2[1]	4×10^{-7}	54	47
$Li_{14}SiP_6$	1.1×10^{-3}	32	30
α-Li_8GeP_4	1.8×10^{-5}	42	35
β-Li_8GeP_4	8.6×10^{-5}	38	34
Li_2GeP_2	1.6×10^{-7} (27 °C)	-	-

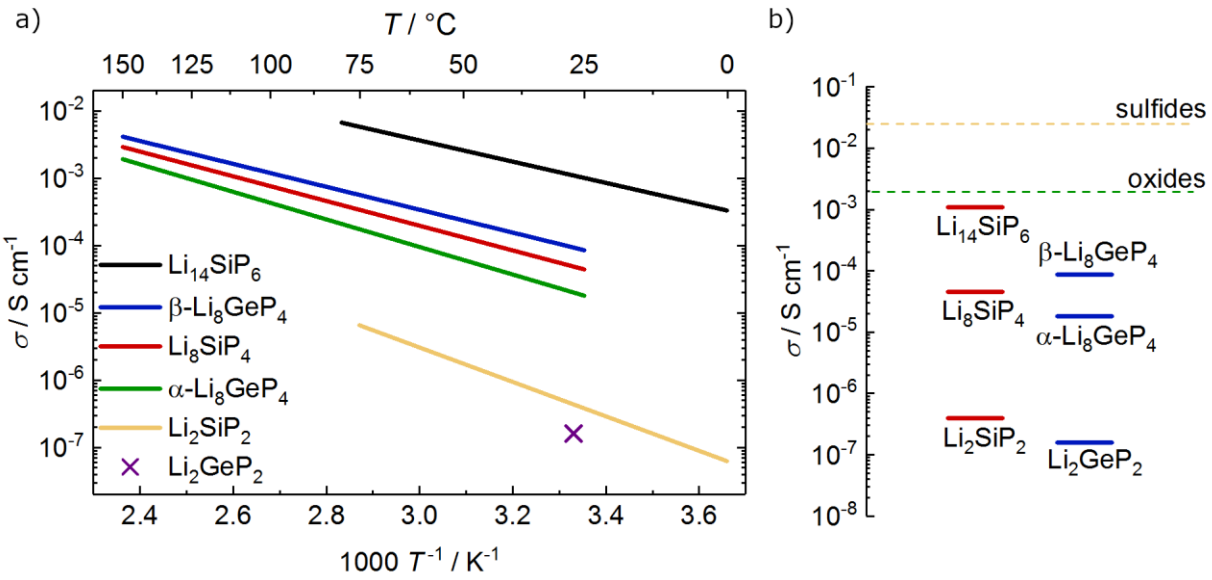

Figure 3.10: a) Temperature dependent ion conductivity of lithium phosphidotetrelates. b) Comparison of ion conductivity of lithium phosphidosilicates (red) and phosphidogermanates (blue) at room temperature. The highest conductivity values found for oxides and sulfides are marked with a green and yellow dashed line, respectively.

3.1.4 Syntheses

Depending on the material and the subsequent analytic method different solid state synthesis strategies are applied. For the preparation of single crystals, samples are synthesized from elements or binary Li/P precursors at temperatures up to 700 °C in sealed ampoules. Especially, Ta ampoules turned out to be beneficial for crystal growth. Additionally, an excess of Li or P is advantageous for crystal growth of certain compounds. However, these samples contained phase mixtures and for high contents of P contaminations resulting from side reactions with the ampoule material to TaP are observed.

To prepare bulk material with high purity, as used for NMR and impedance spectroscopy measurements, a synthesis route including ball milling and a subsequent annealing step is applied for most materials. Therefore, the elements are filled as powder (P, Si, Ge) or small pieces (Li) into the milling jar. After the mechanical milling PXRD measurements of the reactive mixture show sets of broad reflections, which are attributed to a cubic closed pack of P atoms with no ordering of the atoms within its voids. Only small reflections are observed for remaining unreacted *Tt* or formed binary Li/P compounds. For the second step the reactive mixture is pressed into pellets, sealed in carbon coated fused silica glass ampoules and heated to temperatures between 400 and 700 °C. This procedure works well for materials on the lines between Li_3P and "Tt_3P_4" and $LiGe_3P_3$.

$Li_3Si_3P_7$ is prepared with optimal results via a precursor approach from Li_3P_7 and Si at 700 °C. The usage of binary compounds as reactants in high temperature synthesis overcomes difficulties

caused by different physical properties of the elements. As the melting or decomposition point of binaries is higher than of the corresponding elements Li and P, it becomes more compatible with Si and Ge.

For the compounds $Li_{10.68(8)}Si_5P$ and $Li_{10.1(2)}Ge_5P$, no difference between the elements and binary precursors, most likely due to the high content of Li, having a low melting point, is observed. Both compounds are prepared via high temperature synthesis in Ta ampoules.

3.2 Preparation and Characterization of Binary and Ternary Sodium Phosphides

See Chapter 5.6	On the Structure and Conductivity of Na_3P H. Eickhoff, C. Dietrich, W. Klein, W. G. Zeier, T. F. Fässler, manuscript for publication
See Chapter 5.7	$Na_2Ge_3P_3$ & $Na_5Ge_7P_5$: Flexible Systems Built from 1-Dimensional Modular Units H. Eickhoff, V. Hlukhyy, T. F. Fässler, manuscript for publication

Followed by an increasing demand in lithium batteries, depleting lithium supplies as well as different demands for stationary applications the research is expanded to post Li cells. In this respect sodium-based systems are promising to the abundance of Na. Due to that binary and ternary sodium phosphides are interesting for application in sodium ion batteries and sodium ASSB, as trisodium phosphide represents the charged state of high capacity phosphorus anodes[41,42] and sodium phosphidosilicates are reported to exhibit ionic conductivities of 4×10^{-4} S cm^{-1}.[43]

3.2.1 Na_3P

Upon resynthesizing Na_3P, discrepancies between the found and the reported crystal structure emerged and are supported by descriptions found in literature. Systematic refinement of the single crystal diffraction data with various space groups leads to a superstructure with cell parameters of a = 8.61224(10) Å and c = 8.81949(10) Å (V = 568.32(2) Å^3) and space group $P6_3cm$ instead of the reported values of a = 4.9512(5) Å and c = 8.7874(13) Å (V = 186.56(4) Å^3) and space group $P6_3/mmc$ (Fig. 3.11).[44,45] Other refined space groups showed larger residuals and large prolate thermal ellipsoids. The reported model consist of planar sheets of hexagons of alternating P and Na atoms stacking alternatingly with sheets of corrugate Na_6 rings (gray As like). Within the new structure Na atoms are distorted from the formerly planar Na-P sheet. These Na atoms are shifted

above and below the layer, reducing the anisotropy of the thermal ellipsoids. This change conserves the planar P atom coordination. This distortion goes along with a shift of atoms in the Na layer located between the Na-P sheets. The atoms of corrugated Na hexagon layer avoid close contacts to Na-P sheet Na atoms, that leads to tilted PNa_5 trigonal bipyramids and to slightly longer Na-Na distances compared to the reported model. The new structural model of Na_3P is isotypic to Na_3As that was investigated by *Range et al.* in detail.[46,47] These two examples show that reinvestigation of trialkali phosphides leads to new insight into the structures, and superstructures may also be found for further alkali metals.

Investigation of the electric properties of Na_3P yielded mainly electronic conduction of 1.2×10^{-2} S cm^{-1} at room temperature, making this material unsuitable for application as SE but interesting as active material in electrodes.

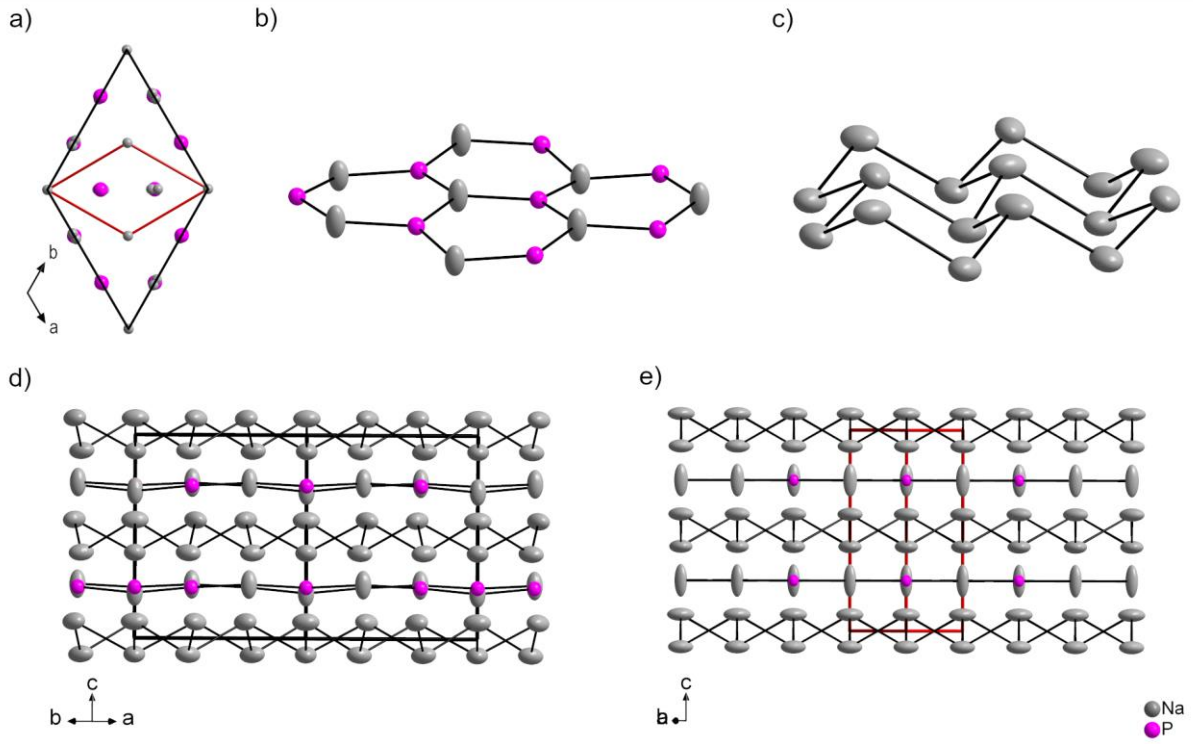

Figure 3.11: a) Comparison of unit cells of the new (black) and reported structural model (red) $Na_3P$with view along the c axis. Sections of layers from the new model consisting of b) almost planar Na-P hexagons and b) corrugated hexagons of Na. d) Extended unit cell (new model) with slightly corrugated Na-P sheets and e) extended unit cell of the reported model. The new model shows a clear distortion of the Na positions but less prolate ellipsoids. Bold black and red lines represent the unit cell.

3.2.2 $Na_2Ge_3P_3$ & $Na_5Ge_7P_5$

Exploration of the Na/Ge/P phase system led to the preparation of $Na_2Ge_3P_3$ and $Na_5Ge_7P_5$. For both compounds the space group *C*2/*m* was determined, with the unit cell parameters a = 17.639(4) Å, b = 3.6176(7) Å, c = 11.354(2) Å, β = 92.74(3)° and a = 16.151(3) Å, a = 16.168(5) Å, b = 3.6776(7) Å, c = 12.924(4) Å, β = 91.30(3)°, respectively (Fig. 3.12). The crystal structures consist of 1-dimensional polyanions separated by Na. For $Na_2Ge_3P_3$ the

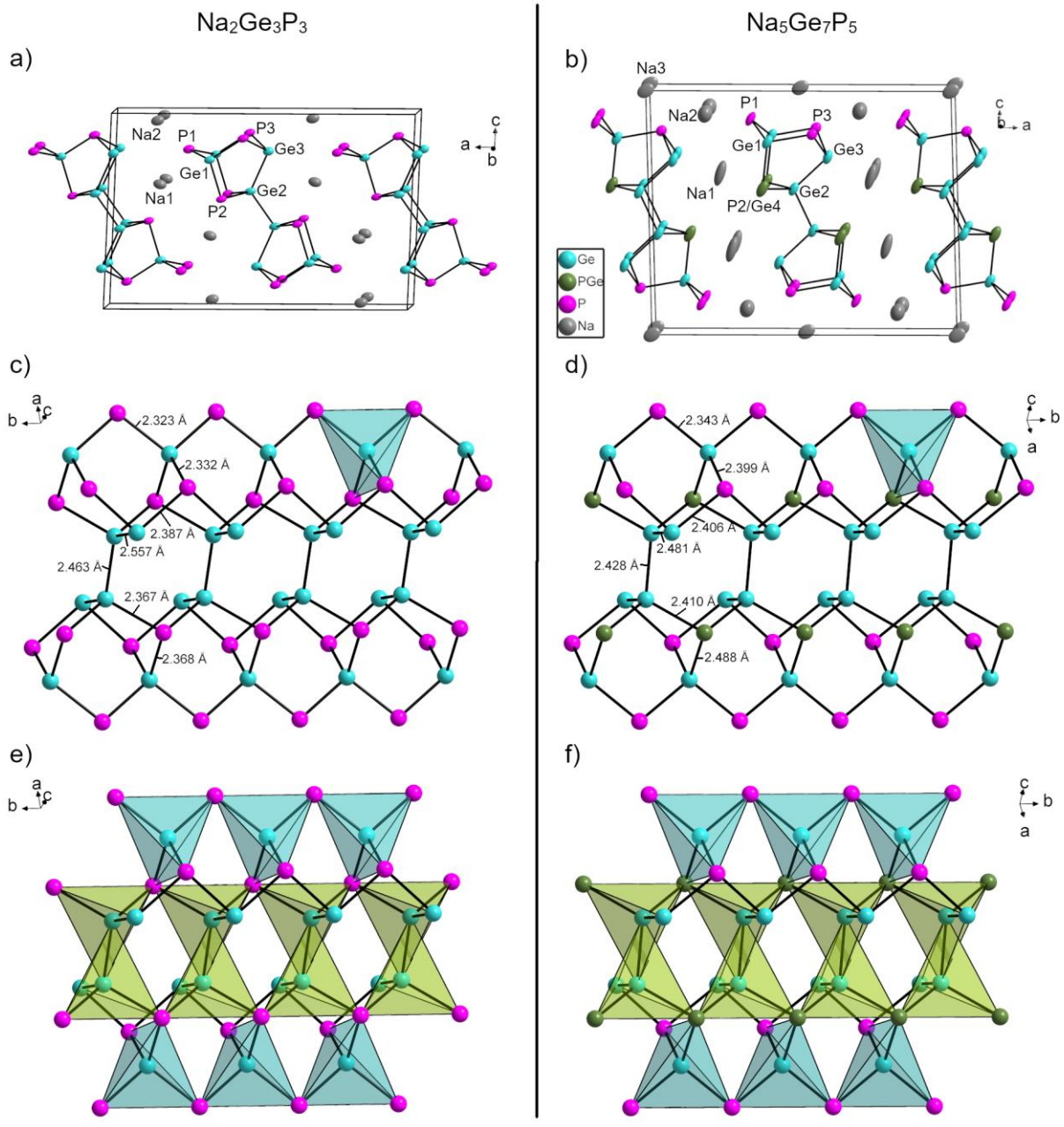

Figure 3.12: Crystal structures and enlarged polyanions of $Na_2Ge_3P_3$ (left) and $Na_5Ge_7P_5$ (right). a) and b): Depiction of the whole unit cell. c) and d): View of the polyanions with covalent bonds. e) and f): View of the polyanions with highlighted GeP_4 and $Ge(P_3Ge)$tetrahedra (light blue) and $Ge(P_2Ge_2)$, $Ge(PGe_3)$ and $Ge(Ge_4)$ tetrahedra (green).

polyanion is built from 9 atom cages condensed via three atoms to tubes. Two tubes are connected via Ge-Ge bonds to pairs.

In $Na_5Ge_7P_5$ similar anions are realized, which differ only in statistical occupation of a P atom site by P:Ge in the ratio 1:1. This difference causes a higher anion charge that is counterbalanced by additional Na, resulting in a rotation of the polyanionic units. This rotation is illustrated by a change in unit cell parameters. The anionic building blocks that are present in the new compounds show similarity to fibrous P[48] and are also known from other alkaline phosphidogermanates and binary germanium phosphides, like GeP, $NaGe_3P_3$ and the previously described $LiGe_3P_3$.[26,49] Comparing $NaGe_3P_3$ and $LiGe_3P_3$, in which GeP_4 and $Ge(P_3Ge)$ tetrahedra occur, which are connected via shared corners and via bonds between P and the Ge corner as well as due to the different connectivity in $Na_2Ge_3P_3$, GeP_4 and GeP_2Ge_2 tetrahedra are present. The GeP_2Ge_2 tetrahedra of the two sides of a tube pair are interpenetrating each other. For $Na_5Ge_7P_5$ beside GeP_4 tetrahedra also $G(P_3Ge)$, $Ge(PGe_3)$ and $Ge(Ge_4)$, as a reason of the mixed P/Ge site. As for the sodium phosphidogermanates also compounds are known that consist solely of GeP_4 tetrahedra ($Na_{10}Ge_2P_6$),[12] these compounds illustrate the structural flexibility of the system.

References

[1] L. Toffoletti, H. Kirchhain, J. Landesfeind, W. Klein, L. van Wüllen, H. A. Gasteiger, T. F. Fässler, *Chem. Eur. J.* **2016**, 22, 17635-17645.

[2] A. Haffner, T. Bräuniger, D. Johrendt, *Angew. Chem.* **2016**, 128, 13783-13786; *Angew. Chem. Int. Ed.* **2016**, 55, 13585-13588.

[3] R. Juza, W. Schulz, *Z. Anorg. Allgem. Chem.* **1954**, 275, 65-78.

[4] Z. Zhang, Y. Shao, B. Lotsch, Y.-S. Hu, H. Li, J. Janek, L. F. Nazar, C.-W. Nan, J. Maier, M. Armand, L. Chen, *Energy Environ. Sci.* **2018**, 11, 1945-1976.

[5] T. Krauskopf, S. P. Culver, W. G. Zeier, *Chem. Mater.* **2018**, 30, 1791-1798.

[6] B. Eisenmann, H. Jordan, H. Schäfer, *Mater. Res. Bull.* **1982**, 17, 95-99.

[7] J. P. Motte, A. el Maslour, *J. Solid State Chem.* **1975**, 15, 253-260.

[8] B. Eisenmann, J. Klein, *Z. Naturforsch B: J. Chem. Sci.* **1988**, 43b, 69-71.

[9] B. Eisenmann, J. Klein, *Z. Naturforsch B: J. Chem. Sci.* **1988**, 43b, 1156-1160.

[10] J.-E. Jørgensen; S. E. Rasmussen; *J. Cryst. Growth* **1979**, 47, 124-126

[11] L. Toffoletti, Dissertation, Technische Universität München, **2016**.

[12] B. Eisenmann, M. Somer, *Z. Naturforsch. B: J. Chem. Sci.* **1985**, 40b, 886-890.

[13] B. Eisenmann, J. Klein, M. Somer, *Z. Kristallogr.* **1991**, 197, 269-270.

[14] J. Peters, B. Krebs, *Acta. Crystallogr. B* **1982**, 38, 1270-1272.

[15] B. Eisenmann, M. Somer, *Z. Naturforsch. B: J. Chem. Sci.* **1984**, 39b, 736-738.

[16] B. Eisenmann, J. Klein, M. Somer, *Z. Kristallogr.* **1991**, 197, 265-266.

[17] B. Eisenmann, J. Klein, M. Somer, *Z. Kristallogr.* **1991**, 197, 267-268.

[18] B. Eisenmann, J. Klein, M. Somer, *Z. Kristallogr.* **1991**, 197, 273-274.

[19] B. Eisenmann, J. Klein, M. Somer, *Angew. Chem.* **1990**, 102, 92-93; *Angew. Chem. Int. Ed.* **1990**, 29, 87-88.
[20] Y. Dong, F. J. DiSalvo, *Acta Cryst. E* **2007**, 63, i97-i98.
[21] E. Zintl; G. Brauer, *Z. Elektrochem.* **1935**, 41, 297-303.
[22] G. Brauer, E. Zintl, *Z. Phys. Chem. B* **1937**, 37, 323-352.
[23] J.-A. Dolyniuk, H. He, A. S. Ivanov, A. I. Boldyrev, S. Bobev, K. Kovnir, *Inorg. Chem.* **2015**, 54, 8608-8616.
[24] H.-G. von Schnering, W. Hönle, *Chem. Rev.* **1988**, 88, 243-273.
[25] U Rößler, Dissertation, Technische Universität Darmstadt, **2000**.
[26] K. Feng, W. Yin, R. He, Z. Lin, S. Jin, J. Yao, P. Fu, Y. Wu, *Dalton Trans.* **2012**, 41, 484-489.
[27] M. Khatun, S. S. Stoyko, A. Mar, *J. Solid State Chem.* **2016**, 238, 229-235.
[28] J. Mark, M. P. Hanrahan, K. E. Woo, S. Lee, A. J. Rossini, K. Kovnir, *Chem. Eur. J.* **2019**, 25, 6392-6401.
[29] A. J. SpringThorpe, *Mater. Res. Bull.* **1969**, 4, 125-128.
[30] T. Wadsten, *Chem. Commun.* **1973**, 7, 1-4.
[31] I. Todorov; S. C. Sevov, *Inorg. Chem.* **2004**, 43, 6490-6494.
[32] R. Nesper, J. Curda, H.-G. von Schnering, *J. Solid State Chem.* **1986**, 62, 199-206.
[33] U. Frank, W. Müller, *Z. Naturforsch. B: J. Chem. Sci.* **1975**, 30b, 313-315.
[34] B. León, J. I. Corredor, J. L. Tirado, C. Pérez-Vincente, *J. Electrochem. Soc.* **2006**, 153, A1829-A1834.
[35] H. Eickhoff, G. Raudaschl-Sieber, T. F. Fässler, *unpublished results*.
[36] R. Nesper, H.-G. von Schnering, J. Curda, *Chem. Ber.* **1986**, *119*, 3576-3590.
[37] A. Kuhn, P. Sreeraj, R. Pöttgen, H.-D. Wiemhöfer, M. Wilkening, P. Heitjans, *Angew. Chem.* **2011**, *123*, 12305-12308; *Angew. Chem. Int. Ed. Engl.* **2011**, *50*, 12099-12102.
[38] S. Dupke, T. Langer, R. Pöttgen, M. Winter, H. Eckert, *Solid State Nucl. Mag.* **2012**, *42*, 17-25.
[39] C. Bernuy-Lopez, W. Manalastas, Jr., J. M. Lopez de Amo, A. Aguadero, F. Aguesse, J. A. Kilner, *Chem. Mater.* **2014**, 26, 3610-3617.
[40] Y. Kato, S. Hori, T. Saito, K. Suzuki, M. Hirayama, A. Mitsui, M. Yonemura, H. Iba, R. Kanno, *Nat. Energy* **2016**, 1, 16030.
[41] J. Deng, W.-B. Luo, S.-L. Chou, H.-K. Liu, S.-X. Dou, *Adv. Energ. Mater.* **2017**, 8, 1701428.
[42] J. Peters, D. Buchholz, S. Passerini, M. Weil, *Energy Environ. Sci.* **2016**, 9, 1744-1751.
[43] A. Haffner, A.-K. Hatz, I. Moudrakovski, B. V. Lotsch, D. Johrendt, *Angew. Chem.* ***2018***, 130, 6263-6268; *Angew. Chem. Int. Ed.* **2018**, 57, 6155-6160.
[44] G. Brauer, E. Zintl, *Z. Phys. Chem. Abt. B* **1937**, 37, 323-352.
[45] Y. Dong, F. J. DiSalvo, *Acta Cryst. E* **2005**, 61, i223-i224.
[46] P. Hafner, K.-J. Range, *J. Alloy. Compd.* **1994**, 216, 7-10.
[47] K.-J. Range, R. Ehrl, P. Hafner, *J. Alloy. Compd.* **1996**, 240, 19-24.
[48] M. Ruck, D. Hoppe, B. Wahl, P. Simon, Y. Wang, G Seifert, *Angew. Chem. Int. Ed.* **2005**, *44*, 7616-7619; *Angew. Chem.* **2005**, *46*, 7788-7792.
[49] T. Wadsten, *Acta Chem. Scand.* **1967**, *21*, 593-594.

4 Conclusion and Outlook

With an increasing renewable energy share, electro mobility and digitalization, advance of energy storage technologies, such as rechargeable batteries, becomes increasingly significant. Within this context phosphide-based materials are investigated as potential materials for application in ASSBs. Depending on the electric properties of these materials they can play a role as SE, as component for composite electrode or during lithiation of binary silicon or germanium phosphides.

Previously, Li_8SiP_4, Li_2SiP_2 and $LiSi_2P_3$ have been the only reported compounds in the Li/Si/P phase system and the even poorer investigated Li/Ge/P phase systems only contained Li_5GeP_3. Within this work, the list of compounds in both phase systems is expanded by various compounds and first attempts to investigate the Na/Ge/P phase system led to further novel compounds.

The exploration of new lithium phosphidosilicates led to the discovery of $Li_3Si_3P_7$, $Li_{10}Si_2P_6$ and $Li_{14}SiP_6$. These compounds expand the known structural motives of lithium phosphidosilicates of isolated and corner sharing SiP_4 tetrahedra by connection via P-P bonds and edge sharing tetrahedra. Also, the combination of SiP_4 and P^{3-} within the same compound as found in $Li_{14}SiP_6$ is unprecedented. Powder neutron diffraction revealed a framework of 3D paths for Li^+ through the structure. Remarkably, the trajectory of lithium hopping does not occur through the center of a face shared by neighboring polyhedra, but through three necks shifted towards its P corners. These paths in the Li richest lithium phosphidosilicate found so far are confirmed by a high ionic conductivity of 1 mS cm^{-1}. This ionic conductivity is comparable to that of materials discussed for application in ASSB and the highest value found for phosphides so far. Comparison with the lithium poorer compounds Li_8SiP_4 (6×10^{-6} S cm^{-1}) and Li_2SiP_2 (4×10^{-7} S cm^{-1})[1] shows a clear trend of increasing ionic conductivity with increasing Li^+ content.

Attempts to analyze the effect of anion sizes on ionic conductivity in phosphides lead to the exploration of the Li/Ge/P phase system. The described lithium phosphidogermanates α-Li_8GeP_4 and β-Li_8GeP_4 are isotypic to Li_8SiP_4 and Li_8SnP_4, respectively, and show a close crystallographic relation via a CaF_2 like aristotype similar to $Li_{14}SiP_6$. Surprisingly, comparison of the ionic conductivity of α-Li_8GeP_4, β-Li_8GeP_4 and Li_8SiP_4 did not show a trend explainable with ion or bottle neck size. The lowest conductivity is found for α-Li_8GeP_4, an intermediate for Li_8SiP_4 and the highest for β-Li_8GeP_4. A reason for this behavior can be found in the distribution of Li atoms over the octahedral voids. In α-Li_8GeP_4 Li^+ is confined to a small number of octahedral voids with high occupation, while in β-Li_8GeP_4 Li^+ is spread over a larger number of voids with lower

occupation. Assuming fast Li conduction can only occur via sites with a significant Li^+ occupation, in β-Li_8GeP_4 more possibilities for ion hopping are conceivable. Additionally, to the fast Li^+ conduction these Ge containing materials also exhibit high electronic conductivities only two to three orders of magnitude lower than the ionic motion, making this material class possible mixed conducting additive for composite cathodes of ASSBs.

The lithium poorer compound Li_2GeP_2, which is isotypic to Li_2SiP_2,[1] exhibits frameworks of Ge_4P_{10} supertratrahedra. The ionic conductivity of $1.6(3)\times10^{-6}$ S cm^{-1} is slightly lower compared to Li_2SiP_2 that is caused by a closing of the channels along [111] direction, due to a rotation and distortion of the supertetrahedra.

In contrast to direct translation of structures from the Li/Si/P to Li/Ge/P phase system presented so far, the compound $LiGe_3P_3$ exhibits structural motives only known from heavier homologues such as $LiGe_3As_3$.[2] The compound consists of layers built from tubes of GeP_4 tetrahedra and Ge dumbbells. With the difference in structure also the properties alter. While all other compounds found in the Li/*Tt*/P (*Tt* = Si, Ge) are highly sensitive to moisture, $LiGe_3P_3$ does not show any degradation in contact with water, representing the first moisture and air stable lithium phosphidogermanate. Additionally, investigations of electric properties revealed mainly electronic conduction of 10^{-4} S cm^{-1}. Nevertheless, by combining construction principles found in fast ion conducting phosphidotetrelates and chemically inert compounds like $LiGe_3P_3$ synthesis of compounds exhibiting positive features of both groups are conceivable.

The investigation of the Si and Ge rich parts of the discussed phase systems yields with $Li_{10.68(8)}Si_5P$ and $Li_{10.1(2)}Ge_5P$ compounds, which do not contain typical tetrahedral building blocks found in phosphidotetrelates. They are the first compounds containing aromatic Si_5 or Ge_5 rings simultaneously to P^{3-} units, emphasizing the structural diversity of the corresponding element combinations.

Comparison of all phases in the Li/Si/P and Li/Ge/P phase systems revealed intriguing trends useful for structural characterization as well as connections of structure and ionic conductivity.

First experiments in Na containing systems lead to the reinvestigation of the structure of Na_3P. Similar to Na_3As[3] it crystallizes with a superstructure to the prior proposed structure in the space group $P6_3/mmc$ with cell parameters a = 8.61224(10) Å and c = 8.81949(10) Å, which is caused by a dislocation from Na atoms from their ideal positions. Na_3P and Na_3As are the first trialkali pnictides revised, making a similar superstructure for more related compounds highly probable.

Further experiments in the Na/Ge/P phase system yield the compounds $Na_2Ge_3P_3$ and $Na_5Ge_7P_5$. Both compounds consist of building blocks recurring in related phase systems but are connected

in a new manner to form 1-dimensional dimers of Ge-P tubes. The presence of a 3-dimensional Na lattice with short Na-Na interactions may enable ionic motion.

References

[1] L. Toffoletti, H. Kirchhain, J. Landesfeind, W. Klein, L. van Wüllen, H. A. Gasteiger, T. F. Fässler, *Chem. Eur. J.* **2016**, 22, 17635-17645.

[2] J. Mark, M. P. Hanrahan, K. E. Woo, S. Lee, A. J. Rossini, K. Kovnir, *Chem. Eur. J.* **2019**, 25, 6392-6401.

[3] K.-J. Range, R. Ehrl, P. Hafner, *J. Alloy. Compd.* **1996**, 240, 19-24.

5 Publications and Manuscripts

5.1 Synthesis and Characterization of the Lithium-Rich Phosphidosilicates $Li_{10}Si_2P_6$ and $Li_3Si_3P_7$

H. Eickhoff, L. Toffoletti, W. Klein, G. Raudaschl-Sieber, T. F. Fässler

published in

Inorg. Chem. **2017**, *56*, 6688-6694.

Inorganic Chemistry

Article

pubs.acs.org/IC

Synthesis and Characterization of the Lithium-Rich Phosphidosilicates $Li_{10}Si_2P_6$ and $Li_3Si_3P_7$

Henrik Eickhoff, Lorenzo Toffoletti, Wilhelm Klein, Gabriele Raudaschl-Sieber, and Thomas F. Fässler*

Department of Chemistry, Technische Universität München, Lichtenbergstrasse 4, 85747 Garching bei München, Germany

Supporting Information

ABSTRACT: The lithium phosphidosilicates $Li_{10}Si_2P_6$ and $Li_3Si_3P_7$ are obtained by high-temperature reactions of the elements or including binary Li−P precursors. $Li_{10}Si_2P_6$ ($P2_1/n$, $Z = 2$, $a = 7.2051(4)$ Å, $b = 6.5808(4)$ Å, $c = 11.6405(7)$ Å, $\beta = 90.580(4)°$) features edge-sharing SiP_4 double tetrahedra forming $[Si_2P_6]^{10-}$ units with a crystal structure isotypic to $Na_{10}Si_2P_6$ and $Na_{10}Ge_2P_6$. $Li_3Si_3P_7$ ($P2_1/m$, $Z = 2$, $a = 6.3356(4)$ Å, $b = 7.2198(4)$ Å, $c = 10.6176(6)$ Å, $\beta = 102.941(6)°$) crystallizes in a new structure type, wherein SiP_4 tetrahedra are linked via common vertices and which are further connected by polyphosphide chains to form unique $^2_\infty[Si_3P_7]^{3-}$ double layers. The two-dimensional Si−P slabs that are separated by Li atoms can be regarded as three covalently linked atoms layers: a defect α-arsenic type layer of P atoms sandwiched between two defect wurzite-type Si_3P_4 layers. The single crystal and powder X-ray structure solutions are supported by solid-state ^{7}Li, ^{29}Si, and ^{31}P magic-angle spinning NMR measurements.

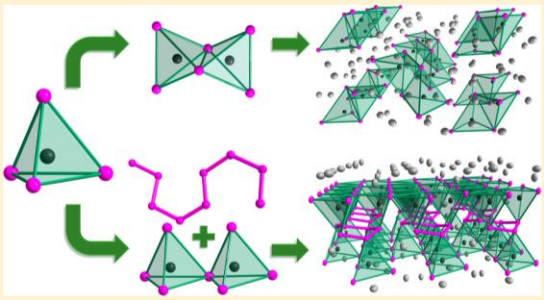

INTRODUCTION

Solid-state ion conductors are in the focus of research, since all solid-state batteries might fulfill the safety issues required for electrochemical energy-storage systems. Thus, the search for new material classes with the potential for Li ion mobility is a great challenge.[1] Recently lithium phosphidosilicates were introduced as a novel class of Li ion conductors, as impedance spectroscopic measurements for Li_8SiP_4 revealed ionic conductivities up to 1.2×10^{-4} S cm^{-1} at 75 °C.[2] Also the use of SiP_2 as anode material has been investigated,[3,4] and for insight into the lithiation process of this material, knowledge of existing lithium phosphidosilicates is crucial as well. SiP_4 tetrahedral building units, as they are found in Li_8SiP_4 and which have previously been observed in Ba_4SiP_4,[5] allow formation of new structures by condensation of tetrahedra. Indeed phosphidosilicates show a large variety of structural motifs originating from covalently bound silicon−phosphorus units or frameworks, where alkaline, alkaline earth, transition metal, or rare earth element atoms serve as counterions. Beside isolated $[SiP_4]^{8-}$ units, SiP_4 tetrahedra act as building blocks, which can arrange in different ways to give rise to edge-sharing double tetrahedra $[Si_2P_6]^{10-}$ in $Na_{10}Si_2P_6$,[6] infinite $^1_\infty[SiP_2]^{2-}$ chains in K_2SiP_2,[7] by connection via common edges, whereas linkage by sharing corners leads to $^2_\infty[Si_2P_3]^-$ layers as found in KSi_2P_3[8] or three-dimensional frameworks as in Li_2SiP_2,[2] $LiSi_2P_3$,[9] and Ag_2SiP_2.[10]

These building principles resemble the well-known oxidosilicates, which are built upon SiO_4 tetrahedra but are usually limited to two bonds per oxygen atom, and the SiN_4 tetrahedra-based nitridosilicates, which are able to form three or in special cases even four bonds per nitrogen atom.[11] Additionally, the possible formation of homoatomic bonds between phosphorus atoms further increases the number of structural motifs realizable by phosphidosilicates. This results in a potentially higher variability of structures for this class of compounds than for the oxido- or nitridosilicates, as illustrated by $Ca_3Si_8P_{14}$[12] and $AlSiP_3$[13] containing phosphorus dumbbells, $LnSi_2P_6$ (Ln = La, Ce, Pr, Nd) with polyanions P_n ($n = 3-6$),[14] and Cu_4SiP_8 with SiP_4 tetrahedra bond to a polyphosphide spiral chain.[15] Besides these numerous examples in the domain of tetrahedral units in phosphidosilicates, also planar carbonate-like $[SiP_3]^{5-}$ units in Cs_5SiP_3 are reported.[16]

Within the group of lithium phosphidosilicates, Li_5SiP_3 was the only known compound for more than 60 years. In 1954 Juza & Schulz proposed a crystal structure including mixed lithium−silicon sites featuring an antifluorite structure type.[17] Until recently, a reinvestigation of the ternary Li−Si−P system revealed the existence of two new phosphidosilicates such as Li_8SiP_4[2] and Li_2SiP_2,[2] shortly after followed by $LiSi_2P_3$.[9] Therein, the structure of Li_8SiP_4 strongly correlates with the antifluorite-type Li_5SiP_3, while synthesis of the latter could not be reproduced.

In this work we present the syntheses and crystal structures of the two new phosphidosilicates, namely, $Li_3Si_3P_7$ and a monoclinic form of Li_5SiP_3, herein named $Li_{10}Si_2P_6$ to emphasize covalently bound $[Si_2P_6]^{10-}$ units, which are characterized via X-ray diffraction and solid-state NMR spectroscopy.

Received: March 29, 2017
Published: May 24, 2017

DOI: 10.1021/acs.inorgchem.7b00755
Inorg. Chem. 2017, 56, 6688−6694

EXPERIMENTAL SECTION

All chemicals were handled under Ar atmosphere in gloveboxes (MBraun, 200B) with moisture and oxygen level below 0.1 ppm or in containers, which were sealed under Ar atmosphere.

Syntheses of $Li_{10}Si_2P_6$ and $Li_3Si_3P_7$. Bulk samples of $Li_{10}Si_2P_6$ and $Li_3Si_3P_7$, single crystals, and the binary precursors Li_3P and Li_3P_7 were synthesized via reactions with temperatures ranging from 400 to 800 °C with a heating rate of 4 °C/min and a cooling rate of 1 °C/min. The educt mixtures were welded in Nb or Ta ampules and sealed in evacuated protective silica-glass containers. In an alternative procedure the educts are pressed to a pellet and sealed in graphitized silica-glass ampules. All syntheses were conducted in muffle (Nabertherm, L5/11/P330) or tubular vertical furnaces (HTM Reetz, LOBA 1200−40−600). As starting materials lithium lumps (Rockwood Lithium, 99%), silicon powder (Wacker, 99.9%), and red phosphorus powder (Sigma-Aldrich, 97%) were used.

Li_3P was prepared via a reaction of 402 mg of Li (57.9 mmol) and 598 mg of P (19.3 mmol). The educts were sealed in a Nb ampule and heated to 400 °C for 24 h. The ampule was opened, and the product was ground, sealed in new identical ampules, and reheated with the same temperature program.

Li_3P_7 was prepared from stoichiometric amounts of Li (132 mg, 18.9 mmol) and P (1369 mg, 44.2 mmol). The educts were sealed in a Ta ampule and heated to 600 °C for 72 h.

For the synthesis of $Li_{10}Si_2P_6$, a reactive mixture was prepared by mechanical milling of Li (334 mg, 48.2 mmol), Si (270 mg, 9.63 mmol), and P (895 mg, 28.9 mmol) in a tungsten carbide milling jar with three Ø15 mm balls (Retsch PM100 Planetary Ball Mill, 350 rpm, 24 h, 10 min interval, 3 min break). This precursor (0.5 g) was sealed in a graphitized silica-glass ampule and heated to 650 °C for 150 h.

A single crystal of $Li_{10}Si_2P_6$ was found in a sample with the nominal composition of "$Li_9Si_2P_9$", where $Li_{10}Si_2P_6$ was in concomitance with Li_2SiP_2. For synthesis 117 mg of Li_3P (1.5 mmol), 43 mg of Si (2.3 mmol), and 140 mg of P (4.5 mmol) were ground and sealed in a Nb ampule and heated to 800 °C for 24 h.

$Li_3Si_3P_7$ was obtained from a reaction of a mixture of Li_3P_7 (369 mg, 1.55 mmol) and Si (131 mg, 4.66 mmol). The educts were sealed in a graphitized silica-glass ampule and heated 24 h to 700 °C.

Gray bar-shaped crystals of $Li_3Si_3P_7$ were obtained from a sample containing Li (22 mg, 3.22 mmol), Si (199 mg, 7.08 mmol), and P (278 mg, 9.01 mmol) in a molar ratio of 5:11:14. The educts were welded into a Ta ampule and heated to 600 °C for 72 h.

Energy-Dispersive X-ray Spectroscopy. $Li_{10}Si_2P_6$ and $Li_3Si_3P_7$ single crystals were measured with JEOL JSM-5900 LV (20.0 kV) and Hitachi TM-1000 Table Top (15 kV) scanning electron microscopes, respectively. Both samples were fixed on a graphite tape on an aluminum cylinder.

Powder X-ray Diffraction. Data were collected at room temperature on a STOE Stadi P diffractometer (Ge(111) monochromator, Cu $K\alpha_1$ radiation, λ = 1.540 56 Å) with a Dectris MYTHEN 1K detector in Debye−Scherrer geometry. Samples were sealed in glass capillaries (Ø 0.3 mm) for measurement. Raw data were processed with WinX-POW[18] software, and Rietveld refinements were executed with JANA2006.[19]

Single-Crystal X-ray Data Collection. Crystals of $Li_{10}Si_2P_6$ and $Li_3Si_3P_7$ were separated from the sample and sealed in glass capillaries (Ø 0.3 mm). Data collection of $Li_{10}Si_2P_6$ was performed on a D8 Kappa Apex II (Bruker AXS) and of $Li_3Si_3P_7$ on an Xcalibur3 (Oxford Diffraction). Both diffractometers are equipped with Mo Kα X-ray sources and graphite monochromators. The program package SHELX-2014[20] was used for structure solution and refinement. The assignment of the Si and P to the heavy atom positions was done by considering coordination and chemical environment of the single atoms. The solutions exhibit the lowest residual values compared to any other configuration (with exchanged Si and P positions) and are in agreement with the NMR data. Further details of the crystal structure investigations are available in the Supporting Information.

Solid-State MAS NMR Spectroscopy. Magic-angle spinning (MAS) NMR spectra were recorded with a Bruker Avance 300 operating at 7.04 T. Resonance frequencies of 116.6, 59.6, and 121.5 MHz, relaxation delays of 4, 300, and 60 s, and pulse width of 13, 6, and 1.33 μs were applied for ^{7}Li, ^{29}Si, and ^{31}P measurements, respectively. Samples were packed in 4 mm or 7 mm ZrO_2 MAS NMR probes and rotated with frequencies of 15 kHz for ^{7}Li and ^{31}P and 5 kHz for ^{29}Si measurements.

RESULTS AND DISCUSSION

Syntheses. $Li_{10}Si_2P_6$ was synthesized by ball milling the stoichiometric amounts of Li, Si, and P. Subsequent annealing of the finely powdered mixtures resulted in a phase-pure product. For the synthesis of $Li_3Si_3P_7$ the presynthesized binary lithium phosphide Li_3P_7 was mixed with elemental Si and treated at elevated temperature. A Rietveld analysis of an X-ray powder diffraction pattern of $Li_{10}Si_2P_6$ revealed a purity of the crystalline phase of greater than 98 wt % with contaminations of Li_8SiP_4 and WC as abrasion product of the milling process with less than 1 wt % each (see Figure 1a). For the main phase

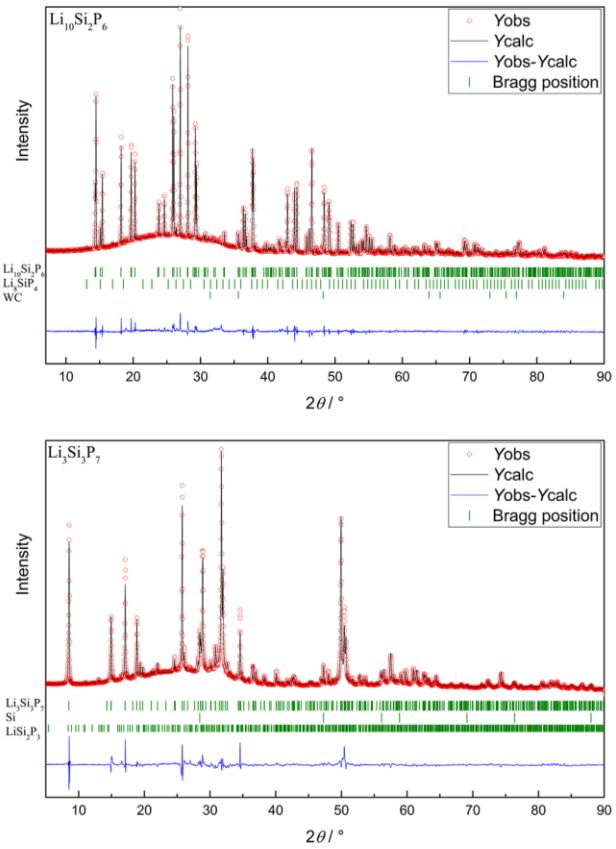

Figure 1. Rietveld analysis of X-ray powder diffractograms of $Li_{10}Si_2P_6$ (top) and $Li_3Si_3P_7$ (bottom). Red circles indicate observed intensities; black lines show calculated intensities. Blue lines show the difference between observed and calculated intensities, and green marks indicate Bragg positions.

of $Li_3Si_3P_7$ large crystalline metallic-gray bars of $Li_3Si_3P_7$ up to 0.5 mm length were obtained. An overall crystalline phase fraction of 94.5 wt % was determined with contaminations of silicon and $LiSi_2P_3$ of less than 3 wt % each (Figure 1b). Crystals of both compounds were investigated by energy-dispersive X-ray (EDX) spectroscopy, and the Si/P ratio was found to be very close to the expected values.

DOI: 10.1021/acs.inorgchem.7b00755
Inorg. Chem. 2017, 56, 6688−6694

Crystal Structure of $Li_{10}Si_2P_6$. $Li_{10}Si_2P_6$ crystallizes as dark red block-shaped crystals in the monoclinic space group $P2_1/n$ isotypic to the previously reported $Na_{10}Tt_2Pn_6$ phases (where Tt = Si, Ge, Sn and Pn = P, As).[6,21,22] In Table 1 the details of the structure refinement from single-crystal diffraction data at 123 K are shown; the corresponding data for a measurement at ambient temperature are given as Supporting Information. The phosphidosilicate contains five Li, one Si, and three P crystallographically independent atomic positions, which all fully occupy general 4e positions. Even though the Tt_2P_6 unit is known for Tt = Si, Ge, and Sn, $Li_{10}Si_2P_6$ represents the first example of such a unit with lithium counterions.

Table 1. Crystallographic Data and Refinement Parameters of $Li_{10}Si_2P_6$ and $Li_3Si_3P_7$ at 123 and 130 K, Respectively

empirical formula	$Li_{10}Si_2P_6$	$Li_3Si_3P_7$
formula weight, g·mol^{-1}	311.40	321.88
crystal size, mm^3	0.20 × 0.15 × 0.10	0.13 × 0.10 × 0.09
crystal color	dark red	gray
T, K	123(2)	130(2)
crystal system	monoclinic	monoclinic
space group	$P2_1/n$ (14)	$P2_1/m$ (11)
unit cell parameters, Å	a = 7.2051(4)	a = 6.3356(4)
	b = 6.5808(4)	b = 7.2198(4)
	c = 11.6405(7)	c = 10.6176(6)
	β = 90.580(4)°	β = 102.941(6)°
Z	2	2
V, Å^3	551.91(6)	473.33(5)
ρ_{calc}, g·cm^{-3}	1.874	2.258
μ, mm^{-1}	1.124	1.609
F(000), e	296	312
θ range, deg	3.34–35.16	3.30–29.98
index range (hkl)	$-11 \le h \le 10$	$-8 \le h \le 8$
	$-9 \le k \le 10$	$-10 \le k \le 10$
	$-14 \le l \le 18$	$-14 \le l \le 14$
reflections collected	9492	7964
independent reflections	2446	1477
R_{int}	0.0373	0.0400
reflections with $I > 2\sigma(I)$	1965	984
absorption correction	multiscan	multiscan
data/restraints/parameters	2446/0/83	1477/0/71
goodness-of-fit on F^2	1.021	0.907
R_1, wR_2 (all data)	0.0411, 0.0466	0.0465, 0.0666
R_1, wR_2 [$I > 2\sigma(I)$]	0.0264, 0.0432	0.0272, 0.0641
largest diff. peak and hole (e·Å^{-3})	0.545/−0.440	0.769/−0.448

In $Li_{10}Si_2P_6$ only heteroatomic covalent bonds are found between Si and P atoms, and its crystal structure consists of isolated $[Si_2P_6]^{10-}$ units surrounded by Li^+ ions. As shown in Figure 2a and highlighted in Figure 2b, the Si_2P_6 units are built by two edge-sharing SiP_4 tetrahedra. Within a Si_2P_6 unit, the Si−P interatomic distances range from 2.2235(4) to 2.3067(4) Å. These distances correlate with Si−P covalent bond lengths found in other binary and ternary phases.[2,6,7,9,23] Because of the occurrence of edge sharing, the SiP_4 tetrahedra are distorted, and the P−Si−P angles ranging from 96.75(1)° to 115.33(2)° deviate from the tetrahedral angle 109.4°. The Si_2P_6 units in $Li_{10}Si_2P_6$ are isolated from each other with nonbonding distances between P atoms of different Si_2P_6 units larger than 3.9 Å. The first coordination sphere consists of lithium ions, and Li−P distances are in the range from 2.484(2) to 2.884(2) Å. The distances are in agreement with distances observed for other binary and ternary phases containing Li and P.[2,9,24,25] Finally, also the shortest Li−Li distances in $Li_{10}Si_2P_6$ (2.722(3) Å) are comparable with those found in the other lithium phosphidosilicates, although considerably longer than those found in the quite Li-rich Li_8SiP_4 (2.383(6) Å).[2]

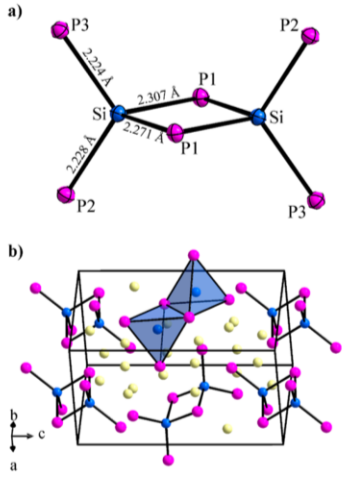

Figure 2. Structure details of $Li_{10}Si_2P_6$. (a) Si_2P_6 unit formed by two edge-sharing SiP_4 tetrahedra. (b) Extended unit cell. SiP_4 tetrahedra are highlighted in blue color. Li, Si, and P atoms are depicted as yellow, blue, and pink thermal ellipsoids, respectively, set at 90% probability.

Considering formally one negative charge for the two-bonded P atoms and two negative charges for the single-bonded P atoms, a formal charge of −10 arises for each Si_2P_6 unit. This is balanced by 10 Li^+ ions per unit, thus establishing $Li_{10}Si_2P_6$ as an electron-precise compound.

$Li_{10}Si_2P_6$ represents the "missing link Li_5SiP_3" within the series obtained by formally diminishing the Li_3P content in lithium phosphidosilicates starting from the ortho compound

$$Li_8SiP_4 \xrightarrow{-Li_3P} Li_5SiP_3 \xrightarrow{-Li_3P} Li_2SiP_2 \xrightarrow{-1/2Li_3P} (LiSi_2P_3)_{1/2}$$

The anionic partial structure mirrors the position in this series, as the double tetrahedra are an intermediate between isolated SiP_4 and three-dimensional networks of corner-sharing tetrahedra in Li_8SiP_4 and Li_2SiP_2, respectively.

The composition of the new phosphidosilicate (5:1:3) is a recurrent one in the A−Tt−Pn systems (A = alkaline metal, Tt = group 14 elements, Pn = group 15 element). However, the crystal structure of such compounds seems to be heavily affected by the size of cations and anions. In fact, the formation of Si_2P_6 units is observed in $Na_{10}Tt_2Pn_6$ phases (where Tt = Si, Ge and Pn = P, As).[6,21,22] An increase of the cation radius (Rb, Cs) leads to cleavage of the dimeric anion into carbonate ion shaped planar units,[16,26] and an increase in size of the anions (by including Sn and Sb atoms) results in a condensation of the $TtPn_4$ units into infinite chains of corner-sharing tetrahedra.[27] $Li_{10}Si_2P_6$ is the first example of Tt_2Pn_6 units present in combination with Li cations and does not solely contain the same structural entity as observed for the sodium compounds but even crystallizes isotypically with the $Na_{10}Tt_2Pn_6$ phases.[6,21,22]

A phase with the same composition, Li_5SiP_3, was previously reported by Juza and Schulz.[17] The crystal structure was crudely described as antifluorite-type structure with P forming a face-centered cubic packing and Li and Si atoms being statistically distributed in the tetrahedral voids.[17] That time the authors

DOI: 10.1021/acs.inorgchem.7b00755
Inorg. Chem. 2017, 56, 6688−6694

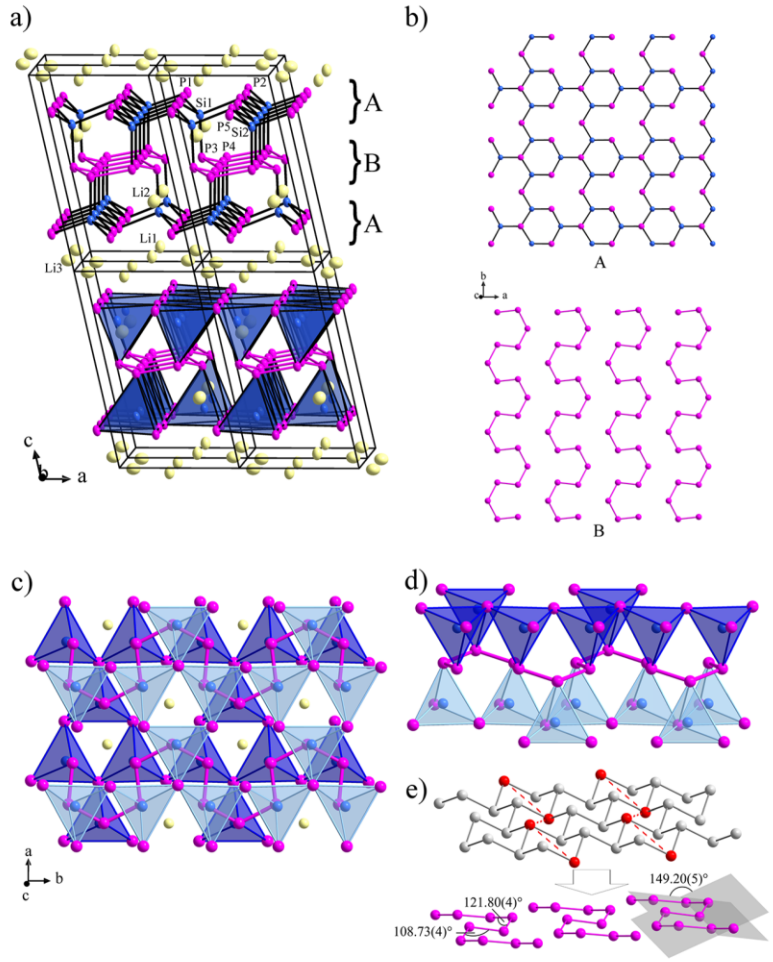

Figure 3. (a) Crystal structure of $Li_3Si_3P_7$. (upper) The covalent Si−P network with Si−P and P−P bonds. (lower) The same arrangement represented with SiP_4 tetrahedra (blue) and P−P bonds. (b) Projections of atom layers of the slab shown in (a). Layer **A** and **B** represent defect atom sheets wurtzite and As_{gray} types, respectively, as they occur in $Li_3Si_3P_7$. (c) Projection perpendicular to the mean plane of layer A and B. (d) Part of a P chain in $Li_3Si_3P_7$ with adjacent SiP_4 tetrahedra. (e) Construction of P chains originating from gray As layers by removing one-fourth of all atoms (red atoms) with angles between planes defined by all P4 and P3 with adjacent P4 atoms and bond angles. Positions of Si, P, and Li atoms are shown with blue, pink, and yellow color, respectively. The P−P chains are shown with pink color, and SiP_4 tetrahedra (top layer: pale blue, bottom layer: vivid blue).

mentioned some impurities, which they were unable to assign and which were not further investigated. In a recent study, we showed that indeed a ternary phosphidosilicate exhibiting an ordered variant of the antifluorite structure type exists but resulting in the composition Li_8SiP_4.[2] Currently, we did not find any relation between the new monoclinic $Li_{10}Si_2P_6$ and an antifluorite phase, as, for example, a reversible structural transition. However, mechanical alloying of a stoichiometric mixture of Li, Si, and red P, which represents the first step of the synthesis of monoclinic $Li_{10}Si_2P_6$, yielded a powder diffraction pattern closely resembling the one reported by Juza and Schulz in their study.

Crystal Structure of $Li_3Si_3P_7$. The X-ray reflection pattern of single crystals of $Li_3Si_3P_7$ were indexed in the monoclinic space group $P2_1/m$. The details on the single-crystal data collection and structure refinement are listed in Table 1; further information as well as the corresponding data for the room-temperature (RT) measurement are given as Supporting Information.

In the crystal structure of $Li_3Si_3P_7$, double layers of SiP_4 tetrahedra reveal a two-dimensional structure type. The slabs of Si and P atoms are separated by Li atoms. The SiP_4 tetrahedra that form the basic building units share vertices and are also arranged to allow the formation of P−P bonds (Figure 3a,c), which is a consequence of the fact that $Li_3Si_3P_7$, so far, is the P-richest compound in this ternary system. The covalently connected P atoms form meandering chains along the [0 1 0] direction (Figure 3d). Parallel oriented chains of P atoms form a corrugated layer B, which, although considerably flattened, strongly resemble a section of the structure of gray arsenic, wherein one-fourth of the atoms are absent in an ordered manner (Figure 3b). The angle between the planes defined by all P4 and by P3 atoms with adjacent P4 atoms is widened to 149.20(5)° (cp. in As_{gray}: 79.95°) leading to P−P−P angles of 121.80(4)° (P3) and 108.73(4)° (P4) (cp. in As_{gray}: 96.66°) as well as torsion angles of 32.52(5)° and 180° (cp. in As_{gray}: 82.46°, 180°)[28] (Figure 3e). Within these chains, the P−P bonds are the shortest interatomic distances in this compound. The average P−P bond length of 2.207 Å lies within the

DOI: 10.1021/acs.inorgchem.7b00755
Inorg. Chem. 2017, 56, 6688−6694

reported range for P−P bonds in related systems such as black phosphorus (2.20 Å)[29] or ionic polyphosphides such as BaP_2 (2.22 Å),[30] and similar to BaP_2, the chain shows a translational repeating unit of six P atoms.

Each P atom of the chains represents the vertex of a SiP_4 tetrahedron, which are alternatingly oriented above and below the mean plane of the P atoms. The P−Si bond vector is oriented almost perpendicular to the layer of P atoms (Figure 3c). The Si atoms are coordinated by four P atoms forming usual SiP_4 tetrahedra. The Si−P bonds can be distinguished in short (2.2097(8)−2.2223(7) Å), intermediate (2.2651(12)−2.2755(8) Å), and long (2.2886(12)−2.2966(7) Å) involving P atoms, which connect two Si atoms, or one Si and two P atoms, or three Si atoms, respectively. Similarly the P−Si−P angles are slightly distorted and range from 106.10(3)° to 112.41(4)°. While the SiP_4 tetrahedra are bound to the P chain with one vertex, all other vertices are shared by at least two SiP_4 groups. The resulting vertex-sharing layers of tetrahedra lie above and below in the *ab* plane, and both two-dimensional sheets of tetrahedra are connected through the chain of P atoms and thus form a double layer (see Figure 3a). The two-dimensional slabs can also be regarded as built by three covalently bonded atom layers: Layer A represents a two-dimensional section of a wurzite-type SiP layer in which one-fourth of the Si atoms are missing. Layer B corresponds to an ordered defect variant of As_{gray}. Another view arises regarding the arrangement of the tetrahedral building units. The connectivity of the tetrahedra within a single layer is represented by Si atoms located at the centers of the tetrahedra. The Si atoms forming regular triangles and hexagons thus represent different types of nodes according to the Schlaefli symbols 3.6.3.6 for Si1 and 3.3.6.6 for Si2. Two of such nets appear above and below the plane of P atoms.

The double layers are separated by Li atoms, which are occupying a tetrahedral void of four P atoms (Li1) or a strongly distorted octahedral void with a 3 + 3 P atom coordination (Li3). The third independent Li2 atom is situated in the hexagonal mesh of the tetrahedral layer, directly coordinated by a less-distorted octahedron of six P atoms, three of them belonging to the P chain. All lithium phosphorus distances range from 2.440(5) to 3.333(5) Å and divide into two groups ranging for most Li−P distances from 2.440(5) to 2.745(6) Å and for one Li3−P2 and Li3−P1 bond from 3.168(6) to 3.333(5) Å. The closest Li−Li neighbors occur at distances of 2.935(8) Å.

In $Li_3Si_3P_7$ all Si atoms and the P2, P3, and P4 atoms form four and three bonds to Si and/or P atoms, respectively; P1 and P5 are only twofold bonded to Si atoms. Therefore, the latter two atoms bear formally a single negative charge, leading to a framework charge of −6 per unit cell, which is compensated by the six Li^+ counterions.

Solid-State MAS NMR Spectroscopy. ^{31}P MAS NMR measurements show for $Li_{10}Si_2P_6$ and $Li_3Si_3P_7$ a set of signals. By considering the spectra with respect to the multiplicities of the Wyckoff positions of the P atoms, and by comparing the signal shifts with those of related compounds in literature such as Li_8SiP_4,[2] Li_2SiP_2,[2] SiP,[31] and black P,[29] the resonances can be assigned to crystallographic positions.

$Li_{10}Si_2P_6$ shows three signals with an intensity ratio of 1:1:1 and shifts of δ = −199.5 ppm, δ = −188.4 ppm, and δ = −124.1 ppm (Figure 4a). An increasing downfield shift is observed for an increasing negative charge at phosphorus atoms.[2] Consequently, the bridging phosphorus P1 atoms are assigned to the signal with δ = −124.1 ppm, while the terminal phosphorus atoms P2 and P3 are assigned to δ = −199.5 ppm, δ = −188.4 ppm. A further differentiation of the terminal phosphorus atoms is not possible due to the similar chemical environment of both positions. A fourth weak signal at δ = −10.4 ppm indicates the presence of small amounts of phosphate[32,33] likely formed during the ball-milling process due to minor leakage over several hours of milling.

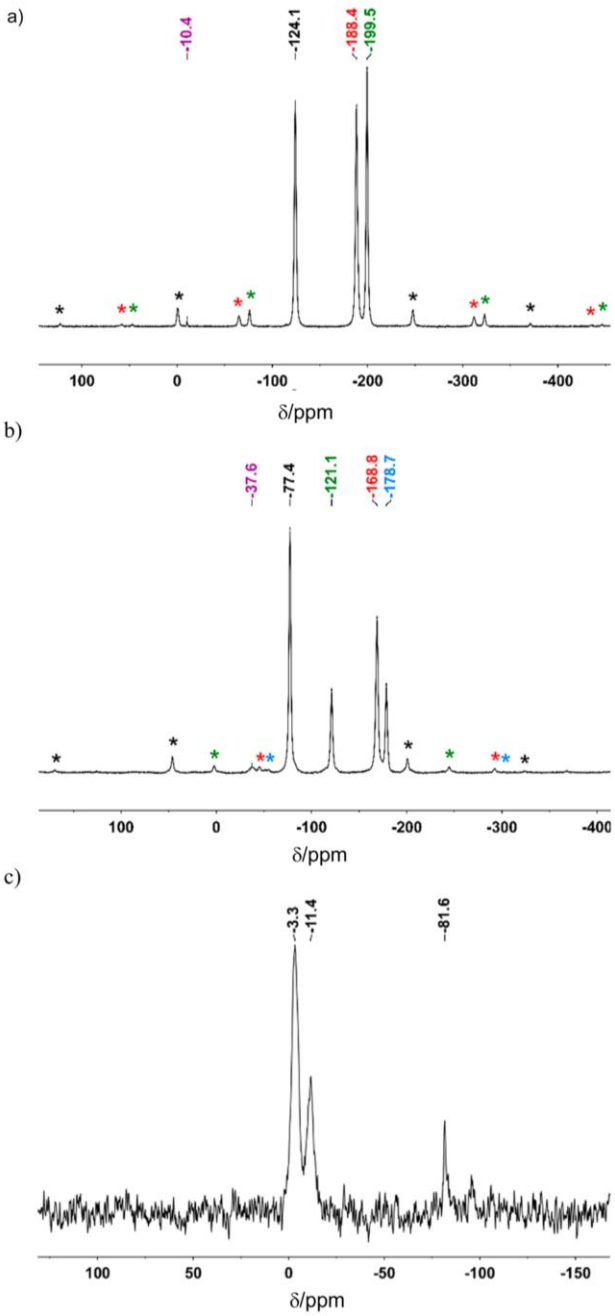

Figure 4. (a) ^{31}P MAS NMR of $Li_{10}Si_2P_6$; (b) ^{31}P MAS NMR of $Li_3Si_3P_7$; (c) ^{29}Si MAS NMR of $Li_3Si_3P_7$. Signals originating from rotational side bands are marked with *.

The ^{31}P NMR spectrum of $Li_3Si_3P_7$ shows four resonances at δ = −178.7 ppm, δ = −168.8 ppm, δ = −121.1 ppm and δ = −77.4 ppm with ratios of 1:2:1:3, respectively. A small resonance at δ = −37.6 ppm indicates a side phase (Figure

DOI: 10.1021/acs.inorgchem.7b00755
Inorg. Chem. 2017, 56, 6688−6694

4b). Because of their comparable chemical environment a similar shift for P1 and P5 and the P atoms in Li_2SiP_2 (δ = −129.1 ppm and δ = −241.5 ppm)[2] is assumed. Regarding the crystallographic multiplicity and NMR intensities the signals with shifts of δ = −178.7 ppm and δ = −168.8 ppm are assigned to P5 (2e) and P1 (4f), respectively. Comparing the intensities of the remaining peaks the signal at δ = −121.1 ppm refers best to P2 (2e), which is consistent with the range of chemical shifts in SiP (δ = −143.6 ppm to δ = −239.6 ppm).[31] The most intense NMR response with a shift of δ = −77.4 ppm fits well to the two remaining positions in the P chains, namely, P3 (2e) and P4 (4f).

A ^{29}Si MAS NMR spectrum of $Li_3Si_3P_7$ (Figure 4c) shows signals with a shift of δ = −11.4 ppm and δ = −3.3 ppm with an intensity ratio of 1:2 referring to Si1 and Si2, respectively. These signals lie within the range for phosphidosilicates[2] and silicon phosphides.[31] A third signal with a shift δ = −81.6 ppm might indicate the presence of silicate compounds. Its intensity resembles a phase fraction of 8%. The spectrum of $Li_{10}Si_2P_6$ does not show any distinct signals due to a poor signal-to-noise ratio.

For ^{7}Li MAS NMR measurements (see Supporting Information) one signal with rotational side bands is observed in both compounds. The different Li positions cannot be resolved, since, by changing the chemical environment in diamagnetic compounds, the signal shift of ^{7}Li atoms differs just within a narrow range, as observed frequently in other ternary and quarternary solid compounds.[2,9,34,35] The resonance of $Li_{10}Si_2P_6$ is observed at a chemical shift of δ = −2.1 ppm, and the resonance of $Li_3Si_3P_7$ is at δ = 3.0 ppm. The spectrum of the latter also shows a small second peak with a shift of δ = −4.8 ppm and compared to the larger peak with an intensity ratio of 1:50. Since the chemical shift of ^{7}Li in $LiSi_2P_3$ is reported to be δ = 2.7 ppm[9] it might indicate a further amorphous phase in the product.

CONCLUSION

Ternary lithium phosphidosilicates are a rapidly growing compound family that show a high lithium ion mobility. Their anionic partial structures are generally built from SiP_4 tetrahedra, and their relative arrangement corresponds sensitively and variably to their composition. The new members $Li_{10}Si_2P_6$ and $Li_3Si_3P_7$ extend the known connectivity motifs known in the ternary system of Li−Si−P. While formerly only isolated and corner-sharing SiP_4 have been observed, with the two new compounds edge-sharing tetrahedra and Si−P−P−Si bridges, respectively, are added as structure motifs. In $Li_{10}Si_2P_6$ the anions are formed by isolated units of two condensed edge-sharing tetrahedra. Contrasting this, in $Li_3Si_3P_7$ layers of corner-sharing tetrahedra are interconnected by polyphosphide chains expressing the high content of phosphorus, to form double layers of tetrahedra. With the light cation lithium structures that are well-known in phosphidosilicate chemistry such as $Li_{10}Si_2P_6$ as well as entirely new structure types can be realized. The lithium mobility and ion conductivity will be subject to further studies.

ASSOCIATED CONTENT

Supporting Information

The Supporting Information is available free of charge on the ACS Publications website at DOI: 10.1021/acs.inorgchem.7b00755.

Details of the structure determinations from single-crystal data of $Li_{10}Si_2P_6$ and $Li_3Si_3P_7$ at ambient and at low temperatures, atomic coordinates and atomic displacement parameters for $Li_{10}Si_2P_6$, selected interatomic distances for $Li_{10}Si_2P_6$, atomic coordinates and atomic displacement parameters for $Li_3Si_3P_7$, selected interatomic distances for $Li_3Si_3P_7$, refinement results from Rietveld analyses of X-ray powder data of $Li_{10}Si_2P_6$ and $Li_3Si_3P_7$ at room temperature, coordination polyhedra of the independent P and Li atomic positions of $Li_{10}Si_2P_6$, coordination polyhedra of the independent atomic positions of $Li_3Si_3P_7$, and ^{7}Li MAS NMR spectra of $Li_{10}Si_2P_6$ and $Li_3Si_3P_7$ (PDF)

Accession Codes

CCDC 1549346−1549349 contains the supplementary crystallographic data for this paper. These data can be obtained free of charge via www.ccdc.cam.ac.uk/data_request/cif, or by emailing data_request@ccdc.cam.ac.uk, or by contacting The Cambridge Crystallographic Data Centre, 12, Union Road, Cambridge CB2 1EZ, UK; fax: +44 1223 336033.

AUTHOR INFORMATION

Corresponding Author

*E-mail: Thomas.Faessler@lrz.tu-muenchen.de.

ORCID

Thomas F. Fässler: 0000-0001-9460-8882

Notes

The authors declare no competing financial interest.

REFERENCES

(1) Bachman, J. C.; Muy, S.; Grimaud, A.; Chang, H.-H.; Pour, N.; Lux, S. F.; Paschos, O.; Maglia, F.; Lupart, S.; Lamp, P.; Giordano, L.; Shao-Horn, Y. Inorganic Solid-State Electrolytes for Lithium Batteries: Mechanisms and Properties Governing Ion Conduction. *Chem. Rev.* **2016**, *116*, 140−162.

(2) Toffoletti, L.; Kirchhain, H.; Landesfeind, J.; Klein, W.; van Wüllen, L.; Gasteiger, H. A.; Fässler, T. F. Lithium Ion Mobility in Lithium Phosphidosilicates: Crystal Structure, ^{7}Li, ^{29}Si, and ^{31}P MAS NMR Spectroscopy, and Impedance Spectroscopy of Li_8SiP_4 and Li_2SiP_2. *Chem. - Eur. J.* **2016**, *22*, 17635−17645.

(3) Wang, X.; Wen, Z.; Liu, Y. A novel nanosized silicon-based composite as anode material for high performance lithium ion batteries. *Electrochim. Acta* **2011**, *56*, 1512−1517.

(4) Duveau, D.; Israel, S. S.; Fullenwarth, J.; Cunin, F.; Monconduit, L. Pioneer study of SiP_2 as negative electrode for Li- and Na-ion batteries. *J. Mater. Chem. A* **2016**, *4*, 3228−3232.

(5) Eisenmann, B.; Jordan, H.; Schäfer, H. Zintl-phasen mit komplexen Anionen: Darstellung und Struktur der *o*-Phosphosilikate und -germanate $E^{II}_4E^{IV}P_4$ (mit E^{II} = Ca, Sr, Ba und E^{IV} = Si, Ge). *Mater. Res. Bull.* **1982**, *17*, 95−99.

(6) Eisenmann, B.; Somer, M. Zur Kenntnis von Oligophosphidosilikaten(IV) und -germanaten(IV): $Na_{10}Si_2P_6$ und $Na_{10}Ge_2P_6$. *Z. Naturforsch., B: Anorg. Chem., Org. Chem.* **1985**, *40*, 886−890.

(7) Eisenmann, B.; Somer, M. K_2SiP_2, ein Phosphidopolysilikat(IV). *Z. Naturforsch. B: Anorg. Chem., Org. Chem.* **1984**, *39*, 736−738.

(8) Feng, K.; Kang, L.; Yin, W.; Hao, W.; Lin, Z.; Yao, J.; Wu, Y. KSi_2P_3: A new layered phosphidopolysilicate (IV). *J. Solid State Chem.* **2013**, *205*, 129−133.

(9) (a) Haffner, A.; Bräuniger, T.; Johrendt, D. Netzwerke aus Supertetraedern und Lithiumionenbeweglichkeit in Li_2SiP_2 und $LiSi_2P_3$. *Angew. Chem.* **2016**, *128*, 13783−13786. (b) *Angew. Chem., Int. Ed.* **2016**, *55*, 13585−13588.

(10) Kaiser, P.; Jeitschko, W. Preparation and Crystal Structures of the Ternary Compounds Ag_2SiP_2 and AuSiP. *Z. Naturforsch., B: J. Chem. Sci.* **1997**, *52*, 462−468.
(11) Zeuner, M.; Pagano, S.; Schnick, W. Nitridosilicate und Oxonitridosilicate: von keramischen Materialien zu struktureller und funktioneller Diversität. *Angew. Chem.* **2011**, *123*, 7898−7920; *Angew. Chem., Int. Ed.* **2011**, *50*, 7754−7775.
(12) Zhang, X.; Yu, T.; Li, C.; Wang, S.; Tao, X. Synthesis and Crystal Structures of the Calcium Silicon Phosphides $Ca_2Si_2P_4$, $Ca_3Si_8P_{14}$ and $Ca_3Si_2P_4$. *Z. Anorg. Allg. Chem.* **2015**, *641*, 1545−1549.
(13) von Schnering, H. G.; Menge, G. $AlSiP_3$, a compound with a novel wurtzite-pyrite intergrowth structure. *J. Solid State Chem.* **1979**, *28*, 13−19.
(14) Kaiser, P.; Jeitschko, W. The Rare Earth Silicon Phosphides $LnSi_2P_6$ (*Ln* = La, Ce, Pr, and Nd). *J. Solid State Chem.* **1996**, *124*, 346−352.
(15) Kaiser, P.; Jeitschko, W. Preparation and crystal structure of the Copper Silicon Polyphosphide Cu_4SiP_8. *Z. Anorg. Allg. Chem.* **1996**, *622*, 53−56.
(16) Eisenmann, B.; Klein, J.; Somer, M. CO_3^{2-}-isostere Anionen in Cs_5SiP_3, Cs_5SiAs_3, Cs_5GeP_3 und Cs_5GeAs_3. *Angew. Chem.* **1990**, *102*, 92−93; *Angew. Chem., Int. Ed. Engl.* **1990**, *29*, 87−88.
(17) Juza, R.; Schulz, W. Ternäre Phosphide und Arsenide des Lithiums mit Elementen der 3. und 4. Gruppe. *Z. Anorg. Allg. Chem.* **1954**, *275*, 65−78.
(18) *Win XPOW*, Version 3.0.2.1; STOE & Cie GmbH: Darmstadt, Germany, 2011.
(19) Petříček, V.; Dušek, M.; Palatinus, L. Crystallographic Computing System JANA2006: General features. *Z. Kristallogr.* **2014**, *229*, 345−352.
(20) Sheldrick, G. M. Crystal structure refinement with *SHELXL*. *Acta Crystallogr., Sect. A: Found. Adv.* **2015**, *71*, 3−8.
(21) Eisenmann, B.; Klein, J.; Somer, M. Crystal structure of decasodium di-μ-arsenidobis(diarsenidogermanate), $Na_{10}Ge_2As_6$. *Z. Kristallogr.* **1991**, *197*, 265−266.
(22) Eisenmann, B.; Klein, J.; Somer, M. Crystal structure of decasodium di-μ-arsenidobis(diarsenidosilicate), $Na_{10}Si_2As_6$. *Z. Kristallogr.* **1991**, *197*, 267−268.
(23) Wadsten, T. Preparative and crystal-structure studies on orthorhombic silicon monophosphide. *Chem. Scr.* **1975**, *8*, 63−69.
(24) Dong, Y.; DiSalvo, F. J. Reinvestigation of trilithium phosphide, Li_3P. *Acta Crystallogr., Sect. E: Struct. Rep. Online* **2007**, *63*, i97−i98.
(25) Manriquez, V.; Hönle, W.; von Schnering, H. G. Zur Chemie und Strukturchemie von Phosphiden und Polyphosphiden. 42. Trilithiumheptaphosphid Li_3P_7: Darstellung, Struktur und Eigenschaften. *Z. Anorg. Allg. Chem.* **1986**, *539*, 95−109.
(26) Eisenmann, B.; Klein, J.; Somer, M. Crystal structure of pentarubidium triphosphidogermanate, Rb_5GeP_3. *Z. Kristallogr.* **1991**, *197*, 263−264.
(27) Eisenmann, B.; Klein, J. Na_5SnSb_3 und K_8SnSb_4, zwei neue Zintlphasen mit tetraedrischen $SnSb_4$-Baueinheiten. *Z. Naturforsch., B: J. Chem. Sci.* **1988**, *43*, 1156−1160.
(28) Schiferl, D.; Barrett, C. S. The Crystal Structure of Arsenic at 4.2, 78 and 299 K. *J. Appl. Crystallogr.* **1969**, *2*, 30−36.
(29) Lange, S.; Schmidt, P.; Nilges, T. Au_3SnP_7@Black Phosphorus: An Easy Access to Black Phosphorus. *Inorg. Chem.* **2007**, *46*, 4028−4035.
(30) Dolyniuk, J.-A.; He, H.; Ivanov, A. S.; Boldyrev, A. I.; Bobev, S.; Kovnir, K. Ba and Sr Binary Phosphides: Synthesis, Crystal Structures, and Bonding Analysis. *Inorg. Chem.* **2015**, *54*, 8608−8616.
(31) Franke, D.; Hudalla, C.; Maxwell, R.; Eckert, H. ^{31}P-^{113}Cd and ^{31}P-^{29}Si CP/MAS-NMR in Inorganic Semiconductors. *J. Phys. Chem.* **1992**, *96*, 7506−7509.
(32) Brow, R. K.; Tallant, D. R.; Myers, S. T.; Phifer, C. C. The short-range structure of zinc polyphosphate glass. *J. Non-Cryst. Solids* **1995**, *191*, 45−55.
(33) Kirkpatrick, R. J.; Brow, R. K. Nuclear magnetic resonance investigation of the structures of phosphate and phosphate-containing glasses: a review. *Solid State Nucl. Magn. Reson.* **1995**, *5*, 9−21.
(34) Zeuner, M.; Pagano, S.; Hug, S.; Pust, P.; Schmiechen, S.; Scheu, C.; Schnick, W. $Li_2CaSi_2N_4$ and $Li_2SrSi_2N_4$ − a Synthetic Approach to Three-Dimensional Lithium Nitridosilicates. *Eur. J. Inorg. Chem.* **2010**, *2010*, 4945−4951.
(35) Pagano, S.; Zeuner, M.; Hug, S.; Schnick, W. Single-Crystal Structure Determination and Solid-State NMR Investigations of Lithium Nitridosilicate Li_2SiN_2 Synthesized by a Precursor Approach Employing Amorphous "$Si(CN_2)_2$. *Eur. J. Inorg. Chem.* **2009**, *2009*, 1579−1584.

DOI: 10.1021/acs.inorgchem.7b00755
Inorg. Chem. 2017, 56, 6688−6694

Synthesis and Characterization of the Lithium-rich Phosphidosilicates $Li_{10}Si_2P_6$ and $Li_3Si_3P_7$

Henrik Eickhoff, Lorenzo Toffoletti, Wilhelm Klein, Gabriele Raudaschl-Sieber, Thomas F. Fässler*

Fakultät Chemie, Technische Universität München,
Lichtenbergstraße 4, 85747 Garching, Germany
Fax: (+49) 89-289-13186
E-mail: thomas.faessler@lrz.tum.de

Supporting Information

Content:

Table S1. Crystallographic data and refinement parameters of $Li_{10}Si_2P_6$ and $Li_3Si_3P_7$ at ambient and at low temperatures, respectively.

empirical formula	$Li_{10}Si_2P_6$		$Li_3Si_3P_7$	
formula weight / gmol^{-1}	311.40		321.88	
crystal size / mm^3	0.20 × 0.15 × 0.10		0.13 × 0.10 × 0.09	
crystal colour	dark red		grey	
T / K	298(2)	123(2)	298(2)	130(2)
unit cell parameters / Å	a = 7.2167(2) b = 6.5934(3) c = 11.6792(5) β = 90.539(2)°	a = 7.2051(4) b = 6.5808(4) c = 11.6405(7) β = 90.580(4)°	a = 6.3402(2) b = 7.2282(2) c = 10.6280(3) β = 102.825(3)°	a = 6.3356(4) b = 7.2198(4) c = 10.6176(6) β = 102.941(6)°
V / Å^3	555.70(4)	551.91(6)	474.91(2)	473.33(5)
crystal system	monoclinic		monoclinic	
space group	$P2_1/n$ (no. 14)		$P2_1/m$ (no. 11)	
Z	2		2	
$\rho_{calc.}$ / gcm^{-3}	1.861	1.874	2.251	2.258
μ / mm^{-1}	1.117	1.124	1.603	1.609
θ range / deg	3.30 – 30.15	3.34 – 35.16	3.30 – 30.98	3.30 – 29.98
index range (hkl)	$-10 \le h \le 10$, $-8 \le k \le 9$, $-16 \le l \le 16$	$-11 \le h \le 10$, $-9 \le k \le 10$, $-14 \le l \le 18$	$-9 \le h \le 9$, $-10 \le k \le 10$, $-15 \le l \le 15$	$-8 \le h \le 8$, $-10 \le k \le 10$, $-14 \le l \le 14$
reflections collected	6240	9492	17204	7958
independent reflections	1637	2446	1566	1476
R_{int}	0.0410	0.0373	0.0478	0.0400
reflections with $I > 2\sigma(I)$	1338	1965	1121	983
absorption correction	multi-scan	multi-scan	multi-scan	multi-scan
data / restraints / parameters	1637 / 0 / 82	2446 / 0 / 83	1566 / 0 / 71	1476 / 0 / 71
goodness-of-fit on F^2	1.011	1.021	1.021	0.865
R_1, wR_2 (all data)	0.0402, 0.0527	0.0411, 0.0466	0.0480, 0.0822	0.0461, 0.0637
R_1, wR_2 [$I > 2\sigma(I)$]	0.0263, 0.0492	0.0264, 0.0432	0.0296, 0.0783	0.0267, 0.0610
largest diff. peak and hole (e·Å^{-3})	0.372 / −0.327	0.545 / −0.440	0.933 / −0.611	0.768 / −0.449
CSD numbers	432634	432635	432636	432637

Table S2. Fractional atomic coordinates and isotropic equivalent atomic displacement parameters for $Li_{10}Si_2P_6$ at room temperature.

Atom	Wyckoff positions	*x*	*y*	*z*	U_{eq} / Å^2
Li1	4*e*	0.1637(5)	−0.0045(5)	0.2639(3)	0.0241(8)
Li2	4*e*	0.5684(4)	0.1281(5)	0.2569(3)	0.0178(7)
Li3	4*e*	0.1883(5)	0.0632(6)	0.5986(3)	0.0261(8)
Li4	4*e*	0.5768(4)	0.1590(5)	0.5811(3)	0.0176(7)
Li5	4*e*	0.3455(5)	0.5313(5)	0.5904(3)	0.0248(8)
Si	4*e*	0.07078(6)	0.35115(7)	0.41092(4)	0.0085(1)
P1	4*e*	0.09622(6)	0.69868(7)	0.42737(4)	0.0099(1)
P2	4*e*	0.35864(6)	0.22858(7)	0.41624(4)	0.0104(1)
P3	4*e*	−0.09830(6)	0.24578(7)	0.26246(4)	0.0107(1)

Table S3. Anisotropic displacement parameters (Å^2) for $Li_{10}Si_2P_6$ at room temperature.

Atom	U_{11}	U_{22}	U_{33}	U_{23}	U_{13}	U_{12}
Li1	0.023(2)	0.023(2)	0.026(2)	−0.006(1)	−0.003(1)	0.005(1)
Li2	0.018(2)	0.019(2)	0.016(1)	−0.001(1)	0.000(1)	0.002(1)
Li3	0.023(2)	0.028(2)	0.028(2)	0.008(2)	0.001(1)	0.003(1)
Li4	0.016(1)	0.022(2)	0.015(1)	0.002(1)	−0.001(1)	0.001(1)
Li5	0.021(2)	0.023(2)	0.030(2)	0.002(2)	−0.001(1)	−0.004(1)
Si	0.0083(2)	0.0081(2)	0.0090(2)	0.0001(2)	0.0007(2)	0.0001(2)
P1	0.0106(2)	0.0088(2)	0.0103(2)	0.0005(2)	0.0015(2)	−0.0007(2)
P2	0.0087(2)	0.0111(2)	0.0116(2)	−0.0003(2)	0.0002(2)	0.0012(2)
P3	0.0112(2)	0.0104(2)	0.0105(2)	−0.0008(2)	−0.0016(2)	−0.0003(2)

Table S4. Fractional atomic coordinates and isotropic equivalent atomic displacement parameters for $Li_{10}Si_2P_6$ at 123 K.

Atom	Wyckoff positions	*x*	*y*	*z*	U_{eq} / Å^2
Li1	4*e*	0.1619(3)	−0.0063(3)	0.2647(2)	0.0143(5)
Li2	4*e*	0.5677(3)	0.1267(3)	0.2569(2)	0.0104(4)
Li3	4*e*	0.1882(3)	0.0658(3)	0.6002(2)	0.0134(5)
Li4	4*e*	0.5770(3)	0.1591(3)	0.5814(2)	0.0108(4)
Li5	4*e*	0.3469(3)	0.5328(3)	0.5908(2)	0.0139(5)
Si	4*e*	0.07036(4)	0.35062(5)	0.41082(3)	0.00503(8)
P1	4*e*	0.09687(4)	0.69872(5)	0.42722(3)	0.00557(8)
P2	4*e*	0.35854(4)	0.22797(5)	0.41599(3)	0.00591(8)
P3	4*e*	−0.09943(4)	0.24457(4)	0.26194(3)	0.00587(8)

Table S5. Anisotropic displacement parameters (Å^2) for $Li_{10}Si_2P_6$ at 123 K.

Atom	U_{11}	U_{22}	U_{33}	U_{23}	U_{13}	U_{12}
Li1	0.013(1)	0.014(1)	0.016(1)	−0.0021(8)	−0.0020(9)	0.0021(8)
Li2	0.009(1)	0.013(1)	0.009(1)	−0.0008(8)	0.0009(8)	-0.0002(8)
Li3	0.011(1)	0.013(1)	0.017(1)	0.0017(9)	−0.0011(9)	0.0009(8)
Li4	0.010(1)	0.012(1)	0.011(1)	0.0004(8)	0.0004(8)	0.0003(7)
Li5	0.014(1)	0.013(1)	0.017(1)	0.0013(9)	−0.0011(9)	−0.0012(8)
Si	0.0051(2)	0.0049(2)	0.0051(2)	0.0001(1)	−0.0000(1)	−0.0001(1)
P1	0.0061(2)	0.0047(2)	0.0059(2)	0.0001(1)	0.0004(1)	−0.0002 (1)
P2	0.0052(1)	0.0060(2)	0.0066(2)	−0.0000(1)	−0.0001(1)	0.0005(1)
P3	0.0064(1)	0.0054(2)	0.0058(2)	−0.0002(1)	−0.0009(1)	−0.0004(1)

Table S6. Selected interatomic distances in $Li_{10}Si_2P_6$ at 298 K and at 123 K.

atom pair		*d* / Å (298 K)	*d* / Å (123 K)	atom pair		*d* / Å (298 K)	*d* / Å (123 K)
Si	P3	2.2221(6)	2.2235(4)	Li1	P3	2.509(3)	2.505(2)
	P2	2.2294(6)	2.2281(4)		P2	2.732(3)	2.727(2)
	P1	2.2739(6)	2.2713(5)		P2	2.746(3)	2.738(2)
	P1	2.3066(7)	2.3067(4)		P1	2.780(4)	2.753(2)
	Li2	2.854(3)	2.839(2)		Li4	2.786(5)	2.774(3)
	Li1	2.970(3)	2.976(2)				
	Li1	2.987(3)	2.978(2)	Li2	P1	2.492(3)	2.484(2)
	Li3	3.102(3)	3.009(2)		P2	2.499(3)	2.490(2)
	Si	3.0441(9)	3.0411(6)		P3	2.528(3)	2.521(2)
					P3	2.540(3)	2.535(2)
P1	Si	2.2739(6)	2.2713(5)		Li3	2.733(5)	2.722(3)
	Si	2.3066(7)	2.3067(4)		Li4	2.880(5)	2.866(3)
	Li2	2.492(3)	2.484(2)		Li3	2.888(5)	2.866(3)
	Li4	2.543(3)	2.532(2)				
	Li3	2.600(3)	2.591(2)	Li3	P1	2.600(3)	2.591(2)
	Li1	2.780(4)	2.753(2)		P3	2.688(3)	2.679(2)
	Li5	2.831(3)	2.828(2)		P2	2.699(3)	2.701(2)
					P3	2.750(3)	2.718(2)
P2	Si	2.2294(6)	2.2281(4)		Li2	2.733(5)	2.722(3)
	Li2	2.499(3)	2.490(2)		Li2	2.888(5)	2.866(3)
	Li4	2.518(3)	2.515(2)		Li4	2.882(5)	2.878(3)
	Li4	2.598(3)	2.590(2)				
	Li5	2.660(3)	2.645(2)	Li4	P2	2.518(3)	2.515(2)
	Li3	2.699(3)	2.701(2)		P1	2.543(3)	2.532(2)
	Li1	2.732(3)	2.727(2)		P3	2.555(3)	2.548(2)
	Li1	2.746(3)	2.738(2)		P2	2.598(3)	2.590(2)
	Li5	2.852(4)	2.860(2)		Li1	2.786(5)	2.774(3)
					Li2	2.880(5)	2.866(3)
P3	Si	2.2221(6)	2.2235(4)		Li3	2.882(5)	2.878(3)
	Li1	2.509(3)	2.505(2)		Li5	2.919(5)	2.907(3)
	Li2	2.528(3)	2.521(2)				
	Li2	2.540(3)	2.535(2)	Li5	P2	2.660(3)	2.645(2)
	Li4	2.555(3)	2.548(2)		P3	2.743(3)	2.726(2)
	Li3	2.688(3)	2.679(2)		P1	2.831(3)	2.827(2)
	Li3	2.750(4)	2.718(2)		P2	2.852(4)	2.860(2)
	Li5	2.743(3)	2.726(2)		P3	2.890(3)	2.885(2)
	Li5	2.890(3)	2.885(2)		Li4	2.919(5)	2.907(3)

Table S7. Fractional atomic coordinates and isotropic equivalent atomic displacement parameters for $Li_3Si_3P_7$ at room temperature.

Atom	Wyckoff positions	*x*	*y*	*z*	U_{eq} / Å^2
Li1	2*e*	0.6548(9)	¼	0.0620(6)	0.022(1)
Li2	2*e*	0.782(1)	¼	0.3470(6)	0.027(1)
Li3	2*e*	0.092(1)	¼	0.9827(7)	0.038(2)
Si1	2*e*	0.2432(1)	¼	0.73574(8)	0.0120(2)
Si2	4*f*	0.23836(9)	0.00089(7)	0.26137(6)	0.0116(2)
P1	4*f*	0.11673(9)	−0.00288(7)	0.81001(6)	0.0142(2)
P2	2*e*	0.6096(1)	¼	0.81761(8)	0.0116(2)
P3	2*e*	0.1775(1)	¼	0.51726(8)	0.0124(2)
P4	4*f*	0.32187(9)	−0.01648(7)	0.48071(6)	0.0128(2)
P5	2*e*	0.3785(1)	¼	0.18832(8)	0.0141(2)

Table S8.Anisotropic displacement parameters (Å^2) for $Li_3Si_3P_7$ at room temperature.

Atom	U_{11}	U_{22}	U_{33}	U_{23}	U_{13}	U_{12}
Li1	0.015(3)	0.030(3)	0.025(3)	0	0.010(2)	0
Li2	0.029(3)	0.030(3)	0.024(4)	0	0.008(3)	0
Li3	0.038(4)	0.049(4)	0.025(4)	0	0.001(3)	0
Si1	0.0104(4)	0.0099(3)	0.0159(4)	0	0.0034(3)	0
Si2	0.0099(3)	0.0093(3)	0.0155(3)	−0.0001(2)	0.0027(2)	−0.0003(2)
P1	0.0105(3)	0.0109(3)	0.0204(3)	0.0025(2)	0.0021(2)	0.0000(2)
P2	0.0099(3)	0.0097(3)	0.0153(4)	0	0.0029(3)	0
P3	0.0115(4)	0.0103(3)	0.0155(4)	0	0.0030(3)	0
P4	0.0122(3)	0.0104(2)	0.0158(3)	0.0000(2)	0.0031(2)	0.0004(2)
P5	0.0131(4)	0.0099(3)	0.0208(4)	0	0.0069(3)	0

Table S9. Fractional atomic coordinates and isotropic equivalent atomic displacement parameters for $Li_3Si_3P_7$ at 130 K.

Atom	Wyckoff positions	*x*	*y*	*z*	U_{eq} / Å^2
Li1	2*e*	0.6567(9)	¼	0.0621(6)	0.015(1)
Li2	2*e*	0.782(1)	¼	0.3455(6)	0.019(1)
Li3	2*e*	0.093(1)	¼	0.9825(6)	0.024(1)
Si1	2*e*	0.2435(2)	¼	0.73562(8)	0.0093(2)
Si2	4*f*	0.2381(1)	0.00081(8)	0.26126(6)	0.0089(2)
P1	4*f*	0.11733(9)	−0.00307(8)	0.81042(6)	0.0100(1)
P2	2*e*	0.6097(1)	¼	0.81775(8)	0.0092(2)
P3	2*e*	0.1770 (1)	¼	0.51693(8)	0.0095(2)
P4	4*f*	0.32184(9)	−0.01654(8)	0.48082(6)	0.0098(1)
P5	2*e*	0.3789(1)	¼	0.18848(8)	0.0103(2)

Table S10.Anisotropic displacement parameters (Å^2) for $Li_3Si_3P_7$ at 130 K.

Atom	U_{11}	U_{22}	U_{33}	U_{23}	U_{13}	U_{12}
Li1	0.012(3)	0.016(3)	0.019(3)	0	0.005(2)	0
Li2	0.021(3)	0.018(3)	0.021(4)	0	0.007(3)	0
Li3	0.023(3)	0.034(4)	0.016(3)	0	0.004(3)	0
Si1	0.0070(4)	0.0091(4)	0.0118(5)	0	0.0019(4)	0
Si2	0.0067(3)	0.0082(3)	0.0116(3)	0.0000(2)	0.0016(2)	−0.0002(2)
P1	0.0070(3)	0.0091(3)	0.0136(3)	0.0015(2)	0.0013(2)	0.0001(2)
P2	0.0068(4)	0.0093(4)	0.0114(4)	0	0.0019(3)	0
P3	0.0074(4)	0.0090(4)	0.0119(4)	0	0.0017(3)	0
P4	0.0076(3)	0.0093(3)	0.0122(3)	-0.0001(2)	0.0018(2)	0.0001(2)
P5	0.0085(4)	0.0090(4)	0.0139(4)	0	0.0033(3)	0

Table S11. Selected interatomic distances in $Li_3Si_3P_7$ at ambient temperature and at 130 K.

atom pair		*d* / Å (298 K)	*d* / Å (130 K)	atom pair		*d* / Å (298 K)	*d* / Å (130 K)
Si1	P1 (2×)	2.2108(8)	2.2120(7)				
	P3	2.2662(12)	2.2651(12)	P5	Si2 (2×)	2.2228(8)	2.2223(7)
	P2	2.2925(10)	2.2886(12)		Li1	2.432(6)	2.440(5)
	Li3	2.987(8)	2.982(6)		Li3	2.513(7)	2.508(6)
					Li2	2.732(6)	2.719(6)
Si2	P1	2.2104(8)	2.2097(8)				
	P5	2.2228(8)	2.2223(7)				
	P4	2.2765(9)	2.2755(8)				
	P2	2.2984(8)	2.2966(7)	Li1	P5	2.432(6)	2.440(5)
					P1 (2×)	2.503(4)	2.489(4)
P1	Si2	2.2104(8)	2.2097(8)		P2	2.550(6)	2.544(6)
	Si1	2.2108(8)	2.2120(7)		Li2	2.956(9)	2.935(8)
	Li1	2.503(4)	2.489(4)		Li3	3.071(10)	3.068(8)
	Li2	2.620(5)	2.607(4)				
	Li3	2.619(6)	2.612(4)	Li2	P1 (2×)	2.620(5)	2.607(4)
					P4 (2×)	2.677(5)	2.687(4)
P2	Si1	2.2925(10)	2.2886(12)		P5	2.732(6)	2.719(6)
	Si2 (2×)	2.2984(8)	2.2966(7)		P3	2.748(6)	2.745(6)
	Li1	2.550(6)	2.544(6)		Li1	2.956(9)	2.935(8)
P3	P4 (2×)	2.2040(7)	2.2024(7)	Li3	P5	2.513(7)	2.508(6)
	Si1	2.2662(12)	2.2651(12)		P1 (2×)	2.619(5)	2.612(4)
	Li2	2.748(6)	2.745(6)		Si1	2.987(8)	2.982(6)
					Li1	3.071(10)	3.067(8)
P4	P3	2.2040(7)	2.2024(7)		P2	3.170(7)	3.168(6)
	P4	2.2171(11)	2.2153(11)		P1 (2×)	3.330(7)	3.333(5)
	Si2	2.2765(9)	2.2755(8)				
	Li2	2.677(5)	2.687(4)				

Table S12. Details of the Rietveld structure refinements of $Li_{10}Si_2P_6$ and $Li_3Si_3P_7$.

empirical formula	$Li_{10}Si_2P_6$	$Li_3Si_3P_7$
T / K	298(2)	298(2)
formula weight / $gmol^{-1}$	311.40	321.88
space group	$P2_1/n$ (no. 14)	$P2_1/m$ (no. 11)
unit cell parameters / Å	a = 7.2293(3) b = 6.6055(3) c = 11.7018(5) β = 90.485(3)°	a = 6.3446(6) b = 7.2338(6) c = 10.6349(7) β = 102.825(9)°
Z	2	2
V / $Å^3$	558.8(4)	475.91(5)
$\rho_{calc.}$ / gcm^{-3}	1.851	2.246
θ range / deg	7.00 – 90.31	3.30 – 30.98
R_p	0.0321	0.0357
wR_p	0.0425	0.0495
R(all)	0.0936	0.1146
wR(all)	0.0812	0.1094
$R(I > 2\sigma)$	0.0859	0.1047
$wR(I > 2\sigma)$	0.0801	0.1081
R_{exp}	0.0204	0.0146
GOF	2.09	3.41
weight fraction / %	98.71(5) [Li_8SiP_4 = 0.99(5)] [WC = 0.30(1)]	94.6(2) [Si = 2.76(4)] [$LiSi_2P_3$ = 2.6(1)]

Coordination polyhedra

In $Li_{10}Si_2P_6$ and $Li_3Si_3P_7$, the Si atoms are coordinated by tetrahedra of P atoms, while all the P atoms are covalently bound to one, two, or three Si atoms, respectively, in $Li_3Si_3P_7$ additionally covalent P-P bonds are present. The coordination shells of the P atoms are completed by Li cations. Vice versa, the Li atoms are coordinated mainly by P atoms, but in some cases, particularly in the Li rich compound $Li_{10}Si_2P_6$, some short Li-Li and even Li-Si distances arise due to packing requirements. The coordination polyhedra of the P and Li atoms are shown below.

$Li_{10}Si_2P_6$: The P atoms in $Li_{10}Si_2P_6$ are surrounded by polyhedra formed by 7 or 9 neighbouring atoms. The polyhedron around P1 can be described as a distorted two times capped tetragonal pyramid, those around P2 and P3 as capped tetragonal antiprisms. The coordination polyhedra of Li consist four or five P atoms, however, if Si and Li atoms in slightly longer distances are considered, irregular polyhedra with up to 12 or 14 vertices are formed.

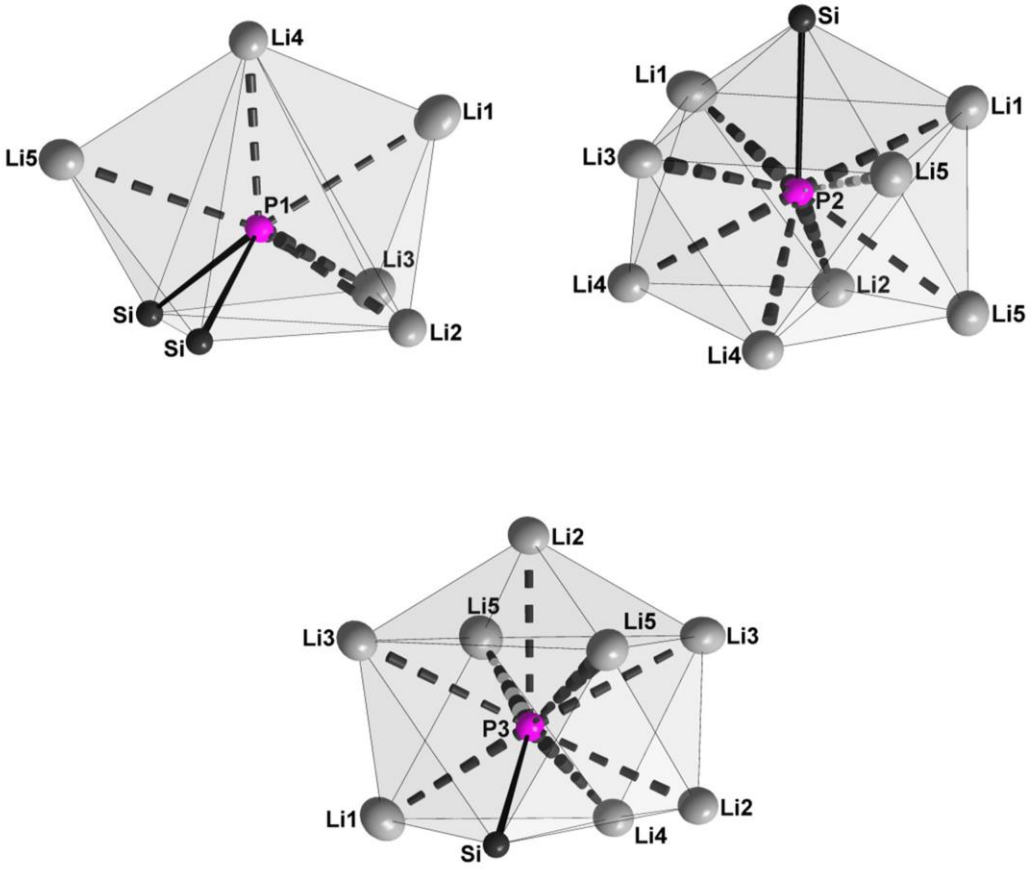

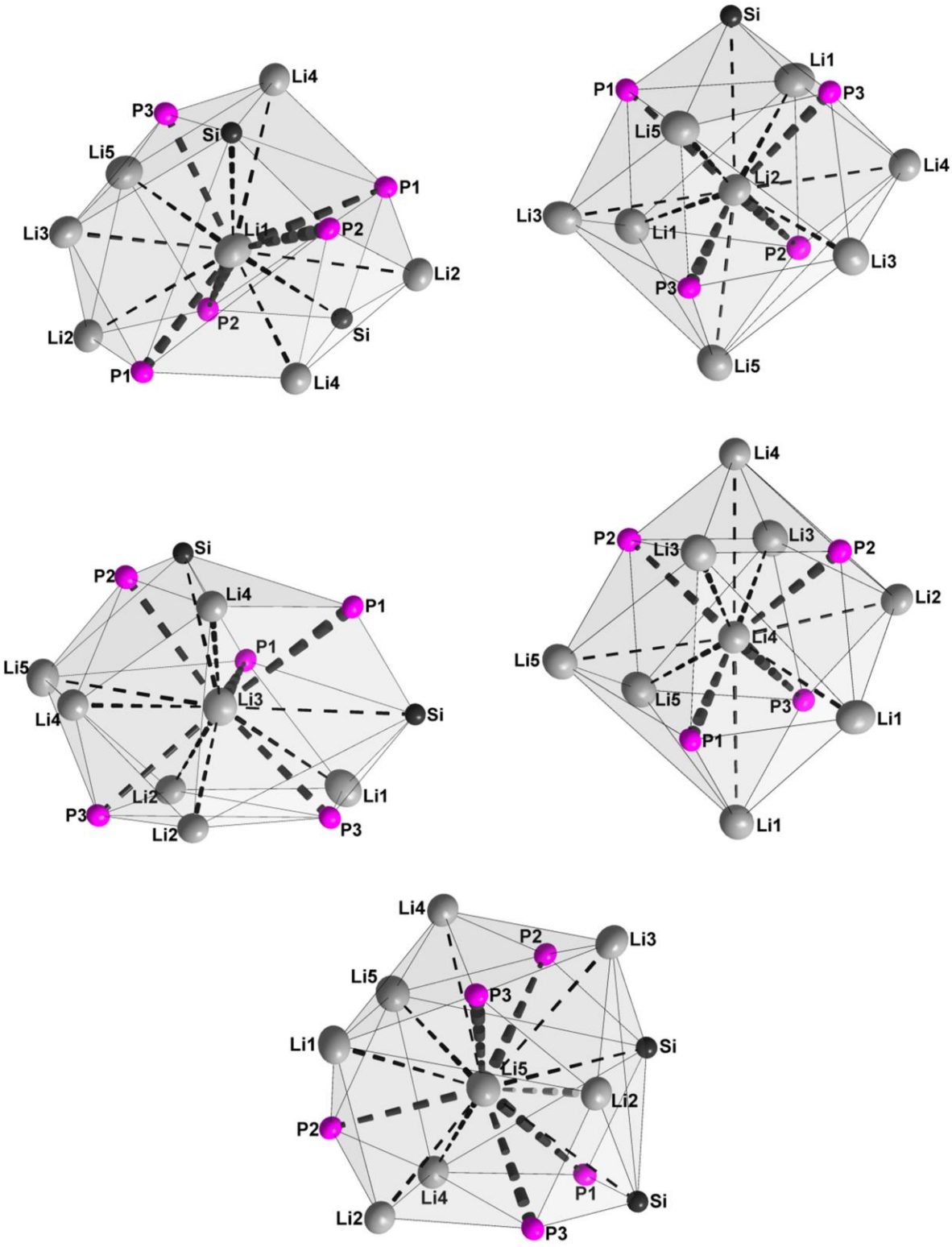

Figure S1. Coordination polyhedra of independent P and Li in $Li_{10}Si_2P_6$. The nearest neighbours form grey polyhedra around the central atoms. Si-P bond are drawn as solid, Li-P bonds as thick and dashed and short Li-Li distances as thin and dashed lines. Ellipsoids are drawn at the 90% probability level.

$Li_3Si_3P_7$: In $Li_3Si_3P_7$, the neighbouring atoms around P1 and P5 form distorted trigonal bipyramids of three Li and two equatorial Si atoms, while the remaining P atoms are surrounded by distorted tetrahedra of one Li and three Si (P2) or one Li, one Si, and two P atoms (P3, P4). In the case of P3 and P4 the tetrahedra exhibit a strongly widened Si-P-Li angle. A tetrahedral coordination with P is observed for Li1, which can be extended by two Li positions (Li2 and Li3) in its vicinity. These are themselves coordinated by distorted octahedra of P atoms. Li3 is moved to one of the faces of the polyhedron leading into the vicinity of Si1.

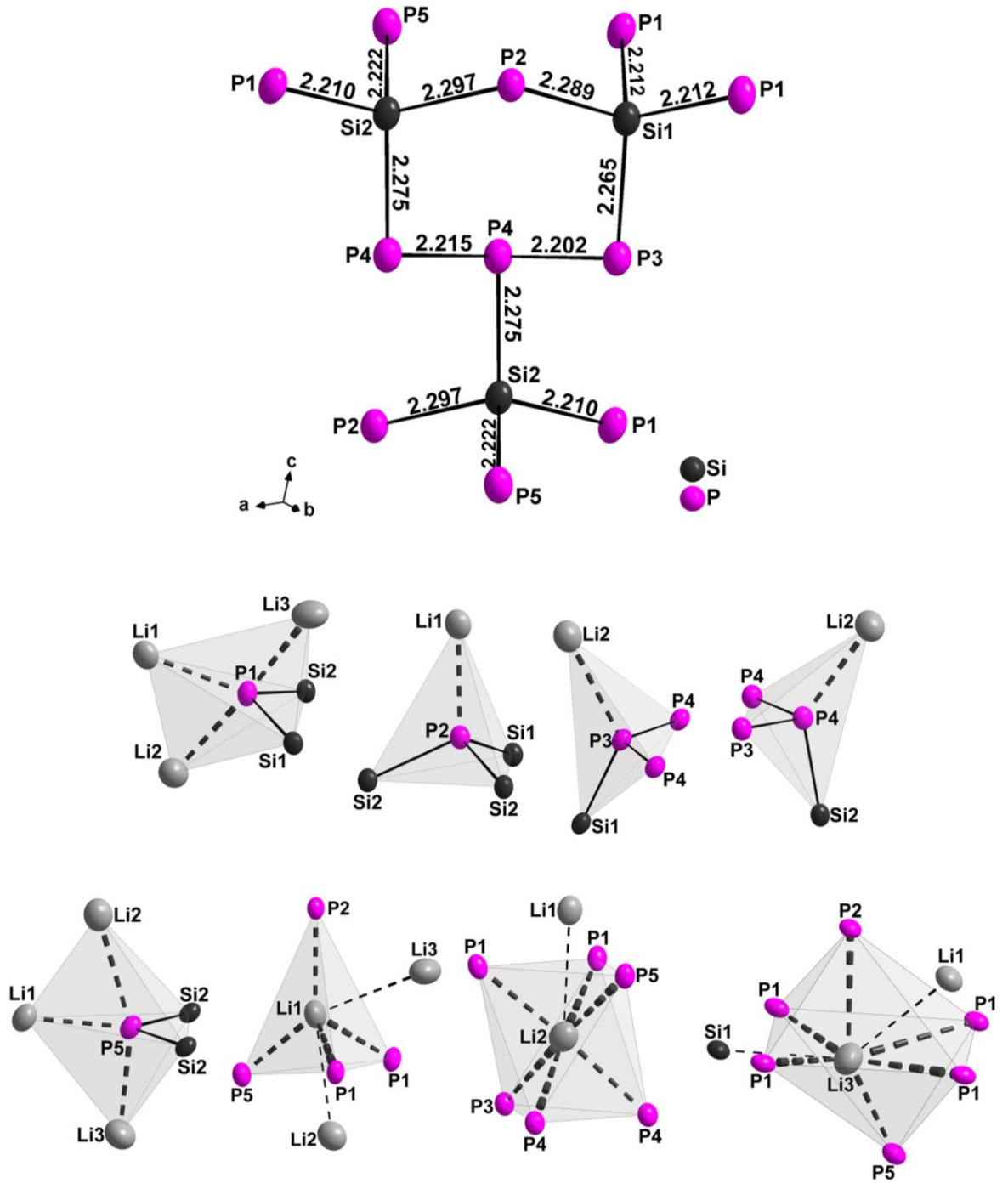

Figure S2. Top: Coordination pattern of Si with Si-P bond lengths in $Li_3Si_3P_7$. Bottom: Coordination spheres of P and Li. Si-P bonds are drawn solid, Li-P bonds thick and dashed and short Li-Li distances thin and dashed. Ellipsoids are drawn at the 90% probability level.

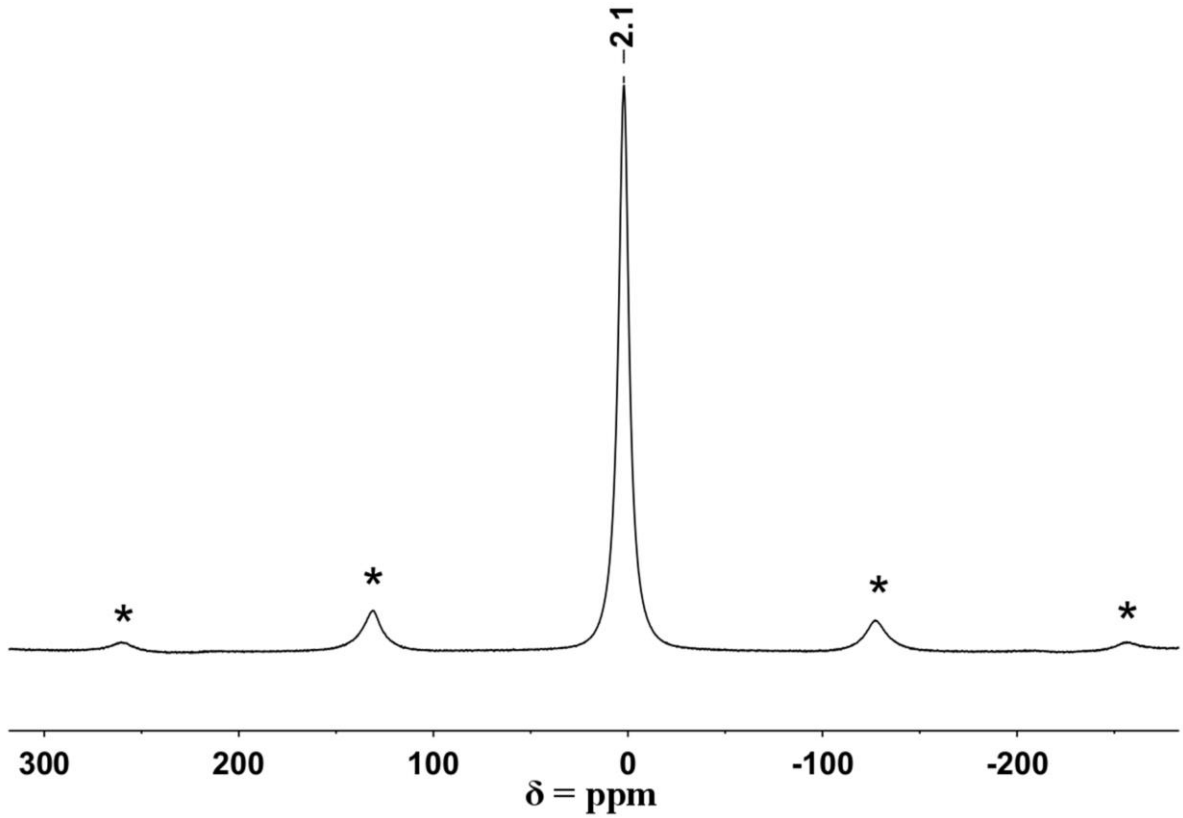

Figure S3. ^{7}Li MAS-NMR of $Li_{10}Si_2P_6$, rotation side bands are indicated with *.

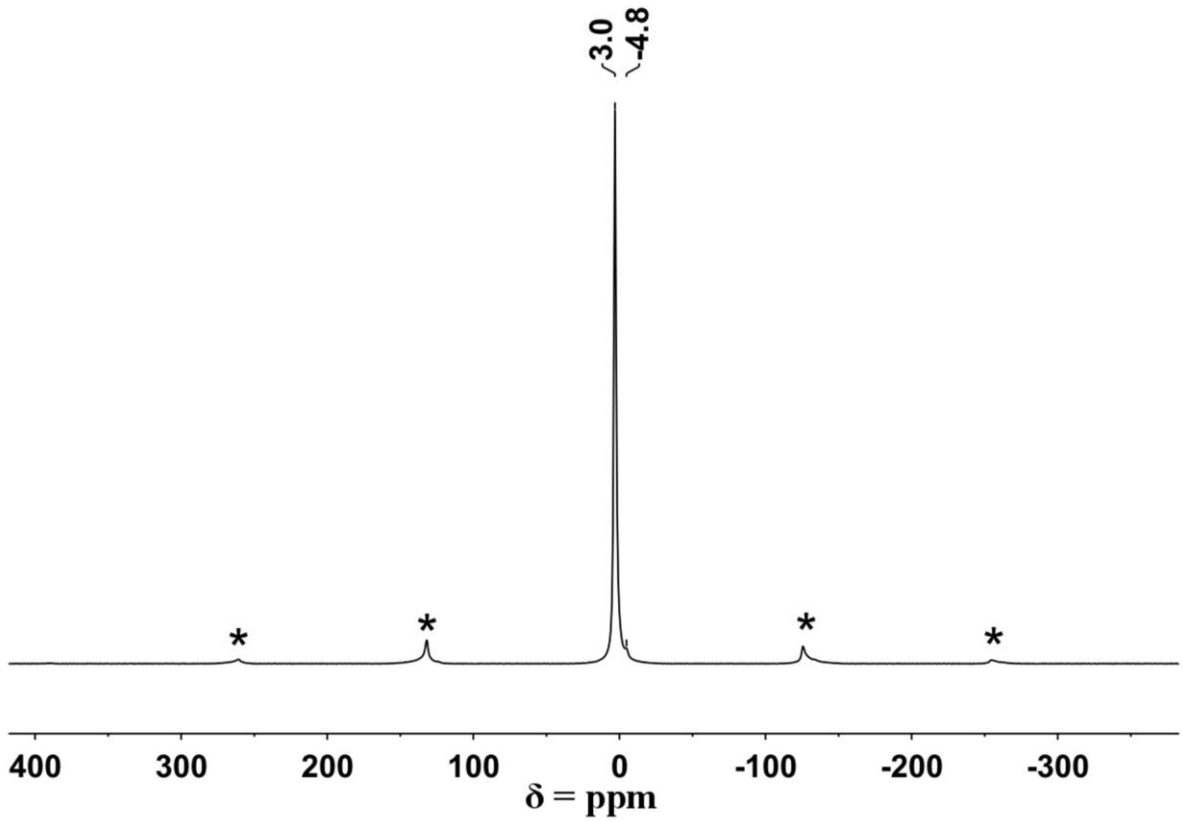

Figure S4. ^{7}Li MAS-NMR of $Li_3Si_3P_7$, rotation side bands are indicated with *.

5.2 Fast Ionic Conductivity in the Novel Lithium-Rich Phosphidosilicate $Li_{14}SiP_6$

S. Strangmüller, H. Eickhoff, D. Müller, W. Klein, G. Raudaschl-Sieber, H. Kirchhain, C. Sedlmeier, V. Baran, A. Senyshyn, V. L. Deringer, L. van Wüllen, H. A. Gasteiger, T. F. Fässler

manuscript for publication

Fast Ionic Conductivity in the Lithium-Rich Phosphidosilicate $Li_{14}SiP_6$

Stefan Strangmüller,[a, ‡] Henrik Eickhoff,[a, ‡] David Müller,[a] Wilhelm Klein,[a] Gabriele Raudaschl-Sieber,[a] Holger Kirchhain,[b] Christian Sedlmeier,[c] Volodymyr Baran,[d] Anatoliy Senyshyn,[d] Volker L. Deringer,[e] Leo van Wüllen,[b] Hubert A. Gasteiger,[c] and Thomas F. Fässler*,[a]

[a]Department of Chemistry, Technische Universität München, Lichtenbergstrasse 4, D-85747 Garching, Germany

[b]Department of Physics, University of Augsburg, Universitätsstrasse 1, D-86159 Augsburg, Germany

[c]Department of Chemistry, Technische Universität München, Lichtenbergstrasse 4, D-85747 Garching, Germany

[d]Heinz Maier-Leibnitz Zentrum, Technische Universität München, Lichtenbergstrasse 1, D-85748 Garching; Germany

[e]Department of Engineering, University of Cambridge, Cambridge CB2 1PZ, United Kingdom

KEYWORDS: Lithium ion conductor, Crystal structure, Phosphidosilicate, Ball mill, 3D Diffusion pathways, Neutron Diffraction.

ABSTRACT: Solid electrolytes with superionic conductivity are required as a main component for all-solid-state batteries. Here we present a novel solid electrolyte with three-dimensional conducting pathways based on "lithium-rich" phosphidosilicates with ionic conductivity of $\sigma > 10^{-3}$ S cm^{-1} at room temperature and activation energy of 30-32 kJ mol^{-1} expanding the recently introduced family of lithium phosphidotetrelates. Aiming towards higher lithium ion conductivities systematic investigations of lithium phosphidosilicates gave access to the so far lithium-richest compound within this class of materials. The crystalline material (space group $Fm\bar{3}m$), which shows reversible thermal phase transitions, can be readily obtained by ball mill synthesis from the elements followed by moderate thermal treatment of the mixture. Lithium diffusion pathways via both, tetrahedral and octahedral voids, are analyzed by temperature-dependent powder neutron diffraction measurements in combination with MEM and DFT calculations. Moreover, the lithium ion mobility structurally indicated by a disordered Li/Si occupancy in the tetrahedral voids plus partially filled octahedral voids, is studied by temperature-dependent impedance and ^{7}Li-onepulse-NMR spectroscopy.

1. Introduction

All-solid-state battery technology is currently attracting considerable interest, as such batteries possess a number of potential advantages over liquid electrolyte systems, including energy density gains and improved safety. As a consequence, a large number of inorganic materials with both crystalline and amorphous structures as well as their composite structures have been investigated experimentally and theoretically as potential solid electrolyte candidates.[1-2] In particular the investigation of lithium ion solid electrolytes in lithium ion batteries (LIBs) has increased rapidly in order to improve the performance of electrochemical energy storage systems.[3]

In order to achieve a significant ionic conductivity in a crystalline solid, at first a high charge carrier density should coincide with a large number of available lattice sites. Secondly, solid electrolytes require a low activation energy for lithium mobility as it is found in materials in which cation sites are arranged in face-sharing polyhedra that are formed by anions.[4] For example, for garnet-type solid electrolytes the effect of polyhedral connectivity on the ionic conductivity has been shown recently.[5] A large polarizability of the anions has been suggested as another factor for lowering the activation barrier for Li^+ mobility,[6] and accordingly sulfides, thiophosphates and materials containing iodine such as Li-argyrodites are investigated as superionic conductors (LISICONs).[7-14] E.g. Li_3PS_4 shows an ionic conductivity which is several orders of magnitudes higher than that of Li_3PO_4, and the same applies for Li_6PS_5Cl versus Li_6PO_5Cl.[15-16] The best superionic conductors are found if a combination of several of these aspects appear as observed e.g. in $Li_{10}GeP_2S_{12}$ (LGPS), which can formally be regarded as variation of pristine Li_3PS_4, combined with the Li-richer Li_4GeS_4 [$Li_{10}(GeS_4)(PS_4)_2$ = 2 Li_3PS_4 + Li_4GeS_4], or in the argyrodites Li_6PS_5X, which formally represent a combination of Li_3PS_4, Li_2S and LiX [$Li_6(PS_4)(S)X$ = Li_3PS_4 + Li_2S + LiX].[6,10]

Following these concepts we recently started to reinvestigate the ternary phase systems Li-Si-P and Li-Ge-P[17] and found ionic conductivities up to 10^{-4} S cm^{-1} at room tem-

perature for pure Li_8SiP_4 and Li_8GeP_4.[18-19] Li_8SiP_4, comprising discrete $[SiP_4]^{8-}$ tetrahedra, fulfills most of the criteria mentioned above: a) It has more than twice the Li^+ concentration of Li_3PS_4; b) the higher formal charge of minus two at the P atoms in the $[SiP_4]^{8-}$ units hints for a higher polarizability than the formally one-fold negatively charged sulfur atoms in PS_4^{3-} and c) most intriguingly, the crystal structure of Li_8SiP_4 is closely related to the anti-structure type of CaF_2. The atom packing of Li_8SiP_4 derives from cubic close packing (*ccp*) of the P atoms which in consequence creates eight tetrahedral and four octahedral voids per formula unit. Out of these twelve voids only one tetrahedral site is filled by a Si atom which can be considered as covalently bound to the four P atoms. In addition eight Li atoms per formula unit can be distributed within the remaining 11 voids and, thus, numerous empty vacancies for a possible Li^+ hopping are present. As an additional advantage in the *ccp*, tetrahedral and octahedral voids share common faces, a fact that enlarges the window for diffusion pathways, compared to edge-sharing polyhedra.[20-21] This concept of cation disorder in lithium phosphidotetrelates should create a promising opportunity to get access to high-performance lithium ion conductors, which has already been successfully applied to the Li-Ge-P system, as indicated by the close structural relationship between Li_8SiP_4 and α- and β-Li_8GeP_4.[19]

However, the Li^+ conductivity can even be further increased by using different or disordered anions. The presence of differently charged anions may allow for a fine-tuning of the Li^+ concentration within the compound, and a disorder may reduce the activation barrier.[22-23] A well-established example for lithium ion conductors in which all these concepts are realized is the recently discovered class of Li-argyrodites Li_6PS_5X (X = Cl, Br, I). Their cubic crystal structure ($F\bar{4}3m$) consists of two different types of anionic building blocks, tetrahedral $[PS_4]^{3-}$ units and isolated S^{2-} or X^- ions in the ratio 1:2, separated by lithium ions.

We now apply the concept of increased anion and cation disorder over a larger number of polyhedral voids on one hand, and of an increased overall Li^+ mobility on the other, to lithium phosphidosilicates (LSiP). The formal addition of more Li-rich Li_3P to one equivalent of Li_8SiP_4 corresponds to a line through Li_3P and Li_8SiP_4[18] in the ternary composition diagram Li-Si-P (Figure 1). Interestingly, at the Li-poor side along this line several compounds such as $Li_{10}Si_2P_6$,[24] Li_2SiP_2,[18, 25] and $LiSi_2P_3$[25] are already known. The line hits the binary border at a nominal stoichiometry of "Si_3P_4".

Here we report on a new compound with a higher Li content than Li_8SiP_4 obtained by a formal addition of Li_3P. Based on the crystal structures of Li_8SiP_4 and Li_3P, one might expect the presence of $[SiP_4]^{8-}$ and P^{3-} as anionic building units similar to the simultaneous appearance of $[PS_4]^{3-}$ and S^{2-} in Li-argyrodites. We found a straightforward and simple synthesis route for the new phosphidosilicate $Li_{14}SiP_6$, which shows the highest Li^+ density among the more complex lithium ion conductors. This route leads to a crystalline material and comprises mechanochemical ball milling of the elements with subsequent annealing of the mixture. The crystal structure was determined by single crystal and by powder X-ray, as well as by powder neutron diffraction methods. The purity of the samples was confirmed by elemental analyses as well as by solid state ^{6}Li, ^{29}Si and ^{31}P MAS NMR spectroscopy. The thermal properties of the material were studied by differential scanning calorimetry and temperature-dependent powder neutron diffraction experiments. Finally, the Li^+ migration has been investigated by electrochemical impedance spectroscopy, temperature-dependent ^{7}Li-onepulse NMR spectroscopy, high-temperature neutron diffraction measurements (maximum entropy method), and density functional theory calculations.

2. Experimental Methods

Synthesis. All syntheses were carried out under Ar atmosphere in glove boxes (MBraun, 200B) with moisture and oxygen levels below 0.1 ppm, or in containers, which were sealed under Ar atmosphere and vacuum ($< 2 \cdot 10^{-2}$ mbar), respectively. Lithium phosphidosilicates are sensitive to oxygen and moisture; in particular, contact with water results in a vigorous reaction including the formation of flammable and toxic gases (e.g. phosphine). Therefore, disposal must be carried out in small amounts at a time and under proper ventilation.

Synthesis of polycrystalline $Li_{14}SiP_6$. The synthesis route includes two steps, using stoichiometric amounts of lithium (Rockwood Lithium, 99%), silicon (Wacker, 99.9%) and red phosphorus (Sigma Aldrich, 97%) aiming for the compositions $Li_{11}SiP_5$, $Li_{14}SiP_6$, $Li_{17}SiP_7$ and $Li_{20}SiP_8$. In the first step a reactive mixture (m = 1.5-5.0 g) is prepared by mechanochemical milling using a Retsch PM100 Planetary Ball Mill (350 rpm, 36 h, 10 min interval, 3 min break) with a tungsten carbide milling jar (V = 50 mL) and three balls with a diameter of 15 mm.

In the second step, the obtained reactive mixture was pressed to pellets, sealed in batches of 0.3 to 3.0 g in carbon-coated silica glass ampoules and heated in a muffle furnace (Nabertherm, L5/11/P330) to 973 K (heating rate: 4 K min^{-1}) for 6-18 h followed by quenching of the hot ampoules in water.

Powder X-ray Diffraction. Data were collected at room temperature on a STOE Stadi P diffractometer (Ge(111) monochromator, Cu $K_{\alpha 1}$ radiation, λ = 1.54056 Å or Mo $K_{\alpha 1}$ radiation, λ = 0.70932 Å) with a Dectris MYTHEN 1K detector in Debye-Scherrer geometry. Samples were sealed in glass capillaries (Ø 0.3 mm) for measurement. Raw data were processed with WinXPOW[26] software prior to further refinement.

Powder Neutron Diffraction. Elastic coherent neutron scattering experiments were performed on the high-resolution powder diffractometer SPODI at the research reactor FRM-II (Garching, Germany).[27] Monochromatic neutrons (λ = 1.5482 Å) were obtained at a 155° take-off angle using the (551) reflection of a vertically-focused composite Ge monochromator. The vertical position-sensitive multidetector (300 mm effective height) consisting of 80 ^{3}He tubes of 1 inch in diameter and covering an angular

range of 160° 2θ was used for data collection. Measurements were performed in Debye-Scherrer geometry. The powder sample (ca. 2 cm^3 in volume) was filled into a Nb tube container (10 mm diameter, 0.5 mm wall thickness) under argon and welded using an arc-melting apparatus. The Nb container with the sample was mounted in the top-loading closed-cycle refrigerator. ^{4}He was used as a heat transmitter. The instantaneous temperature was measured using two thin film resistance cryogenic temperature sensors Cernox and controlled by a LakeShore340 temperature controller. Two dimensional diffraction data were collected at fixed temperatures in the range of 4-300 K using 20 K temperature steps upon heating and then corrected for geometrical aberrations and the curvature of the Debye-Scherrer rings.

For measurements at high temperature the Nb container with the sample was mounted in the vacuum furnace equipped with Nb heating elements. Measurements and temperature control were carried out using two Type L thermocouples and a Eurotherm 2400 controller. The data were collected in the temperature range 297-1023 K using a temperature increment of 50 K. At temperatures below 573 K, ^{4}He was used as a thermal exchange medium, whereas at higher temperatures the furnace regulation was achieved using an isolation vacuum.

Rietveld Refinement. The data analysis was performed using the full profile Rietveld method implemented in the FullProf program package.[28] For the shaping of the peak profile, the pseudo-Voigt function was chosen. The background contribution was determined using a linear interpolation between selected data points in non-overlapping regions. The scale factor, zero angular shift, profile shape parameters, resolution (Caglioti) parameters, asymmetry and lattice parameters as well as fractional coordinates of atoms and their displacement parameters were varied during the fitting.

In accordance with the composition gained from elemental analyses the stoichiometry was set to $Li_{14}SiP_6$ (Z = 0.67) or $Li_{2.33}Si_{0.17}P$ (Z = 4), respectively. Besides the Nb reflections only reflections consistent with cubic symmetry and face centering, according e.g. to the space group $Fm\bar{3}m$ (no. 225) of antifluorite, are present in the neutron diffraction patterns. The diffraction intensities of $Li_{14}SiP_6$ have been modelled with the P atoms located at the 4*a* site and a mixed Li/Si site occupation of the residual 4*b* and 8*c* sites. Constraining the overall Li and Si concentrations to the ones from elemental analyses, along with the assumptions of full 8*c* site occupation it can be concluded that the 8*c* site is fully occupied by Si and Li, and that there is no Si located on the 4*b* site.

A co-refinement of the powder neutron diffraction data at 300 K and of the Mo powder X-ray diffraction data at the same temperature was carried out approving the accuracy of the two methods. All structures were visualized using VESTA.[29]

Single Crystal X-ray Structure Determination. Single crystals of $Li_{14}SiP_6$ were obtained by a high-temperature reaction of the reactive mixture in a corundum crucible, which was sealed in a steel ampoule under Ar. The pressed sample was annealed for 6 h at 1273 K (heating rate: 4 K min^{-1}), slowly cooled to 973 K (cooling rate: 0.05 K min^{-1}) and quenched after another 8 h in water.

A single crystal of $Li_{14}SiP_6$ was isolated and sealed in a glass capillary (0.1 mm). For diffraction data collection, the capillary was positioned in a 150 K cold N_2 gas stream. Data collection was performed with a STOE StadiVari (Mo $K_{\alpha 1}$ radiation) diffractometer equipped with a DECTRIS PILATUS 300 K detector. The structure was solved by Direct Methods (SHELXS-2014) and refined by full-matrix least-squares calculations against F^2 (SHELXL-2014).[30]

Elemental Analyses. Elemental analyses were performed by the microanalytical laboratory at the Department of Chemistry of the Technische Universität München. The amount of lithium in the samples was analyzed via atomic absorption spectroscopy using a 280FS AA spectrometer (Agilent Technologies). The amount of phosphorous was determined by photometry applying both the vanadate method and the molybdenum blue method, leading to almost identical values. The amount of silicon was also determined photometrically via silicon molybdate. To overcome disturbances of phosphorous and lithium, blank tests have been applied to calculate occurring deviations. The corresponding photometric analyses were carried out using a Cary UV-Vis spectrometer (Agilent Technologies).

The analyses reveal the following composition: lithium 29.4%, silicon 8.23% and phosphorus 57.89% (vanadate method) or 57.68% (molybdenum blue method). The observed overall loss of about 5% maybe caused by abrasion of small amounts of WC during ball milling and impurities within the educts (e.g. purity of Li ≥ 99% or P ≥ 97%) or formation of volatile decomposition products. Conversion and scaling of the determined values result in a stoichiometry of $Li_{13.64}Si_{0.94}P_6$.

Differential Scanning Calorimetry (DSC). For the investigation of the thermal behavior of the compounds a Netzsch DSC 404 Pegasus device was used. Niobium crucibles were filled with the samples and sealed by arc-welding. Empty sealed crucibles served as a reference. Measurements were performed under an Ar flow of 75 mL min^{-1} and a heating/cooling rate of 10 K min^{-1}. Data collection and handling was carried out with the Proteus Thermal Analysis program.[31]

Solid-State NMR Spectroscopy. Magic angle spinning (MAS) NMR spectra have been recorded on a Bruker Avance 300 NMR device operating at 7 T by the use of a 4 mm ZrO2 rotor. The resonance frequencies of the investigated nuclei are 44.167 MHz, 59.627 MHz and 121.495 MHz for ^{6}Li, ^{29}Si and ^{31}P, respectively. The rotational frequency was set to 8 kHz (^{29}Si), 12 kHz (^{31}P) and 15 kHz (^{6}Li and ^{31}P). The MAS NMR spectra have been acquired at room temperature with recycle delays from 10 s to 45 s and 200 to 1064 scans. All spectra regarding ^{6}Li were referenced to LiCl (1 M, aq) and LiCl (s) offering chemical shifts of 0.0 ppm and 1.15 ppm, respectively. Tetrakis(trimethylsilyl)silane was used as an external standard for the ^{29}Si spectra showing a chemical shift of –9.8 ppm referred to TMS.

The ^{31}P spectra were referred to ammonium dihydrogen phosphate (s) with a chemical shift of 1.11 ppm regarding concentrated H_3PO_4. All spectra were recorded using single-pulse excitation.

Static ^{7}Li NMR experiments have been performed using a Bruker Avance III spectrometer operating at a magnetic field of 7 T employing a 4 mm WVT MAS probe. The resonance frequencies of the measured ^{7}Li nucleus is 116.6 MHz. The sample has been sealed in a 4 mm glass tube to avoid contact with air and moisture. The temperature calibration for the measurements has been performed using the temperature-dependent ^{207}Pb NMR shift of lead nitrate as chemical shift thermometer, which has also been measured in a sealed glass tube. The static ^{7}Li satcomb onepulse measurements were carried out in the temperature range from room temperature to 159 K with recycle delays from 30 s to 60 s and 4 scans. All spectra were referenced to LiCl (aq), for ^{7}Li.

Impedance Spectroscopy and DC Conductivity Measurements. The ionic conductivity of $Li_{14}SiP_6$ was determined by electrochemical impedance spectroscopy (EIS) in an in-house designed cell. The setup consists of two stainless-steel current collectors, a stainless-steel casing, a PEEK tube, hardened stainless-steel dies and pistons comprising a gasket for tightening the cell as well as six screws for fixing the cell. Powdered samples of $Li_{14}SiP_6$ (510 mg) were placed between two 8 mm dies, and the screws were fastened with a torque of 30 Nm, compressing the samples to 79% of the crystal density. For the determination of the compressed pellet thickness, six holes in a symmetric configuration were drilled into the current collectors, and the distance in between was measured using a precision caliper. Impedance spectra were recorded on a Bio-Logic potentiostat (SP-200) in a frequency range from 3 MHz to 50 mHz at a potentiostatic excitation of ±50 mV. Data were treated using the software EC-Lab (V 11.26). The measurements were performed in an Ar-filled glove box at 298 K. The electronic conductivity was determined with the same setup using a potentiostatic polarization applying voltages of 50, 100 and 150 mV for 16 h each. For the determination of the activation energy of the lithium ion conduction, the cell temperature was set to 273, 298, 313, 333, and 353 K using a climate chamber (ESPEC, LU-114). The exact temperature profile is described in the Supporting Information as well as in Figure S12. Prior to EIS measurements, the cell rested 120 min to allow for thermal equilibration. EIS measurements were performed at both heating and cooling cycles. Temperature-dependent measurements were conducted outside the glove box, and the pistons were additionally greased to ensure a tight sealing of the cell from the ambient environment.

DFT Simulations. Density functional theory (DFT) total energy computations and DFT-based molecular dynamics (MD) simulations were carried out to complement the experimentally derived structures. Comparable DFT-MD techniques were recently used to study the related Li_2SiP_2 system.[32] In the present case, mixed occupations in the structure make it necessary to construct a supercell model with discrete occupations (Supporting Information). In brief, we used a 3×3×3 expansion of the conventional unit cell, ensuring an approximately isotropic distribution of Si atoms on the 8*c* position (such as to avoid close Si···Si contacts), and assessed different discrete occupation models for the Li-containing sites. Total-energy computations using CASTEP[33] confirmed that a full occupation of the position 8*c* and a vacancy formation on 4*b* is preferred over the alternative scenario of vacancy formation on 8*c*, corroborating the experimental refinement results. For the final 378-atom supercell model, DFT-MD simulations were carried out using cp2k[34]. The system was gradually heated to 1300 K (30 ps), held at 1023 K (2.5 ps), followed by a production run at that temperature (5 ps), all with a timestep of 0.5 fs. Details of the protocol are provided as Supporting Information.

3. Results and Discussion

Syntheses and Structure of $Li_{14}SiP_6$. For the search of novel Li-rich compositions we investigated stoichiometric ratios along the line connecting Li_3P and Li_8SiP_4 in the Li-Si-P Gibbs triangle (Figure 1). Extrapolation of this sequence to higher amounts of lithium by the formal addition of "Li_3P" units results in the nominal compositions "$Li_{11}SiP_5$", "$Li_{14}SiP_6$", "$Li_{17}SiP_7$", and "$Li_{20}SiP_8$". Materials of these compositions were prepared applying a recently described preparative route for phosphidotetrelates starting from mechanical alloying of the elements in the stoichiometric amounts, followed by a high-temperature reaction of the mixtures in sealed, carbon-coated silica glass ampoules.[19] After the mechanical alloying process, PXRD data reveal the initial formation of a cubic antifluorite structure type. However, the extremely broadened reflections indicate small crystal sizes and a dominant amorphous state at this stage of the synthesis. Microcrystalline, single-phase $Li_{14}SiP_6$ is obtained by quenching the hot ampoule with the ball-milled product in water after 6-18 h of annealing. Co-refinement of powder Mo X-ray and neutron diffraction shows a high agreement of the two methods and confirms the structure model (Figure 2). Details of the Rietveld refinements are shown in Table 1.

Experiments with the nominal stoichiometry of "$Li_{11}SiP_5$" in analogy to $Li_{14}SiP_6$ reveal a mixture of $Li_{14}SiP_6$ and Li_8SiP_4[18], whereas investigations of compositions with a higher amount of lithium and phosphorus ("$Li_{17}SiP_7$" and "$Li_{20}SiP_8$") lead to a mixture of $Li_{14}SiP_6$ and Li_3P (Figure S3 in the Supporting Information). According to these results $Li_{14}SiP_6$ is assumed to be the lithium-richest compound on the quasi-binary line between Li_3P and "Si_3P_4". Moreover, no significant phase width according to "$Li_{14-4x}Si_{1+x}P_6$" is found at the Li_3P-rich side, while at the Li_3P-poor side a Si-enriched composition "$Li_{14-4x}Si_{1+x}P_6$" seems to exist (Supporting Information).

The lithium-rich compound $Li_{14}SiP_6$ crystallizes in the Li_3Bi structure type[35] with the cubic space group $Fm\bar{3}m$ (no. 225) and a lattice parameter of 5.91566(6) Å at 4 K (Figure 3). The crystal structure was determined from the data of a single crystal X-ray diffraction measurement at 123 K, of temperature-dependent powder neutron diffraction meas-

urements between 4 K and 1023 K and from a co-refinement of powder neutron and X-ray diffraction patterns obtained at 300 K. Atomic coordinates and anisotropic displacement parameters as well as the results from the powder neutron diffraction measurement at 4 K and from the single crystal X-ray diffraction at 123 K are given in the Supporting Information.

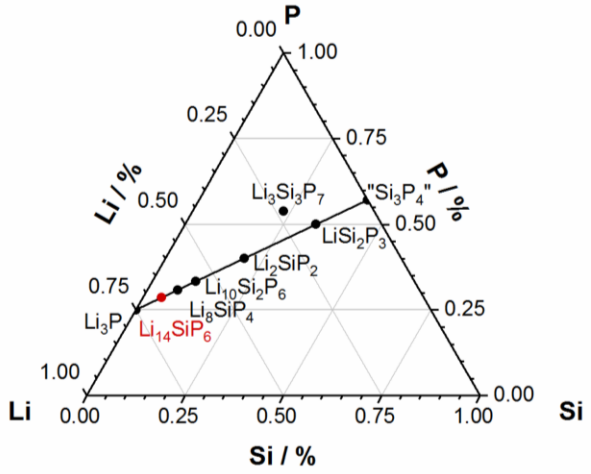

Figure 1. Gibbs triangle of the ternary Li-Si-P composition diagram with formulae of known compounds. The new compound $Li_{14}SiP_6$ is highlighted in red.

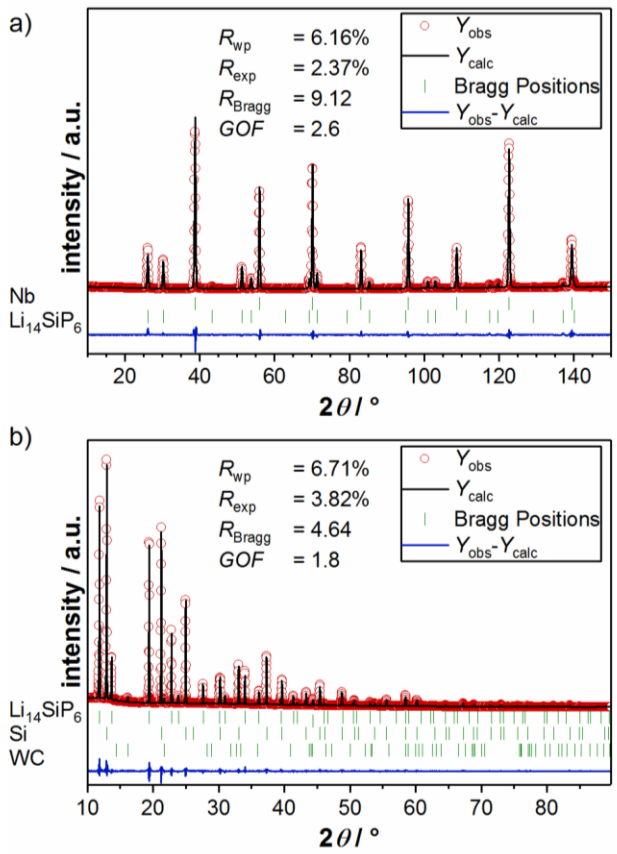

Figure 2. Results from the co-refinement of $Li_{14}SiP_6$. a) Rietveld analysis of the powder neutron diffraction pattern (λ = 1.5482 Å) of $Li_{14}SiP_6$ at 300 K. b) Rietveld analysis of the powder X-ray diffraction pattern (λ = Mo $K_{\alpha 1}$) of $Li_{14}SiP_6$ at 300 K. In both diffraction patterns red circles indicate observed intensities Y_{obs}, black lines show calculated intensities Y_{calc}, blue lines reveal the difference between observed and calculated intensities, and green marks indicate Bragg positions of $Li_{14}SiP_6$ and Nb (ampoule) or $Li_{14}SiP_6$, Si (added as internal standard to the PXRD sample) and WC (abrasion), respectively.

Table 1. Details of the Rietveld structure refinement (co-refinement) of $Li_{14}SiP_6$ from neutron and X-ray diffraction measurements at 300 K

empirical formula	$Li_{2.33}Si_{0.17}P$ (neutron diffraction)	$Li_{2.33}Si_{0.17}P$ (X-ray diffraction)
T / K	300	300
formula weight / g mol^{-1}	51.86	51.86
space group (no.)	$Fm\bar{3}m$ (225)	$Fm\bar{3}m$ (225)
unit cell parameters / Å	a = 5.93927(1)	a = 5.93927(1)
Z	4	4
V / Å^3	209.507(1)	209.507(1)
$\rho_{calc.}$ / g cm^{-3}	1.644	1.644
λ / Å	1.5482	0.70926
2θ range / deg	9.0000-151.89999	10.0000-89.78600
R_p	4.62%	4.79%
R_{wp}	6.16%	6.71%
R_{exp}	2.37%	3.82%
X^2	6.73	3.07
GOF	2.6	1.8
R_{Bragg}	9.12	4.64
R_f	5.79	14.8
depository no.	CSD-1915806	CSD-1915824

The unit cell of $Li_{14}SiP_6$ contains three crystallographic atom positions (P1, Li1/Si1 and Li2). The structure is closely related to the antifluorite type of structure, as it is based on a cubic close packing (*ccp*) of P atoms on the 4*a* site, with all tetrahedral voids (8*c* site) fully occupied by Li1 and Si1 atoms in a mixed occupancy ratio of 11:1. Additionally, all octahedral voids (4*b* site) are occupied by Li atoms (Li2) with a probability of 50%. All interatomic Si-P distances (2.5616(1) Å; due to symmetry identical: Li1-P, Li2-Si, Li1-Li2), Li2-P (2.96964(1) Å) and P-P distances (4.19970(1) Å) are within the range of those found for related ternary or binary compounds like Li_8SiP_4[18], Li_2SiP_2,[18,25] $LiSi_2P_3$,[25] $Li_{10}Si_2P_6$[24], Li_3P[36], and $Li_{17}Si_4$[37]. As a consequence of the occupational disorder of Li1 and Si1, the structure contains

$[SiP_4]^{8-}$ tetrahedra (ortho-phosphidosilicate) and P^{3-} ions in a ratio of 1:2; the negative charge is compensated by 14 lithium ions located in close vicinity.

The presence of isolated tetrahedral SiP_4 anions is confirmed by the ^{29}Si MAS NMR spectrum showing one distinct resonance at 10.4 ppm (Figure S8 in the Supporting Information) which is rather close to the value of 11.5 ppm observed for discrete $[SiP_4]^{8-}$ tetrahedra in Li_8SiP_4, whereas the signals of covalently connected tetrahedra occur in the range from –3.3 to –14.8 ppm as observed for Li_2SiP_2 and $Li_3Si_3P_7$.[18, 24]

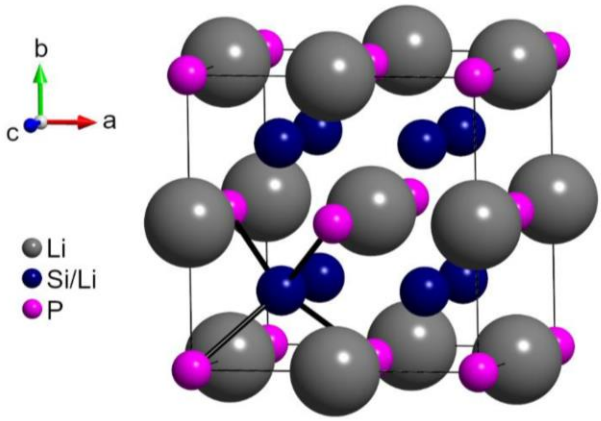

Figure 3. Structure of $Li_{14}SiP_6$ at 4 K. Li, Li/Si (mixed site) and P atoms are depicted as grey, indigo and pink displacement ellipsoids, respectively, set at 90% probability. Black lines mark (Li/Si)-P bonds resulting in (Li/Si)P4 tetrahedra.

Although the crystal structure contains only one crystallographic P site, two broad, distinct signals are detected in the ^{31}P MAS NMR spectra at –226.9 and –316.8 ppm (12 kHz, Figure S9 in the Supporting Information). In spite of the disorder of Li and Si, the P atoms are situated in different chemical environments – either surrounded by eight Li atoms or by one Si atom and seven Li atoms in the neighboring tetrahedral voids – and by a different number of atoms in the six, partially filled octahedral voids. These considerably different chemical environments lead to a strong broadening of the signals.[38] As observed in the ^{31}P MAS NMR spectra of related compounds,[18, 24] a covalent Si-P bond has a significant effect on the chemical shift: the lower the number of neighboring Si atoms and thus the higher the negative partial charge of the P atom is, the stronger is the upfield shift of the signal. Consequently, the signal at –226.9 ppm can be assigned to the terminal phosphorus atoms in the covalently bound $[SiP_4]^{8-}$ units that matches well the characteristic range of terminal phosphorus atoms of $[SiP_4]^{8-}$ tetrahedra in Li_8SiP_4[18] and $Li_{10}Si_2P_6$,[24] whereas the signal at –316.8 ppm is assigned to the isolated P^{3-} units without covalent bonds and surrounded by eight lithium ions in a cubic arrangement.

According to the ratio of one $[SiP_4]^{8-}$ tetrahedron containing four P atoms and two P^{3-} anions, the ratio of the total integrated intensity of the two ^{31}P NMR signals should be 2:1. The slightly higher experimental ratio of 2.3:1 (12 kHz) results either from an overlap of the signals with the spinning sidebands of the respective adjacent signals, as their accessible spinning frequencies are in the range of the chemical shift difference of the two signals, or it indicates the additional presence of bridging P atoms between edge- or corner-sharing SiP_4 tetrahedra. Such bridging P atoms might cause a larger shift between –120 and –240 ppm,[18,24,38] which could overlap with the signals of terminal P atoms. However, the probability of a subsequent occupation of neighboring tetrahedral voids by Si atoms leading to sharing corners or edges of SiP_4 tetrahedra, should be rather small, owing to the electrostatic repulsion of the formally fourfold positively charged Si atoms.

As known from all other lithium phosphidosilicates the ^6Li-MAS NMR spectrum of $Li_{14}SiP_6$ shows only one signal at 5.4 ppm (Figure S7 in the Supporting Information).[18,24-25]

Thermal Properties of $Li_{14}SiP_6$. In order to apply the maximum entropy method at 1023 K, $Li_{14}SiP_6$ was studied by temperature-dependent powder neutron diffraction experiments. Within the investigated temperature range from 4 to 1023 K, the unit cell parameter increases from 5.9158(1) to 6.0785(3) Å in the lower temperature range. Between 623 and 673 K $Li_{14}SiP_6$ decomposes entirely, indicating a fast transition. The phase mixture is thermodynamically stable up to temperatures between 873 and 923 K. The lithium-rich phase $Li_{14}SiP_6$ reappears at 923 K with a proportion of about 80% and is completely converted at 973 K (Figure 4). During these transition processes all Bragg reflections of the involved compounds remain distinct with narrow line widths, suggesting the formation of large crystal domains. The transition temperatures are confirmed by differential scanning calorimetry (DSC) of $Li_{14}SiP_6$ and the corresponding evaluation is given as Supporting Information.

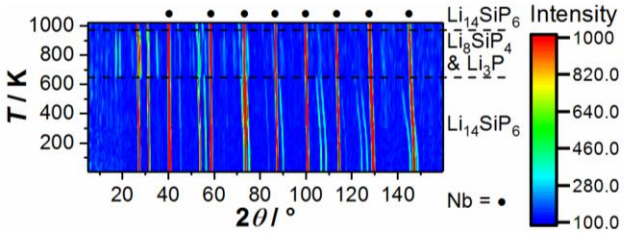

Figure 4. 2D plot of the data of temperature-dependent neutron diffraction measurements from 4 to 1023 K in a 2θ range from 5 to 160° (sample sealed under Ar). With increasing temperature $Li_{14}SiP_6$ decomposes into Li_8SiP_4 and Li_3P, and is reformed again. The ampoule material Nb is indicated with solid circles.

The supplementary evaluation of the executed Rietveld refinements from temperature-dependent neutron diffraction experiments exhibited a nonlinear increase of the lattice parameters of $Li_{14}SiP_6$ upon heating (Figure 5). Furthermore, the quasi-linear trend of increasing lattice parameters observed prior to the phase transition is continued at 973 and 1023 K, indicating a complete recovery of the initial structure obtained via quenching. The lattice dimension of Li_8SiP_4, as normalized to formula units, has

been found systematically smaller and is characterized by a lower thermal expansion rate than that of $Li_{14}SiP_6$.

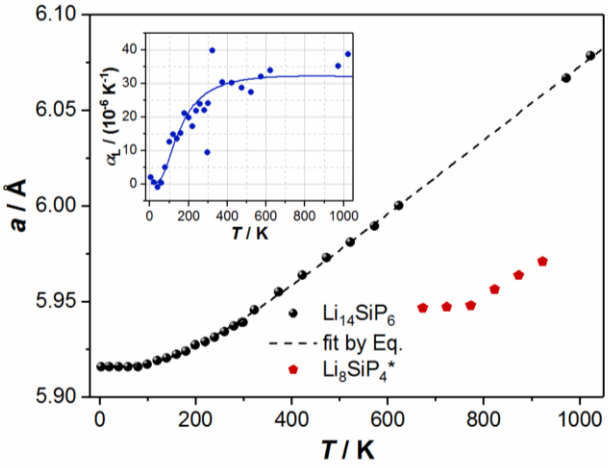

Figure 5. Thermal-dependence of the lattice parameters a and of the thermal expansion coefficient (calculated as $\alpha_l(T) = \partial \ln l(T) / \partial T$) (inset) of the $Li_{14}SiP_6$ sample upon heating under Ar. The normalized $a/2$ lattice parameters for the intermediate phase Li_8SiP_4 are shown by red points.

Similar to other thermodynamic quantities the temperature evolution of the lattice dimensions, and, correspondingly, the thermal expansion can be modeled. As it has been shown in previous studies[39-41] the thermal dependency of the lattice parameter can be modeled by means of the first order Grüneisen approximation

$$V(T) = (a(T))^3 = V_o + \frac{\gamma}{K_T} U(T)$$

$$= V_o + \frac{\gamma}{K_T} \left[9 N k_B T \left(\frac{T}{\theta_D} \right)^3 \int_o^{\theta_D/T} \frac{x^3}{e^x - 1} dx \right] \quad (1)$$

where V_o denotes the hypothetical cell volume at zero temperature, γ is the Grüneisen constant, K_T is the bulk modulus, and U is the internal energy of the system. Both γ and K_T are assumed to be temperature independent, and the use of the Debye approximation for the internal energy U in Eq. 1 with the characteristic temperature θ_D usually provides a reasonable description.

The least-square minimization fit of the experimental temperature dependence of cell volumes by Eq. 1 yields 207.093 ± 0.066 Å^3, 2507 · 10^{-14} ± 37 · 10^{-14} Pa^{-1} and 659 ± 31 K for V_o, the γ/K_T ratio and θ_D, respectively. The fit was characterized by a high coefficient of determination 0.999965, and the graphical results are shown in Figure 5 by dashed lines.

The linear thermal expansion coefficient was calculated from the thermal evolution of the lattice parameter via $\alpha_l(T) = \partial \ln l(T) / \partial T$, and the result is shown in the inset of Figure 5. The thermal expansion of $Li_{14}SiP_6$ grows upon heating from 0 K to ca. 27.5 · 10^{-6} K^{-1} and becomes almost temperature independent α_l = 32 · 10^{-6} K^{-1} above 500 K, which is corresponding to ca. 0.8 θ_D, indicating a quasi-classical behavior of $Li_{14}SiP_6$ at these temperatures.

Lithium Ion Mobility. The dynamic behavior of the lithium ions was investigated via the temperature-dependent evolution of the static ^{7}Li NMR line width in the relevant temperature range. Since the central transition of the I = 3/2 nucleus ^{7}Li is only broadened by the homo- (^{7}Li-^{7}Li) and heteronuclear (here: ^{7}Li-^{31}P) dipolar couplings, and both types of interactions scale with the second Legendrian ($3\cos^2\beta$-1), any dynamic process should produce a (partial) averaging of the orientational dependence and hence entail a narrowing of the NMR line.

The temperature-dependent evolution of the ^{7}Li-onepulse-NMR spectrum is shown in Figure 6a. Only one Lorentzian-shaped signal at 4.8 ppm is visible at room temperature with a linewidth of 523 Hz. Upon cooling of the $Li_{14}SiP_6$ sample, this signal gradually broadens and develops a Gaussian lineshape with a linewidth of 10.2 kHz at 159 K. Figure 6b shows the temperature-dependent evolution of the linewidth (FWHH) of the static ^{7}Li-onepulse measurements. A rough estimation of the activation energy can be done by the empirical Waugh-Fedin relation, $E_A^{NMR} = 0.156 \cdot T_{onset}$. The onset temperature was determined to 190 K which leads to an activation energy of 30 kJ mol^{-1} (~ 0.31 eV).

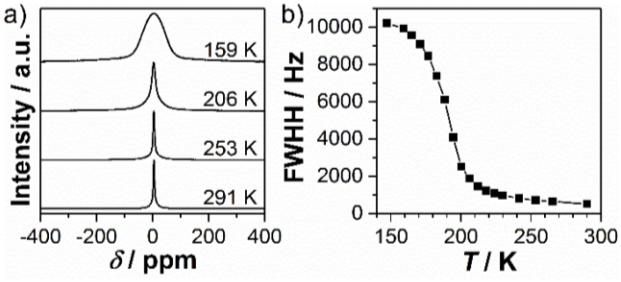

Figure 6. a) ^{7}Li-onepulse-NMR spectrum of $Li_{14}SiP_6$ recorded at different temperatures. A saturation comb was used prior to data acquisition. b) Evolution of the temperature-dependent ^{7}Li-linewidths of $Li_{14}SiP_6$. Solid line serves only as a guide to the eye.

In addition, the lithium ion conductivity of $Li_{14}SiP_6$ was determined from impedance measurements in a blocking electrode configuration. Impedance spectra at different temperatures (273, 298, 313, 333, and 353 K, according to the temperature profile shown in the inset) are displayed in Figure 7a, featuring a semi-circle at high frequencies and a low frequency tail. The semi-circle can be described as parallel circuit element of a resistor and a constant phase element (R/Q), with R representing both intragrain and grain boundary contributions to the lithium ion transport, which could not be resolved, and thus only the total ionic resistance of the sample could be determined. The fitted α values (> 0.98) of the constant phase elements are reasonable close to 1, hence, the constant phase exponent was neglected, in which case the Q parameter becomes essentially equivalent to a capacitance, with a value of ≈ 4.2 · 10^{-10} F for 298 K. This value lies in between the typical range for intragrain (≈ 10^{-12} F) and grain boundary (≈ 10^{-9} F) capacities.[42] The ionic conductivity was determined to

$\sigma_{Li}(Li_{14}SiP_6)$ = (1.09 ± 0.06) · 10^{-3} S cm^{-1} at 298 K (obtained from three independently measured cells). The activation energy for lithium ion transport (Figure 7b) is investigated by temperature-dependent impedance measurements in a range from 273 to 353 K, yielding an E_A^{PEIS} of 32.2 ± 0.6 kJ mol^{-1} (~ 0.33 eV); this was determined from three independently measured cells, using the $\sigma_{Li} \cdot T$ values of only the first heating and cooling cycle of each sample. The temperature ramp of a heating and cooling cycle is displayed in the inset of Figure 7a. Colored dots indicate at which temperatures PEIS measurements were performed. In this context it shall be mentioned that conductivities (and thus the product of $\sigma_{Li} \cdot T$) for heating and cooling differ by less than 5% at 298 and 333 K, whereas at 313 K the $\sigma_{Li} \cdot T$ values obtained in the cooling branch are clearly higher than those obtained in the heating branch (by ≈ 58%), although the cell was in thermal equilibrium. This hysteresis was reproducibly observed for all measured cells of this compound (three independently built and measured cells) and hence is no artifact, but rather must be a compound related phenomenon. The exact reason for the observed hysteresis is still under investigation. Error bars are calculated separately for heating and cooling steps by taking the mean of three independent measurements. DC polarization measurements in the range from 50 to 150 mV reveal an electronic conductivity of (1.64 ± 0.04) · 10^{-7} S cm^{-1} at 298 K (based on the standard deviation of three cells).

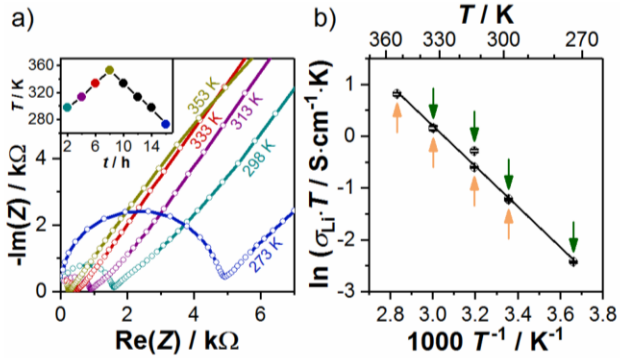

Figure 7. a) Nyquist plot of $Li_{14}SiP_6$ measured under blocking conditions, with spectra recorded at temperatures between 273 and 353 K during a heating cycle, according to color coding of the inset which shows the temperature profile of a cycle for these temperature dependent measurements. Colored dots indicate the temperatures at which impedance was measured. b) Arrhenius plot of the product of conductivity and temperature ($\sigma_{Li} \cdot T$) obtained in the heating as well as in the cooling branch, with error bars for each based on the standard deviation from independent measurements with three cells; the shown linear fit through both branches was used to obtain the activation energy E_A^{PEIS}. Since the differences of the average ($\sigma_{Li} \cdot T$) values obtained during heating vs cooling are very small, they are marked by the orange and green arrows, respectively.

Lithium Diffusion Pathways in $Li_{14}SiP_6$. In $Li_{14}SiP_6$ only lithium (in its natural isotope composition) possesses a negative scattering length (b_{Li} = –1.9 fm). This is very beneficial, since the study of experimental lithium diffusion pathways may be limited to the analysis of the distribution of negative components in nuclear density maps. Accurate nuclear density maps were extracted from the experimental structure factors and phases measured at 1023 K by the maximum entropy method (MEM). This method in general is based on the estimation of 3D scattering densities from a limited amount of information by maximizing information entropy under restraints, consistent with experimental observations.[43] Compared to Fourier analysis the MEM often delivers more accurate electron/nuclear density maps from powder diffraction datasets having "limited" statistics, i.e. termination effects and artefacts of various kinds often occur to be less pronounced in MEM evaluations.

Negative nuclear density maps for $Li_{14}SiP_6$ reconstructed from experimental structure factors using the program Dysnomia[44] are plotted in Figure 8. The MEM analysis of the nuclear densities yields 3D lithium diffusion pathways in $Li_{14}SiP_6$ involving both of the lithium sites 4*b* and 8*c*. Large sphere-like volumes on negative nuclear density maps correspond to the lithium location and are connected by well-resolved necks, which define the energy barrier for lithium diffusion in $Li_{14}SiP_6$. As illustrated, it is obvious that there is a connection between face-sharing tetrahedral and octahedral voids. Thus, neither lithium diffusion via edge-sharing tetrahedral voids nor a lithium ion hopping mechanism between edge-sharing octahedral voids could be ascertained for $Li_{14}SiP_6$. The latter is also hindered by the large interatomic distances of the adjacent Li2 atoms centered in the octahedral voids (4*b*).

The lithium motion, which is visualized in Figure 9a, occurs from the 8*c* site (Li1) to a vacancy on the 4*b* site. Interestingly the diffusion does not occur along the direct connection (shortest distance) between the two adjacent sites 8*c* and 4*b*, but proceeds via a well-defined neck (i.e. ●) with the lattice coordinates of 96*k* (0.40276 | 0.59724 | 0.305) and ..*m* site symmetry.

Assuming a quasi-classical behavior of $Li_{14}SiP_6$ at temperatures above 500 K, the experimental nuclear/probability densities can be analyzed in the form of an activation energy landscape. Since the lithium is the only negative scatterer in $Li_{14}SiP_6$ the one-particle potential (OPP) for lithium was recalculated from negative nuclear densities. Its 2D distribution in the (110, d = 1.0) plane is shown in Figure 9b. The direct Li1-Li2 pathway is characterized by an activation barrier larger than 1.4 eV (~ 135 kJ mol^{-1}) at 32*f* (0.36 | 0.64 | 0.36). A sufficiently lower activation barrier of 0.44 eV (~ 42 kJ mol^{-1}) occurs along the pathway involving the previously mentioned neck at 96*k*, i.e. Li1-●-Li2. The small activation barrier at the Li2 site is considered as an artefact of the data evaluation.

DFT-MD simulations at high temperature corroborate the mechanism for lithium diffusion in the title compound. At a simulation temperature around that of the MEM analysis (1023 K), the Li atoms are highly mobile and frequently change positions (Figure 10a-b); several instances of Li atom motion across the 8*c* → 4*b* → 8*c* sites were observed. On the other hand, the heavier Si and P atoms show thermal vibrations but the *ccp*-like anion sublattice and the $[SiP_4]^{8-}$ units remain intact otherwise, providing further

evidence for the validity of the structural model (Figure 10c).

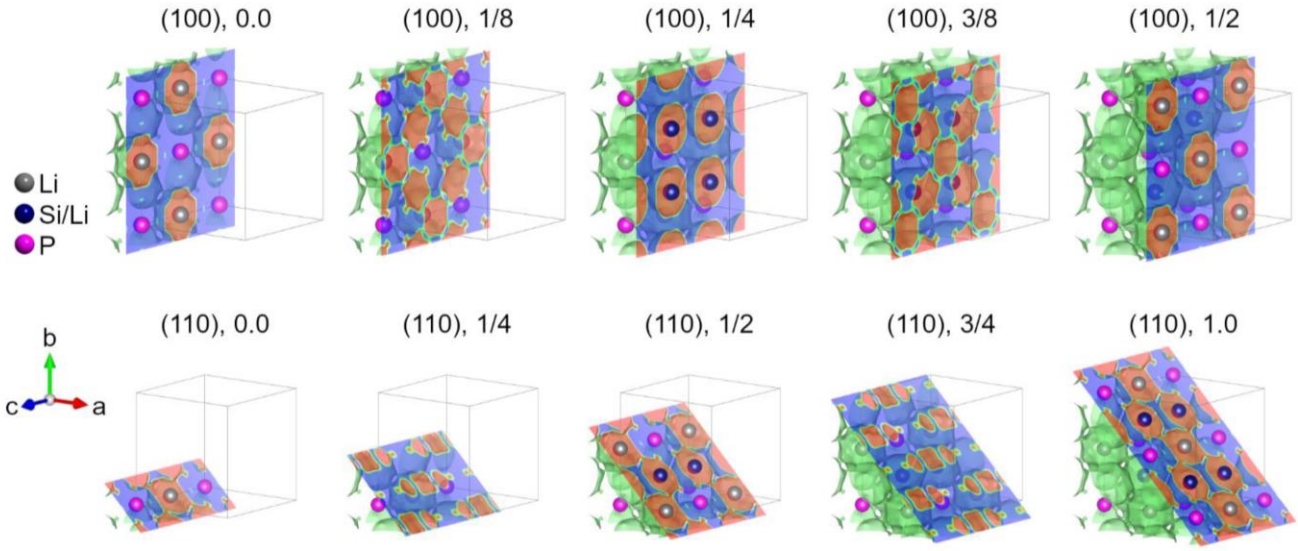

Figure 8. Negative nuclear density distribution in $Li_{14}SiP_6$ reconstructed from experimental structure factors at 1023 K using the maximum entropy method (surface threshold –0.01 fm/Å^3, cell grid 256×256×256) for various lattice planes defined by Miller indices (h, k, l) and number of position. Li, P and mixed Li/Si sites are shown as grey, pink and dark blue spheres, respectively.

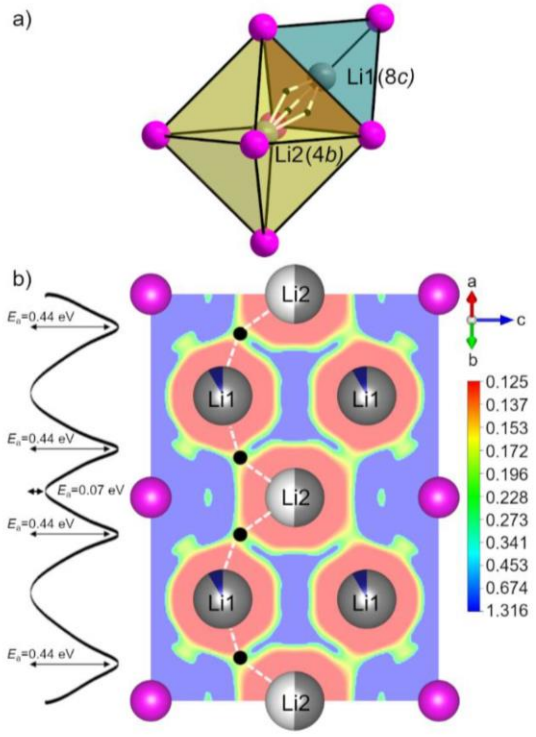

Figure 9. a) Sketch of diffusion pathways in $Li_{14}SiP_6$ between face-sharing tetrahedral (8*c*) and octahedral voids (4*b*) indicated by white lines going straight through the neck ● at the general position (0.40276 | 0.59724 | 0.305). Li and P are shown as grey and pink spheres, respectively. b) The 2D section cut (110, d = 1 plane) of the lithium one-particle-potential (OPP, red ≙ low, blue ≙ high) and its 1D section along dashed lines connecting five Li atoms in a chain Li2-●-Li1-●-Li2-●-Li1-●-Li2, where ● corresponds to the neck connecting neighboring sites with partial Li occupations. Li, P and mixed Li/Si sites are shown as grey, pink and dark blue spheres, respectively.

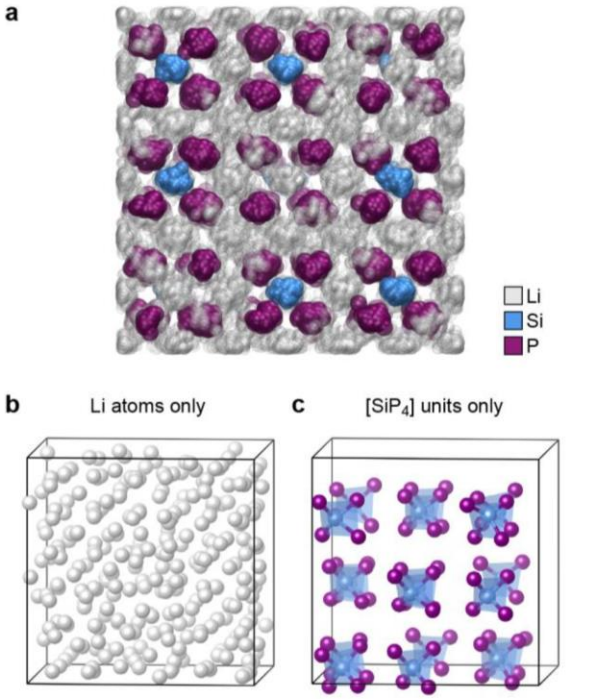

Figure 10. DFT-MD modeling of Li^+ dynamics in $Li_{14}SiP_6$. a) Snapshots from a trajectory at around 1023 K, showing atoms as partially translucent spheres (Li/Si, smaller; P, larger) and overlaying 100 equidistant images to provide an impression of the atomic mobility. The cell has been shifted by (*a*/4, *a*/4, 0) to ease visualization. b) Final image of the simulation, showing the Li atoms only, and indicating the boundaries of the

simulation cell by a thin line. c) Same but showing only the Si atoms and the P atoms in their direct vicinity; the tetrahedral $[SiP_4]^{8-}$ units remain intact during the simulation, as emphasized by shading. Structures were visualized using VMD[45] and VESTA[29]. Details of the supercell model construction are provided as Supporting Information.

4. Conclusion

The so far lithium-richest phosphidosilicate $Li_{14}SiP_6$ crystallizes in the highly symmetric space group $Fm\bar{3}m$ (no. 225). The formation of the cubic structure starts already during the mechanical milling process, as the powder X-ray diffraction experiments reveal the corresponding admittedly broadened but evident reflection pattern, and is finished upon a heat treatment at 973 K. DSC analyses and temperature-dependent neutron diffraction experiments revealed a remarkable thermal behavior of the novel compound. $Li_{14}SiP_6$ is a high-temperature phase and decomposes at temperatures below 973 K into Li_8SiP_4 and Li_3P. The decomposition and reformation proceeds within a distinct temperature range and, therefore, in order to obtain pure $Li_{14}SiP_6$ rapid cooling of the samples after the heat treatment is essential. Structural analysis combining both neutron and X-ray diffraction methods as well as static and MAS solid-state NMR spectroscopy exhibited a disorder of Si and Li atoms within the tetrahedral voids of the *ccp* of P atoms. An investigation of the negative nuclear density distribution via MEM affords a clearer understanding of the lithium ion motion within the crystal structure. The data show that the 3D lithium ion diffusion involves both 4*b* and 8*c* lithium sites, and that it occurs preferably between face-sharing tetrahedral and octahedral voids. The material shows an ionic conductivity of about $1.1 \cdot 10^{-3}$ S cm^{-1} at 298 K, an electronic conductivity of $1.6 \cdot 10^{-7}$ S cm^{-1} at 298 K and an activation energy of 30-32 kJ mol^{-1}. Hence, compared to the related compound Li_8SiP_4, the incorporation of supplementary lithium ions as well as the structural change and the occurring cation disorder within the structure result in considerably increased ionic conductivity, higher mobility and lower activation energy.[18-19]

Since the first report of Li ion conductivity in lithium phosphidotetrelates,[18] the ionic conductivity in $Li_{14}SiP_6$ has increased over two orders of magnitude within three years. With only a moderate number of known examples in hands, the reported conductivities almost match those of well-established crystalline lithium ion conductors[16], and a further enhancement of the ionic transport via manipulation by chemical, electronic and structural means is anticipated. Regarding this trend and further advantageous properties such as the low density, this class of materials may become a very promising candidate for ion conductors with interesting applications e.g. in all-solid-state batteries, namely as solid electrolyte which can be used as separator or as ion-conductive compound in the cathode electrode. However, the chemical and electrochemical stability in the composites still needs to be studied in more detail in future experiments.

ASSOCIATED CONTENT

Supporting Information. Details of the crystal structure determination, Coordination polyhedra, Phase width analysis, Differential scanning calorimetry (DSC), ^{6}Li, ^{29}Si and ^{31}P MAS NMR spectroscopy, Impedance measurement procedure and examination of cell tightness, DFT simulations.
This material is available free of charge via the Internet at http://pubs.acs.org."

AUTHOR INFORMATION

Corresponding Author

*E-mail: Thomas.faessler @lrz.tu-muenchen.de.

Author Contributions

The manuscript was written through contributions of all authors. / All authors have given approval to the final version of the manuscript. / ‡ S.S. and H.E.: These authors contributed equally to this work.

Funding Sources

The work was carried out as part of the research project ASSB coordinated by ZAE Bayern. The project is funded by the Bavarian Ministry of Economic Affairs, Regional Development and Energy.

Notes

No additional relevant notes.

ACKNOWLEDGMENT

Volker L. Deringer acknowledges a Leverhulme Early Career Fellowship and support from the Isaac Newton Trust. This work used the ARCHER UK National Supercomputing Service via EPSRC Grant EP/P022596/1.The authors greatly acknowledge Tassilo Restle for DSC measurements, and Johannes Landesfeind and Tanja Zünd for the design of the conductivity measurement cell.

REFERENCES

(1) Janek, J.; Zeier, W. G. A Solid Future for Battery Development. *Nat. Energy* **2016**, *1*, 16141.

(2) Kireeva, N.; Pervov, V. S. Materials Space of Solid-State Electrolytes: Unraveling Chemical Composition-Structure-Ionic Conductivity Relationships in Garnet-Type Metal Oxides Using Cheminformatics Virtual Screening Approaches. *Phys. Chem. Chem. Phys.* **2017**, *19*, 20904-20918.

(3) Richards, W. D.; Miara, L. J.; Wang, Y.; Kim, J. C.; Ceder, G. Interface Stability in Solid-State Batteries. *Chem. Mater.* **2016**, *28*, 266-273.

(4) West, A. R., *Solid State Chemistry and its Applications*. 2nd Ed., Student Ed.; John Wiley & Sons, Ltd: West Sussex, United Kingdom, 2014.

(5) Zeier, W. G.; Zhou, S.; Lopez-Bermudez, B.; Page, K.; Melot, B. C. Dependence of the Li-Ion Conductivity and Activation Energies on the Crystal Structure and Ionic Radii in $Li_6MLa_2Ta_2O_{12}$. *ACS Appl. Mater. Interfaces* **2014**, *6*, 10900-10907.

(6) Kraft, M. A.; Culver, S. P.; Calderon, M.; Böcher, F.; Krauskopf, T.; Senyshyn, A.; Dietrich, C.; Zevalkink, A.; Janek, J.; Zeier, W. G. Influence of Lattice Polarizability on the Ionic Conductivity in the Lithium Superionic Argyrodites Li_6PS_5X (X = Cl, Br, I). *J. Am. Chem. Soc.* **2017**, *139*, 10909-10918.

(7) Kanno, R.; Hata, T.; Kawamoto, Y.; Irie, M. Synthesis of a New Lithium Ionic Conductor, thio-LISICON–Lithium Germanium Sulfide System. *Solid State Ionics* **2000**, *130*, 97-104.

(8) Murayama, M.; Kanno, R.; Irie, M.; Ito, S.; Hata, T.; Sonoyama, N.; Kawamoto, Y. Synthesis of New Lithium Ionic Conductor thio-LISICON—Lithium Silicon Sulfides System. *J. Solid State Chem.* **2002**, *168*, 140-148.

(9) Murayama, M.; Kanno, R.; Kawamoto, Y.; Kamiyama, T. Structure of the thio-LISICON, Li_4GeS_4. *Solid State Ionics* **2002**, *154–155*, 789-794.

(10) Deiseroth, H.-J.; Kong, S.-T.; Eckert, H.; Vannahme, J.; Reiner, C.; Zaiß, T.; Schlosser, M. Li_6PS_5X: A Class of Crystalline Li-Rich Solids with an Unusually High Li^+ Mobility. *Angew. Chem., Int. Ed.* **2008**, *47*, 755-758.

(11) Kamaya, N.; Homma, K.; Yamakawa, Y.; Hirayama, M.; Kanno, R.; Yonemura, M.; Kamiyama, T.; Kato, Y.; Hama, S.; Kawamoto, K.; Mitsui, A. A Lithium Superionic Conductor. *Nat. Mater.* **2011**, *10*, 682-686.

(12) Bron, P.; Johansson, S.; Zick, K.; Schmedt auf der Günne, J.; Dehnen, S.; Roling, B. $Li_{10}SnP_2S_{12}$: An Affordable Lithium Superionic Conductor. *J. Am. Chem. Soc.* **2013**, *135*, 15694-15697.

(13) Kuhn, A.; Gerbig, O.; Zhu, C.; Falkenberg, F.; Maier, J.; Lotsch, B. V. A New Ultrafast Superionic Li-Conductor: Ion Dynamics in $Li_{11}Si_2PS_{12}$ and Comparison with other Tetragonal LGPS-Type Electrolytes. *Phys. Chem. Chem. Phys.* **2014**, *16*, 14669-14674.

(14) Kato, Y.; Hori, S.; Saito, T.; Suzuki, K.; Hirayama, M.; Mitsui, A.; Yonemura, M.; Iba, H.; Kanno, R. High-Power All-Solid-State Batteries Using Sulfide Superionic Conductors. *Nat. Energy* **2016**, *1*, 16030.

(15) Wang, B.; Chakoumakos, B. C.; Sales, B. C.; Kwak, B. S.; Bates, J. B. Synthesis, Crystal Structure, and Ionic Conductivity of a Polycrystalline Lithium Phosphorus Oxynitride with the γ-Li_3PO_4 Structure. *J. Solid State Chem.* **1995**, *115*, 313-323.

(16) Bachman, J. C.; Muy, S.; Grimaud, A.; Chang, H.-H.; Pour, N.; Lux, S. F.; Paschos, O.; Maglia, F.; Lupart, S.; Lamp, P.; Giordano, L.; Shao-Horn, Y. Inorganic Solid-State Electrolytes for Lithium Batteries: Mechanisms and Properties Governing Ion Conduction. *Chem. Rev.* **2016**, *116*, 140-162.

(17) Juza, R.; Schulz, W. Ternäre Phosphide und Arsenide des Lithiums mit Elementen der 3. und 4. Gruppe. *Z. Anorg. Allg. Chem.* **1954**, *275*, 65-78.

(18) Toffoletti, L.; Kirchhain, H.; Landesfeind, J.; Klein, W.; van Wüllen, L.; Gasteiger, H. A.; Fässler, T. F. Lithium Ion Mobility in Lithium Phosphidosilicates: Crystal Structure, ^{7}Li, ^{29}Si, and ^{31}P MAS NMR Spectroscopy, and Impedance Spectroscopy of Li_8SiP_4 and Li_2SiP_2. *Chem. Eur. J.* **2016**, *22*, 17635-17645.

(19) Eickhoff, H.; Strangmüller, S.; Klein, W.; Kirchhain, H.; Dietrich, C.; Zeier, W. G.; van Wüllen, L.; Fässler, T. F. Lithium Phosphidogermanates α- and β-Li_8GeP_4—A Novel Compound Class with Mixed Li^+ Ionic and Electronic Conductivity. *Chem. Mater.* **2018**, *30*, 6440-6448.

(20) Boyce, J. B.; Huberman, B. A. Superionic Conductors: Transitions, Structures, Dynamics. *Phys. Rep.* **1979**, *51*, 189-265.

(21) Wang, Y.; Richards, W. D.; Ong, S. P.; Miara, L. J.; Kim, J. C.; Mo, Y.; Ceder, G. Design Principles for Solid-State Lithium Superionic Conductors. *Nat. Mater.* **2015**, *14*, 1026.

(22) Carette, B.; Ribes, M.; Souquet, J. L. The Effects of Mixed Anions in Ionic Conductive Glasses. *Solid State Ionics* **1983**, *9-10*, 735-737.

(23) Deng, Y.; Eames, C.; Fleutot, B.; David, R.; Chotard, J.-N.; Suard, E.; Masquelier, C.; Islam, M. S. Enhancing the Lithium Ion Conductivity in Lithium Superionic Conductor (LISICON) Solid Electrolytes through a Mixed Polyanion Effect. *ACS Appl. Mater. Interfaces* **2017**, *9*, 7050-7058.

(24) Eickhoff, H.; Toffoletti, L.; Klein, W.; Raudaschl-Sieber, G.; Fässler, T. F. Synthesis and Characterization of the Lithium-Rich Phosphidosilicates $Li_{10}Si_2P_6$ and $Li_3Si_3P_7$. *Inorg. Chem.* **2017**, *56*, 6688-6694.

(25) Haffner, A.; Bräuniger, T.; Johrendt, D. Supertetrahedral Networks and Lithium-Ion Mobility in Li_2SiP_2 and $LiSi_2P_3$. *Angew. Chem., Int. Ed.* **2016**, *55*, 13585-13588.

(26) *WinXPOW V3.0.2.1.*, 3.0.2.1.; STOE & Cie GmbH: Darmstadt, Germany, 2011.

(27) Hoelzel, M.; Senyshyn, A.; Juenke, N.; Boysen, H.; Schmahl, W.; Fuess, H. High-Resolution Neutron Powder Diffractometer SPODI at Research Reactor FRM II. *Nucl. Instrum. Methods Phys. Res. A* **2012**, *667*, 32-37.

(28) Rodriguez-Carvajal, J.; Gonzales-Platas, J. *FullProf Suite 2. 05*, Institute Laue-Langevin Grenoble: France, 2011.

(29) Momma, K.; Izumi, F. VESTA 3 for Three-Dimensional Visualization of Crystal, Volumetric and Morphology Data. *J. Appl. Crystallogr.* **2011**, *44*, 1272-1276.

(30) Sheldrick, G. M. Crystal Structure Refinement with SHELXL. *Acta Crystallogr., Sect. C: Struct. Chem.* **2015**, *71*, 3-8.

(31) *Proteus Thermal Analysis V4.8.2*, Netzsch-Gerätebau GmbH: Selb, 2006.

(32) Yeandel, S. R.; Scanlon, D. O.; Goddard, P. Enhanced Li-Ion Dynamics in Trivalently Doped Lithium Phosphidosilicate Li_2SiP_2: A Candidate Material as a Solid Li Electrolyte. *J. Mater. Chem. A* **2019**, *7*, 3953-3961.

(33) Clark, S. J.; Segall, M. D.; Pickard, C. J.; Hasnip, P. J.; Probert, M. J.; Refson, K.; Payne, M. C. First Principles Methods Using CASTEP. *Z. Kristallogr.* **2005**, *220*, 567-570.

(34) VandeVondele, J.; Krack, M.; Mohamed, F.; Parrinello, M.; Chassaing, T.; Hutter, J. Quickstep: Fast and Accurate Density Functional Calculations Using a Mixed Gaussian and Plane Waves Approach. *Comput. Phys. Commun.* **2005**, *167*, 103-128.

(35) Zintl, E.; Brauer, G. Konstitution der Lithium-Wismut-Legierungen: 14. Mitteilung über Metalle u. Legierungen. *Z. Elektrochem.* **1935**, *41*, 297-303.

(36) Dong, Y.; DiSalvo, F. J. Reinvestigation of Trilithium Phosphide, Li_3P. *Acta Crystallogr., Sect. E: Struct. Rep. Online* **2007**, *63*, i97-i98.

(37) Zeilinger, M.; Benson, D.; Häussermann, U.; Fässler, T. F. Single Crystal Growth and Thermodynamic Stability of $Li_{17}Si_4$. *Chem. Mater.* **2013**, *25*, 1960-1967.

(38) Franke, D.; Hudalla, C.; Maxwell, R.; Eckert, H. Phosphorus-31-Cadmium-113 and Phosphorus-31-Silicon-29 CP/MAS-NMR in Inorganic Semiconductors. *J. Phys. Chem.* **1992**, *96*, 7506-7509.

(39) Vočadlo, L.; Knight, K. S.; Price, G. D.; Wood, I. G. Thermal Expansion and Crystal Structure of FeSi between 4 and 1173 K Determined by Time-of-Flight Neutron Powder Diffraction. *Phys. Chem. Miner.* **2002**, *29*, 132-139.

(40) Senyshyn, A.; Boysen, H.; Niewa, R.; Banys, J.; Kinka, M.; Ya, B.; Adamiv, V.; Izumi, F.; Chumak, I.; Fuess, H. High-Temperature Properties of Lithium Tetraborate $Li_2B_4O_7$. *J. Phys. D: Appl. Phys.* **2012**, *45*, 175305.

(41) Baran, V.; Dolotko, O.; Mühlbauer, M. J.; Senyshyn, A.; Ehrenberg, H. Thermal Structural Behavior of Electrodes in Li-Ion Battery Studied In Operando. *J. Electrochem. Soc.* **2018**, *165*, A1975-A1982.

(42) Hodge, I. M.; Ingram, M. D.; West, A. R. Impedance and Modulus Spectroscopy of Polycrystalline Solid Electrolytes. *J. Electroanal. Chem.* **1976**, *74*, 125-143.

(43) Gilmore, C. Maximum Entropy and Bayesian Statistics in Crystallography: A Review of Practical Applications. *Acta Crystallogr., Sect. A: Found. Crystallogr.* **1996**, *52*, 561-589.

(44) Momma, K.; Ikeda, T.; Belik, A. A.; Izumi, F. Dysnomia, a Computer Program for Maximum-Entropy Method (MEM) Analysis and its Performance in the MEM-Based Pattern Fitting. *Powder Diffr.* **2013**, *28*, 184-193.

(45) Humphrey, W.; Dalke, A.; Schulten, K. VMD: Visual Molecular Dynamics. *J. Mol. Graphics* **1996**, *14*, 33-38.

Supporting Information

Fast Ionic Conductivity in the Lithium-Rich Phosphidosilicate $Li_{14}SiP_6$

Stefan Strangmüller,[a, ‡] Henrik Eickhoff,[a, ‡] David Müller,[a] Wilhelm Klein,[a] Gabriele Raudaschl-Sieber,[a] Holger Kirchhain,[b] Christian Sedlmeier,[c] Volodymyr Baran,[d] Anatoliy Senyshyn,[d] Volker L. Deringer,[e] Leo van Wüllen,[b] Hubert A. Gasteiger,[c] and Thomas F. Fässler*,[a]

Content

Details of the crystal structure determination of $Li_{14}SiP_6$

Table S1. Atomic coordinates for $Li_{14}SiP_6$ from co-refinement at 300 K.

atom	wyckoff positions	*x*	*y*	*z*	s.o.f.
P1	4*a*	0	0	0	
Si1	8*c*	1/4	1/4	1/4	0.08329(1)
Li1	8*c*	1/4	1/4	1/4	0.91527(1)
Li2	4*b*	1/2	0	0	0.50264(1)

Table S2. Anisotropic displacement parameters ($Å^2$) for $Li_{14}SiP_6$ from co-refinement at 300 K.

atom	U_{11}	U_{22}	U_{33}	U_{23}	U_{13}	U_{12}
P1	0.04001(1)	0.04001(1)	0.04001(1)	0.0	0.0	0.0
Si1	0.04957(1)	0.04957(1)	0.04957(1)	0.0	0.0	0.0
Li1	0.04957(1)	0.04957(1)	0.04957(1)	0.0	0.0	0.0
Li2	0.12027(1)	0.12027(1)	0.12027(1)	0.0	0.0	0.0

Table S3. Selected interatomic distances in $Li_{14}SiP_6$ from co-refinement at 300 K.

atom pair			*d* / Å	atom pair			*d* / Å
P1	Si1/Li1	8×	2.5718(1)	Si1/Li1	P1	4×	2.5718(1)
	Li2	6×	2.9696(1)		Li2	4×	2.5718(1)
Li2	Si1/Li1	8×	2.5718(1)		Si1/Li1	6×	2.9696(1)
	P1	6×	2.9696(1)				

Results of the Rietveld structure refinement of $Li_{14}SiP_6$ via powder neutron diffraction at 4 K

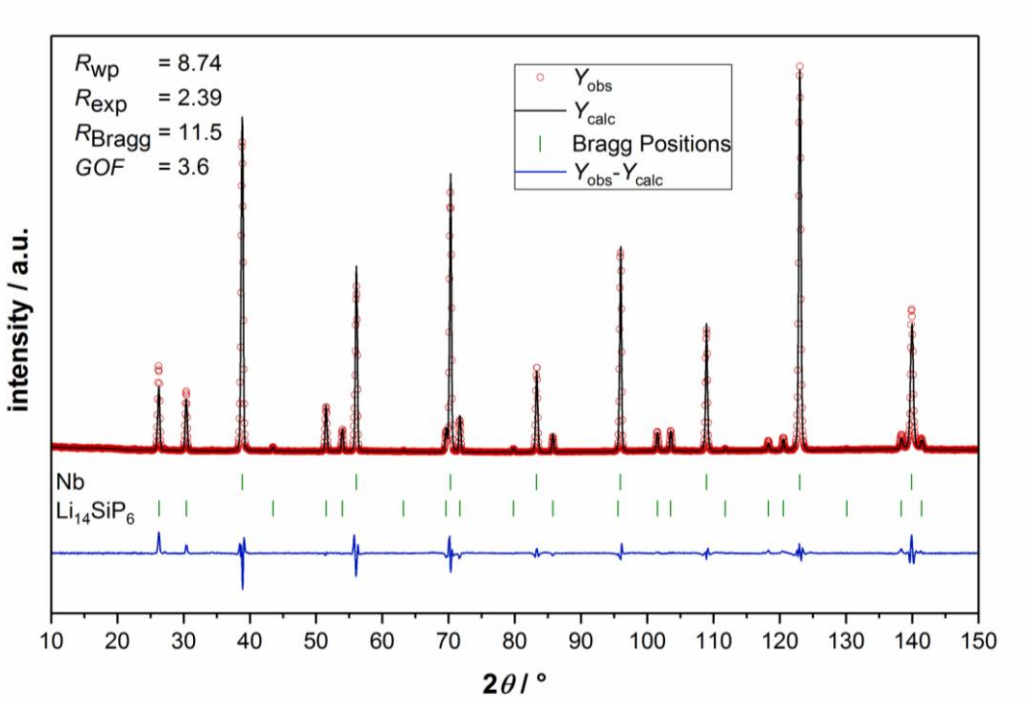

Figure S1. Rietveld analysis of the powder neutron diffraction pattern of $Li_{14}SiP_6$ at 4 K. Red circles indicate observed intensities Y_{obs}, black lines show calculated intensities Y_{calc}, blue lines reveal the difference between observed and calculated intensities, and green marks indicate Bragg positions of $Li_{14}SiP_6$ and Nb (ampoule).

Table S4. Details of the Rietveld structure refinement of $Li_{14}SiP_6$ from powder neutron diffraction measurements at 4 K.

empirical formula	$Li_{2.33}Si_{0.17}P$
T / K	4
formula weight / g mol^{-1}	51.86
space group (no.)	$Fm\bar{3}m$ (225)
unit cell parameters / Å	a = 5.91566(6)
Z	4
V / Å^3	207.019(3)
$\rho_{calc.}$ / g cm^{-3}	1.664
2θ range / deg	9.0000-150.0000
R_p	0.0609
R_{wp}	0.0874
R_{exp}	0.0239
X^2	13.4
GOF	3.6
R_{Bragg}	11.5
R_f	5.79
depository no.	CSD-1915817

Table S5. Atomic coordinates for $Li_{14}SiP_6$ at 4 K.

atom	wyckoff positions	*x*	*y*	*z*	s.o.f.
P1	4*a*	0	0	0	
Si1	8*c*	1/4	1/4	1/4	0.0834(2)
Li1	8*c*	1/4	1/4	1/4	0.916(2)
Li2	4*b*	1/2	0	0	0.505(7)

Table S6. Anisotropic displacement parameters ($Å^2$) for $Li_{14}SiP_6$ at 4 K.

atom	U_{11}	U_{22}	U_{33}	U_{23}	U_{13}	U_{12}
P1	0.0256(6)	0.0256(6)	0.0256(6)	0.0	0.0	0.0
Si1	0.040(2)	0.040(2)	0.040(2)	0.0	0.0	0.0
Li1	0.040(2)	0.040(2)	0.040(2)	0.0	0.0	0.0
Li2	0.131(9)	0.131(9)	0.131(9)	0.0	0.0	0.0

Table S7. Selected interatomic distances in $Li_{14}SiP_6$ at 4 K.

atom pair			*d* / Å	atom pair			*d* / Å
P1	Si1/Li1	8×	2.5616(1)	Si1/Li1	P1	4×	2.5616(1)
	Li2	6×	2.9578(1)		Li2	4×	2.5616(1)
Li2	Si1/Li1	8×	2.5616(1)		Si1/Li1	6×	2.9578(1)
	P1	6×	2.9578(1)				

Results of the single crystal structure determination of $Li_{14}SiP_6$

Table S8. Crystallographic data and refinement parameters of $Li_{14}SiP_6$ from single crystal X-ray diffraction measurements at 123 K.

empirical formula	$Li_{2.33}Si_{0.17}P$
formula weight / g mol^{-1}	51.86
crystal size / mm^3	0.05 × 0.045 × 0.03
crystal color	orange
T / K	123(2)
crystal system	cubic
space group (no.)	$Fm\bar{3}m$ (225)
unit cell parameters / Å	a = 5.9253(7)
Z	4
V / Å^3	208.03(7)
$\rho_{calc.}$ / g cm^{-3}	1.655
μ / mm^{-1}	1.347
F(000) / e	146
ϑ range / deg	5.963 – 40.236
index range (hkl)	$-10 \le h \le 10$, $-10 \le k \le 10$, $-10 \le l \le 10$
reflections collected	554
independent reflections	54
R_{int}	0.0146
reflections with $I > 2\sigma(I)$	48
absorption correction	multi-scan
data / restraints / parameters	54 / 0 / 5
goodness-of-fit on F^2	1.191
R_1, wR_2 (all data)	0.0513, 0.0900
R_1, wR_2 [$I > 2\sigma(I)$]	0.0401, 0.0856
largest diff. peak and hole (e Å^{-3})	0.442 / −0.528
depository no.	CSD-1915822

Table S9. Atomic coordinates for $Li_{14}SiP_6$.

atom	wyckoff positions	*x*	*y*	*z*	s.o.f.
P1	4*a*	0	0	0	
Si1	8*c*	1/4	1/4	1/4	0.0833
Li1	8*c*	1/4	1/4	1/4	0.9167
Li2	4*b*	1/2	0	0	0.5

Table S10. Anisotropic displacement parameters ($Å^2$) for $Li_{14}SiP_6$.

atom	U_{11}	U_{22}	U_{33}	U_{23}	U_{13}	U_{12}
P1	0.0267(7)	0.0267(7)	0.0267(7)	0.0	0.0	0.0
Si1	0.019(1)	0.019(1)	0.019(1)	0.0	0.0	0.0
Li1	0.019(1)	0.019(1)	0.019(1)	0.0	0.0	0.0
Li2	0.09(2)	0.09(2)	0.09(2)	0.0	0.0	0.0

Table S11. Selected interatomic distances in $Li_{14}SiP_6$.

atom pair			*d* / Å	atom pair			*d* / Å
P1	Si1/Li1	8×	2.5657(3)	Si1/Li1	P1	4×	2.5657(3)
	Li2	6×	2.9627(4)		Li2	4×	2.5657(3)
Li2	Si1/Li1	8×	2.5657(3)		Si1/Li1	6×	2.9627(4)
	P1	6×	2.9627(4)				

Coordination polyhedra of $Li_{14}SiP_6$

In $Li_{14}SiP_6$ the disordered atoms (Li1/Si1) are tetrahedrally coordinated by four P1 and four Li2 atoms, each building up a cubic coordination sphere. The atoms Li2 are centered in a perfectly cubic arrangement of mixed atoms Li1/Si1. In the second coordination sphere Li2 is octahedrally coordinated by six atoms P1.

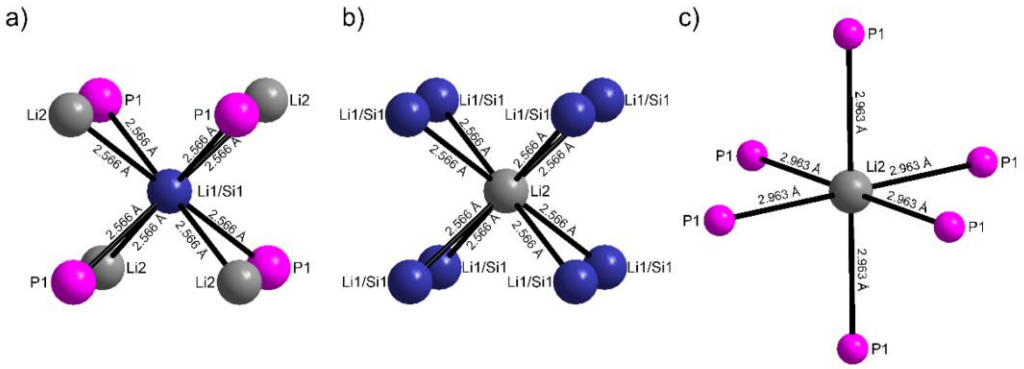

Figure S2. Coordination polyhedra of Si and Li atoms in the crystal structure of $Li_{14}SiP_6$ according to a single crystal structure determination at 123 K. The nearest neighbors of the atoms Si1/Li1 and Li2 are arranged in a highly symmetric cubic coordination. In the next nearest coordination sphere Li2 is surrounded by P atoms in an octahedral arrangement.

Phase width analysis

To investigate a possible phase width regarding the amount of lithium and silicon, respectively, a series of powder X-ray diffraction measurements (Figure S3) followed by Rietveld refinements of the recorded diffraction patterns were carried out. The stoichiometry of the compounds should correlate with the applied amounts of the used reagents, and thus, are expected to be 1:1 ($Li_{14}SiP_6$: Li_8SiP_4) for "$Li_{11}SiP_5$", 1:1 ($Li_{14}SiP_6$: Li_3P) for "$Li_{17}SiP_7$" and 1:2 ($Li_{14}SiP_6$: Li_3P) for "$Li_{20}SiP_8$". The obtained values of the corresponding primary-phase-to-side-phase ratios are in good agreement with the expected results. The observed deviation could either be the result of various uncertainties during the measurement or the refinement, or a phase width or solid solution may be present (Table S12). Considering the latter cases, a high amount of Si within the structure causes a lower absolute number of atoms per formula unit and entails additional short, covalent Si-P bonds, both resulting in a smaller unit cell. The cubic cell parameter for $Li_{14}SiP_6$ refined for the aforementioned samples is the largest in pure $Li_{14}SiP_6$, but slightly smaller for the remaining three samples. Therefore a phase width at the Li_3P-rich side can be excluded, while at the Li_3P-poor side a Si-enriched composition "$Li_{14-4x}Si_{1+x}P_6$" seems to be possible. However, the extent of Si enrichment without structural changes must be small, because even in "$Li_{11}SiP_5$" the lattice parameter is close to that of $Li_{14}SiP_6$. It is also considerably larger than half of the Li_8SiP_4 cell parameter, which would correspond x = 0.5 in the composition stated above.

Analogous to the annealed samples the corresponding cell parameters of the reactive mixtures after ball milling have been indexed. The cell parameters of the reactive mixtures are in general distinctly larger than the corresponding parameters of the annealed samples. In combination with the crystalline, elemental Si in the sample this could be a hint for a metastable solid solution with an even higher amount of lithium. During the following annealing process the elemental Si is incorporated into the structure ending up in a smaller unit cell caused by the emerging covalent Si-P interactions (Figure S4 and Table S13).

Powder X-ray diffraction patterns and Rietveld refinement results

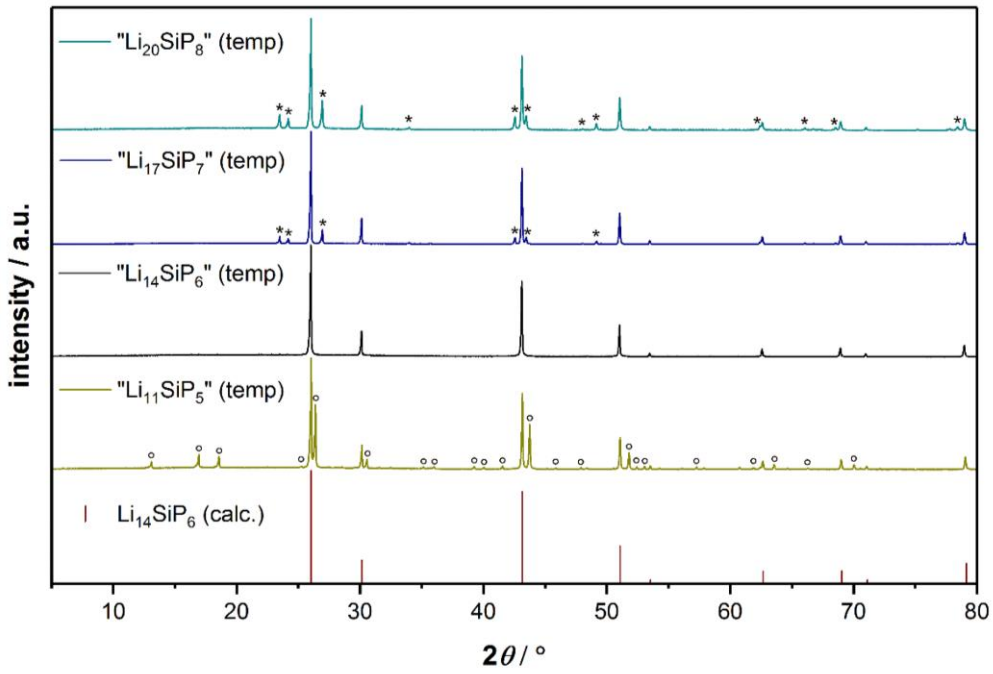

Figure S3. Powder X-ray diffraction patterns of the reactive mixtures "$Li_{20}SiP_8$" (cyan), "$Li_{17}SiP_7$ (navy)", "$Li_{14}SiP_6$" (black) and "$Li_{11}SiP_5$" (dark yellow) after annealing at 973 K for 6 h and subsequent quenching. Li_3P (*), Li_8SiP_4 (°) and WC (#) occur as side-phases. The calculated reflex positions and corresponding intensities of $Li_{14}SiP_6$ are shown in red.

Table S12. Rietveld refinement results of the reactive mixtures after annealing.

nominal compositions	product after annealing	relative portions of the obtained compounds
$Li_{11}SiP_5$	$Li_{14}SiP_6$ + Li_8SiP_4	1.00(1) : 0.73(1); expected 1:1
$Li_{14}SiP_6$	$Li_{14}SiP_6$	1.00(2)
$Li_{17}SiP_7$	$Li_{14}SiP_6$ + Li_3P	1.00(1) : 1.10(3); expected 1:1
$Li_{20}SiP_8$	$Li_{14}SiP_6$ + Li_3P	1.00(1) : 2.33(2); expected 1:2

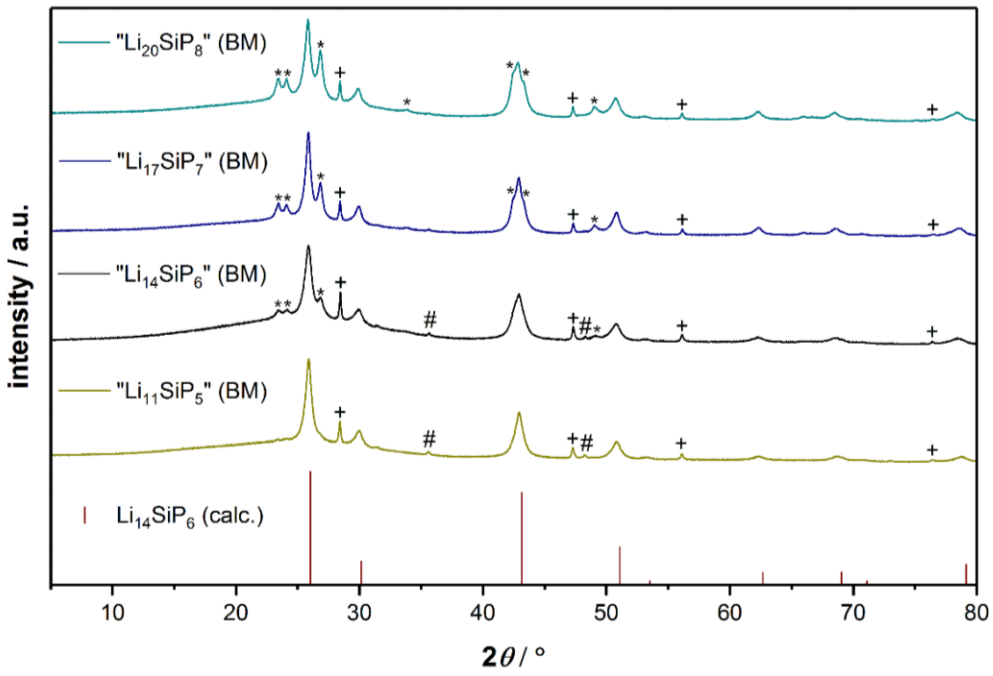

Figure S4. X-ray powder diffraction patterns of the reactive mixtures "$Li_{20}SiP_8$" (cyan), "$Li_{17}SiP_7$ (navy)", "$Li_{14}SiP_6$" (black) and "$Li_{11}SiP_5$" (dark yellow) obtained via ball milling of the elements. Li_3P (*), Si (+) and WC (#) occur as side-phases. The calculated reflex positions and corresponding intensities of $Li_{14}SiP_6$ are shown in red.

Table S13. List of refined cell parameters of the reactive mixtures "$Li_{11}SiP_5$", "$Li_{14}SiP_6$", "$Li_{17}SiP_7$" and "$Li_{20}SiP_8$" before and after annealing.

nominal composition	cell parameter after BM	cell parameter after annealing
$Li_{11}SiP_5$	5.947(2) Å	5.93291(8) Å
$Li_{14}SiP_6$	5.957(3) Å	5.9380(2) Å
$Li_{17}SiP_7$	5.956(2) Å	5.9361(1) Å
$Li_{20}SiP_8$	5.961(2) Å	5.9356(1) Å

The cell parameters of the reactive mixtures have been evaluated via the "Index and Refine" WinXPOW software-tool, and the cell parameters of the annealed samples have been determined by Rietveld refinement executed with FullProf.

Differential scanning calorimetry (DSC)

DSC analysis was carried out from room temperature to 1023 K. Starting from the crystalline, disordered phase $Li_{14}SiP_6$ leads to a strong and exothermal signal with an onset temperature of 790.9 K (Figure S5), indicating the formation of Li_8SiP_4 as seen during powder neutron diffraction at elevated temperatures. However, the effect occurs at a much higher temperature compared to the above mentioned neutron diffraction data. Hence, also the second, endothermal thermal effect with an onset temperature of 936.6 K representing the reformation of $Li_{14}SiP_6$ appears deferred. As observed during supplementary experiments, slow cooling of the sample induces the decomposition of the high-temperature phase into Li_8SiP_4 and Li_3P. However, in the DSC measurement, due to the relatively high cooling rate of 10 K min^{-1} the decomposition of $Li_{14}SiP_6$ is eluded, which was also observed in the neutron diffraction experiments. This leads to a reappearance of the decomposition (onset temperature 746.2 K) as well as of the formation signal (onset temperature 935.8 K) during the second heating cycle. The diffraction pattern of $Li_{14}SiP_6$ after the DSC measurement shows the preservation of almost phase-pure $Li_{14}SiP_6$. Only extremely weak reflections of Li_3P and Li_8SiP_4 are observed (Figure S6).

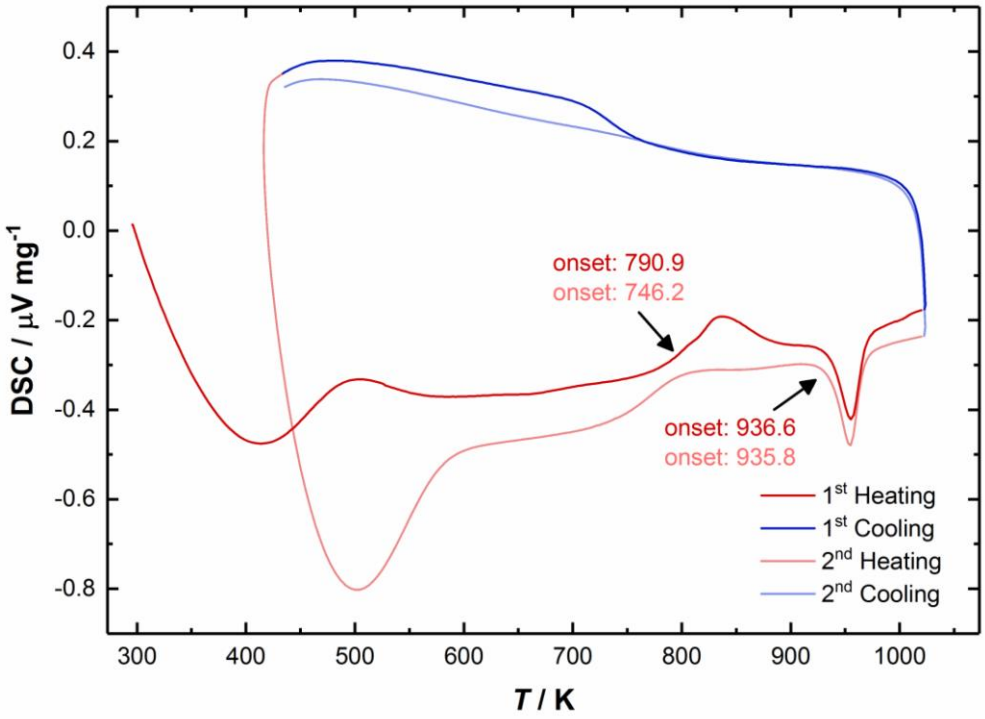

Figure S5. DSC thermogram of $Li_{14}SiP_6$. The arrows and numbers indicate the onset temperatures of the corresponding thermal effects.

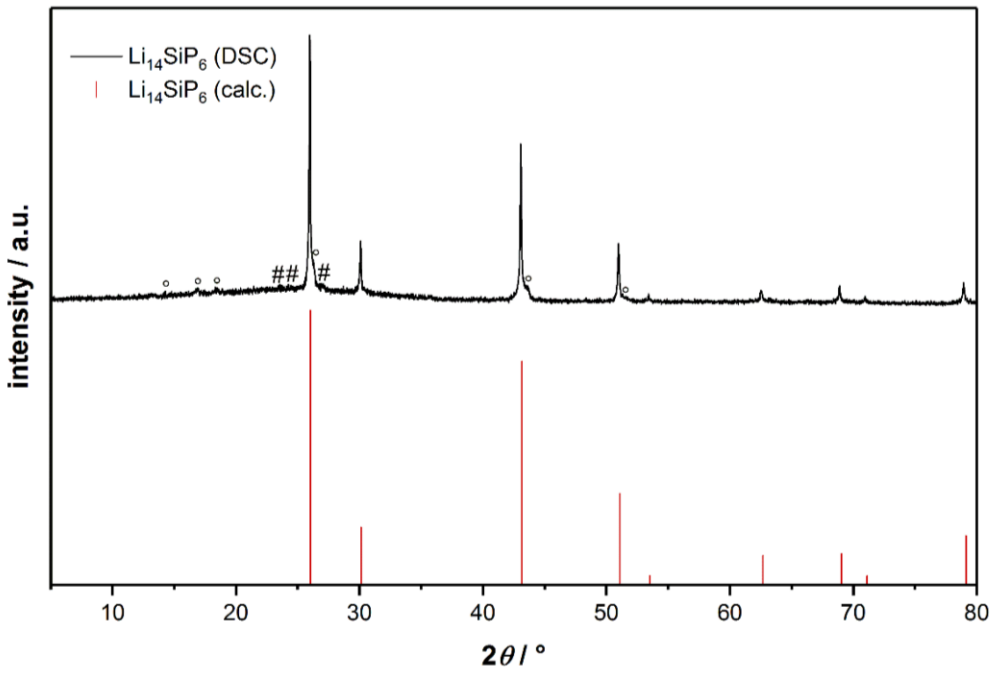

Figure S6. Powder X-ray diffractogram of crystalline $Li_{14}SiP_6$ (black) after DSC measurement. Li_3P (*) and Li_8SiP_4 (°) occur as side phases. The calculated reflex positions and corresponding intensities of $Li_{14}SiP_6$ are shown in red.

^{6}Li, ^{29}Si, and ^{31}P MAS NMR spectroscopy

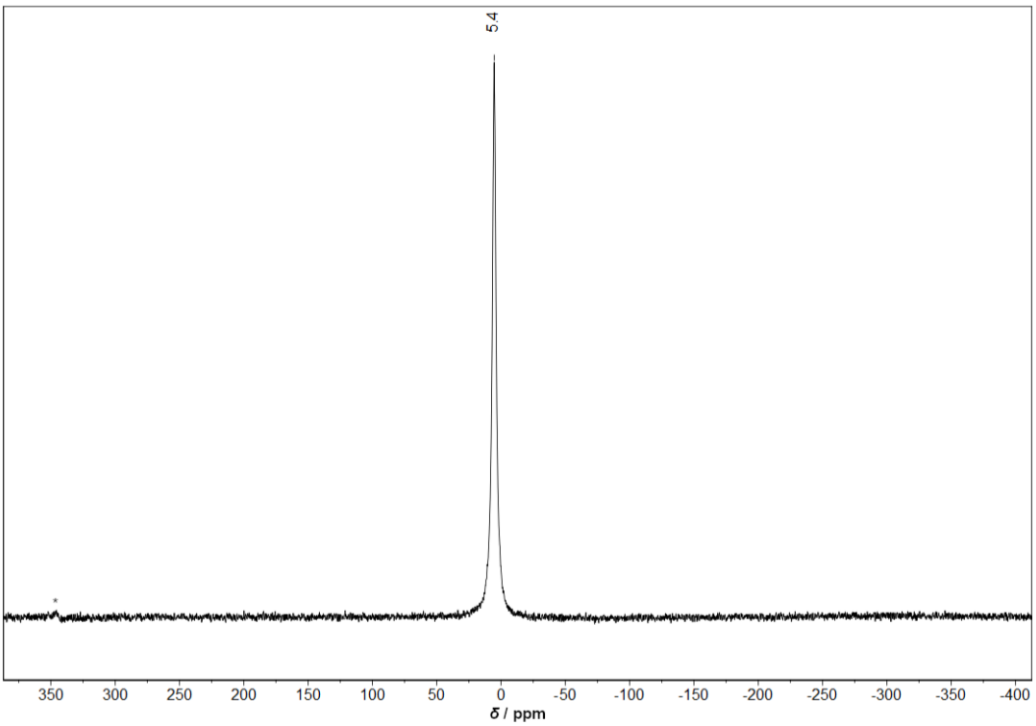

Figure S7. ^{6}Li MAS NMR spectrum of $Li_{14}SiP_6$. Spinning sideband marked by *.

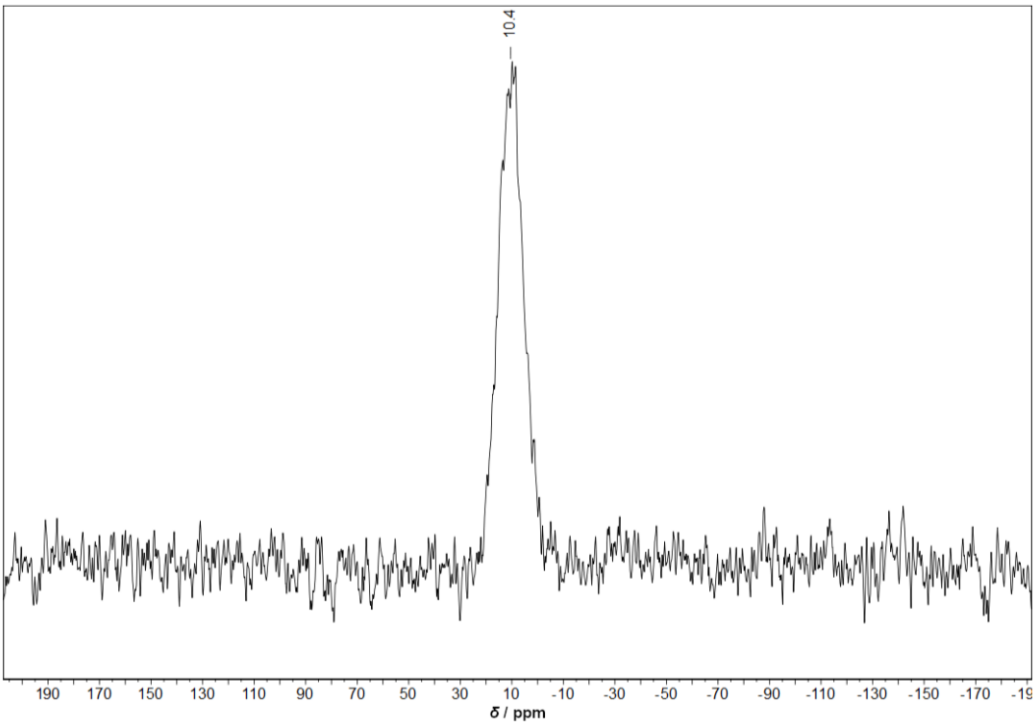

Figure S8. ^{29}Si MAS NMR spectrum of $Li_{14}SiP_6$.

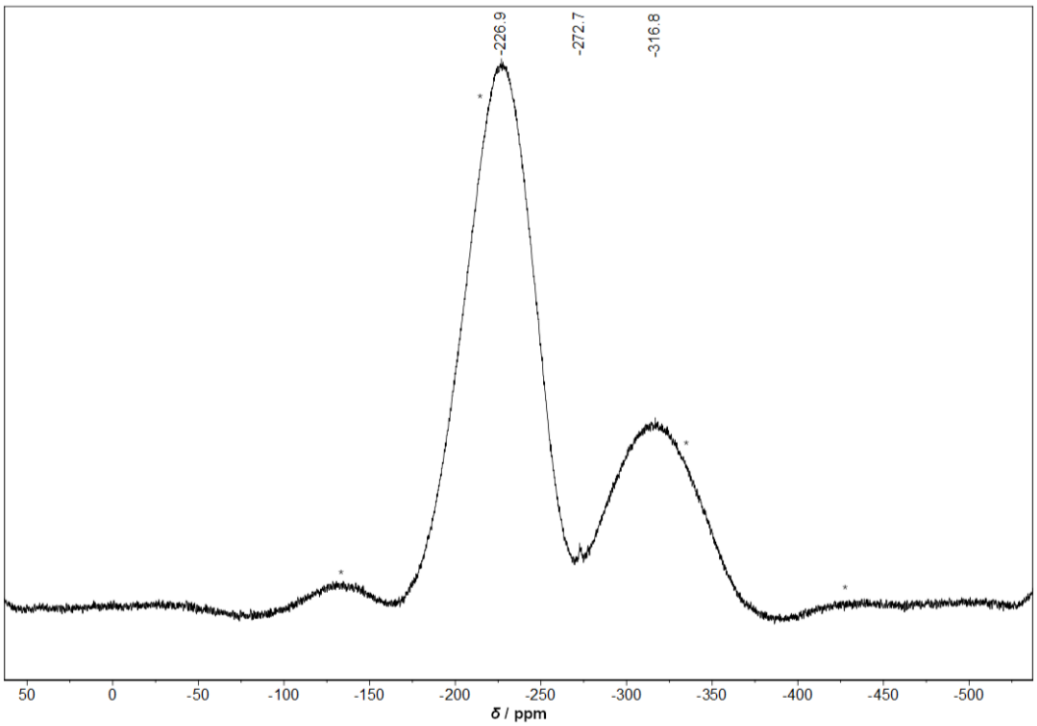

Figure S9. ^{31}P MAS NMR spectrum of $Li_{14}SiP_6$ (12 kHz). Spinning sidebands marked by *.

Regarding the ^{31}P MAS NMR spectrum recorded at 15 kHz the two broad, distinct signals are slightly shifted (−227.3 and −314.9 ppm), and the ratio of the total integrated intensity of the two signals is 2.5:1 (Figure S10). These deviations are assumed to be a consequence of the extreme broadening of the signals. The low intense signal at −272.7 ppm indicates the presence of small amounts of Li_3P (−278 ppm) in both spectra.[1, 2]

The ^{31}P MAS NMR spectrum of $Li_{14}SiP_6$ after impedance spectroscopy and DC conductivity measurements shows an additional signal at 9.9 ppm indicating the formation of phosphates during data collection.[3-5]

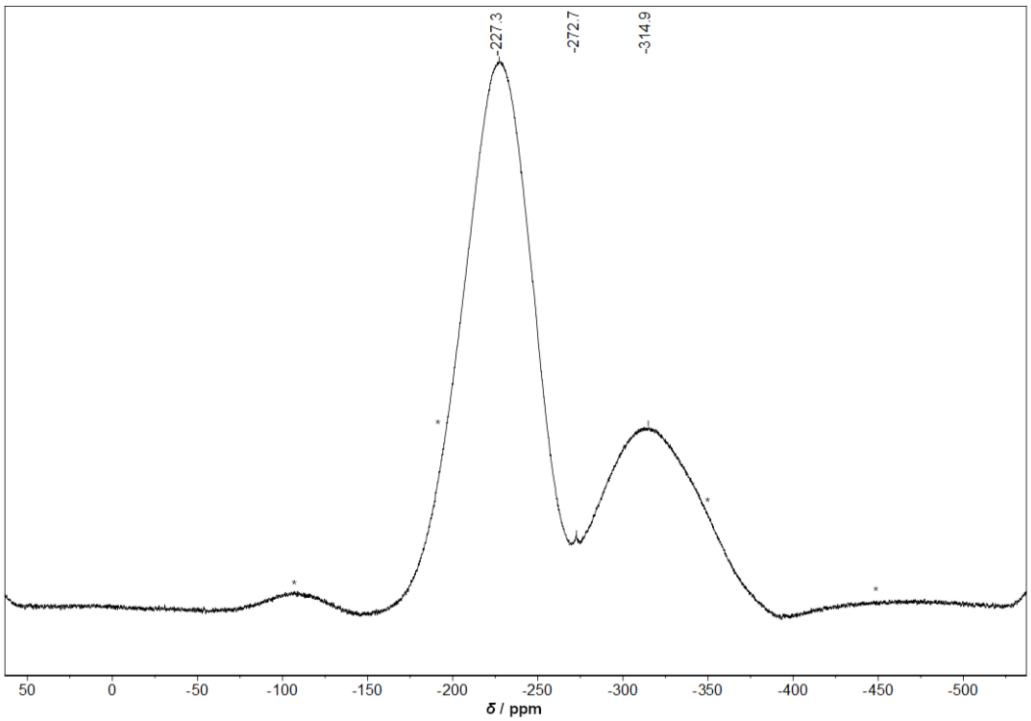

Figure S10. ^{31}P MAS NMR spectrum of $Li_{14}SiP_6$ (15 kHz). Spinning sidebands marked by *.

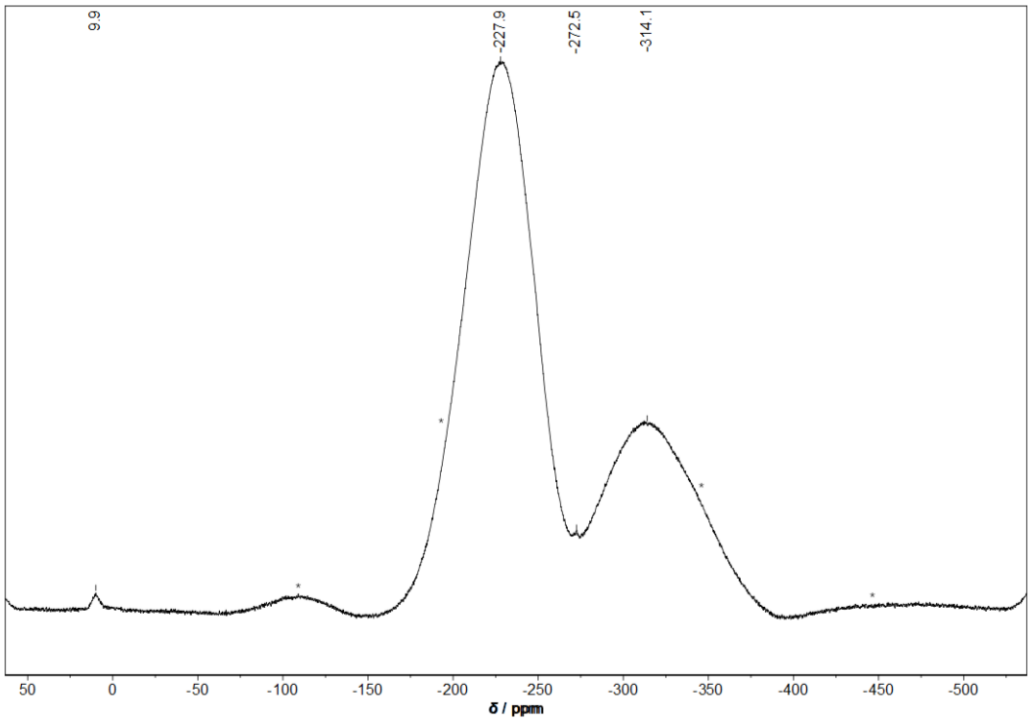

Figure S11. ^{31}P MAS NMR spectrum of $Li_{14}SiP_6$ (15 kHz) after impedance spectroscopy. Spinning sidebands marked by *.

Impedance measurement procedure and examination of cell tightness

The impedance analysis approach in this work comprises two different measurement types for each cell. First, lithium ion conductivity at room temperature was measured inside an Ar filled glovebox. Secondly, the cell was taken out of the glovebox and temperature dependent measurements were performed in a climate chamber in order to determine E_A^{PEIS}. Thereby, one cycle comprises heating the cell from 298 K to 353 K and a subsequent cool down to 273 K. During a cycle, the impedance was measured two times each at 298, 313 and 333 K (once during heating and once during cooling) and one time each at 353 and 273 K, as shown in Figure S12a. One complete measurement comprises four experimental steps: cycle 0, which is the measurement at 298 K inside the glovebox, followed by cycles 1, 2 and 3, which are temperature dependent measurements outside the glovebox according to the described temperature ramp. The quality of the sealing of the cell against ambient air was evaluated by comparing ionic conductivities of cycle 0 taken at 298 K inside the glovebox with the first 298 K measurement points of cycles 1–3 taken outside the glovebox, marked by the red diamonds in Figure S12a. Comparing the thus obtained conductivities, a slight decrease in conductivity is observed when operating the cell outside the glovebox (≈ 8% over the course of ≈ 34 h; see Figure S12b), presumably due imperfect cell sealing against ambient air which might lead to decomposition reactions of the solid electrolyte with ambient air. Hence, for determining E_A^{PEIS} only cycle 1 of three independent measurements was used. In this case, the experimental error in the conductivity due to cell leakiness was estimated to be approximately 8%, compared to measuring under inert gas atmosphere.

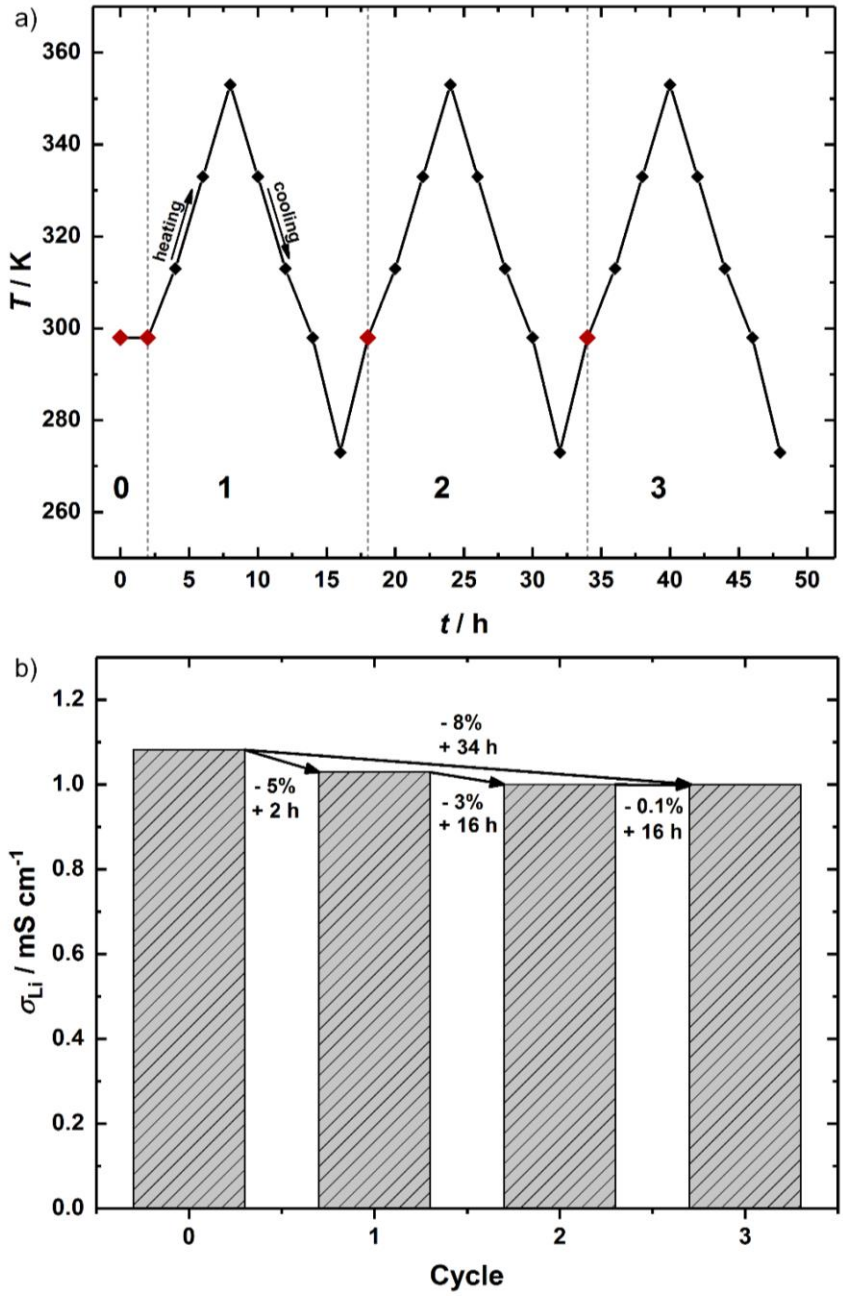

Figure S12. a) Temperature versus time profile of the lithium ion conductivity of $Li_{14}SiP_6$ in order to assess the sealing quality of the cell against ambient air. Black diamonds represent impedance measurements during heating and cooling cycles, red diamonds mark the points taken at 298 K, either still within the Ar-filled glovebox (cycle 0) or at the beginning of subsequent temperature cycles (cycles 1-3) during which the cell is exposed to ambient air. Individual cycles are indicted by numbers and separated by dashed lines. b) Lithium ion conductivity progression from cycle 0-1 (at 298 K), including the relative conductivity loss from cycle to cycle over the specified amount of time.

DFT simulations (I): A supercell model for $Li_{14}SiP_6$

Despite its formally simple crystallographic description (three Wyckoff sites in the highly symmetric space group $Fm\bar{3}m$), the title compound has a rather intricate structure, because two of the sites show mixed and/or partial occupations. In the conventional unit cell (as given by the refinement of the diffraction data; Table 1), there are four formula units of $Li_{2.33}Si_{0.17}P$. However, to carry out first-principles computations one needs to construct a discrete structural model in which all atomic positions are fully occupied (thereby lowering the symmetry of the simulation cell to $P1$). We decided to construct a 378-atom cell based on a 3×3×3 expansion (with a resulting lattice parameter of 17.74698 Å), which preserves the cubic cell shape and allows us to achieve an approximately even distribution of Si atoms. The process is illustrated in Figure S13.

The distribution of Li atoms on the 4*b* and 8*c* sites was evaluated based on single-point DFT computations (Figure S13), performed using CASTEP 8.0[6] and on-the-fly pseudopotentials. The Perdew-Burke-Ernzerhof (PBE) functional[7] was employed to treat exchange and correlation. Reciprocal space was sampled at the Γ point, and a Gaussian smearing scheme with width 0.2 eV was applied. The electronic convergence criterion was 10^{-7} eV per atom. The cut-off energy was 500 eV, and an extrapolation scheme was used to counteract finite-basis effects[8]. The most favorable occupation model (set as energy zero in Figure S14) was used as a starting point for subsequent DFT-MD simulations.

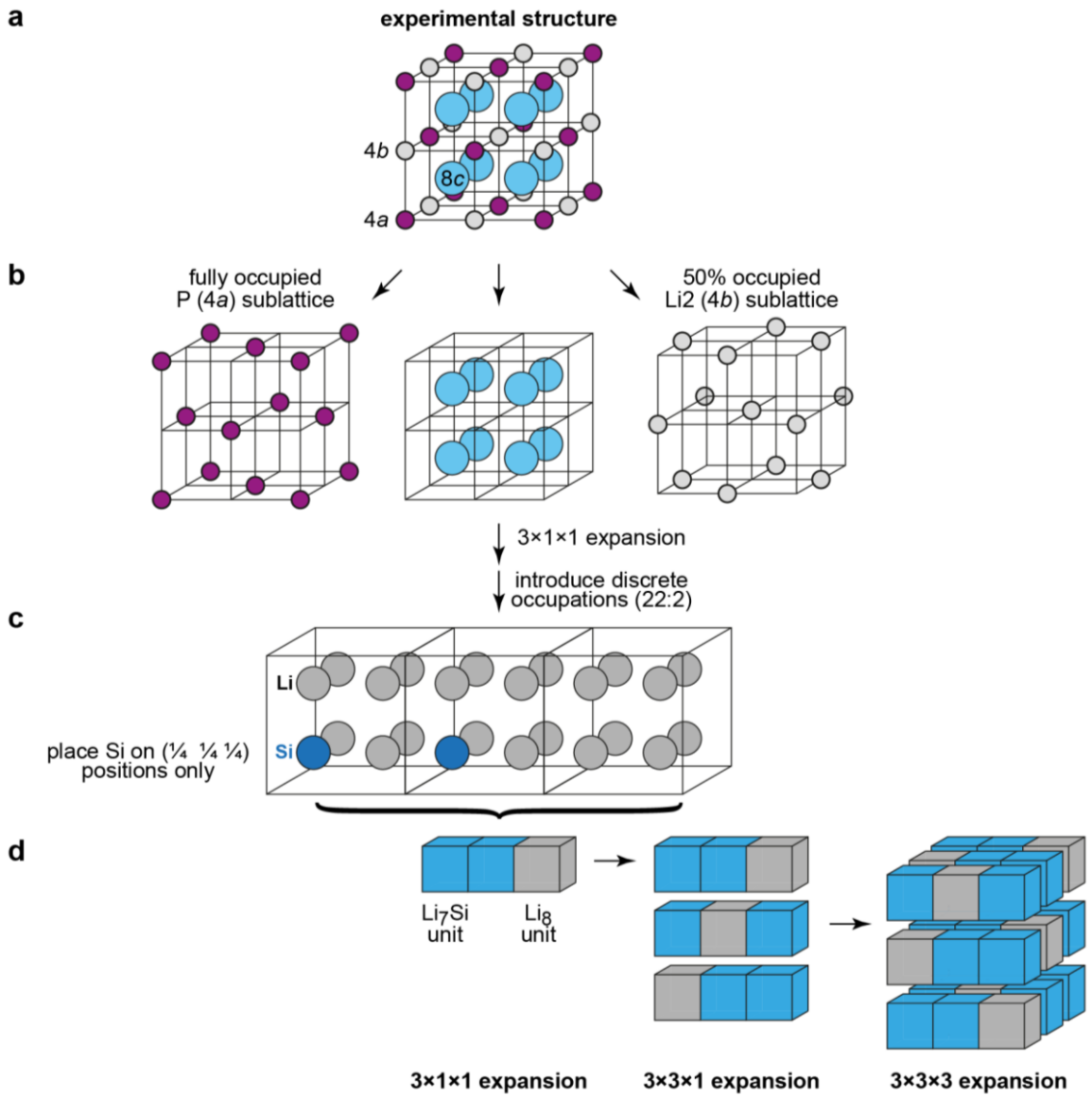

Figure S13. The construction of a discrete structural model to enable the computational modeling of $Li_{14}SiP_6$. a) The experimental structure, in which the 4*a* (occupied by P), 4*b* (half-occupied by Li) and 8*c* (mixed occupation of Li/Si) sites are relevant. b) Sketch of the three separate sublattices. The 4*a* site is taken to be fully occupied (*left*), and for the moment we assume a fully random occupation on 4*b* (*right*), using a random number generator. The 8*c* site is the most challenging one, as we need to distribute Li and Si atoms on it, in a way that preserves the stoichiometric composition. c) Using a 3×1×1 expansion, the correct composition (22 Li sites and 2 Si sites) can be achieved. d) In order to arrive at a cubic and more isotropic structural model, we create a 3×3×3 expansion of the conventional unit cell as shown.

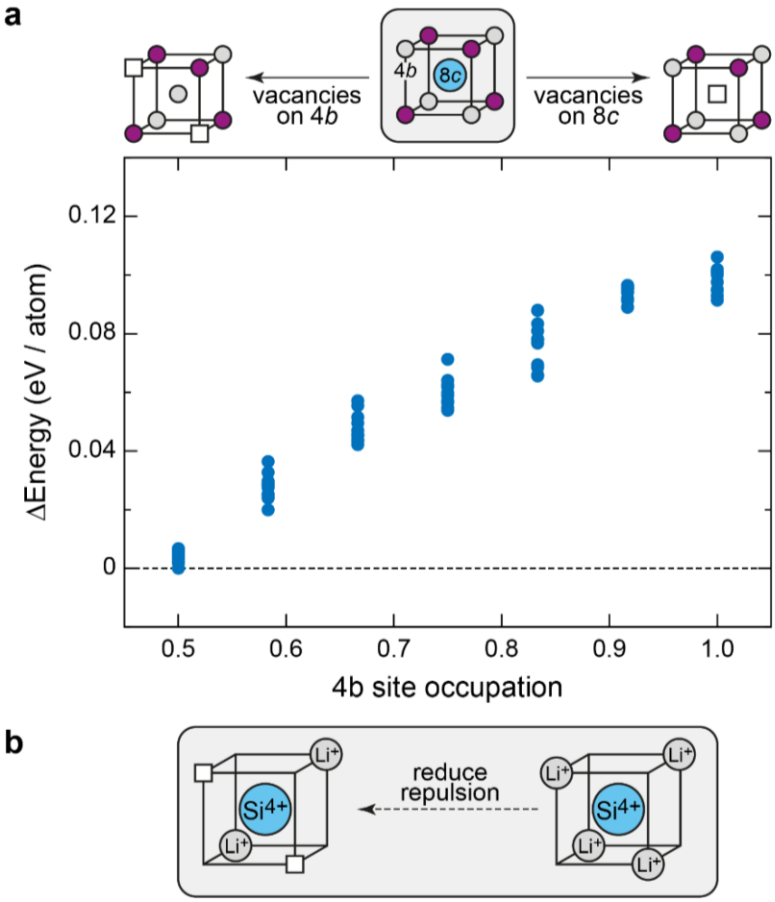

Figure S14. Probing possible 8*c* → 4*b* intermixing of Li atoms, which is not observed in the refinement at $T = 4$ K, but which is needed for the proposed conduction mechanism. a) Energy per atom from DFT total-energy computations, given relative to the most stable structure, for an ensemble of 7 × 10 randomly occupied structural models that differ in how the Li atoms are distributed on the 8*c* and 4*b* sites. b) Simplified sketch rationalizing the preference for vacancies on 4*b* rather than 8*c* in the ground state.

DFT simulations (II): Molecular dynamics simulations

MD simulations in the NVT ensemble were carried out using the mixed Gaussian and plane-wave DFT approach as implemented in cp2k / Quickstep[9]. We used Goedecker-Teter-Hutter pseudopotentials[10] and the local density approximation. The time step was 0.5 fs throughout. The temperature was controlled using the canonical sampling through velocity rescaling thermostat[11].

Starting from the most favorable structural model determined by total-energy computations (see above), MD simulations were performed subsequently at 300, 500, 700, 900, 1100, and 1300 K. These initial simulations were run for 6 × 10000 steps (30 ps total), using single-ζ basis sets and a cutoff energy of 200 Ry, and serve only to provide a reasonable initial structure for the subsequent simulation at 1023 K. For the latter, we switched to optimized ("Molopt-SR") double-ζ basis sets[12] and increased the cutoff energy to 300 Ry. The system was thermostatted with a small time constant (τ = 10 fs) for 5000 steps (2.5 ps), and a final production run was then performed with τ = 100 fs for 10000 steps (5 ps).

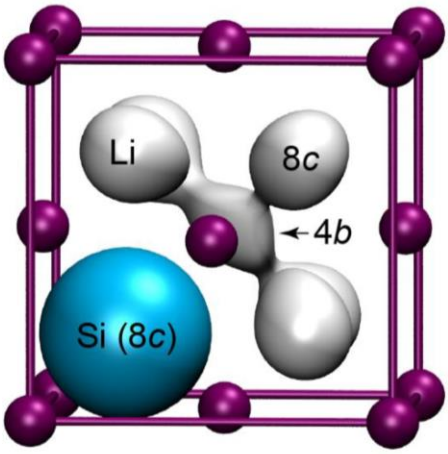

Figure S15. Isosurface plot for mass density maps of Si (blue) and Li (gray) atoms. To obtain this visualization, all atomic coordinates from the DFT-MD trajectory were translated back into the conventional unit cell and collected over 100 equidistant snapshots. Periodic boundary conditions have been switched off; therefore, only diffusion paths from and to the central 4*b* position are seen. The Si density isosurface is shown with arbitrary scaling and centered on (¼ ¼ ¼), the position on which Si atoms are introduced in the computational structural model (Figure S12c). The positions of P atoms in the idealized model (4*a*) and the boundaries of the conventional unit cell are shown as a guide to the eye (purple).

References

[1] S. Boyanov, J. Bernardi, E. Bekaert, M. Ménétrier, M. L. Doublet and L. Monconduit, *Chem. Mater.* **2009**, *21*, 298-308.
[2] B. León, J. I. Corredor, J. L. Tirado and C. Pérez-Vicente, *J. Electrochem. Soc.* **2006**, *153*, A1829-A1834.
[3] R. J. Kirkpatrick and R. K. Brow, *Solid State Nucl. Magn. Reson.* **1995**, *5*, 9-21.
[4] R. K. Brow, D. R. Tallant, S. T. Myers and C. C. Phifer, *J. Non-Cryst. Solids* **1995**, *191*, 45-55.
[5] Y. Deng, C. Eames, J.-N. Chotard, F. Lalère, V. Seznec, S. Emge, O. Pecher, C. P. Grey, C. Masquelier and M. S. Islam, *J. Am. Chem. Soc.* **2015**, *137*, 9136-9145.
[6] S. J. Clark, M. D. Segall, C. J. Pickard, P. J. Hasnip, M. J. Probert, K. Refson and M. C. Payne, *Z. Kristallogr.* **2005**, *220*, 567-570.
[7] J. P. Perdew, K. Burke and M. Ernzerhof, *Phys. Rev. Lett.* **1996**, *77*, 3865-3868.
[8] G. P. Francis and M. C. Payne, *J. Phys.: Condens. Matter* **1990**, *2*, 4395-4404.
[9] J. VandeVondele, M. Krack, F. Mohamed, M. Parrinello, T. Chassaing and J. Hutter, *Comput. Phys. Commun.* **2005**, *167*, 103-128.
[10] S. Goedecker, M. Teter and J. Hutter, *Phys. Rev. B* **1996**, *54*, 1703-1710.
[11] G. Bussi, D. Donadio and M. Parrinello, *J. Chem. Phys.* **2007**, *126*, 014101.
[12] J. VandeVondele and J. Hutter, *J. Chem. Phys.* **2007**, *127*, 114105.

5.3 Lithium Phosphidogermanates α- and β-Li_8GeP_4 – A Novel Compound Class with Mixed Li^+ Ionic and Electronic Conductivity

H. Eickhoff, S. Strangmüller, W. Klein, H. Kirchhain, C. Dietrich, W. G. Zeier, L. van Wüllen, T. F. Fässler

published in

Chem. Mater. **2018**, *30*, 6440-6448.

CHEMISTRY OF MATERIALS
Cite This: Chem. Mater. 2018, 30, 6440−6448
Article
pubs.acs.org/cm

Lithium Phosphidogermanates α- and β-Li_8GeP_4—A Novel Compound Class with Mixed Li^+ Ionic and Electronic Conductivity

Henrik Eickhoff,[†,‡] Stefan Strangmüller,[†,‡] Wilhelm Klein,[†] Holger Kirchhain,[§] Christian Dietrich,[∥] Wolfgang G. Zeier,[∥] Leo van Wüllen,[§] and Thomas F. Fässler*[,†]

[†]Department of Chemistry, Technische Universität München, Lichtenbergstrasse 4, 85747 Garching bei München, Germany
[§]Department of Physics, University of Augsburg, Universitätsstrasse 1, 86159 Augsburg, Germany
[∥]Institute of Physical Chemistry, Justus-Liebig-University Giessen, Heinrich-Buff-Ring 17, 35392 Giessen, Germany

Supporting Information

ABSTRACT: To utilize all-solid-state batteries as high power and energy density energy storage devices it is necessary to improve the current electrolyte materials and the cell architecture. In this work, we present α- and β-Li_8GeP_4 as potential compounds for the use in cathode composites of solid-state batteries because of their ability to conduct both Li^+ ion and electrons. Each polymorph was synthesized via mechanical alloying of the elements and subsequent annealing. Structural analysis of α- and β-Li_8GeP_4 via X-ray diffraction reveals isolated $[GeP_4]^{8-}$ tetrahedra. α-Li_8GeP_4 ($Pa\bar{3}$) and β-Li_8GeP_4 ($P\bar{4}3n$) are isotypic with Li_8SiP_4 and Li_8SnP_4, respectively. The lithium ion mobility indicated by partially filled octahedral voids was investigated by temperature-dependent nuclear magnetic resonance and electrochemical impedance spectroscopy and reveals low activation energies for lithium hopping in the range from 34 and 42 kJ mol^{-1} as well as high ionic conductivities of up to 8×10^{-5} S cm^{-1} and electronic conductivities of up to 4×10^{-7} S cm^{-1} at 293 K. These results combine a new substance class with a systematic synthesis approach for materials with high ionic carrier densities.

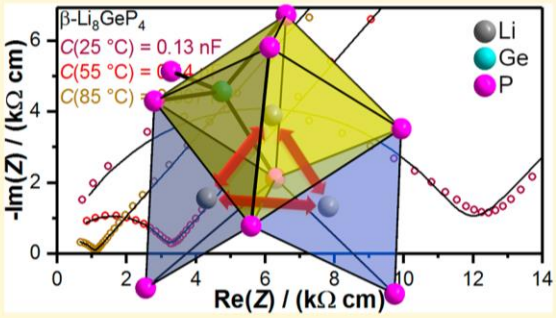

INTRODUCTION

The investigation of solid Li ionic conductors has been rapidly increased in recent years, because of their promising great potential to improve the safety and performance of state-of-the art battery technology. All-solid-state batteries (ASSB) are thought to excel as advanced electrochemical energy-storage systems.[1−4] While a lot of work is done to optimize solid ion conductors, which are typical electronically insulating as solid electrolytes, such as optimizing the lattice softness, width of diffusion pathways, and changes in the carrier densities,[4−12] it is also necessary to include these materials in composite cathodes to obtain high power and energy densities.[13,14] On one hand, coating of active material particles has been proven to be necessary to decrease interfacial resistances.[15] On the other hand, besides a high ionic conductivity for thick electrode configurations,[16] fast electronic percolation in the electrodes is mandatory. Usually in liquid electrolyte-based batteries a fast electronic percolation in cathode composites is achieved using conductive carbons that have shown to be detrimental in ASSBs.[17] Transferring these findings to all-solid-state batteries, the utilization of a mixed ionic and electronic conductor as a potential additional electrolyte may provide improved power densities without using large fractions of electrolyte and carbon in the electrodes.[18]

Recently, lithium phosphidosilicates have gained attention due to their wide range of structural diversity and their ability to conduct both ions and electrons.[19] After the initial report of this material class by Juza et al.[20] in the 1950s, further investigations were not carried on until 2016, when the structures of Li_8SiP_4 and Li_2SiP_2 followed by $LiSi_2P_3$, $Li_{10}Si_2P_6$, and $Li_3Si_3P_7$ were reported.[19,21,22] The building principles of phosphidosilicates are closely related to oxidosilicates, thiosilicates, and thiophosphates as they offer a large variety of structural motifs based on covalently connected $[SiP_4]^{8-}$ tetrahedra sharing edges and corners to form networks, where alkaline, alkaline earth, transition metal, or rare earth element atoms serve as counterions.[19−27] The lithium phosphidosilicate with the so-far highest reported ionic conductivity of 6×10^{-6} S cm^{-1} at room temperature, Li_8SiP_4, is built up by isolated $[SiP_4]^{8-}$ ortho-phosphidosilicate tetrahedra[19] resembling the building blocks in sulfide-based solid electrolytes such as $Li_{10}GeP_2S_{12}$. The higher formal charge of $[TtP_4]^{8-}$ compared to $[TtS_4]^{4-}$ and $[PS_4]^{3-}$ leads to the incorporation of larger amounts of lithium per formula unit, which may further come with an increased activation barrier due to

Received: June 30, 2018
Revised: August 16, 2018
Published: August 20, 2018

DOI: 10.1021/acs.chemmater.8b02759
Chem. Mater. 2018, 30, 6440−6448

stronger Li^+ interactions with the anion sublattice as seen in $Li_{10}GeP_2S_{12}$.[8] However, in Li_8TtP_4 lithium occupies all remaining tetrahedral and a part of the octahedral voids in the distorted cubic close packing of P atoms, allowing good percolation networks for three-dimensional ionic diffusion. Additionally, the electronic conductivity is reported to be only 2−3 orders of magnitude smaller than the ionic conductivity.[19]

In recent years the synthesis of new materials including electrolytes via one- or two-step synthesis routes involving mechanochemical milling experiments has gained in importance. Amorphous or glassy materials obtained by mechanical alloying may lead to novel materials which are not accessible by classical high-temperature approaches.[28−33] In this class of materials, combining mechanical alloying with subsequent annealing of the obtained reactive mixtures results in lithium phosphidosilicates of high purity.[21]

In this work, we report the novel mixed ionic and electronic conductors α-Li_8GeP_4 and β-Li_8GeP_4, prepared in high purities, using a new synthetic strategy for the material class of phosphidogermanates combining mechanical alloying and subsequent annealing. As this synthesis route is also applicable for the lithium phosphidosilicate Li_8SiP_4, a direct comparison between the materials can be made. The compounds are characterized with X-ray diffraction, electrochemical impedance spectroscopy, and temperature-dependent ^7Li NMR spectroscopy. This work shows that there is a vast variety of possible compounds in the class of lithium ionic conducting phosphidosilicates and phosphidogermanates that need to be explored.

■ EXPERIMENTAL SECTION

All chemicals were handled under Ar atmosphere in Gloveboxes (MBraun, 200B) with moisture and oxygen levels below 0.1 ppm or in containers which were sealed under Ar atmosphere and vacuum (<2 × 10^{-2} mbar), respectively. The lithium phosphidotetrelates are sensitive to oxygen and moisture; in particular, contact with water results in a vigorous reaction including the formation of flammable and toxic gases (e.g., phosphine). Therefore, disposal must be addressed in small amounts at a time under proper ventilation.

Ball Mill Experiments. All compounds were synthesized in a two-step synthesis route. In the first step a reactive mixture was prepared by mechanochemical milling (350 rpm, 36 h, 10 min interval, 3 min break) of the corresponding elements in stoichiometric amounts using a Retsch PM100 Planetary Ball Mill with a 50 mL tungsten carbide milling jar and three balls with a diameter of 15 mm.

Heat Treatment Experiments. The reactive mixtures obtained from ball mill experiments were pressed to pellets (0.5 g), sealed in a graphitized silica-glass ampule, and heated in a muffle furnace (Nabertherm, L5/11/P330) to 500−700 °C for 24−72 h (heating rate 4 °C min^{-1}, cooling rate 1 °C min^{-1}).

Synthesis of Li_8SiP_4. Li_8SiP_4 was obtained by stoichiometric reaction of lithium (401.4 mg, 7.23 mmol, Rockwood Lithium, 99%), silicon (203.0 mg, 7.23 mmol, Wacker, 99.9%), and red phosphorus (895.6 mg, 7.23 mmol, Sigma-Aldrich, 97%) via mechanical milling and subsequent annealing of pellets of the mixture to 700 °C for 24 h.

Synthesis of α- and β-Li_8GeP_4. The synthesis of both modifications α- and β-Li_8GeP_4 starts with the preparation of a reactive mixture by mechanical milling of lithium (330.4 mg, 5.95 mmol, Rockwood Lithium, 99%), germanium (432.2 mg, 5.95 mmol, EVOCHEM GmbH, 99.999%), and red phosphorus (737.3 mg, 5.95 mmol, Sigma-Aldrich, 97%). α-Li_8GeP_4 and β-Li_8GeP_4 are obtained by annealing of pellets of the reactive mixtures to 500 °C for 72 h and 700 °C for 24 h, respectively.

Isothermal Phase Transition Experiments. For the investigation of the phase transitions between the two polymorphs pellets of the crystalline phases α- and β-Li_8GeP_4 were prepared and heated to 600 °C for 12 h and 500 °C for 72 h, respectively.

Preparation of Spark Plasma Sintered Sample of Li_8SiP_4. The sample densification was carried out using a SPS 530ET spark plasma sintering machine. During the sintering process the sample (Ø = 13 mm) was heated up to 520 °C and pressed with 50−60 MPa. At the end of sintering the temperature was rapidly cooled down to 200 °C.

Powder X-ray Diffraction. Data were collected at room temperature on a STOE Stadi P diffractometer (Ge(111) monochromator, Cu $K\alpha_1$ radiation, λ = 1.54056 Å) with a Dectris MYTHEN 1K detector in Debye−Scherrer geometry. Samples were sealed in glass capillaries (Ø 0.3 mm) for measurement. Raw data were processed with WinXPOW[34] software, and Rietveld refinements were executed with FullProf.[35] The atomic displacement parameters for all atoms have been calculated isotropically. Displacement parameters of all Li atoms were equalized, and occupation factors were set to fit a stoichiometry of Li_8TtP_4. Free refinement led to slightly lower occupations of Li almost exclusively on the octahedrally coordinated positions resulting in sum formulas of $Li_{7.64(8)}SiP_4$ for Li_8SiP_4, $Li_{7.42(2)}GeP_4$ for α-Li_8GeP_4, and $Li_{7.67(1)}GeP_4$ for β-Li_8GeP_4, respectively. Atomic coordinates and isotropic displacement parameters as well as the data of the measurement at room temperature are given in the Supporting Information. Further data may be obtained from Fachinformationszentrum Karlsruhe, D-73644 Eggenstein-Leopoldshafen, Germany (Fax: (+49)7247-808-666; E-mail: crysdata@fiz-karlsruhe.de) on quoting the depository numbers CSD-434683 (Li_8SiP_4, 293 K), CSD-434684 (α-Li_8GeP_4, 293 K), and CSD-434685 (β-Li_8GeP_4, 293 K).

Single-Crystal X-ray Data Collection. A single crystal of β-Li_8GeP_4 was isolated and sealed in a glass capillary (0.3 mm). Data were collected on a single-crystal X-ray diffractometer equipped with a FR591 rotating anode with Mo $K\alpha$ radiation (λ = 0.71073 Å) and a Montel optic, a CCD detector (APEX II, κ-CCD), by using the *APEX 2* software package.[36] The crystal structure was solved by direct methods with ShelXS97; for structure refinement the program package SHELX-2014[37] was used. The crystal has been refined as an inversion twin, however, with a small weight of the second individual and a Flack parameter of 0.02(3). All atoms were refined with anisotropic displacement parameters, except for Li1 and Li6 atoms which were refined isotropically. The occupation factors were set to 8 Li per GeP_4 unit. Free refinement resulted in a lower occupation of the octahedrally coordinated Li positions. Further data may be obtained from Fachinformationszentrum Karlsruhe, D-73644 Eggenstein-Leopoldshafen, Germany (Fax: (+49)7247-808-666; E-mail: crysdata@fiz-karlsruhe.de) on quoting the depository number CSD-434686 (β-Li_8GeP_4, 293 K).

Differential Scanning Calorimetry (DSC). For investigation of the thermal behavior of the compounds a Netzsch DSC 404 Pegasus device was used. Niobium crucibles were filled with the samples and sealed by arc welding. Empty sealed crucibles served as reference. Measurements were performed under an Ar flow of 75 mL min^{-1} and a heating/cooling rate of 10 K min^{-1}. Data collection and handling were carried out with the Proteus Thermal Analysis program.[38]

Solid-State NMR Spectroscopy. Solid-state NMR experiments have been performed using a Bruker Avance III spectrometer operating at a magnetic field of 7 T employing a 4 mm WVT MAS probe. The resonance frequency of the measured ^7Li nucleus is 116.6 MHz. The samples have been sealed in a glass tube to avoid contact with air and moisture. The temperature calibration for the ^7Li measurements has been performed using the temperature-dependent ^{207}Pb NMR shift of lead nitrate ($PbNO_3$) as chemical-shift thermometer,[39] which has also been measured in a sealed glass tube. For α-Li_8GeP_4 the static ^7Li single-pulse-excitation measurements were performed in the temperature range from room temperature to 183 K with recycle delays from 30 to 60 s and 4 repetitions. For β-Li_8GeP_4 the static ^7Li single-pulse-excitation measurements were performed in the temperature range from room temperature to 168 K with a recycle delay of 60 s and 4 repetitions.

DOI: 10.1021/acs.chemmater.8b02759
Chem. Mater. 2018, 30, 6440−6448

For both samples a presaturation comb was used. All spectra were referenced to a 9.7 M LiCl solution.

Impedance Spectroscopy and dc Conductivity Measurements. Electrical conductivities were measured by ac impedance spectroscopy using a custom-built setup. Powder samples of Li_8SiP_4 and α- and β-Li_8GeP_4 were placed between two stainless steel rods 10 mm in diameter and pressed at 3 t for 2 min resulting in geometric densities of 82%, 56%, and 76%, respectively. Electrochemical impedance analysis (EIS) was conducted in the temperature range of 25−150 °C using a SP300 impedance analyzer (Biologic) at frequencies from 7 MHz to 10 Hz with an amplitude of 20 mV. The partial electronic conductivity was determined with the same setup via a simple polarization method, applying a voltage of 0.3−2.0 V for 10 h each.

RESULTS AND DISCUSSION

Syntheses. After discovering various new compounds in the Li−Si−P system,[19,21,22] we extended our experimental efforts toward the corresponding systems in which Si is substituted by the heavier homologue Ge, in particular aiming at the compound containing the so far highest possible Li amount and potentially enhanced conductivities, Li_8GeP_4. Simultaneously, we varied and improved the preparative methods also for the Si-based materials. After applying a two-step synthesis route starting from ball milling of the elements followed by a high-temperature reaction of the reactive mixtures within sealed, graphitized silica-glass ampules, we not only confirmed a high-yield synthesis of Li_8SiP_4 but also obtained the new Li_8GeP_4 in two different polymorphic modifications. Polycrystalline samples of both modifications, α-Li_8GeP_4 after 72 h at 500 °C and β-Li_8GeP_4 after 24 h at 700 °C, as well as of Li_8SiP_4, are obtained in high purity, as indicated by the Rietveld analyses shown in Figure 1. In the case of Li_8GeP_4, both the α and β modifications crystallize in the cubic crystal system with very similar lattice parameters, however, with different space groups. Fairly illustrating the position of Ge as an intermediate between the homologue elements Si and Sn, the α modification is isotypical with Li_8SiP_4 while β-Li_8GeP_4 adopts the Li_8SnP_4 structure type.[40] DSC measurements up to 750 °C of both modifications of Li_8GeP_4 showed only weak signals, probably indicating a higher melting point and a rather slow transformation from α- to β-Li_8GeP_4 and vice versa. The slow phase transition is also in agreement with isothermal interconversion experiments performed with bulk material in ampules, which led to full or partial conversion (Figure S9 in Supporting Information).

Crystal Structure of α-Li_8GeP_4. To evaluate possible Li^+ conduction pathways the crystal structures of the two Li_8GeP_4 polymorphs are analyzed.

The α modification crystallizes in the cubic space group $Pa\bar{3}$ (205) with a lattice parameter of 11.80146(4) Å (Figure 2a). The structure was analyzed using Rietveld refinements; the corresponding results are shown in Table 1. The structure comprises isolated, highly charged $[GeP_4]^{8-}$ tetrahedra (Figure 2), which are separated by eight Li^+ ions per formula unit and consists of eight fully occupied crystallographically independent atom positions (Li1, Li2, Li3, Li4, Li5, Ge, P1, and P2). Analogously to the crystal structure of Li_8SiP_4,[19] the structure is closely related to the fluorite type where the Ca^{2+} ions form a cubic closest packed (*ccp*) arrangement and F^- is occupying all tetrahedral voids whereas octahedral voids remain unoccupied. The present compound belongs to the antifluorite type, and the lattice is based on a slightly distorted *ccp* of P atoms with all tetrahedral and 25% of the octahedral voids filled by Ge and

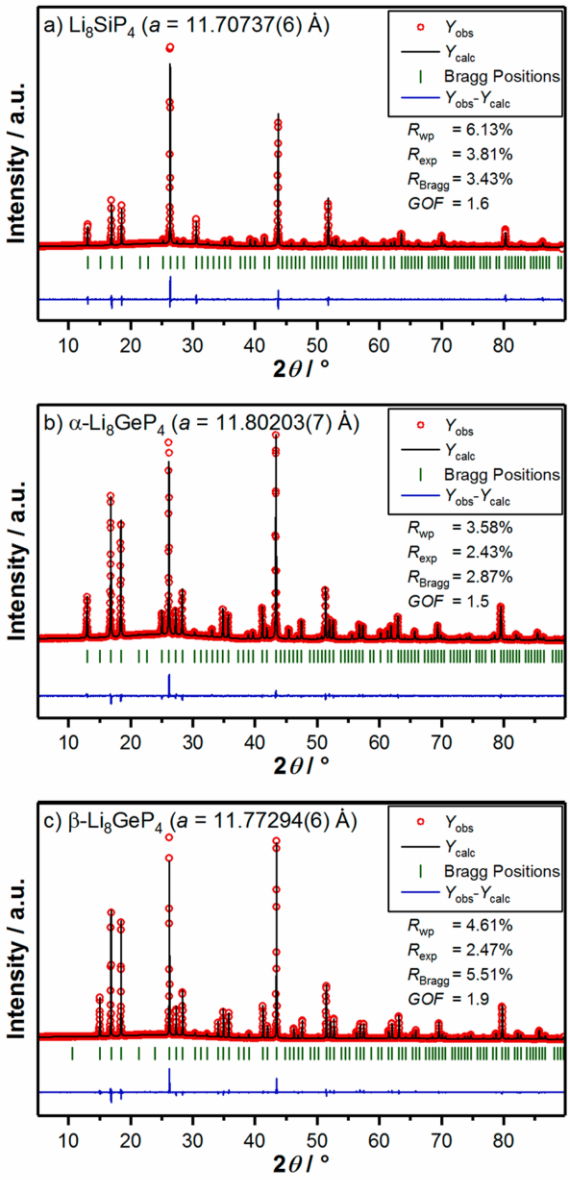

Figure 1. Rietveld analyses of X-ray powder diffraction patterns of (a) Li_8SiP_4, (b) α-Li_8GeP_4, and (c) β-Li_8GeP_4. Red circles indicate observed intensities Y_{obs}, black lines show calculated intensities Y_{calc}, blue lines reveal the difference between observed and calculated intensities, and green marks indicated Bragg positions.

Li in an ordered manner. Notice that occupying the tetrahedral void with Ge results in covalent bonding to the P atoms, whereas lithium can be considered as ionic. Within this structure, the tetrahedral voids are fully occupied by Ge and Li (Li1−Li3) in a ratio of 1:7. According to the space group $Pa\bar{3}$, the octahedral voids are centered by three different crystallographic sites according to the Wyckoff positions 4*a*, 4*b*, and 24*d*. In contrast to the structure of Li_8SiP_4,[19] sites 4*a* and 4*b* are completely occupied, whereas no electron density is observed at the 24*d* site.

In reference to the isotypic Li_8SiP_4,[19] the special arrangement of the Ge atoms results in a 2 × 2 × 2 superstructure based on the *ccp* of the P atoms (Figure 2b and 2c) in

DOI: 10.1021/acs.chemmater.8b02759
Chem. Mater. 2018, 30, 6440−6448

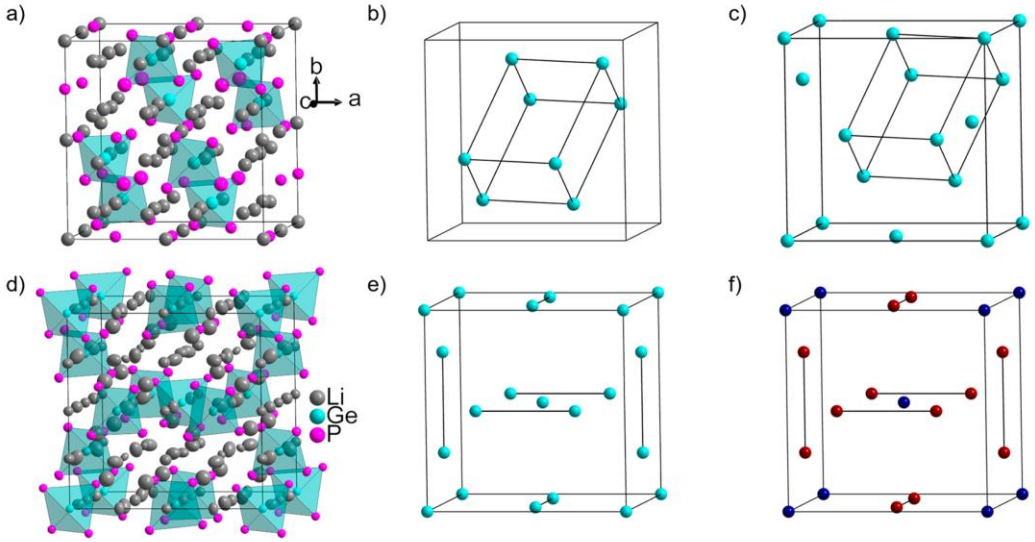

Figure 2. (a) Structure of α-Li_8GeP_4. (b) Rhombohedral arrangement of Ge atoms within the unit cell of α-Li_8GeP_4. (c) As in b but with a shift of the origin of the unit cell by the vector (0.1272|0.1272|0.1272) for comparison with the β modification. (d) Structure of β-Li_8GeP_4. (e) Arrangement of Ge1 and Ge2 atoms within the unit cell of β-Li_8GeP_4. Black lines mark one-dimensional chains drawing through the structure. (f) Unit cell of an A15 phase (Cr_3Si structure type[43]). Cr and Si atoms are shown in dark red and dark blue, respectively. Black lines mark the direction of the one-dimensional chains. Li, Ge, and P atoms are depicted as gray, turquoise, and pink thermal ellipsoids, respectively, set at 90% probability. GeP_4 tetrahedra are highlighted in turquoise.

Table 1. Details of the Rietveld Structure Refinement of α-Li_8GeP_4

empirical formula	α-Li_8GeP_4
T (K)	293
fw (g mol^{-1})	252.0
space group (no.)	$Pa\bar{3}$ (no. 205)
unit cell parameters (Å)	a = 11.80203(7)
Z	8
V (Å^3)	1643.88(2)
ρ_{calcd} (g cm^{-3})	2.037
2ϑ range (deg)	5.006−89.846
R_p	2.55
R_{wp}	3.58
R_{exp}	2.43
X^2	2.17
GOF	1.5
R_{Bragg}	2.87
R_f	2.68

accordance with the CaF_2 unit cell. Within the current larger unit cell, the arrangement of Ge can be demonstrated by Ge atoms spanning a rhombohedron. Each of these atoms is surrounded by four P atoms. The resulting $[GeP_4]^{8-}$ tetrahedra have similar Ge−P bond lengths of 2.381(5) and 2.396(3) Å for Ge−P1 and Ge−P2 (3×), respectively. These bond lengths are within the characteristic range of Ge−P interactions of related compounds such as $Na_{10}Ge_2P_6$ (2.334(1)−2.425(1) Å),[25] $NaGe_3P_3$ (2.314(4)−2.446(2) Å),[41] and GeP (2.34−2.38 Å).[42] The P−Ge−P angles are in the narrow range of 109.3(1)° and 109.6(1)°, thus forming an almost perfect T_d symmetric $[GeP_4]^{8-}$ unit. In consequence, the P atoms are slightly shifted with respect to an ideal position of a *ccp* packing.

The occupation of the remaining tetrahedral voids with Li1, Li2, and Li3 leads to Li−P distances between 2.47(2) and 2.91(1) Å. In contrast, the octahedrally coordinated Li4 and Li5 show six identical Li−P bond lengths of 2.884(1) and 3.028(4) Å, respectively, illustrating the less favored octahedral coordination of Li^+. The high lithium content of the compound induces a short Li−Li bond length. The shortest can be categorized in different sets: face-sharing Li^+-centered tetrahedra and octahedra result in shorter Li−Li distances of 2.33(1)−2.56(2) Å, and edge-sharing polyhedra lead to longer distances of 2.84(2)−3.23(3) Å.

Crystal Structure of β-Li_8GeP_4. The second polymorph β-Li_8GeP_4 (Figure 2d) crystallizes in the cubic space group $P\bar{4}3n$ (218) with a lattice parameter of 11.7831(1) Å. The details of the structure refinement at 293 K are shown in Table 2. Atomic coordinates and anisotropic displacement parameters as well as the data of the measurement at room temperature are given in the Supporting Information. The refined crystallographic parameters from Rietveld analysis on the powder sample (Figure 1b and Supporting Information) confirm the single-crystal data results.

The crystal structure also comprises isolated $[GeP_4]^{8-}$ tetrahedra and Li^+ ions distributed over 10 crystallographically independent positions (Ge1, Ge2, P1, P2, and Li1−Li6) with three of the Li positions (Li1, Li5, and Li6) being partially occupied. As in the α modification the P atoms form a slightly distorted *ccp* arrangement, and the distortion is caused by a slight shift of the P atoms toward the Ge atom positions, which are situated in 1/8th of all of the tetrahedral voids. The remaining 7/8th of the tetrahedral voids are occupied by Li^+ (Li1−5), as no additional electron density of Ge atoms can be found. Of those the positions Li1 and Li5 are partially occupied with S.O.F. values of 0.78(3) and 0.887(9), respectively. The remaining Li^+ ions (Li6) occupy approximately 38% of the larger octahedral voids as the S.O.F. value of the Li6 atom at a general Wyckoff site 24*i* amounts to 0.502(9). Another crystallographic site centering the octahedral voids, the Wyckoff position 8*e* according to the space group $P\bar{4}3n$ (218), is completely empty.

DOI: 10.1021/acs.chemmater.8b02759
Chem. Mater. 2018, 30, 6440−6448

Table 2. Crystallographic Data and Refinement Parameters of β-Li_8GeP_4 at 293 K

empirical formula	Li_8GeP_4
fw (g mol^{-1})	252.0
cryst size (mm^3)	0.08 × 0.08 × 0.07
cryst color	dark red
T (K)	293(2)
cryst syst	cubic
space group (no.)	$P\bar{4}3n$ (no.218)
unit cell parameters (Å)	a = 11.7831(1)
Z	8
V (Å^3)	1635.98(4)
ρ_{calcd} (g cm^{-3})	2.046
μ (mm^{-1})	4.420
$F(000)$ (e)	928
ϑ range/deg	2.444−29.948
index range (hkl)	$-16 \le h \le 10$
	$-15 \le k \le 11$
	$-16 \le l \le 16$
no. of reflns collected	10 400
no. of independent rns	297
R_{int}	0.0286
no. of reflns with $I > 2\sigma(I)$	629
abs corr	multiscan
data/restraints/params	808/0/41
foodness-of-fit on F^2	1.036
R_1, wR_2 (all data)	0.0520, 0.0540
R_1, wR_2 [$I > 2\sigma(I)$]	0.0256, 0.0479
largest diff. peak and hole (e Å^{-3})	0.747/−0.450

The arrangement of the Ge atoms with respect to each other significantly differs from the α phase. In β-Li_8GeP_4 the Ge atoms arrange according to a homoatomic $A15$ structure (Cr_3Si[43] structure type), pointing out the structural difference of α- and β-Li_8GeP_4. In β-Li_8GeP_4 the body-centered cubic (bcc) substructure of the $A15$ structure type is formed by the Ge1 atoms, whereas the Ge2 atoms are arranged in pairs on the cubic faces resulting in one-dimensional rows drawing through all three spatial directions (Figure 2e and 2f). Hence, similar to the α polymorph, a 2 × 2 × 2 superstructure based on the ccp arrangement of the P atoms is obtained.

The Ge1 atoms are surrounded by four P1 atoms, and the Ge2 atoms occupy the center of four atoms on position P2, resulting in a structure of isolated $[GeP_4]^{8-}$ tetrahedra separated by Li^+ ions. The bond lengths between 2.369(3) and 2.378(2) Å are slightly shorter than those of the α modification. However, the interatomic Ge−P distances are also comparable with Ge−P bonds of related compounds.

The remaining sites are occupied by Li^+ ions, resulting in three different $[LiP_4]$ environments as well as one $[LiP_6]$ octahedron centered by Li6. Similar to α-Li_8GeP_4, the resulting Li−P distances within the tetrahedra are 2.50(1)−2.69(1) Å, reasonably shorter compared to those in octahedra with 2.82(2)−3.05(2) Å. However, induced by the different symmetry the $[LiP_6]$ octahedra are more distorted. For Li−Li distances also the same trend is observed as for the α phase. Such distances between Li^+ ions in face-sharing P_n polyhedra are shorter (2.49(2)−2.66(2) Å) than those in edge-sharing P_n polyhedra (2.84(1)−3.07(1) Å).

Lithium Migration Network. Comparing the coordination network of Li-centered P polyhedra in both polymorphs (Figure 3) provides possible lithium diffusion pathways in the

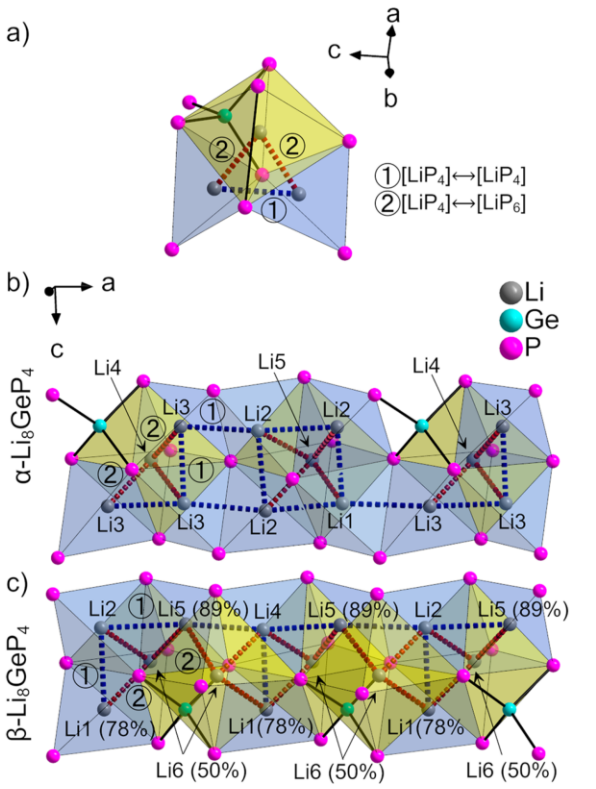

Figure 3. Structural representation of the Li^+ coordination network showing possible Li^+ hopping pathways. (a) Example of two different Li^+-hopping mechanisms between edge-sharing tetrahedra (1) (blue dashed lines) and face-sharing tetrahedra and octahedra (2) (red dashed lines). (b) Possible Li^+-hopping pathways in α-Li_8GeP_4. (c) Possible Li^+-hopping pathways in β-Li_8GeP_4 with partially filled Li^+ (occupation in %). While in β-Li_8GeP_4 these jumps between face-sharing tetrahedra and octahedra and edge-sharing tetrahedra (1) are always possible, in α-Li_8GeP_4 a jumping mechanism via edge-sharing tetrahedra (1) is assumed for macroscopic Li^+ transport.

structure. In both polymorphs lithium is coordinated in either a tetrahedral or an octahedral environment. However, while in α-Li_8GeP_4 two octahedral positions exist, β-Li_8GeP_4 exhibits only one octahedral lithium position. In all crystal structures of the Li_8TtP_4 compounds the octahedral polyhedra share common faces with the tetrahedral sites, whereas all tetrahedra share edges. In Figure 3a a typical arrangement of a P_6 octahedron that share faces with adjacent P_4 tetrahedra and two P_4 tetrahedra that share edges as it occurs in both polymorphs are shown. Pathways of possible Li migration are from octahedral to tetrahedral sites through common faces (1) and between two tetrahedra that share edges (2). While it is typically believed that low-energy pathways for ion jumps are connected to face-sharing polyhedra, changing coordination numbers leads to larger activation barriers.[10] The assumption of a three-dimensional ion jump pathway along more tetrahedron−octahedron−tetrahedron positions likely leads to higher energetic barriers in a potential energy landscape compared to face-sharing tetrahedra. On the other hand, a jumping mechanism via edge-sharing tetrahedra (1, Figure 3) is not uncommon. However, it is actually the rate-determining step in the fast ionically conducting lithium argyrodites,[6,44] and the edges between two LiP_4 tetrahedra are indeed a bit longer than those between one LiP_4 and one GeP_4 unit, 4.199(3)-

DOI: 10.1021/acs.chemmater.8b02759
Chem. Mater. 2018, 30, 6440−6448

4.365(3) and 3.853(2)-3.944(2) Å, respectively. While in both polymorphs the tetrahedra share edges and three-dimensional conduction seems possible, the Li–Li distances in β-Li_8GeP_4 are shorter than in α-Li_8GeP_4, suggesting faster ionic exchange.[33]

In addition to the coordination environments, the octahedrally coordinated Li^+ in β-Li_8GeP_4 is distributed on a 24*i* site and partially occupied and a hopping pathway appears to be more probable compared to α-Li_8GeP_4, where Li^+ is exclusively located on a fully occupied 4*a* and 4*b* site. In other words, the polyhedral connectivity of β-Li_8GeP_4 suggests potentially lower activation barriers for the ionic motion, and the higher fraction of Li at partially occupied sites in β-Li_8GeP_4 suggests a higher number of mobile charge carriers within the structure.

Solid-State NMR Spectroscopy. The dynamic behavior of the Li^+ ions in α-Li_8GeP_4 and β-Li_8GeP_4 was investigated via the temperature-dependent evolution of the static ^7Li NMR line width in the relevant temperature range (Figure 4a and 4b). Since the central transition of the $I = 3/2$ nucleus ^7Li is only broadened via the homo- (^7Li–^7Li) and heteronuclear (here ^7Li–^{31}P) dipolar couplings and both types of interactions scale with the second Legendrian ($3\cos^2 ß - 1$), any dynamic process should produce a (partial) averaging of the orientational dependence and hence entail a narrowing of the NMR line. Thus, the data presented in Figure 4c, which shows the temperature-dependent evolution of the line widths for the two investigated compounds, clearly illustrates the onset of Li^+ ion mobility in α- and β-Li_8GeP_4 around 220 K.

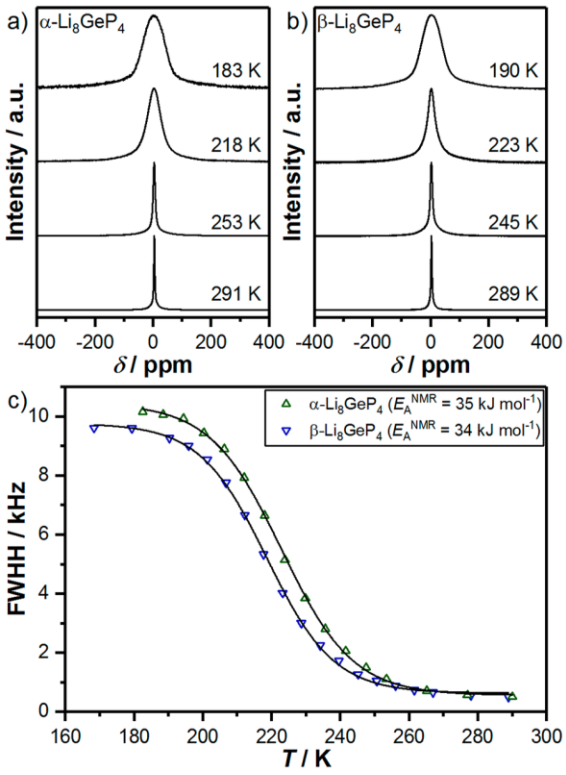

Figure 4. ^7Li single-excitation NMR spectra recorded at different temperatures of (a) α-Li_8GeP_4 and (b) β-Li_8GeP_4. Saturation comb was used prior to data acquisition. (c) Evolution of the temperature-dependent ^7Li line widths of α-Li_8GeP_4 and β-Li_8GeP_4. Solid lines are guides to the eye only.

For both samples only one Lorentzian-shaped signal is visible at room temperature with line widths of 500 and 510 Hz for α- and β-Li_8GeP_4, respectively. Upon cooling of the samples, the signals gradually broaden, developing a Gaussian line shape in the "rigid-lattice" plateau at temperatures < 190 K with line widths of 10.1 and 9.6 kHz for α- and β-Li_8GeP_4, respectively. Taking the onset temperature T_{onset} as the temperature at which the line width is given by $(\nu_{rigid\ lattice} - \nu_{mot.\ narrowing})/2$ and employing the Waugh Fedin relation, $E_A^{NMR} = 0.156 \times T_{onset}$,[45,46] a rough estimation of the activation energy E_A^{NMR} (in kJ mol^{-1}) for the motional process may be obtained.

From this, onset temperatures of 224 and 219 K, translating into activation energies of 35 and 34 kJ mol^{-1} for α-Li_8GeP_4 and β-Li_8GeP_4, respectively, are obtained.

Impedance Spectroscopy and dc Conductivity Measurements. Nyquist plots (Figure 5a, 5b, and 5c) derived from impedance spectroscopy measurements to determine the Li^+ ion conductivity feature a semicircle and a tail of the blocking electrodes. The high-frequency semicircle represents contribu-

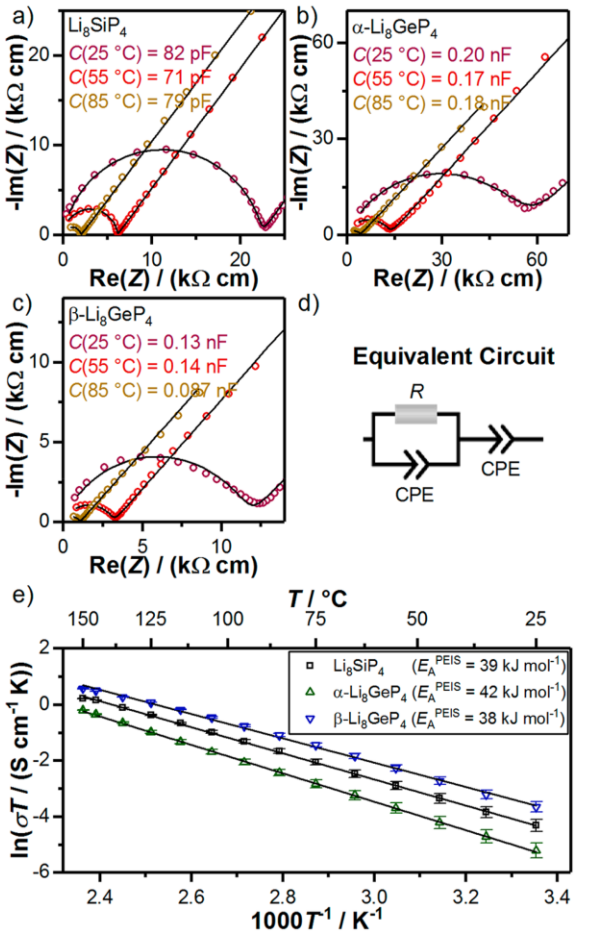

Figure 5. Normalized Nyquist plots of (a) Li_8SiP_4, (b) α-Li_8GeP_4, and (c) β-Li_8GeP_4 with curves observed at 25 (largest semicircle), 55 (medium semicircle), and 85 °C (smallest semicircle), respectively, with capacitances of the semicircle, and (d) equivalent circuits used for fitting (red). (e) Arrhenius plot of the three different compounds with error bars and linear fit to obtain activation energies E_A^{PEIS}.

DOI: 10.1021/acs.chemmater.8b02759
Chem. Mater. 2018, 30, 6440–6448

tions of intragrain and grain boundary Li^+ transport, which could not be resolved. All Nyquist plots were fitted with a series connection of a constant phase element (CPE) for the blocking electrodes and a parallel CPE/resistor component. The obtained capacitances ranging from 7×10^{-11} to 2×10^{-10} F show that the resistor element represents the sum of intragrain and grain boundary resistances, resulting in ionic conductivities of $\sigma_{Li}(Li_8SiP_4) = 4.5 \times 10^{-5}$ S cm^{-1}, $\sigma_{Li}(\alpha\text{-}Li_8GeP_4) = 1.8 \times 10^{-5}$ S cm^{-1}, and $\sigma_{Li}(\beta\text{-}Li_8GeP_4) = 8.6 \times 10^{-5}$ S cm^{-1} at 25 °C. Temperature-dependent impedance measurements in a range of 25−155 °C (Figure 5e) revealed activation energies E_A^{PEIS} of 39, 42, and 38 kJ mol^{-1}, respectively. The minor deviations between the E_A values as obtained from NMR and impedance spectroscopy may result from the grain boundary contributions to the impedance data.

dc polarization experiments in the range of 0.3−0.7 V to estimate the partial electronic conductivity led to $\sigma_{e^-}(Li_8SiP_4) = 6.0 \times 10^{-8}$ S cm^{-1}, $\sigma_{e^-}(\alpha\text{-}Li_8GeP_4) = 7.2 \times 10^{-8}$ S cm^{-1}, and $\sigma_{e^-}(\beta\text{-}Li_8GeP_4) = 4.2 \times 10^{-7}$ S cm^{-1}.

While the materials are mainly ionic conductors the electronic conductivities for α-Li_8GeP_4 and β-Li_8GeP_4 are only 2 orders of magnitude lower. Compared to Li_8SiP_4 the substitution of Si by Ge decreased the difference between ionic and electronic by 1 order of magnitude. Comparing the ionic conductivities of all phases, the β-Li_8GeP_4 exhibits the highest conductivity for lithium as well as the lowest energy barrier for migration, possibly due to the smaller jump distances via the tetrahedral sites, higher number of tetrahedron−octahedron−tetrahedron transitions, as well as a larger number of partially occupied sites for lithium to jump into.

Crystallographic Group−Subgroup Relationship of α- and β-Li_8GeP_4. The existence of the two polymorphs with conductivities varying by almost 1 order of magnitude raises questions about their relationship and the possible existence of more phases with different ordering of the Ge atoms on crystallographic sites and improved charge carrier mobilities. Therefore, we applied the method brought to the front by Bärnighausen[47] and determined the crystallographic tree through group−subgroup relationships.

The crystal structures of the two modifications of Li_8GeP_4 are very closely related, as indicated, for example, by the same (cubic) crystal system with very similar lattice parameters or by finding the same main building units, isolated GeP_4 tetrahedra and Li^+ ions. Furthermore, both structures can be derived from the antitype of CaF_2 as in both cases the P atoms form an only slightly distorted cubic closest packing where all tetrahedral voids are filled by Ge and Li^+ ions in an ordered way. The genuine antiflourite type of structure was postulated for a compound addressed as "Li_5GeP_3" (and "Li_5SiP_3") with a complete disorder of lithium and tetrel atom by Juza and Schulz.[20] To realize the composition Li_8GeP_4, besides the $2n$ tetrahedral voids arising from a *ccp* of n P atoms additionally some Li^+ ions have to occupy octahedral voids. In both modifications the *ccp* of P atoms is slightly distorted due to a shift of the P atoms toward the covalently bonded Ge atoms. Besides these similarities, the cubic space groups of the two polymorphs, $Pa\bar{3}$ for α- and $P\bar{4}3n$ for β-Li_8GeP_4, are in fact connected via group−subgroup relationships to the space group of CaF_2, $Fm\bar{3}m$ (Figure 6a, symmetry degradation trees corresponding to Bärnighausen[47] are given as Supporting Information). Although derived from the same aristotype, these two space groups are surprisingly not related via a direct group−subgroup relation. The straight phase transition is

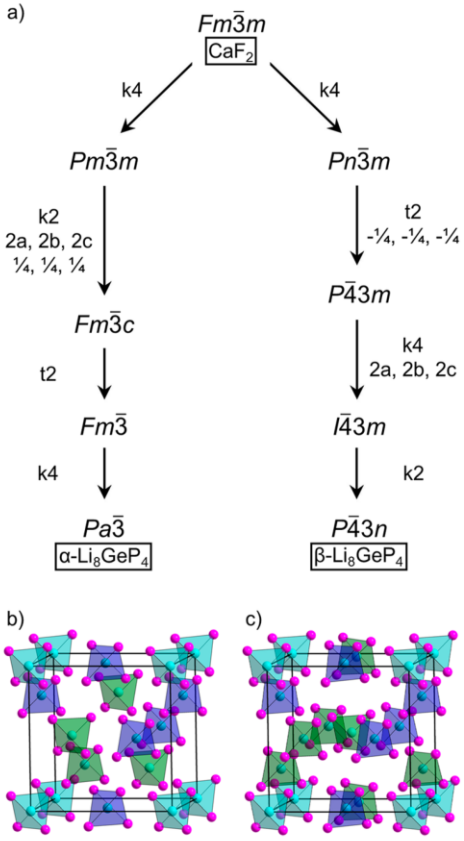

Figure 6. (a) Group−subgroup relationship between CaF_2 and the two modifications of Li_8GeP_4. In both cases the symmetry is degraded via one translationengleiche and three klassengleiche transitions, one of the latter including the doubling of the lattice parameters. (b) Unit cell of α-Li_8GeP_4, shifted by (0.1272|0.1272|0.1272) to locate the Ge atoms at the origin for better comparison. (c) Unit cell of β-Li_8GeP_4. Ge and P atoms are depicted as turquoise and pink solid balls; Li atoms are omitted for reasons of clarity. GeP_4 tetrahedra are highlighted in different colors to illustrate the similarities and differences in the arrangement of the Ge atoms within the structures. Turquoise tetrahedra, forming a primitive cubic cell, and blue tetrahedra, located at the faces of the unit cell, are packed in an almost identical manner, while green tetrahedra, representing 50% of all tetrahedra, are differently arranged in the two Li_8GeP_4 polymorphs, inside the cell in α and at the faces as well as in the center of the unit cell in β-Li_8GeP_4.

hampered according to the weak and inconclusive signals in DSC experiments.

Further heating experiments take some days at the respective emerging temperature to transform β-Li_8GeP_4 partially into α-Li_8GeP_4 and vice versa. Finally, the assumption of a kinetically hindered mechanism of the phase transition between α- and β-Li_8GeP_4 below the melting point is illustrated by regarding the crystal structures, as the comparison of the packing of the $[GeP_4]^{8-}$ tetrahedra (Figure 6b and 6c) reveals that during a structural transition formally one-half of the Ge atoms or $[GeP_4]^{8-}$ units have to shift between neighboring tetrahedral voids including the cleavage of the same amount of all Ge−P bonds or alternatively 50% of the GeP_4 tetrahedra have to change their places; of course, all possible procedures are accompanied by a rearrangement of the corresponding Li^+ ions. The shift of $[GeP_4]^{8-}$ units could also be connected to

DOI: 10.1021/acs.chemmater.8b02759
Chem. Mater. 2018, 30, 6440−6448

the rearrangement of closed packed P atom layers and in consequence also with a simultaneous rotation of $[GeP_4]^{8-}$ tetrahedra.

Obviously, the formation of the different modifications is strongly dependent on the experimental conditions, i.e., the annealing time and temperature. Comparing the structures of the related compounds Li_8SiP_4 and Li_8SnP_4 reveals that for smaller tetrahedral anions or in an alternative consideration for a larger space demand of the cations the α structure seems to be more stable, while for larger anions or less cations the β type could be favored. This is also supported, e.g., by other compounds with a lower space requirement of the cations like M_4SiP_4 (M = Ca, Sr, Ba) which show the same space group and tetrahedral packing as the β-type structure.[24]

CONCLUSION

With the polymorphs α-Li_8GeP_4 and β-Li_8GeP_4 two new lithium phosphidogermanates are synthesized and thoroughly characterized. While both materials show similar building blocks, there is no direct crystallographic group−subgroup relation between both occurring space groups. Consequently, a transition between these phases is hindered and occurs only in a slow manner. For phase-pure samples, a two-step synthesis route via mechanical milling and subsequent heat treatment is applied, which also performs well for Li_8SiP_4.

These materials show ionic conductivities of 10^{-5}−10^{-4} S cm^{-1} at 25 °C in combination with electronic conductivities of 2−3 orders of magnitude lower. The activation energies of 38−42 kJ mol^{-1} obtained from PEIS and of 34−36 kJ mol^{-1} from temperature-dependent static ^{7}Li NMR experiments are in a reasonable range for ion conductors. The high electronic conductivities make the new materials unsuitable as solid electrolyte separators. However, the mixed conductivity may be interesting for application in the electrode composites in all-solid-state batteries; however, the chemical and electrochemical stability in the composites needs to be evaluated.

The successful substitution of Si by Ge shows the possibility of ion replacement in the host lattice with only a small effect on the overall structure. Further isoelectronic and aliovalent substitutions of the metal cation may possibly improve the conductivity via broadening of the diffusion pathways or introducing more mobile charge carriers. Addressing the electron mobility, doping of the materials with transition metals has been shown to increase the electronic conductivity in certain cases by several orders of magnitude.[48] In addition, impedance measurements on Li_8SiP_4 showed that the sample preparation has a strong influence on the observed Li^+ ion conductivity. Preliminary optimization using spark-plasma sintering of Li_8SiP_4 shows a further increased Li^+ ion conductivity of up to 10^{-4} S cm^{-1} at room temperature, while the investigated phase seems to be stable against this harsh preparation method. This technique will be further investigated.

The ordering of $[GeP_4]^{8-}$ tetrahedra in the two polymorphs hints for the possibility of more polymorphs with other ion ordering. In addition, the view of the structures as derivatives of *ccp* of P atoms and Li^+ ions occupying tetrahedral and octahedral voids allows the outlook that also compounds with an even higher Li^+ content may be realized.

ASSOCIATED CONTENT

Supporting Information

The Supporting Information is available free of charge on the ACS Publications website at DOI: 10.1021/acs.chemmater.8b02759.

Crystallographic information (CIF)

Crystallographic information (CIF)

Details of the crystal structure determinations of α- and β-Li_8GeP_4, coordination polyhedra of α- and β-Li_8GeP_4, group−subgroup relationship between CaF_2 and α- and β-Li_8GeP_4, investigation of spark plasma-sintered samples of Li_8SiP_4, dc polarization measurements, phase transition experiments, ^{31}P NMR spectroscopy, IR spectra of Li_8SiP_4 and α- and β-Li_8GeP_4 (PDF)

AUTHOR INFORMATION

Corresponding Author

*E-mail: thomas.faessler@lrz.tu-muenchen.de.

ORCID

Wilhelm Klein: 0000-0002-6351-9921

Wolfgang G. Zeier: 0000-0001-7749-5089

Thomas F. Fässler: 0000-0001-9460-8882

Author Contributions

‡H.E. and S.S.: These authors contributed equally to this work.

Notes

The authors declare no competing financial interest.

ACKNOWLEDGMENTS

The authors greatly acknowledge Tassilo Restle and Maria Müller for DSC measurements, Johannes Sicklinger for IR spectroscopy, Johannes Landesfeind and Prof. Hubert A. Gasteiger for advice on impedance data, Lucas Niederegger for first synthetic experiments, and Prof. Ulrich Häussermann and co-workers for spark plasma sintering of the Li_8SiP_4 sample.

REFERENCES

(1) Richards, W. D.; Miara, L. J.; Wang, Y.; Kim, J. C.; Ceder, G. Interface Stability in Solid-State Batteries. *Chem. Mater.* **2016**, *28*, 266−273.

(2) Robinson, A. L.; Janek, J. Solid-state batteries enter EV fray. *MRS Bull.* **2014**, *39*, 1046−1047.

(3) Janek, J.; Zeier, W. G. A solid future for battery development. *Nat. Energy* **2016**, *1*, 16141.

(4) Kato, Y.; Hori, S.; Saito, T.; Suzuki, K.; Hirayama, M.; Mitsui, A.; Yonemura, M.; Iba, H.; Kanno, R. High-power all-solid-state batteries using sulfide superionic conductors. *Nat. Energy* **2016**, *1*, 16030.

(5) Bachman, J. C.; Muy, S.; Grimaud, A.; Chang, H.-H.; Pour, N.; Lux, S. F.; Paschos, O.; Maglia, F.; Lupart, S.; Lamp, P.; Giordano, L.; Shao-Horn, Y. Inorganic Solid-State Electrolyte for Lithium Batteries: Mechanisms and Properties Governing Ion Conduction. *Chem. Rev.* **2016**, *116*, 140−162.

(6) Kraft, M. A.; Culver, S. P.; Calderon, M.; Böcher, F.; Krauskopf, T.; Senyshyn, A.; Dietrich, C.; Zevalkink, A.; Janek, J.; Zeier, W. G. Influence of Lattice Polarizability on the Ionic Conductivity in the Lithium Superionic Agyrodites Li_6PS_5X (X = Cl, Br, I). *J. Am. Chem. Soc.* **2017**, *139*, 10909−10918.

(7) Krauskopf, T.; Pompe, C.; Kraft, M. A.; Zeier, W. G. Influence of Lattice Dynamics on Na^+ Transport in the Solid Electrolyte $Na_3PS_{4-x}Se_x$. *Chem. Mater.* **2017**, *29*, 8859−8869.

(8) Krauskopf, T.; Culver, S. P.; Zeier, W. G. Bottleneck of Diffusion and Inductive Effects in $Li_{10}Ge_{1-x}Sn_xP_2S_{12}$. *Chem. Mater.* **2018**, *30*, 1791−1798.

(9) Muy, S.; Bachman, J. C.; Giordano, L.; Chang, H.-H.; Abernathy, D. L.; Bansal, D.; Delaire, O.; Hori, S.; Kanno, R.; Maglia, P.; Lupart, S.; Lamp, P.; Shao-Horn, Y. Tuning mobility and stability of lithium ion conductors based on lattice dynamics. *Energy Environ. Sci.* **2018**, *11*, 850−859.
(10) Wang, Y.; Richards, W. D.; Ong, S. P.; Miara, L. J.; Kim, J. C.; Mo, Y.; Ceder, G. Design principles for solid-state lithium superionic conductors. *Nat. Mater.* **2015**, *14*, 1026−1031.
(11) Hori, S.; Suzuki, K.; Hirayama, M.; Kato, Y.; Saito, T.; Yonemura, M.; Kanno, R. Synthesis, structure, and ionic conductivity of solid solution $Li_{10+\delta}M_{1+\delta}P_{2-\delta}S_{12}$ (M = Si, Sn). *Faraday Discuss.* **2014**, *176*, 83−94.
(12) Bron, P.; Johansson, S.; Zick, K.; Schmedt auf der Günne, J.; Dehnen, S.; Roling, B. $Li_{10}SnP_2S_{12}$: An Affordable Lithium Superionic Conductor. *J. Am. Chem. Soc.* **2013**, *135*, 15694−15697.
(13) Shin, B. R.; Nam, Y. J.; Oh, D. Y.; Kim, D. H.; Kim, J. W.; Jung, Y. S. Comparative Study of TiS_2/Li-In All-Solid-State Lithium Batteries Using Glass-Ceramic Li_3PS_4 and $Li_{10}GeP_2S_{12}$ Solid Electrolytes (TiS_2). *Electrochim. Acta* **2014**, *146*, 395−402.
(14) Jung, Y. S.; Oh, D. Y.; Nam, Y. J.; Park, K. H. Issues and Challenges for Bulk-Type All-Solid-State Rechargeable Lithium Batteries Using Sulfide Solid Electrolytes. *Isr. J. Chem.* **2015**, *55*, 472−485.
(15) Zhang, W.; Weber, D. A.; Weigand, H.; Arlt, T.; Manke, I.; Schröder, D.; Koerver, R.; Leichtweiss, T.; Hartmann, P.; Zeier, W. G.; Janek, J. Interfacial Processes and Influence of Composite Cathode Microstructure Controlling the Performance of All-Solid-State Lithium Batteries. *ACS Appl. Mater. Interfaces* **2017**, *9*, 17835−17845.
(16) Kato, Y.; Shiotani, S.; Morita, K.; Suzuki, K.; Hirayama, M.; Kanno, R. All-Solid-State Batteries with Thick Electrode Confugurations. *J. Phys. Chem. Lett.* **2018**, *9*, 607−613.
(17) Zhang, W.; Leichtweiß, T.; Culver, S. P.; Koerver, R.; Das, D.; Weber, D. A.; Zeier, W. G.; Janek, J. The Detrimental Effects of Carbon Additives in $Li_{10}GeP_2S_{12}$-Based Solid-State Batteries. *ACS Appl. Mater. Interfaces* **2017**, *9*, 35888−35896.
(18) Hu, Y.-S. Batteries: Getting Solid. *Nat. Energy* **2016**, *1*, 16042.
(19) Toffoletti, L.; Kirchhain, H.; Landesfeind, J.; Klein, W.; van Wüllen, L.; Gasteiger, H. A.; Fässler, T. F. Lithium Ion Mobility in Lithium Phosphidosilicates: Crystal Structure, ^{7}Li, ^{29}Si and ^{31}P MAS NMR Spectroscopy, and Impedance Spectroscopy of Li_8SiP_4 and Li_2SiP_2. *Chem. - Eur. J.* **2016**, *22*, 17635−17645.
(20) Juza, R.; Schulz, W. Ternäre Posphide und Arsenide des Lithiums mit Elementen der 3. und 4. Gruppe. *Z. Anorg. Allg. Chem.* **1954**, *275*, 65−78.
(21) Eickhoff, H.; Toffoletti, L.; Klein, W.; Raudaschl-Sieber, G.; Fässler, T. F. Synthesis and Characterization of the Lithium-Rich Phosphidosilicates $Li_{10}Si_2P_6$ and $Li_3Si_3P_7$. *Inorg. Chem.* **2017**, *56*, 6688−6694.
(22) Haffner, A.; Bräuniger, T.; Johrendt, D. Supertetrahedral Networks and Lithium-Ion Mobility in Li_2SiP_2 and $LiSi_2P_3$. *Angew. Chem., Int. Ed.* **2016**, *55*, 13585−13588.
(23) Eisenmann, B.; Somer, M. K_2SiP_2, ein Phosphidopholysilikat-(IV)/K_2SiP_2, a Phosphidopolysilicate (IV). *Z. Naturforsch., B: J. Chem. Sci.* **1984**, *39*, 736−738.
(24) Eisenmann, B.; Jordan, H.; Schäfer, H. Zintl-phasen mit komplexen anionen: Darstellung und struktur der o-phosphidosilikate und − germanate $E^{II}_4E^{IV}P_4$ (MIT E^{II} = Ca, Sr, Ba und E^{IV} = Si, Ge). *Mater. Res. Bull.* **1982**, *17*, 95−99.
(25) Eisenmann, B.; Somer, M. Zur Kenntnis von Oligophosphidosilikaten (IV) und -germanaten (IV): $Na_{10}Si_2P_6$ und $Na_{10}Ge_2P_6$. *Z. Naturforsch.* **1985**, *40b*, 886−890.
(26) Feng, K.; Kang, L.; Yin, W.; Hao, W.; Lin, Z.; Yao, J.; Wu, Y. KSi_2P_3: A new layered phosphidopolysilicate (IV). *J. Solid State Chem.* **2013**, *205*, 129−133.
(27) Kaiser, P.; Jeitschko, W. Preparation and Crystal Structures of the Ternary Compounds Ag_2SiP_2 and AuSiP. *Z. Naturforsch., B: J. Chem. Sci.* **1997**, *52*, 462−468.
(28) Xu, R.-c.; Xia, X.-h.; Li, S.-h.; Zhang, S.-z.; Wang, X.-l.; Tu, J.-p. All-solid-state lithium-sulfur batteries based on a newly designed $Li_7P_{2.9}Mn_{0.1}S_{10.7}I_{0.3}$ superionic conductor. *J. Mater. Chem. A* **2017**, *5*, 6310−6317.
(29) Chen, M.; Yin, X.; Reddy, M. V.; Adams, S. All-solid-state MoS_2/Li_6PS_5Br/In-Li batteries as a novel type of Li/S battery. *J. Mater. Chem. A* **2015**, *3*, 10698−10702.
(30) Huang, B.; Yao, X.; Huang, Z.; Guan, Y.; Jin, Y.; Xu, X. Li_3PO_4-doped $Li_7P_3S_{11}$ glass-ceramic electrolytes with enhanced lithium ion conductivities and application in all-solid-state batteries. *J. Power Sources* **2015**, *284*, 206−211.
(31) Yu, R.; Du, Q.-X.; Zou, B.-K.; Wen, Z.-Y.; Chen, C.-H. Synthesis and characterization of perovskite-rype $(Li,Sr)(Zr,Nb)O_3$ quaternary solid electrolyte for all-solid-state batteries. *J. Power Sources* **2016**, *306*, 623−629.
(32) Xu, R.-c.; Xia, X.-h.; Wang, X.-l.; Xia, Y.; Tu, J.-p. Tailored Li_2S-P_2S_5 glass-ceramic electrolyte by MoS_2 doping, possessing high ionic conductivity for all-solid-state lithium-sulfur batteries. *J. Mater. Chem. A* **2017**, *5*, 2829−2834.
(33) Dietrich, C.; Weber, D. A.; Culver, S.; Senyshyn, A.; Sedlmaier, S. J.; Indris, S.; Janek, J.; Zeier, W. G. Synthesis, Structural Characterization, and Lithium Ion Conductivity of the Lithium Thiophosphate $Li_2P_2S_6$. *Inorg. Chem.* **2017**, *56*, 6681−6687.
(34) *WinXPOW*; STOE & Cie GmbH,: Darmstadt, Germany, 2011.
(35) Rodriguez-Carvajal, J.; Gonzales-Platas, J. *FullProf Suite 2.05*; Institute Laue-Langevin Grenoble: Grenoble, France, 2011.
(36) *APEX 2: APEX suite of crystallographic software*, version 2008.4; Bruker AXS Inc.: Madison, WI, 2008.
(37) Sheldrick, G. M. SHELXT − Integrated space-group and crystal-structure determination. *Acta Crystallogr., Sect. A: Found. Adv.* **2015**, *71*, 3−8.
(38) *Proteus Thermal Analysis V4.8.2*; Netzsch-Gerätebau GmbH: Selb, 2006.
(39) Bielecki, A.; Burum, D. P. Temperature Dependence of ^{207}Pb MAS Spectra of Solid Lead Nitrate. An Accurate, Sensitive Thermometer for Variable-Temperature MAS. *J. Magn. Reson., Ser. A* **1995**, *116*, 215−220.
(40) Motte, J. P.; Greenwood, N. N. Etude par effet Mössbauer de la structure et des propriétés de diffusion de la phase antifluorine nonstoechiométrique: Li_8SnP_4. *J. Solid State Chem.* **1975**, *13*, 41−48.
(41) Feng, K.; Yin, W.; He, R.; Lin, Z.; Jin, S.; Yao, J.; Fu, P.; Wu, Y. $NaGe_3P_3$: a new ternary germanium phosphide featuring an unusual $[Ge_3P_7]$ ring. *Dalton Trans.* **2012**, *41*, 484−489.
(42) Lee, K.; Synnestvedt, S.; Bellard, M.; Kovnir, K. GeP and $(Ge_{1-x}Sn_x)(P_{1-y}Ge_y)$ (x≈0.12, y≈0.05): Synthesis, structure, and properties of two-dimensional layered tetrel phosphides. *J. Solid State Chem.* **2015**, *224*, 62−70.
(43) Jørgensen, J.-E.; Rasmussen, S. E. Growth of chromium silicide, Cr_3Si, crystals. *J. Cryst. Growth* **1979**, *47*, 124−126.
(44) de Klerk, N. J. J.; Rosłoń, I.; Wagemaker, M. Diffusion Mechanism of Li Agyrodite Solid Electrolytes for Li-Ion Batteries and Prediction of Optimized Halogen Doping: The Effect of Li Vacancies, Halogens, and Halogen Disorder. *Chem. Mater.* **2016**, *28*, 7955−7963.
(45) Waugh, J. S.; Fedin, E. I. On determination of barriers to hindered rotation in solid. *Fiz. Tverd. Tela* **1962**, *4*, 2233−2237.
(46) Waugh, J. S.; Fedin, E. I. Determination of hindered-rotation barriers in solids. *Soviet Physics-Solid State* **1963**, *4*, 1633−1636.
(47) Bärnighausen, H. Group-subgroup relationis between space groups: a useful tool in crystal chemistry. *MATCH* **1980**, *9*, 139−175.
(48) Chung, S.-Y.; Bloking, J. T.; Chiang, Y.-M. Eletronically conductive phosphor-olivines as lithium storage electrodes. *Nat. Mater.* **2002**, *1*, 123−128.

DOI: 10.1021/acs.chemmater.8b02759
Chem. Mater. 2018, 30, 6440−6448

Supporting Information

Lithium Phosphidogermanates α- and β-Li_8GeP_4 – A Novel Compound Class with Mixed Li^+ Ionic and Electronic Conductivity

Henrik Eickhoff,[a,+] Stefan Strangmüller,[a,+] Wilhelm Klein,[a] Holger Kirchhain,[b] Christian Dietrich,[c] Wolfgang G. Zeier,[c] Leo van Wüllen,[b] and Thomas F. Fässler*[a]

Content

Details of the crystal structure determinations of α- and β-Li_8GeP_4

Table S1. Details of the Rietveld structure refinements of α- and β-Li_8GeP_4.

empirical formula	α-Li_8GeP_4	β-Li_8GeP_4
T / K	293	293
formula weight / g mol^{-1}	252.0	252.0
space group (no.)	$Pa\bar{3}$ (205)	$P\bar{4}3n$ (218)
unit cell parameters / Å	a = 11.80203(7)	a = 11.77294(6)
Z	8	8
V / Å^3	1643.88(2)	1631.75(1)
$\rho_{calc.}$ / g cm^{-3}	2.037	2.053
θ range / deg	5.006-89.846	5.015-89.870
R_p	2.55	3.05
R_{wp}	3.58	4.61
R_{exp}	2.43	2.47
X^2	2.17	3.47
GOF	1.5	1.9
R_{Bragg}	2.87	5.51
R_f	2.68	5.58

Table S2. Atomic coordinates and isotropic atomic displacement parameters for α-Li_8GeP_4.

Atom	Wyckoff positions	x	y	z	U_{eq} / Å^2
Li1	8*c*	0.386(1)	0.386(1)	0.386(1)	0.027(1)
Li2	24*d*	0.388(1)	0.137(2)	0.126(1)	0.027(1)
Li3	24*d*	0.377(2)	0.379(1)	0.113(1)	0.027(1)
Li4	4*a*	0	0	0	0.027(1)
Li5	4*b*	0.5	0.5	0.5	0.027(1)
Ge	8*c*	0.1272(1)	0.1272(1)	0.1272(1)	0.0239(3)
P1	8*c*	0.2437(4)	0.2437(4)	0.2437(4)	0.031(2)
P2	24*d*	0.0062(3)	0.2439(2)	0.0135(1)	0.0198(7)

Table S3. Selected interatomic distances in α-Li_8GeP_4.

atom pair		*d* / Å		atom pair		*d* / Å	
Li1	Li5	1×	2.33(1)	Li4	Li3	6×	2.43(2)
	P2	3×	2.50(1)		Ge	2×	2.601(2)
	Li2	3×	2.84(2)		P2	6×	2.884(1)
	P1	1×	2.91(1)	Li5	Li1	2×	2.33(1)
	Li3	3×	3.23(2)		Li2	6×	2.56(2)
Li2	P1	1×	2.53(2)		P2	6×	3.028(1)
	Li5	1×	2.56(2)	Ge	P1	1×	2.381(5)
	P2	1×	2.58(2)		P2	3×	2.396(3)
	P2	1×	2.63(2)		Li4	1×	2.601(2)
	P2	1×	2.65(2)		Li3	3×	2.94(2)
	Li1	1×	2.84(2)		Li2	3×	3.08(2)
	Li3	1×	2.87(2)	P1	Ge	1×	2.381(5)
	Li2	2×	2.94(3)		Li2	3×	2.53(2)
	Li3	1×	2.97(2)		Li3	3×	2.72(2)
	Ge	1×	3.08(1)		Li1	1×	2.91(1)
Li3	Li4	1×	2.43(2)	P2	Ge	1×	2.396(3)
	P2	1×	2.47(2)		Li3	1×	2.47(2)
	P2	1×	2.52(2)		Li1	1×	2.50(1)
	P2	1×	2.58(2)		Li3	1×	2.52(2)
	P1	1×	2.72(2)		Li2	1×	2.58(2)
	Li3	2×	2.79(3)		Li3	1×	2.58(2)
	Li2	1×	2.87(2)		Li2	1×	2.63(2)
	Ge	1×	2.94(2)		Li2	1×	2.65(2)
	Li2	1×	2.97(3)		Li4	1×	2.884(2)
	Li1	1×	3.23(2)		Li5	1×	3.028(2)

Table S4. Atomic coordinates and isotropic atomic displacement parameters for β-Li_8GeP_4.

Atom	Wyckoff positions	*x*	*y*	*z*	S.O.F.	U_{eq} / Å^2
Li1	6*b*	0	1/2	0	0.9(1)	0.004(2)
Li2	6*d*	0	1/2	1/4		0.004(2)
Li3	8*e*	0.255(3)	0.255(3)	0.255(3)		0.004(2)
Li4	12*f*	0	0.260(2)	0		0.004(2)
Li5	24*i*	0.244(2)	0.235(1)	0.007(3)	0.875(1)	0.004(2)
Li6	24*i*	0.354(2)	0.381(2)	0.172(2)	0.483(1)	0.004(2)
Ge1	2*a*	1/2	1/2	1/2		0.0119(8)
Ge2	6*c*	1/4	1/2	0		0.0162(4)
P1	8*e*	0.3839(2)	0.3839(2)	0.3839(2)		0.021(5)
P2	24*i*	0.1372(2)	0.3863(1)	0.1228(1)		0.020(2)

Results of the single crystal structure determination of β-Li_8GeP_4

Table S5. Atomic coordinates and isotropic atomic displacement parameters for β-Li_8GeP_4.

Atom	Wyckoff positions	*x*	*y*	*z*	S.O.F.	U_{eq} / Å^2
Li1	6*b*	0	1/2	0	0.78(3)	0.004(6)
Li2	6*d*	0	1/2	1/4		0.021(6)
Li3	8*e*	0.255(1)	0.255(1)	0.255(1)		0.008(4)
Li4	12*f*	0	0.257(1)	0		0.020(5)
Li5	24*i*	0.240(1)	0.241(1)	0.008(2)	0.887(9)	0.034(6)
Li6	24*i*	0.379(2)	0.374(3)	0.125(2)	0.502(9)	0.050(1)
Ge1	2*a*	1/2	1/2	1/2		0.0097(5)
Ge2	6*c*	1/4	1/2	0		0.0128(3)
P1	8*e*	0.3839(2)	0.3839(2)	0.3839(2)		0.0111(8)
P2	24*i*	0.1372(2)	0.3863(1)	0.1228(1)		0.0136(4)

Table S6. Anisotropic displacement parameters (Å^2) for β-Li_8GeP_4.

Atom	U_{11}	U_{22}	U_{33}	U_{23}	U_{13}	U_{12}
Li2	0.021(8)	0.021(8)	0.02(1)	0	0	0
Li3	0.008(4)	0.008(4)	0.008(4)	0.002(3)	0.002(3)	0.002(3)
Li4	0.019(8)	0.014(7)	0.026(8)	0	0.000(6)	0
Li5	0.041(9)	0.026(8)	0.03(1)	0.005(8)	-0.008(8)	-0.002(6)
Ge1	0.0097(5)	0.0097(5)	0.0097(5)	0	0	0
Ge2	0.0110(7)	0.0137(4)	0.0137(4)	0	0	0
P1	0.0111(8)	0.0111(8)	0.0111(8)	-0.0002(5)	-0.0002(5)	-0.0002(5)
P2	0.0144(6)	0.0134(9)	0.0130(9)	0.0008(5)	0.0021(6)	-0.0010(6)

Table S7. Selected interatomic distances in β-Li_8GeP_4.

atom pair				atom pair			
Li1	Li6	4×	2.53(2)	Li6	Li3	1×	2.54(2)
	P2	4×	2.550(1)		Li5	1×	2.57(4)
	Li4	2×	2.87(1)		Ge2	1×	2.59(3)
	Ge2	2×	2.94578(3)		Li5	1×	2.65(4)
	Li2	2×	2.94578(3)		Li5	1×	2.66(2)
Li2	Li6	4×	2.51(3)		P2	1×	2.81(4)
	P2	4×	2.579(2)		P2	1×	2.86(3)
	Li1	2×	2.94578(3)		P2	1×	2.94(3)
	Li5	4×	3.07(1)		P2	1×	2.96(3)
Li3	Li6	2×	2.54(2)		P2	1×	3.04(2)
	P2	3×	2.596(8)		P1	1×	3.06(2)
	P1	1×	2.63(3)	Ge1	P1	4×	2.369(3)
	Li5	3×	2.92(4)		Li4	6×	3.02(1)
	Li5	3×	2.98(4)	Ge2	P2	4×	2.378(2)
Li4	Li6	2×	2.49(2)		Li6	4×	2.58(4)
	P1	2×	2.545(9)		Li1	2×	2.94578(3)
	P2	2×	2.655(8)		Li5	4×	3.06(1)
	Li5	2×	2.84(1)	P1	Ge1	1×	2.369(3)
	Li5	2×	2.84(1)		Li5	3×	2.53(2)
	Li1	1×	2.87(1)		Li4	3×	2.545(9)
	Ge1	1×	3.02(1)		Li3	1×	2.63(3)
Li5	P2	1×	2.50(1)		Li6	3×	3.06(2)
	P1	1×	2.53(2)	P2	Ge2	1×	2.378(2)
	P2	1×	2.60(2)		Li5	1×	2.50(1)
	P2	1×	2.69(1)		Li1	1×	2.550(1)
	Li6	1×	2.58(4)		Li2	1×	2.579(2)
	Li6	1×	2.65(4)		Li3	1×	2.596(8)
	Li6	1×	2.65(2)		Li5	1×	2.60(2)
	Li4	2×	2.84(1)		Li4	1×	2.655(8)
	Li3	1×	2.92(3)		Li5	1×	2.69(1)
	Li3	1×	2.98(3)		Li6	1×	2.81(2)
	Ge2	1×	3.06(1)		Li6	1×	2.86(3)
	Li2	1×	3.07(1)		Li6	1×	2.94(3)
Li6	Li4	1×	2.49(2)		Li6	1×	2.96(3)
	Li2	1×	2.51(3)		Li6	1×	3.04(2)
	Li1	1×	2.53(2)				

Coordination polyhedra of α-and β-Li_8GeP_4

In α-Li_8GeP_4 the Ge atom is surrounded by four P2 atoms in a slightly distorted tetrahedral geometry. The next nearest Li neighbors (3 × Li2, 3 × Li3) are arranged in a distorted octahedral geometry around the Ge atom with one Li4 capping the face spanned by three Li3 atoms. The Li1-3 atoms are each surrounded by one P1 and three P2 atoms building up distorted tetrahedra, whereas the Li4 and Li5 atoms are centered in octahedra formed by six P2 atoms each.

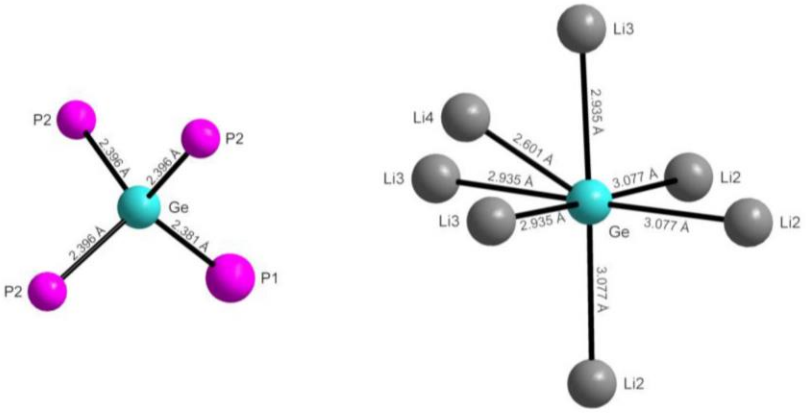

Figure S1. Coordination polyhedra of Ge atoms in α-Li_8GeP_4. The nearest neighbors are arranged in a tetrahedral coordination whereas the next nearest neighbors are arranged in a slightly distorted octahedral arrangement with Li4 capping the trigonal face above the three Li3 atoms.

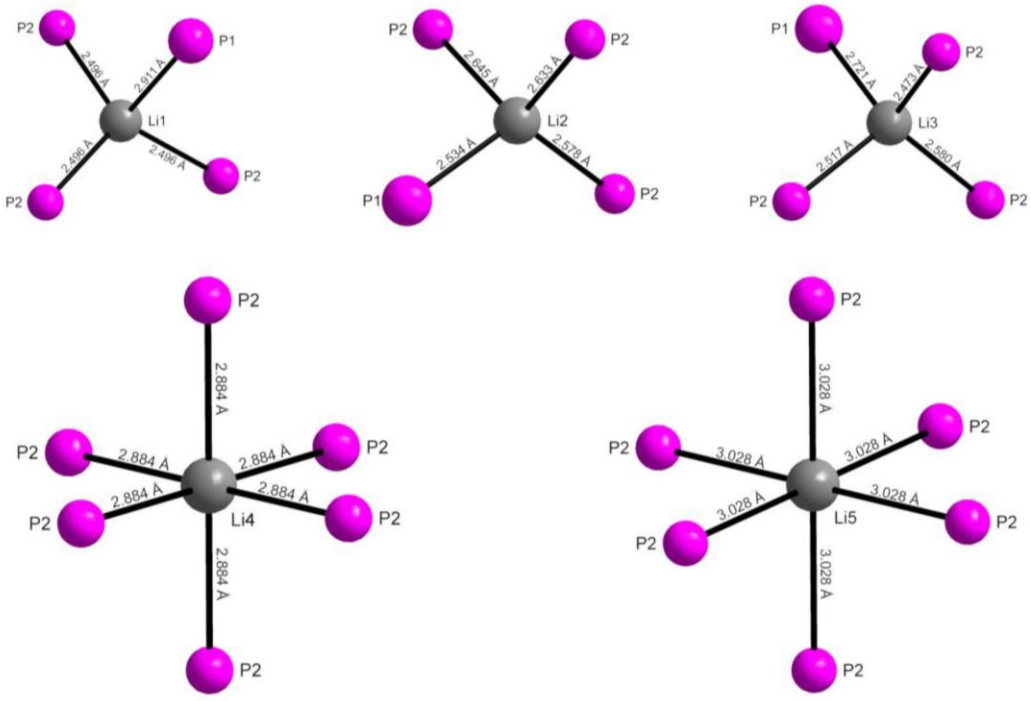

Figure S2. Coordination polyhedra of Li atoms in α-Li_8GeP_4. The nearest neighbors of the atoms Li1, Li2 and Li3 are arranged in a slightly distorted tetrahedral coordination whereas the atoms Li4 and Li5 are surrounded by P atoms in an octahedral arrangement.

In β-Li_8GeP_4 the Ge atoms are centering regular tetrahedra of P atoms. The Ge2 atoms are further surrounded by four Li6 atoms resulting in a slightly distorted cubic arrangement of P and Li atoms. Regarding the next nearest Li neighbors, for Ge1 six Li4, for Ge2 two Li1 and four Li5 atoms are forming distorted octahedra. The Li1 and Li2 atoms are perfectly centered in tetrahedral voids generated by four P2 atoms, while Li3, Li4, and Li5 are surrounded by more irregular tetrahedra of one P1 and three P2 (Li3) or by two P1 and two P2 atoms (Li4, Li5). Li6 is situated in an octahedral void of six P2 atoms.

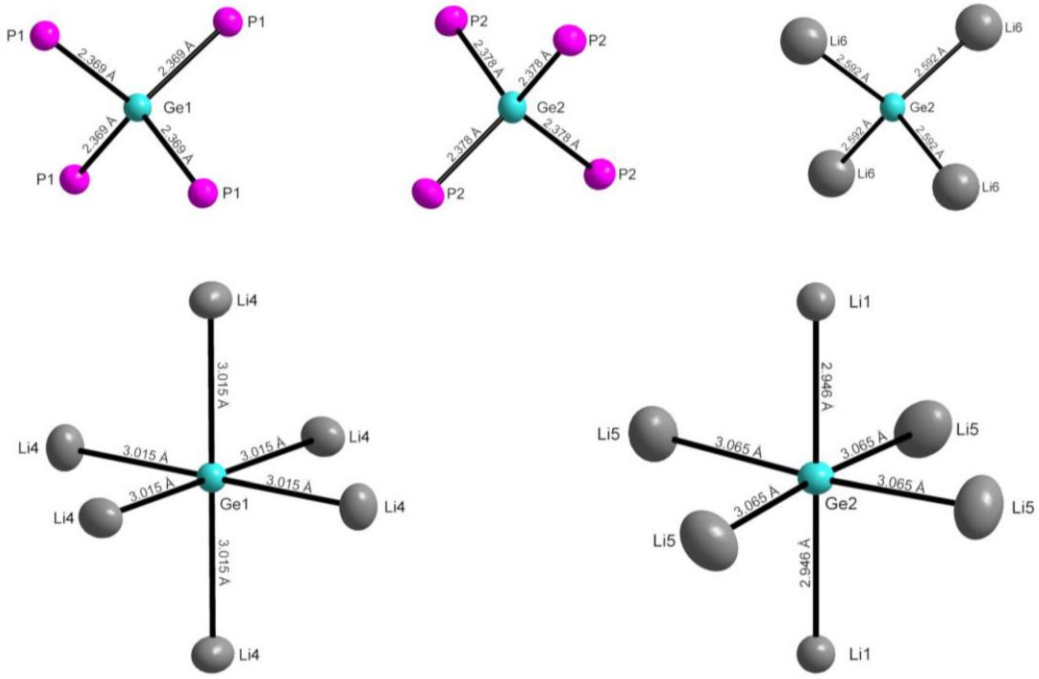

Figure S3. Coordination polyhedra of Ge atoms in β-Li_8GeP_4. The nearest neighbors are arranged in a tetrahedral coordination whereas the next nearest neighbors are arranged in a slightly distorted octahedral arrangement.

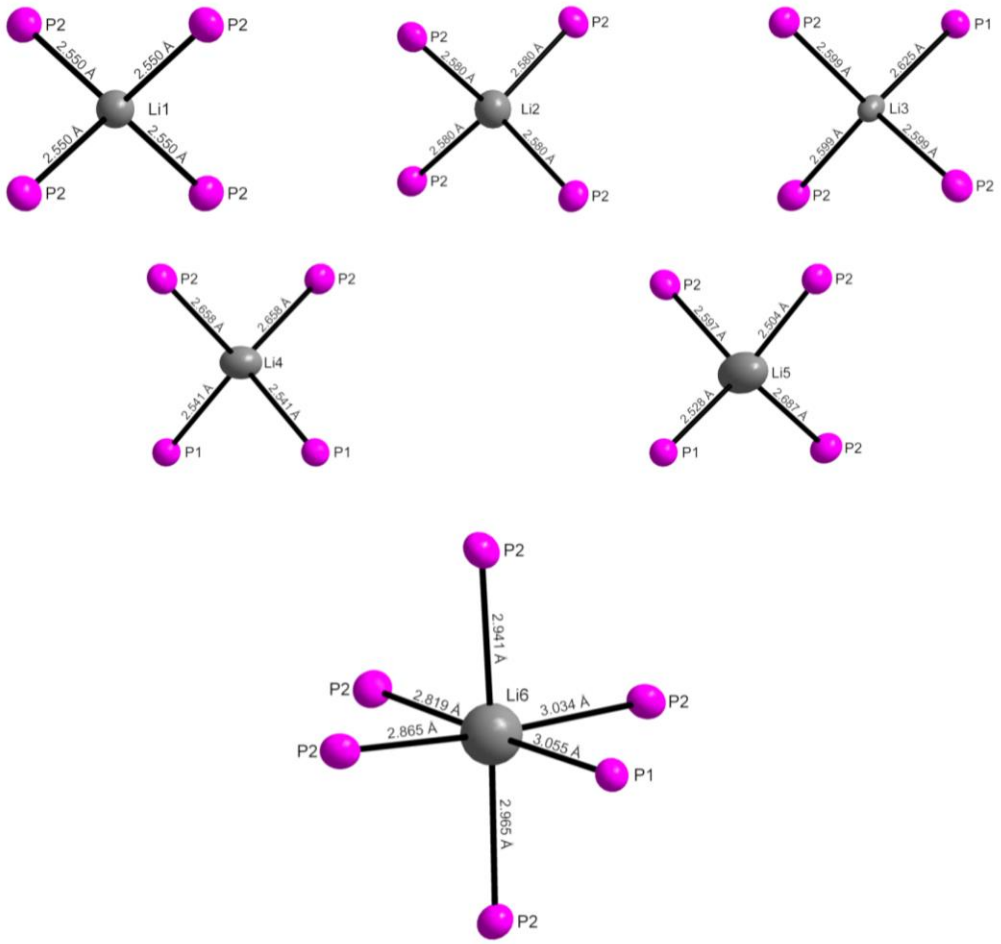

Figure S4. Coordination polyhedra of Li atoms in β-Li_8GeP_4. The nearest neighbors of the Li1 and Li2 atoms are arranged in a tetrahedral coordination, whereas Li3, Li4 and Li5 are surrounded by P atoms in a slightly distorted tetrahedral arrangement. The nearest neighbors of Li6 are arranged in a slightly distorted octahedral configuration.

Group-subgroup relationship between CaF_2 and α-and β-Li_8SiP_4

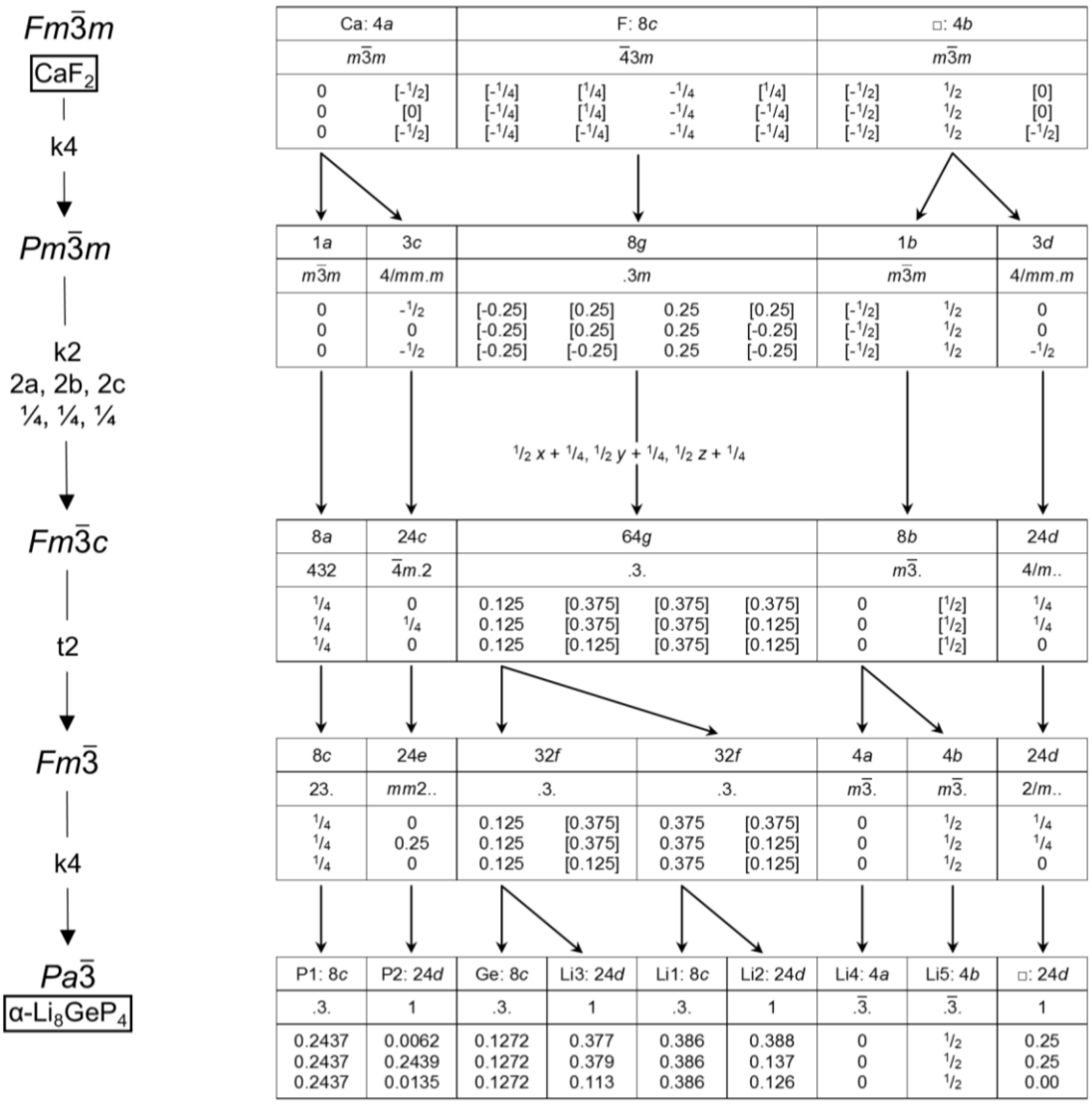

Figure S5. Symmetry degradation according to Bärnighausen for α-Li_8GeP_4 starting from CaF_2.

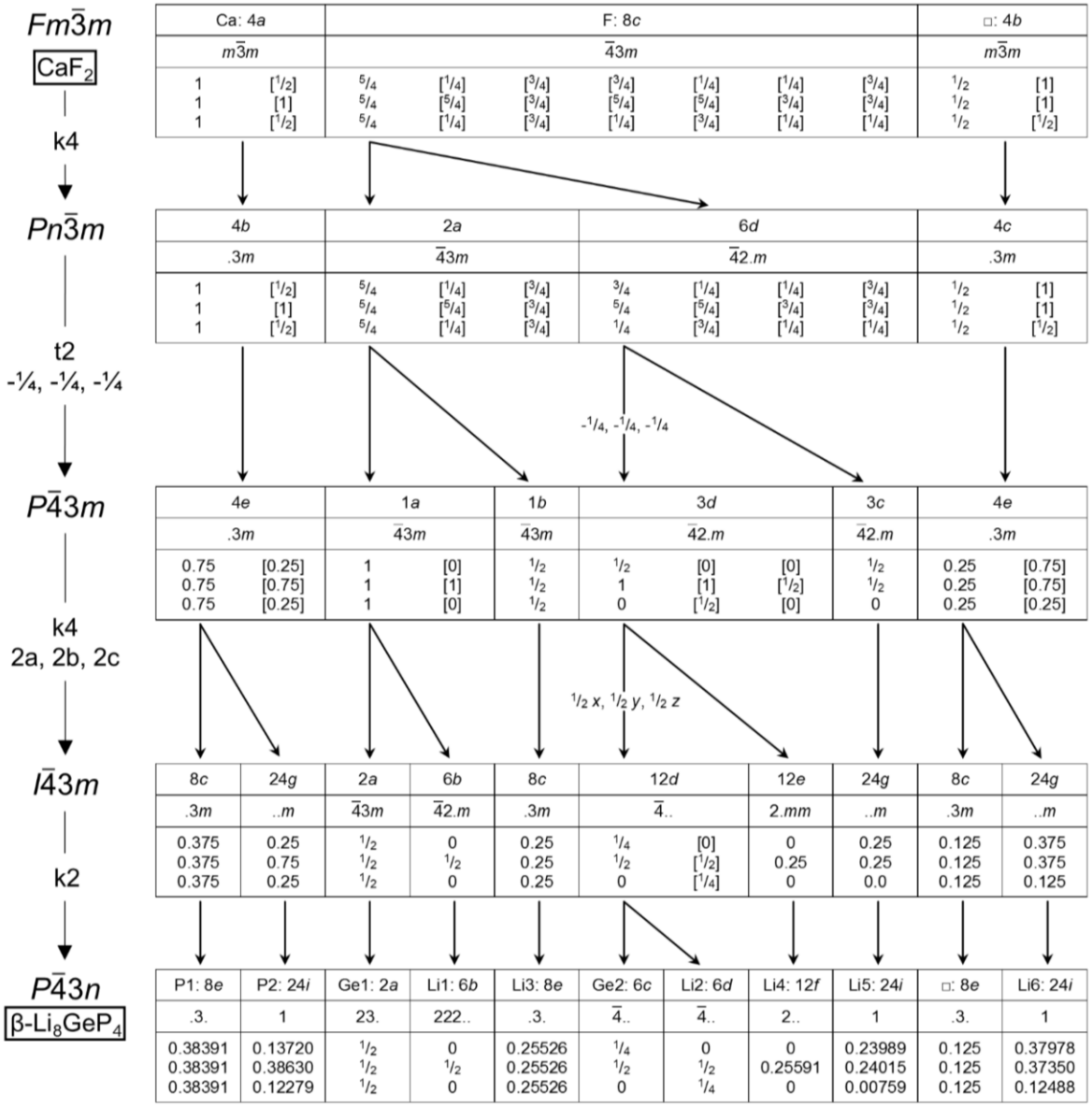

Figure S6. Symmetry degradation according to Bärnighausen for β-Li_8GeP_4 starting from CaF_2.

Table S8. List of cell parameters a obtained from indexing different samples with average value $\bar{a}$.

α-Li_8GeP_4	**β-Li_8GeP_4**
$\bar{a}$ = 11.8056(4) Å	**$\bar{a}$ = 11.7754(4) Å**
a = 11.80203(7) Å	a = 11.77294(6) Å
a = 11.7964(2) Å	a = 11.7722(1) Å
a = 11.8028(7) Å	a = 11.7668 (3) Å
a = 11.8112(3) Å	a = 11.7541(4) Å
a = 11.8123(4) Å	a = 11.7927(7) Å
a = 11.8091(5) Å	a = 11.7939(8) Å

Investigation of spark plasma sintered samples of Li_8SiP_4

X-ray powder diffraction measurements and Rietveld refinement of the spark plasma sintered sample showed a composition of 98.2(3) % Li_8SiP_4 and 1.8(2) % Li_3P.

The pellet with a cross section area of 26 mm^2 and a height of 5.0 mm was plated with Au in a sputtering device (Jeol, JFC-1300) for 120 s with a current of 10 mA. For the measurement the pellet was sandwiched between two gold discs (∅ = 13 mm, 25 µm, >99.965%, Advent Research Materials Ltd.) for improving contacts, two carbon tissues (∅ = 12 mm, 360 µm, Sainergy Fuel Cell India Pvt Ltd.) and copper spacers (∅ = 13 mm). This stack was inserted into a steel cell body and sealed. In the sealed cell the carbon cloths were compressed to 25-30% of their original thickness resulting in a compression pressure of ca. 10 MPa.

Impedance spectra were recorded in a temperature range of 0-75 °C using a VMP3 multichannel workstation (Biologic) at frequencies from 500 kHz to 50 mHz with an amplitude of 50 mV. The partial electronic conductivity was determined using a polarization method with voltages of 50 mV, 100 mV and 150 mV.

The measured AC impedance curves were fitted with series circuits of two CPE with parallel resistances. The sample shows an ionic conductivity of σ_{Li}(sintered Li_8SiP_4) = $8.2 \cdot 10^{-5}$ S cm^{-1} at temperatures of 20 °C. Interpolating the ionic conductivity to estimate the conductivity at 25 °C yielded a doubled conductivity of $1.1 \cdot 10^{-4}$ S cm^{-1} compared to the pressed powder. An activation energy of 40 kJ mol^{-1} and an electronic conductivity increased by one order of magnitude to σ_{e^-}(sintered Li_8SiP_4) = $5.1 \cdot 10^{-7}$ S cm^{-1} were observed.

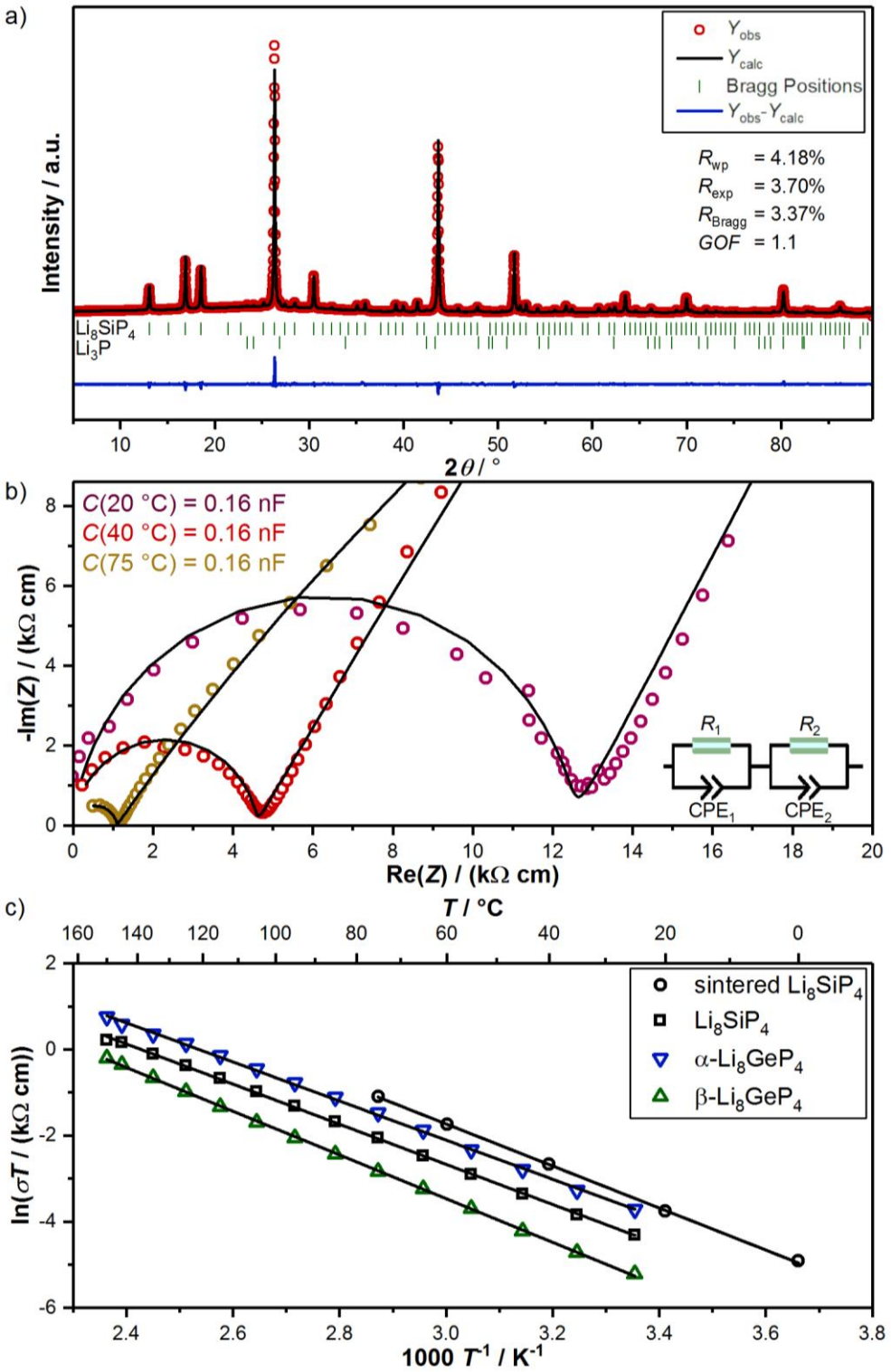

Figure S7. a) Rietveld analysis of X-ray powder diffraction pattern of spark plasma sintered Li_8SiP_4. b) Normalized Nyquist plots of spark plasma sintered Li_8SiP_4 with observed data at 20 °C (largest semicircle), 40 °C (medium semicircle) and 75 °C (smallest semicircle), fitted curves (red) and equivalent circuit. c) Arrhenius plot of spark plasma sintered and powder samples.

DC polarization measurements

DC polarization measurements with higher applied voltages showed a non-linear I-V relationship (Figure S9). This might correlate with an issue observed in the DC polarization curve of α-Li_8GeP_4 of an increasing current after one hour of equilibration, which could be the result of a lithium deposition at the pellet surface or a reaction with the electrodes.

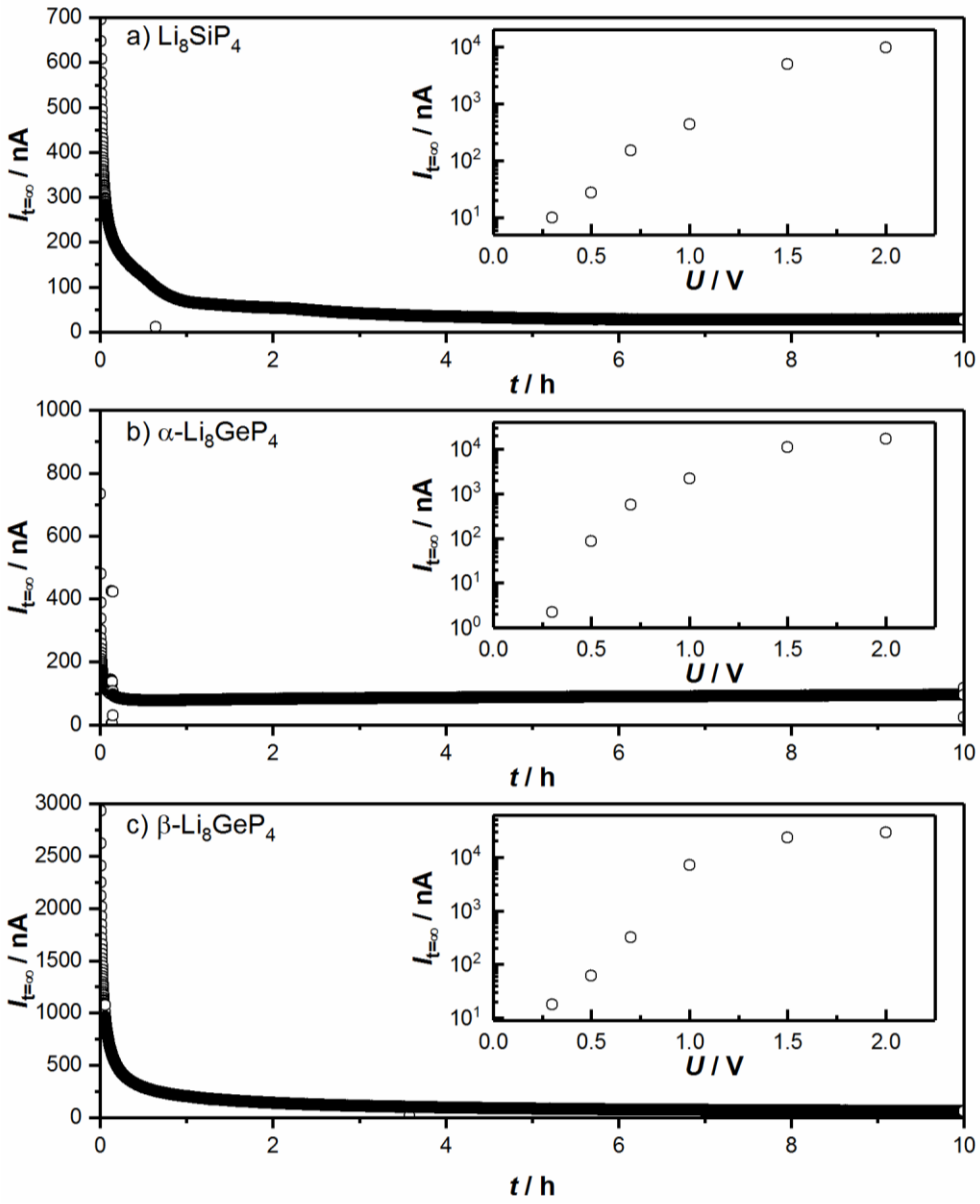

Figure S8. Polarization curves of a) Li_8SiP_4, b) α-Li_8GeP_4 and c) β-Li_8GeP_4 obtained at 500 mV and current $I_{t=\infty}$ depending on the applied voltage U (box inserts).

Phase transition experiments

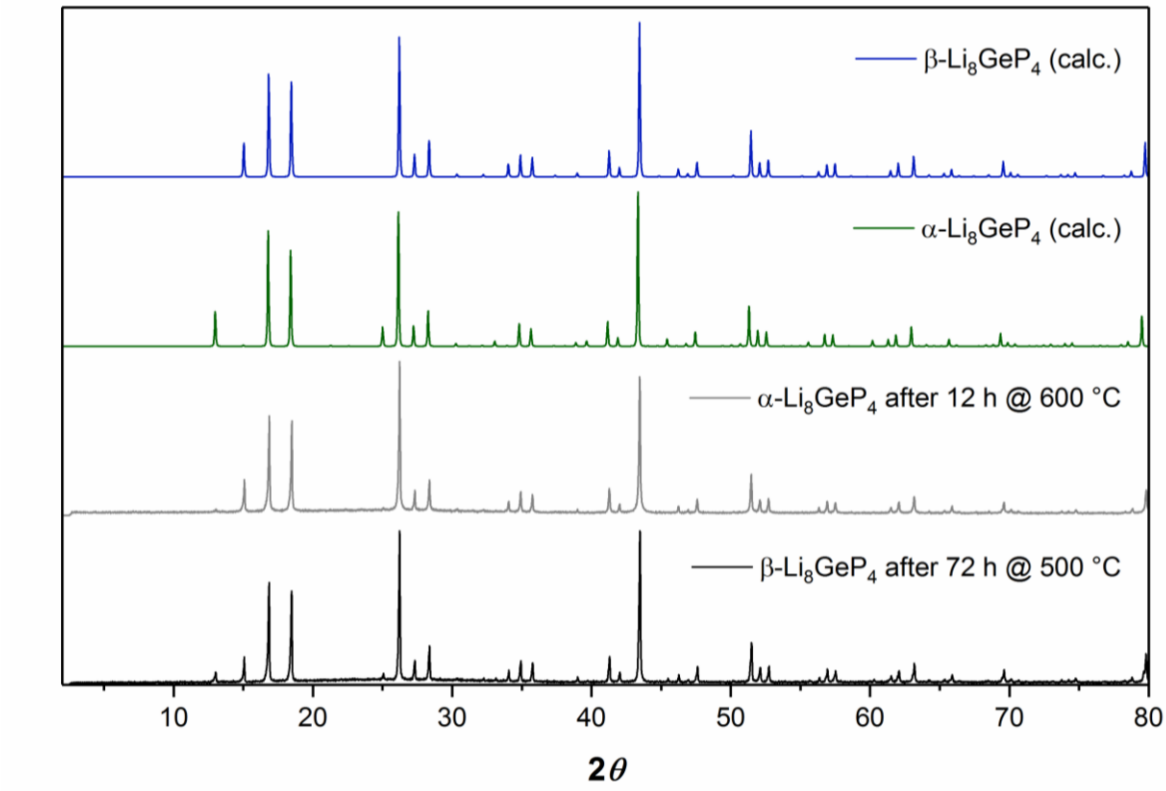

Figure S9. X-ray powder diffractogram of β-Li_8GeP_4 after annealing at 500 °C for 72 h (black) and of α-Li_8GeP_4 after annealing at 600 °C for 12 h (gray) compared to calculated X-ray powder diffractograms of α- (red) and β-Li_8GeP_4 (blue). In both experiments a phase transition is observed.

31P-NMR-Spectroscopy

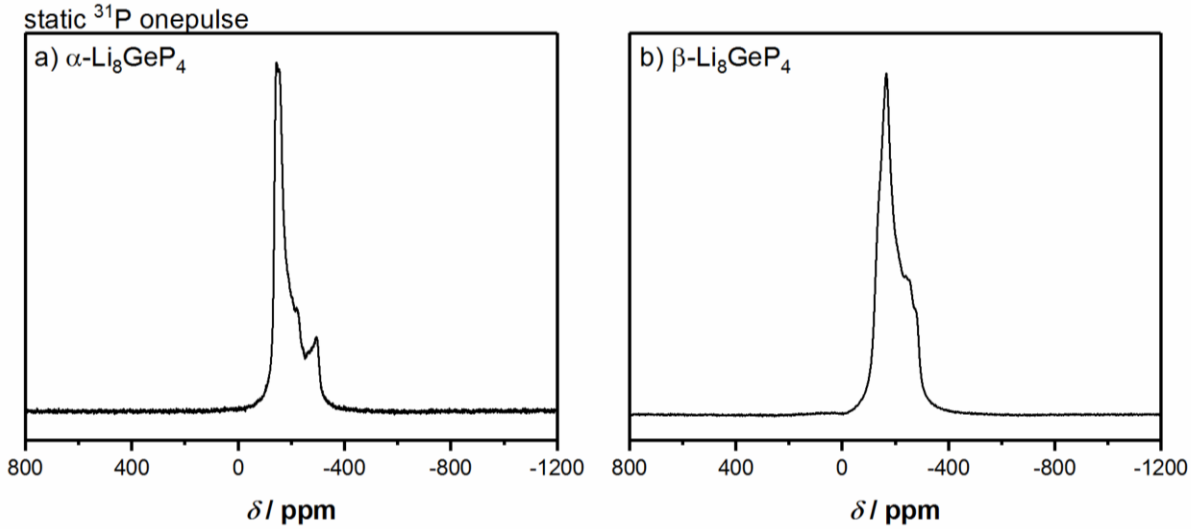

Figure S10. Static ^{31}P onepulse NMR spectrum of a) α-Li_8GeP_4 and b) β-Li_8GeP_4 at room temperature. Both compounds show similar, broad signals from 0 to −400 ppm, while the signal of α-Li_8GeP_4 exhibits more distinct features.

IR spectroscopy

IR spectra were recorded on a Spectrum Two ATR-FTIR device (Perkin-Elmer) including a diamond ATR crystal and resolution of 4 cm^{-1}.

IR-spectra of Li_8SiP_4 showed a set of modes at 486 cm^{-1} and below. For α- and β-Li_8GeP_4 again the expected shift to lower wavenumbers is observed and the signals occur at ca. 460 cm^{-1} and below. The Ge containing compounds also show weak modes between 1000 and 1100 cm^{-1}.

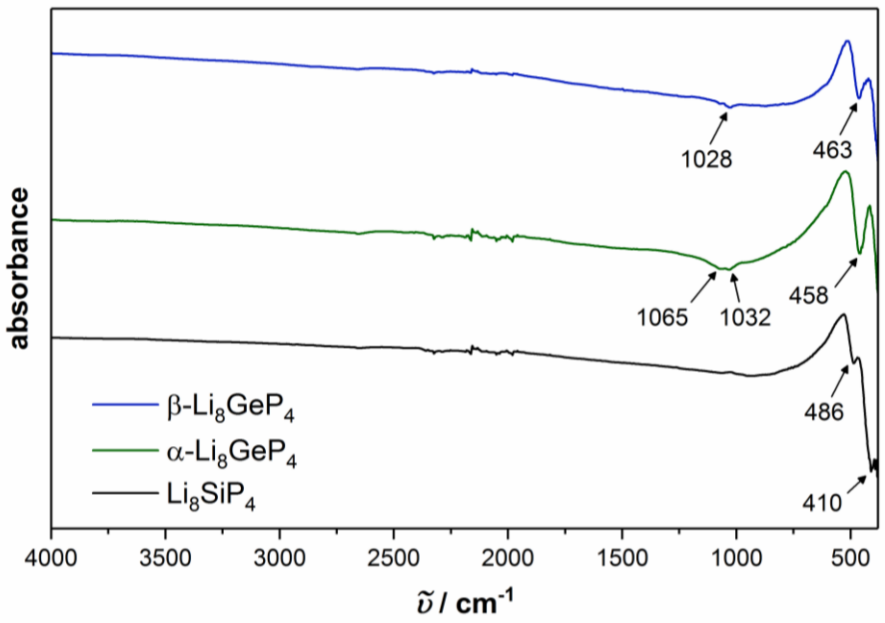

Figure S11. IR spectra of Li_8SiP_4 (black), α-Li_8GeP_4 (red) and β-Li_8GeP_4 (blue). The arrows and numbers indicate the modes and the corresponding wavenumbers in the spectra.

5.4 Polyanionic Frameworks in the Lithium Phosphidogermanates Li_2GeP_2 and $LiGe_3P_3$

H. Eickhoff, C. Sedlmeier, W. Klein, G. Raudaschl-Sieber, H. A. Gasteiger, T. F. Fässler

Manuscript for publication

Polyanionic frameworks in the lithium phosphidogermanates Li_2GeP_2 and $LiGe_3P_3$

Henrik Eickhoff, Christian Sedlmeier, Wilhelm Klein, Gabriele Raudaschl-Sieber, Hubert A. Gasteiger, Thomas F. Fässler

Department of Chemistry, Technische Universität München,
Lichtenbergstrasse 4, 85747 Garching bei München, Germany
* E-mail: Thomas.Faessler@lrz.tu-muenchen.de

Abstract

In the context of material development for all solid state batteries the ternary Li/Ge/P phase system has been investigated and two new lithium phosphidogermanates have been obtained. Li_2GeP_2 crystallizes in space group $I4_1/acd$ with unit cell parameters of a = 12.3069(1) Å and c = 19.0306(4) Å and is isotypic to Li_2SiP_2. Li_2GeP_2 consists of frameworks of Ge_4P_{10} supertetrahedra and exhibits ionic conductivity of $1.6(3)\times10^{-7}$ S cm^{-1} at 27 °C. $LiGe_3P_3$ crystallizes in *Pbam* with a = 9.8459(5) Å, b = 15.7489(7) Å and c = 3.5995(2) Å, and is isotypic to $Li_{0.9}Ge_{2.9}As_{3.1}$. $LiGe_3P_3$ forms polyanionic slabs of GeP_4 and $Ge(P_3Ge)$ tetrahedra (Ge_2 dumbbells). A semiconducting behavior with an electronic conductivity of ~10^{-4} S cm^{-1} and a remarkable stability versus air and moisture is observed.

Introduction

Recently binary and ternary tetrel and phosphide based materials have been reported as conceivable materials for various applications in batteries. While binary compounds like SiP and SiP_2 have been shown to exhibit large capacities as electrode materials,[1-4] ternary Li and sodium containing compounds like Li_8SiP_4, β-Li_8GeP_4 and $NaSi_2P_3$ show fast ion conduction in the range from 10^{-5} to 10^{-3} S cm^{-1}.[5-7] The fast ionic conduction in this material class makes phosphide based compounds a new group of solid electrolytes for all solid state batteries, for which new materials with optimized properties are highly demanded.[8,9] Despite the alternating composition lithium phosphidosilicates, which are named after their structural similarity to oxidosilicates, consist of tetrahedral building blocks also found in conventional fast ion conductors. These units can be isolated or conjoined by shared corners or edges forming ortho phosphidosilicates Li_8SiP_4, dimeric units in $Li_{10}Si_2P_6$, layers in $Li_3Si_3P_7$ and three dimensional networks in Li_2SiP_2 and $LiSi_2P_3$.[5,7,10] The TtP_4 (*Tt* = Si, Ge) tetrahedron as exclusive building block stays in contrast to the structural chemistry of the heavier homologues of *A*/*Tt*/*Pn* (*A* = Na, K, Rb; *Tt* = Si, Ge Sn; *Pn* = P, As) compounds. Compounds containing heavy *A* and *Pn* elements show a higher tendency to form homatomic tetrel bonds and formal negatively charged tetrel atoms, which are not found in Li/Si/P compounds, but e.g. found in $K_6Sn_3As_5$ and KSnAs.[11] A further, frequently occurring, composition is ATt_3Pn_3 (*A* = Li, Na, K, Rb ; *Tt* = Si, Ge, Sn; *Pn* = P, As).[12-14] These compounds consist of *Tt*-*Pn* slabs which are separated by *A* atoms. In the cross section the slabs appear as chains of pentagonal rings bridged with attached *Pn* atoms. The rings represent tubes built from 9 atom cages or corner sharing $TtPn_4$ tetrahedra connected via Tt_2 dumbbells. Various stacking orders of the slabs lead to diverse structure types. The structural flexibility of this system is also exhibited by KSi_3As_3,[15] in which certain *Tt* and *Pn* positions are swapped, leading to a different connectivity of the tubes, and by Li_3NaSi_6,[16] in which the slabs are solely built from Si.

While various compounds are known for the heavier homologues and also lithium phosphidosilicates the intermediate lithium phosphidogermanates are sparsely investigated. With α-Li_8GeP_4 and β-Li_8GeP_4 this system has been shown to realize structure types same as found for light (Li_8SiP_4) and heavy tetrel elements (Li_8SnP_4), respectively.[6] Beside these two compounds the only further compound reported is Li_5GeP_3, crystallizing in the CaF_2 structure type.[17] These three so far known compounds consist exclusively of isolated GeP_4 tetrahedra. Regarding the structural diversity of the related phase systems many more compounds are conceivable. Additionally, as already seen for the α-Li_8GeP_4 and β-Li_8GeP_4 the substitution of Si by Ge can lead to alternating properties, which is also confirmed by predictions concerning substitution of Si in Li_2SiP_2 leading to dramatically increased ionic conductivity.[18] In this context the Li/Ge/P phase

system is further explored and the new lithium phosphidogermanates Li_2GeP_2 and $LiGe_3P_3$ are presented.

Experimental Section

All syntheses are carried out under Ar atmosphere in Gloveboxes (MBraun, 200B) with moisture and oxygen level below 1 ppm or in containers, which are sealed under Ar atmosphere.

Bulk synthesis via ball milling and annealing

For both compounds the synthesis route includes two steps, using lithium (Rockwood Lithium, 99%), germanium (EVOCHEM GmbH, 99.999%) and red phosphorus (ChemPur, 99.999%). In the first step reactive mixtures (3 g) are prepared by mechanochemical milling using a Retsch PM100 Planetary Ball Mill (350 rpm, 36 h, 10 min interval, 3 min break) with a tungsten carbide milling jar (V = 50 mL) and three balls with a diameter of 15 mm. In the second step 300 mg fractions of the reactive mixture are pressed to pellets, sealed in a carbon coated silica glass ampoules and are annealed. To reduce the amount of side phases such as Ge, a slight excess of Li is used for synthesis of both compounds.

Single crystals of Li_2GeP_2 and $LiGe_3P_3$ are obtained by a high temperature reaction of mixtures with the element ratios for Li, Ge and P of 2:1:2 and 3:3:7, respectively. The samples (300 mg) are heated in a tantalum ampoule to 700 °C for 24 h and slowly cooled to room temperature (rate: 1 °C min^{-1}). Li_2GeP_2 crystallizes as red transparent blocks and $LiGe_3P_3$ forms black bar-shaped crystals.

For Li_2GeP_2 294.4 mg (42.4 mmol) Li, 1467.6 mg (20.2 mmol) Ge and 1251.6 mg (40.4 mmol) P are loaded into the ball mill and for the annealing process the sample was heated to 600 °C with a rate of 4 °C min^{-1} and dwelled for 24 h, afterwards slowly cooled for 24 h to 500 °C and finally cooled to room temperature with a rate of 1 °C min^{-1}.

$LiGe_3P_3$ is prepared from 70.0 mg (10.1 mmol) Li, 2057.2 mg (28.3 mmol) Ge and 877.3 mg (28.3 mmol) P. The fractions used for annealing are heated to 500 °C with a rate of 4 °C min^{-1}, dwelled for 48 h and cooled to room temperature with a rate of 1 °C min^{-1}.

Powder X-ray diffraction

Data are collected at room temperature on a STOE Stadi P diffractometer equipped with a Ge(111) monochromator, a Cu $K_{\alpha1}$ radiation source (λ = 1.54056 Å) and a Dectris MYTHEN 1K detector in Debye-Scherrer geometry. Samples are sealed in glass capillaries (Ø 0.3 mm) for measurement. The sample of $LiGe_3P_3$ is diluted with diamond powder to reduce X-ray absorption and all

diffraction patterns are referenced against a Si standard. Raw data were processed with WinXPOW[19] software and Rietveld refinements were executed with FullProf.[20] During Rietveld refinement Li displacement parameters are kept constant and the reflections of added diamond powder are refined by profile fitting.

Single crystal X-ray data collection

Single crystal of Li_2GeP_2 and $LiGe_3P_3$ are isolated and sealed in a glass capillary (0.3 mm). For diffraction data collection, the capillary is mounted on a Xcalibur3 (Oxford Diffraction, Mo K_α radiation, $\lambda = 0.71073$) diffractometer equipped with a Sapphire 3 CCD detector and a nitrogen jet cooling system for measurements at 120 K. Structures are solved by Direct Methods (SHELXS-2014) and refined by full-matrix least-squares calculations against F^2 (SHELXL-2014).[21]

Differential scanning calorimetry (DSC)

For investigation of the thermal behavior of the compounds a Netzsch DSC 404 Pegasus device is used. Niobium crucibles are filled with 50 mg to 100 mg sample and sealed by arc-welding. Empty sealed crucibles served as reference. Measurements are performed under an Ar flow of 75 ml min^{-1} and a heating/cooling rate of 10 K min^{-1} up to a temperature of 750 °C. Data collection and handling was carried out with the Proteus Thermal Analysis program.[22]

Solid state MAS NMR spectroscopy

Magic angle spinning nuclear magnetic resonance (MAS NMR) spectra were recorded with a Bruker Avance 300 operating at 7.04 T. Resonance frequencies of 44.2 and 121.5 MHz and pulse widths of 6 and 1.33 µs are applied for ^6Li and ^{31}P measurements, respectively. For both nuclei relaxation delays of 30 s are set. Samples are diluted with Nb_2O_5 in a 1:2 ratio, packed in 4 mm ZrO MAS NMR probes and rotated with frequencies of 15 kHz during the measurements. The spectra are referenced to 1 mol L^{-1} LiCl solution, solid LiCl and $(NH_4)H_2PO_3$.

Electric conductivity measurements

The ionic and electronic conductivities of Li_2GeP_2 and $LiGe_3P_3$ at room temperature are determined by electrochemical impedance spectroscopy (EIS) in a custom build cell. The setup consists of two stainless-steel current collectors, a stainless-steel casing, a PEEK tube, hardened stainless-steel dies and pistons comprising a gasket for tightening the cell as well as six screws for fixing the cell. Between the two 8 mm dies powdered samples (100 mg) are loaded and the screws

were fastened with a torque of 30 Nm, compressing the samples to at least 93% of the crystal density. For the determination of the compressed pellet thickness, distances between six holes in the current collectors are measured using a precision caliper. Impedance spectra are recorded on a Bio-Logic potentiostat (SP-200) in a frequency range from 3 MHz to 50 mHz at a potentiostatic excitation of ±50 mV. Data are processed using the software EC-Lab (V 11.26). The measurements are performed in an Ar-filled glove box at 298 K. The electronic conductivity is determined with the same setup using a potentiostatic polarization applying voltages of 50, 100 and 150 mV for 16 h each. All measurements were conducted in a tempered glove box at 27(1) °C.

Results and Discussion

Li_2GeP_2

As recently seen for α-Li_8GeP_4 and Li_8SiP_4 lithium phosphidogermanates are capable of realizing similar structures to their lighter homologues, the lithium phosphidosilicates. Also Li_2GeP_2 is isotypic to known Li_2SiP_2.[5] A single crystal prepared via synthesis from elements in a Ta ampoule at 700 °C shows the space group $I4_1/acd$ with unit cell parameters of a = 12.3069(1) Å and c = 19.0306(4) Å (120 K) (Tab. 1). The structure contains one crystallographic position for Ge, and three independent positions for P and Li, respectively. All P atoms form a strongly distorted cubic closed packing with Li and Ge atoms in warped tetrahedral voids. As a result, every Ge atom is covalently bound to four P atoms, one P1 (Wyckoff pos. 16*d*), one P2 (16*e*) and two P3 (32*g*), forming tetrahedral GeP_4 units. In these building blocks Ge-P distances of 2.3147(5) - 2.3445(4) Å occur, which are slightly shorter than the Ge-P bonds in α- and β-Li_8GeP_4 ($d_{Ge\text{-}P}$ = 2.369 - 2.405 Å). Four tetrahedra are conjoined via common corners to supertetrahedra which are further connected via shared corners to diamond- or β-cristobalite-like frameworks. A second, identical network occupies the interstitial positions of the first (Fig. 1). While all Ge atoms are coordinated by 4 P atoms, the P atoms are only bound to two Ge atoms resulting in a formal charge of −1 per P atom. The negative charge is balanced by Li atoms occupying pseudo tetrahedral voids of the *ccp* of P atoms ($d_{Li\text{-}P}$ = 2.548(4) - 2.7376(11) Å; Li_2SiP_2: 2.444(2) - 2.767(2) Å) between the frameworks. The resulting coordination sphere for all P atoms consists of four Li^+ beside the two Ge atoms.

The number and intensity of signals observed in ^{31}P NMR spectra agrees well with the crystallographic data. Three signals with a chemical shift of δ = −59.9, −164.8, −178,4 ppm and a relative intensity of 1:1:2 are assigned to the P positions P2, P1 and P3, respectively (Fig. 2). The different chemical shift of P2 is attributed to the different chemical environment. This atom represents the shared corner of condensed supertetrahedra, while P1 and P3 are situated on the edges of the supertetrahedra, therefore exhibiting a very similar surrounding. Compared to that,

Li_2SiP_2 exhibits only two strongly downfield shifted NMR signals (δ = −129.1, −241.5 ppm) by ~70 ppm with a relative intensity of 1:3.[5] These two signals are assigned to P2 and not resolved peaks of P1 and P3, respectively. The splitting of the P1 and P3 signal can be attributed to differences in the structure. While the local coordination of all P atoms within L_2GeP_2 and L_2SiP_2 is very similar a variation of Ge-P-Ge bond angles is observed. The Ge-P-Ge angles (101.7° at P1, 105.0° at P3) on the two positions show an increased deviation of 3.3° compared to the corresponding Si-P-Si angles of 2.1° (103.0°, 105.1°).[5]

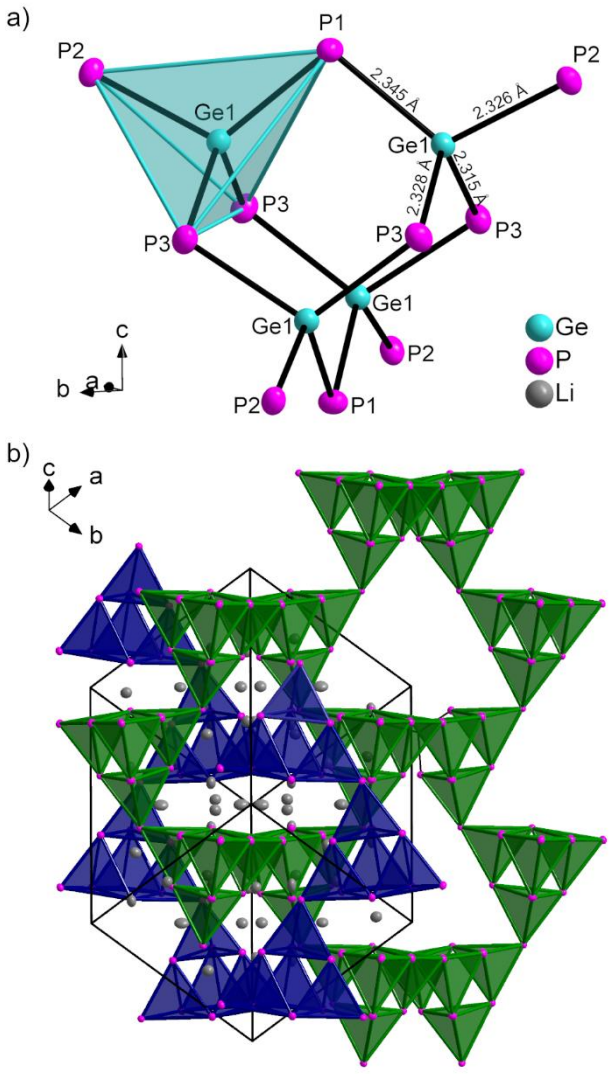

Figure 1: Structural features of Li_2GeP_2. a) A covalently bound Ge_4P_{10} supertetrahedron with bond lengths. A single GeP_4 tetrahedron is highlighted in light blue. b) The unit cell with the two independent diamond like frameworks of supertetrahedra depicted in dark blue and green.

Table 1: Refinement data of the single crystal diffraction data of Li_2GeP_2 and $LiGe_3P_3$ at 120 K.

Sum formula	Li_2GeP_2	$LiGe_3P_3$
Molar mass / g mol^{-1}	148.458	317.751
Crystal system	tetragonal	orthorhombic
Space group	$I4_1/acd$ (142)	$Pbam$ (55)
Radiation λ / Å	0.71073 (Mo K_α)	0.71073 (Mo K_α)
Crystal size / mm^3	0.40 × 0.21 × 0.19	0.55 × 0.07 × 0.01
Crystal color, shape	red, block	black, bar
Cell parameters / Å	$a = b = 12.3070(1)$	$a = 9.8459(5)$
	$c = 19.0307(4)$	$b = 15.7489(7)$
		$c = 3.5995(2)$
Cell volume / Å^3	2882.42(9)	558.15(5)
Z	32	4
ρ (calc.) / g cm^{-3}	2.736	3.780
μ / mm^{-1}	9.109	16.750
$F(000)$	2176	576
Temperature / K	120	120
Reflections collected	22367	6903
Independent reflections	1057	927
Reflections with $I > 2\sigma(I)$	967	733
Observed hkl	$-17 \le h \le 17$,	$-13 \le h \le 13$,
	$-17 \le k \le 17$,	$-21 \le k \le 22$,
	$-26 \le l \le 26$	$-5 \le l \le 5$
Measuring range $\theta_{min/max}$ / °	3.17 / 29.99	3.31 / 30.00
Goodness-of-fit on F_0^2	1.115	0.986
R_{int} / R_σ	0.0326 / 0.0123	0.0524 / 0.0362
R indices ($F_0^2 \le 2\sigma(F_0^2)$)	$R1 = 0.0120$, $wR2 = 0.0283$	$R1 = 0.0306$, $wR2 = 0.0757$
R indices (all data)	$R1 = 0.0141$, $wR2 = 0.0287$	$R1 = 0.0409$, $wR2 = 0.0775$
Largest diff. peak/hole / e Å^{-3}	0.37 / −0.35	1.44 / −1.09

Along the [111] direction the tetrahedra frameworks span large channels, which are connected to a 3D network and occupied by Li^+. In combination with only two signals found in ^{6}Li MAS NMR (δ = 2.4 ppm, 3.6 ppm) for three different crystallographic Li sites indicating a high degree of mobility this hints to possible ionic conductivity which has been detected in Li_2SiP_2, too. For an estimation of the ion conduction potential of Li_2GeP_2 geometric parameters are compared with those from the silicon containing compound. As expected the shortest Li-Li distances within the

channels increase slightly with substitution of Si by Ge from a range of 2.916(9) Å - 3.229(9) Å to 2.940(5) Å - 3.290(5) Å, respectively. In contrast to the increasing Li-Li distances and unit cell parameters the bottle neck size, indicated by shortest P-P distances within the channel, shrinks, due to a rotation and distortion of the supertetrahedra. These distances decrease from 3.954(2) Å and 4.0012(9) Å to 3.9161(8) Å and 3.978(5) Å. Both effects might be responsible for the lower ionic conductivity of $1.6(3)\times10^{-7}$ S cm^{-1} in Li_2GeP_2 at 27 °C compared to 4×10^{-7} S cm^{-1} in Li_2SiP_2 at 25 °C.[5] However, this conductivity is a combination of bulk and grain boundary resistances as both contributions cannot be resolved in the impedance spectrum and differences in conductivity cannot be contributed exclusively to structural changes. The electronic contribution of 10^{-8} S cm^{-1} to the conductivity is neglectable and in the same order of magnitude as reported for Li_2SiP_2.[5]

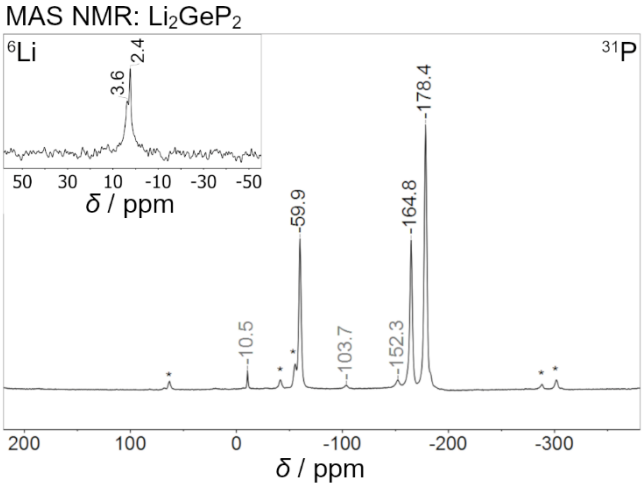

Figure 2: ^{31}P MAS NMR spectrum of Li_2GeP_2 with inset for ^{6}Li MAS NMR spectrum. Signals from side phases are indexed with grey colored chemical shifts and rotation side bands are marked with asterisks.

$LiGe_3P_3$

The second new compound, $LiGe_3P_3$, is isotypic to $Li_{0.9}Ge_{2.9}As_{3.1}$[13] and comprises similar building blocks known from other compounds of heavier homologues like $NaGe_3P_3$ but a different arrangement.[12] Single crystals of LiGe3P3 prepared from the elements in a Ta ampoule at 700 °C crystallizes in the orthorhombic space group *Pbam* with the unit cell parameters of a = 9.8459(5) Å, b = 15.7489(7) Å and c = 3.5995(2) Å (120 K) (Tab. 1). Atoms from seven crystallographic independent positions, one Li, three Ge and three P, form covalently bound polyanions of Ge and P separated by Li. As shown in Fig. 3 Ge1 and all P sites from chains of corner-sharing GeP_4 tetrahedra. These are a reoccurring structural motive in phosphidogermanates. P1 and P3, which are not connected to two GeP_4 centers, are bridged to the neighboring tetrahedra via Ge_2 dumbbells. With a length of 2.54391(9) Å the Ge-Ge single bonds are longer than those

in elemental Ge (2.450 Å)[23] and GeP (2.369, 2.393 Å)[24] but significantly shorter than in $NaGe_3P_3$ (2.627 Å). P1 is bound to Ge3 and P3 to Ge2, forming with the tetrahedra corrugated hexagons of alternating Ge and P atoms. This connectivity pattern leads to the formation of tubes parallel to the *c* axis. Further bonds between P2 atoms to Ge3 atoms of the neighboring tubes result in two dimensional sheets in the *ac* plane. Additionally, this connectivity pattern leads to the formation of a second species of tetrahedra, $Ge(P_3Ge)$, which are strongly distorted due to the connectivity of the formally negatively charged Ge2 corner. The latter are connected via shared corners and bonds between P3 and Ge2 atoms. Within these slabs, all P atoms are connected to three Ge atoms, leading to a formal charge of 0. The similarity of the sites is confirmed by ^{31}P MAS NMR spectroscopy. As shown in Fig. 4 three signals occur with an intensity ratio of 1:1:1 and within a small chemical shift window (δ = −59.5, −119.4, −126.3 ppm). The atoms Ge1 and

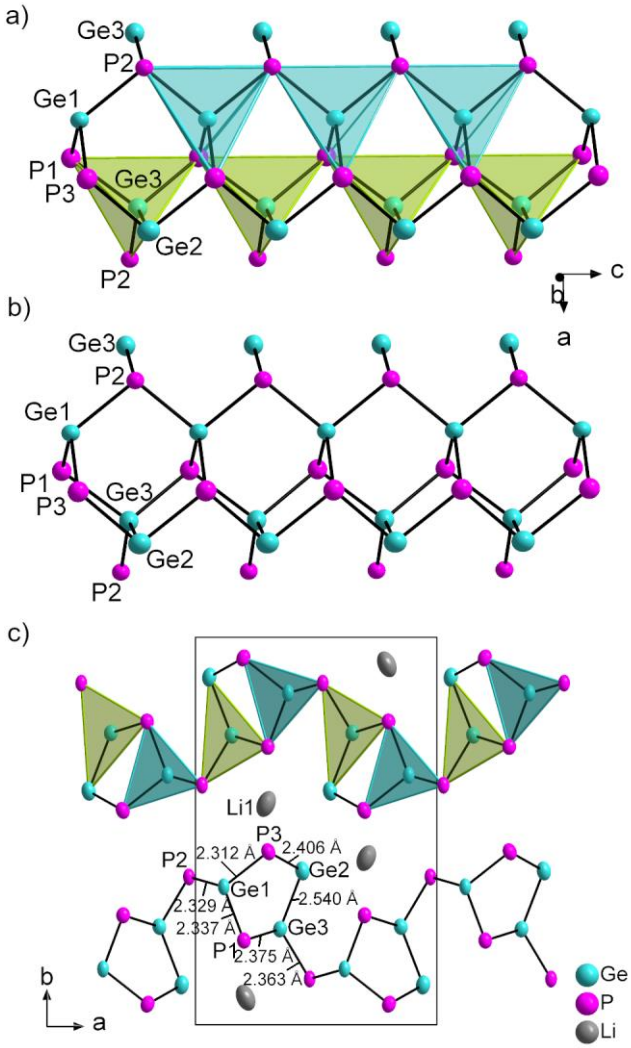

Figure 3: Structural features of $LiGe_3P_3$. a) Detailed view of a Ge_3P_3 tube consisting of corner sharing GeP_4 tetrahedra (light blue) and GeP_3Ge tetrahedra (green). b) Detailed view of a Ge_3P_3 tube without highlighted tetrahedra. c) Expanded unit cell with slabs of Ge-P tubes. Tetrahedra are highlighted to emphasize the conductivity.

Ge3 form four bonds to four P atoms or to three P atoms and one Ge atom, respectively. Ge2 only forms bonds to two P atoms and one Ge atom leading to a formal charge of −1. $LiGe_3P_3$ is therefore the first lithium phosphidotetrelate comprising formally negatively charged Ge atoms.

The negative framework charge is balanced by lithium cations separating the slabs. According to only one independent crystallographic site for Li, in the ^{6}Li MAS NMR spectrum a single signal at δ = 2.4 ppm is detected. The Li atoms is situated in a strongly distorted tetrahedral coordination of three P ($d_{Li\text{-}P}$ = 2.644(10) - 2.936(10) Å) and one Ge ($d_{Li\text{-}Ge}$ = 2.659(12) Å). With the second coordination sphere the distorted tetrahedron is supplemented by two P atoms and two Ge atoms to a two times capped, heavily distorted octahedron. Since the relatively large coordination polyhedron might allow Li motion within the *a*-*c* plane electric properties are determined. However, impedance spectroscopy and polarization measurements yielded dominant electronic conduction of ~10^{-4} S cm^{-1} and no ionic share could be detected. The electronic conductivity is the highest one reported electronic conductivity of lithium phosphidogermanates so far.

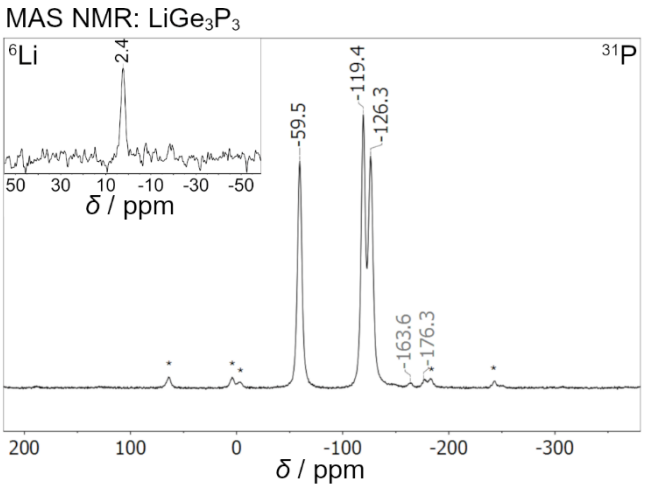

Figure 4: ^{31}P MAS NMR spectrum of $LiGe_3P_3$ with inset for ^{6}Li MAS NMR spectrum. Signals from side phase Li_2GeP_2 are indexed with grey colored chemical shifts and rotation side bands are marked with asterisks.

Syntheses

Bulk material of Li_2GeP_2 and $LiGe_3P_3$ is prepared from a two-step synthesis route, including mechanochemical milling and subsequent annealing. The mechanical processing reduces grain sizes, improves the distribution of elements and, additionally, leads to the formation of precursor compounds in a reactive mixture. Temperatures of 600 °C and 500 °C, respectively, applied in the following annealing step are chosen based on DSC measurements. For Li_2GeP_2 an onset for melting and solidifying is observed between 684 °C and 677 °C, respectively. In $LiGe_3P_3$ these thermal events are assigned to distinct peaks is observed with onsets of 701 °C and 647 °C. All

samples were synthesized with an excess of 5-7% Li. Compared to stoichiometric mixtures this excess reduces the phase fraction of side phases, especially unreacted Ge, in the final product. Following that approach phase fractions can be determined via Rietveld refinement (Fig. 5) to be 97% for $LiGe_3P_3$, containing 1% Ge and 2% Li_2GeP_2. Since additional reflections occur in the diffraction pattern of Li_2GeP_2 which cannot be assigned to a known compound, an exact determination of the phase fractions is not possible. Comparison of the Li_2GeP_2 and Ge content leads to a ratio of 86:1. While Li_2GeP_2, similar to all other known lithium phosphidogermanates and lithium phosphidosilicates, shows vigorous reactions in contact with water, $LiGe_3P_3$ exhibits a remarkable stability. By deliberately exposing $LiGe_3P_3$ samples to air and water for 24 h each, followed by PXRD measurements, no change in crystallinity and ratio of $LiGe_3P_3$ and Ge is detected, while the Li_2GeP_2 side phase clearly degrades.

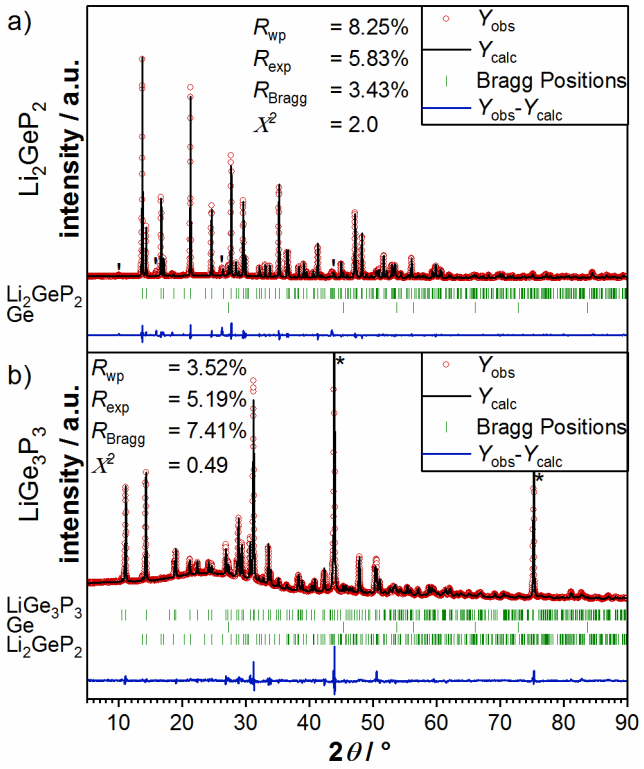

Figure 5: Rietveld refinement plots of a) Li_2GeP_2 and b) $LiGe_3P_3$ samples. Y_{obs} is the observed and Y_{calc} the calculated intensity. The unknown side phase in Li_2GeP_2 is marked with ticks (‘) and added diamond powder reflection with asterisks (*) and are truncated for better visualization of the sample reflections.

Conclusion

The new lithium phosphidogermanates Li_2GeP_2 and $LiGe_3P_3$ are the first compounds with large polyanions in the Li/Ge/P phase system and comprise three- and two-dimensional anionic substructure, respectively. The realized structure types are known for lighter and heavier homologues, respectively, and both contain GeP_4 units, which are a common building block for all lithium phosphidotetrelates. In Li_2GeP_2, which is isotypic to Li_2SiP_2, the tetrahedra form frameworks of Ge_4P_{10} supertetrahedra and large channels for Li^+. In contrast to the increasing unit cell parameters, compared to Li_2SiP_2, the channel size shrinks significantly due to rotation and warping of the supertetrahedra, leading to lower ionic conductivities of $1.6(3)\times10^{-7}$ S cm^{-1}. The compound $LiGe_3P_3$ is isotypic to $Li_{0.9}Ge_{2.9}As_{3.1}$ and consists identical polyanions as $NaGe_3P_3$. $LiGe_3P_3$ forms slabs of GeP_4 tetrahedra and Ge_2 dumbbells and is the first lithium phosphidotetrelate comprising formally negatively charged tetrel atoms. Although very similar polyanions are observed in various compounds they often realize different structure types. The cation size seems to have a particular effect on the structure type. The two Li containing compounds $LiGe_3P_3$ and $Li_{0.9}Ge_{2.9}As_{3.1}$ crystallize in the same structure type containing two polyanionic slabs in the unit cell, but even by replacing Li with Na in $NaGe_3P_3$ a different structure type with only one slab within the unit cell is realized. The difference in the crystal structure of $LiGe_3P_3$ compared to the so far known lithium phosphidotetrelates is also indicated by an altering macroscopic behavior. While in $LiGe_3P_3$ the electric properties are dominated by electronic conduction, an unprecedented stability in contact with water is observed. The information about the broad set of properties found in the new phosphidogermanates can help designing new generations of ionic conductors.

Acknowledgements

The authors greatly acknowledge Tassilo Restle for DSC measurements and Johannes Landesfeind and Tanja Zünd for design of the impedance measurement cell.

References

[1] Kwon, H.-T.; Lee, C. K.; Jeon, K.-J.; Park, C.-M.; Silicon Diphosphide: A Si-Based Three-Dimensional Crystalline Framework as a High-Performance Li-Ion Battery Anode, *ACS Nano* **2016**, *10*, 5701-5709.

[2] Reinhold, R.; Stoeck, U.; Grafe, H.-J.; Mikhailova, D.; Jaumann, T.; Oswald, S.; Kaskel, S.; Giebeler, L.; Surface and Electrochemical Studies on Silicon Diphosphide as Easy-to-Handle Anode Material for Lithium-Based Batteries-the Phosphorus Path, *ACS Appl. Mater Interfaces*, **2018**, *10(8)*, 7096-7106.

[3] Coquil, G.; Fraisse, B.; Dupré, N.; Monconduit, L.; Versatile Si/P System as Efficient Anode for Lithium and Sodium Batteries: Understanding of an Original Electrochemical Mechanism by a Full XRD-NMR Study, *ACS Appl. Energy Mater.* **2018**, *1(8)*, 3778-3789.

[4] Reinhold, R.; Mikhailova, D.; Gemming, T.; Missyul, A. B.; Nowka, C.; Kaskel, S.; Giebeler, L.; Silicon monophosphide as a possible lithium battery anode material, *J. Mater. Chem. A* **2018**, *6*, 19974-19978.

[5] Toffoletti, L.; Kirchhain, H.; Landesfeind, J.; Klein, W.; van wüllen, L.; Gasteiger, H. A.; Fässler, T. F.; Lithium Ion Mobility in Lithium Phosphidosilicates: Crystalstructure, ^{7}Li, ^{29}Si, and ^{31}P MAS NMR Spectroscopy, and Impedance Spectroscopy of Li_8SiP_4 and Li_2SiP_2, *Chem.-Eur. J.* **2016**, *22*, 17635-17645.

[6] Eickhoff, H.; Strangmüller, S.; Klein, W.; Kirchhain, H.; Dietrich, C.; Zeier, W. G.; van Wüllen, L.; Fässler, T. F.; Lithium Phosphidogermanates α- and β-Li_8GeP_4 – A Novel Coumpound Class with Mixed Li^+ Ionic and Electronic Conductivity, *Chem. Mater.* **2018**, *30*, 6440-6448.

[7] Haffner, A.; Hatz, A.-K.; Moudrakovski, I.; Lotsch, B. V.; Johrendt, D.; Fast Sodium-Ion Conductivity in Supertetrahedral Phosphidosilicates, *Angew. Chem.* **2018**, *130*, 6263-6268; *Angew. Chem. Int. Ed.* **2018**, *57*, 6155-6160.

[8] Lotsch, B. V.; Maier, J.; Relevance of solid electrolytes for lithium-based batteries: A realistic view, *J. Electroceram.* **2017**, *38*, 128-141.

[9] Janek, J.; Zeier, W. G.; A solid future for battery development, *Nat. Energy* **2016**, *1*, 1-4.

[10] Eickhoff, H.; Toffoletti, L.; Klein, W.; Raudschl-Sieber, R.; Fässler, T. F.; Synthesis and Characterization of the Lithium-Rich Phosphidosilicates $Li_{10}Si_2P_6$ and $Li_3Si_3P_7$, *Inorg. Chem.* **2017**, *56*, 6688-6694.

[11] Klein, J.; Eisenmann, B.; Zintl-phasen mit komplexen Anionen: Darstellung und Einkristallstrukturbestimmung von KSnAs und $K_6Sn_3As_5$, *Mater. Res. Bull.* **1988**, *23*, 587-594.

[12] Feng, K.; Yin, W.; He, R.; Lin, Z.; Jin, S.; Yao, J.; Fu, P.; Wu, Y.; $NaGe_3P_3$: a new ternary germanium phosphide featuring an unusual $[Ge_3P_7]$ ring, *Dalton Tans.* 2012, *41*, 484-489.

[13] Mark, J.; Hanrahan, M. P.; Woo, K. E.; Lee, S.; Rossini, A. J.; Kovnir, K.; Chemical and Electrochemical Lithiation of van der Waals Tetrel-Arsenides, *Chem. Eur. J.* 2019, *25*, 6392-6401.

[14] Khatun, M.; Stoyko, S. S.; Mar, A.; Ternary arsenides ATt_3As_3 (*A*=K, Rb; *Tt*=Ge, Sn) with layered structures, *J. Solid State Chem.* 2016, *238*, 229-235.

[15] Hurng, W.-M.; Corbett, J. D.; Wang, S.-L.; Jacobson, R. A.; A Zintl Phase with a Layered Structure, KSi_3As_3, *Inorg. Chem.* 1987, *26*, 2392-2395.

[16] von Schnering, H.-G.; Schwarz, M.; Nesper, R.; The lithium sodium silicide Li_3NaSi_6 and the formation of allo-silicon, *J. Less-Common Met.* 1988, *137*, 297-310.
[17] Juza, R.; Schulz, W.; Ternäre Phosphide und Arsenide des Lithiums mit Elementen der 3. und 4. Gruppe, *Z. Anorg. Allg. Chem.* 1954, *275*, 65-78.
[18] Yeandel, S. R.; Scanlon, D. O.; Goddard, P.; Enhanced Li-ion dynamics in trivalently doped lithium phosphidosilicate Li_2SiP_2: a candidate material as solid Li electrolyte, *J. Mater. Chem. A* 2019, *7*, 3953-3961.
[19] *WinXPOW V3.0.2.1.*, 3.0.2.1.; STOE & Cie GmbH: Darmstadt, Germany, **2011**.
[20] Rodriguez-Carvajal, J.; Gonzales-Platas, J. *FullProf Suite 2. 05*, Institute Laue-Langevin Grenoble: France, 2011.
[21] Sheldrick, G. M. Crystal Structure Refinement with SHELXL. *Acta Crystallogr., Sect. C: Struct. Chem.* **2015**, *71*, 3-8
[22] *Proteus Thermal Analysis V4.8.2*, Netzsch-Gerätebau GmbH: Selb, 2006.
[23] M. E. Straumanis, E. Z. Aka, Lattice parameters, coefficients of thermal expansion and weights of purest silicon and germanium, *J. Appl. Phys.* **1952**, *23*, 330-334.
[24] T. Wadsten, The Crystal Structures of SiP_2, $SiAs_2$ and GeP, *Acta Chem. Scand.* **1967**, *21*, 593-594.

Supporting Information

Polyanionic frameworks in the lithium phosphidogermanates Li_2GeP_2 and $LiGe_3P_3$

Henrik Eickhoff, Christian Sedlmeier, Wilhelm Klein, Gabriele Raudaschl-Sieber, Hubert A. Gasteiger, Thomas F. Fässler

Department of Chemistry, Technische Universität München,
Lichtenbergstrasse 4, 85747 Garching bei München, Germany
* E-mail: Thomas.Faessler@lrz.tu-muenchen.de

Single Crystal X-Ray Diffraction

Li_2GeP_2 at 120K

Refinement parameters and description of the measurement at 120 K are found in the discussion part of the main article.

Table S1: Atom coordinates of Li_2GeP_2 at 120 K from single crystal diffraction data.

Atom	**Wyck.**	***x***	***y***	***z***	U_{iso}
Ge1	32*g*	0.38142(2)	0.33808(2)	0.05570(2)	0.00636(5)
P1	16*d*	0.5000	0.2500	−0.02212(3)	0.00768(10)
P2	16*e*	0.2500	0.44300(4)	0.0000	0.00714(9)
P3	32*g*	0.28249(3)	0.22328(3)	0.12775(2)	0.00793(7)
Li1	16*f*	0.0946(2)	0.1554(2)	0.1250	0.0148(7)
Li2	16*f*	0.1563(2)	0.4063(2)	0.1250	0.0186(8)
Li3	32*g*	0.3746(2)	0.0991(2)	0.03521(13)	0.0156(5)

Table S2: Anisotropic displacement parameters of Li_2GeP_2 at 120 K from single crystal diffraction data.

Atom	U_{11}	U_{22}	U_{33}	U_{23}	U_{13}	U_{12}
Ge1	0.00629(8)	0.00649(7)	0.00631(8)	0.00018(5)	−0.00050(5)	0.00024(5)
P1	0.0084(2)	0.0084(2)	0.0062(2)	0	0	0.00079(17)
P2	0.0071(2)	0.0060(2)	0.0083(2)	0	−0.00167(17)	0
P3	0.00654(16)	0.00833(16)	0.00892(16)	0.00161(12)	−0.00011(12)	−0.00012(11)
Li1	0.0148(11)	0.0148(11)	0.0147(18)	−0.0013(9)	−0.0013(9)	−0.0019(13)
Li2	0.0189(12)	0.0189(12)	0.0180(19)	−0.0004(10)	0.0004(10)	0.0067(15)
Li3	0.0167(13)	0.0150(12)	0.0151(13)	−0.0004(10)	0.0000(10)	−0.0009(10)

Table S3: Selected distances and angles in Li_2GeP_2 at 120 K from single crystal diffraction data.

Atom 1	**Atom 2**	$d_{1\text{-}2}$ **/ Å**	
Ge1	P3	2.3147(5)	
Ge1	P2	2.3258(4)	
Ge1	P3	2.3280(5)	
Ge1	P1	2.3445(4)	
Ge1	Li3	2.969(3)	
Ge1	Li3	3.083(3)	
Ge1	Li3	3.124(4)	
Ge1	Li2	3.179(2)	
P1	Li1	2.557(3)	2×
P1	Li3	2.653(3)	2×
P2	Li3	2.548(4)	2×
P2	Li2	2.679(2)	2×
P3	Li1	2.460(2)	
P3	Li3	2.590(3)	
P3	Li3	2.626(4)	
P3	Li2	2.7376(11)	

Atom 1	**Atom 2**	$d_{1\text{-}2}$ **/ Å**	
Li1	Li2	3.184(5)	2×
Li1	Li3	3.155(4)	2×
Li1	Li1	3.290(10)	
Li2	Li3	2.941(4)	2×
Li3	Li3	3.353(7)	

Atom 1		**Atom 2**		**Atom 3**	**Angle**
P3	–	Ge1	–	P2	104.070(14)
P3	–	Ge1	–	P3	110.535(11)
P2	–	Ge1	–	P3	101.862(17)
P3	–	Ge1	–	P1	114.785(14)
P2	–	Ge1	–	P1	113.691(14)
P3	–	Ge1	–	P1	110.972(14)
Ge1	–	P2	–	Ge1	112.51(3)
Ge1	–	P1	–	Ge1	101.66(2)
Ge1	–	P3	–	Ge1	104.993(19)

Li_2GeP_2 at 293K

Table S4: Refinement data of the single crystal diffraction data of Li_2GeP_2 at 293 K.

Sum formula	Li_2GeP_2
Molar mass / g mol^{-1}	148.458
Crystal system	tetragonal
Space group	$I4_1/acd$ (142)
Diffractometer	Xcalibur 3 (*Oxford Instruments*)
Radiation λ / Å	0.71073 (Mo K_α)
Crystal size / mm^3	0.40 × 0.21 × 0.19
Crystal color, shape	red, block
Cell parameters / Å	$a = b$ = 12.3223(1)
	c = 19.0123(4)
Cell volume / Å^3	2886.81(8)
Z	32
ρ (calc.) / g cm^{-3}	2.732
μ / mm^{-1}	9.095
F(000)	2176
Temperature / K	293(2)
Reflections collected	52916
Independent reflections	1368
Reflections with $I > 2\sigma(I)$	1185
Observed hkl	$-17 \le h \le 18$, $-18 \le k \le 18$, $-29 \le l \le 29$
Measuring range $\theta_{min/max}$ / °	3.17 / 32.99
Goodness-of-fit on F_0^2	1.190
R_{int} /R_σ	0.0892 / 0.0213
R indices ($F_0^2 \le 2\sigma(F_0^2)$)	$R1$ = 0.0203, $wR2$ = 0.0522
R indices (all data)	$R1$ = 0.0250, $wR2$ = 0.0529
Largest diff. peak and hole / e Å^{-3}	0.56 / −0.67

Table S5: Atom coordinates of Li_2GeP_2 at 293 K from single crystal diffraction data.

Atom	**Wyck.**	***x***	***y***	***z***	U_{iso}
Ge1	32*g*	0.38104(2)	0.33726(2)	0.05590(2)	0.01187(7)
P1	16*d*	0.5000	0.2500	−0.02191(4)	0.01412(13)
P2	16*e*	0.2500	0.44187(5)	0.0000	0.01299(13)
P3	32*g*	0.28284(4)	0.22180(4)	0.12764(3)	0.01500(11)
Li1	16*f*	0.0947(3)	0.1553(3)	0.1250	0.0247(12)
Li2	16*f*	0.1563(4)	0.4063(4)	0.1250	0.0368(15)
Li3	32*g*	0.3756(4)	0.0978(3)	0.0348(2)	0.0283(9)

Table S6: Anisotropic displacement parameters of Li_2GeP_2 at 293 K from single crystal diffraction data.

Atom	U_{11}	U_{22}	U_{33}	U_{23}	U_{13}	U_{12}
Ge1	0.01105(10)	0.01149(10)	0.01308(11)	0.00060(7)	−0.00122(7)	0.00045(6)
P1	0.0148(3)	0.0156(3)	0.0121(3)	0.000	0.000	0.0023(2)
P2	0.0119(3)	0.0103(3)	0.0167(3)	0.000	−0.0035(2)	0.000
P3	0.0112(2)	0.0152(2)	0.0187(3)	0.00391(17)	−0.00008(17)	−0.00008(15)
Li1	0.0242(16)	0.0242(16)	0.026(3)	−0.0013(15)	−0.0013(15)	−0.005(2)
Li2	0.041(2)	0.041(2)	0.029(3)	−0.0005(18)	0.0005(18)	0.017(3)
Li3	0.031(2)	0.0244(19)	0.029(2)	−0.0001(16)	−0.0001(18)	−0.0074(17)

Table S7: Selected distances and angles in Li_2GeP_2 at 293 K from single crystal diffraction data.

Atom 1	**Atom 2**	$d_{1\text{-}2}$ **/ Å**		**Atom 1**	**Atom 2**	$d_{1\text{-}2}$ **/ Å**	
Ge1	P3	2.3128(5)		Li1	Li2	3.185(8)	2×
Ge1	P2	2.3235(4)		Li1	Li3	3.142(5)	2×
Ge1	P3	2.3258(5)		Li1	Li1	3.301(12)	
Ge1	P1	2.3438(5)		Li2	Li3	2.943(6)	2×
Ge1	Li3	2.978(4)		Li3	Li3	3.366(9)	
Ge1	Li3	3.090(5)					
Ge1	Li3	3.130(4)		**Atom 1**	**Atom 2**	**Atom 3**	**Angle**
Ge1	Li2	3.181(3)		P3 –	Ge1 –	P2	104.324(16)
P1	Li1	2.562(4)	2×	P3 –	Ge1 –	P3	110.765(12)
P1	Li3	2.652(4)	2×	P2 –	Ge1 –	P3	101.588(19)
P2	Li3	2.554(4)	2×	P3 –	Ge1 –	P1	114.661(16)
P2	Li2	2.678(3)	2×	P2 –	Ge1 –	P1	113.607(17)
P3	Li1	2.459(3)		P3 –	Ge1 –	P1	110.974(16)
P3	Li3	2.599(5)		Ge1 –	P2 –	Ge1	112.61(3)
P3	Li3	2.636(5)		Ge1 –	P1 –	Ge1	101.72(2)
P3	Li2	2.7573(15)		Ge1 –	P3 –	Ge1	104.84(2)

$LiGe_3P_3$ at 120K

Refinement parameters and description of the measurement at 120 K are found in the discussion part of the main article.

Table S8: Atom coordinates of $LiGe_3P_3$ at 120 K from single crystal diffraction data.

Atom	**Wyck.**	***x***	***y***	***z***	U_{iso}
Ge1	4*g*	0.38362(7)	0.14362(4)	0.0000	0.00843(17)
Ge2	4*h*	0.05770(7)	0.10283(4)	0.5000	0.01208(17)
Ge3	4*h*	0.15069(7)	0.25321(4)	0.5000	0.00919(17)
P1	4*g*	0.30064(16)	0.28278(10)	0.0000	0.0093(3)
P2	4*h*	0.52772(16)	0.11779(10)	0.5000	0.0087(3)
P3	4*g*	0.19870(16)	0.05294(10)	0.0000	0.0100(3)
Li1	4*h*	0.7931(13)	0.0699(9)	0.5000	0.025(3)

Table S9: Anisotropic displacement parameters of $LiGe_3P_3$ at 120 K from single crystal diffraction data.

Atom	U_{11}	U_{22}	U_{33}	U_{23}	U_{13}	U_{12}
Ge1	0.0051(3)	0.0125(3)	0.0078(3)	0	0	0.0001(2)
Ge2	0.0089(3)	0.0158(3)	0.0115(4)	0	0	−0.0004(2)
Ge3	0.0070(3)	0.0123(3)	0.0082(3)	0	0	0.0005(2)
P1	0.0065(7)	0.0125(7)	0.0087(7)	0	0	0.0001(5)
P2	0.0055(7)	0.0138(7)	0.0067(7)	0	0	−0.0001(5)
P3	0.0076(7)	0.0135(7)	0.0089(7)	0	0	−0.0012(6)
Li1	0.018(7)	0.033(7)	0.025(7)	0	0	0.006(5)

Table S10: Selected distances and angles in $LiGe_3P_3$ at 120 K from single crystal diffraction data.

Atom 1	**Atom 2**	$d_{1\text{-}2}$ **/ Å**		**Atom 1**		**Atom 2**		**Atom 3**	**Angle**
Ge1	P3	2.3140(17)		P3	–	Ge1	–	P2	111.82(5)
Ge1	P2	2.3275(11)	2×	P2	–	Ge1	–	P2	101.29(7)
Ge1	P1	2.3389(17)		P3	–	Ge1	–	P1	107.66(6)
Ge2	P3	2.4049(12)	2×	P2	–	Ge1	–	P1	112.13(5)
Ge2	Ge3	2.5391(9)		P3	–	Ge2	–	P3	96.90(6)
Ge2	Li1	2.657(13)		P3	–	Ge2	–	Ge3	95.54(4)
Ge2	Li1	3.092(14)		P2	–	Ge3	–	P1	98.62(5)
Ge3	P2	2.3650(17)		P1	–	Ge3	–	P1	98.60(6)
Ge3	P1	2.3740(11)	2×	P2	–	Ge3	–	Ge2	128.07(5)
Ge3	Li1	3.119(14)		P1	–	Ge3	–	Ge2	114.03(4)
P1	Li1	2.938(11)	2×	Ge1	–	P1	–	Ge3	91.92(5)
P2	Li1	2.719(13)		Ge3	–	P1	–	Ge3	98.60(6)
P3	Li1	2.643(10)	2×	Ge1	–	P2	–	Ge1	101.29(7)
				Ge1	–	P2	–	Ge3	99.32(5)
				Ge1	–	P3	–	Ge2	104.63(5)
				Ge2	–	P3	–	Ge2	96.90(6)

$LiGe_3P_3$ at 293K

Table S11: Refinement data of the single crystal diffraction data of $LiGe_3P_3$ at 293 K.

Sum formula	$LiGe_3P_3$
Molar mass / g mol^{-1}	317.751
Crystal system	orthorhombic
Space group	*Pbam* (55)
Diffractometer	Xcalibur 3 (*Oxford Instruments*)
Radiation λ / Å	0.71073 (Mo K_α)
Crystal size / mm^3	0.55 × 0.07 × 0.01
Crystal color, shape	black, bar
a = 9.8459(5)	a = 9.8397(5)
b = 15.7489(7)	b = 15.7838(8)
c = 3.5995(2)	c = 3.6062(1)
Cell volume / Å^3	560.07(4)
Z	4
ρ (calc.) / g cm^{-3}	3.767
μ / mm^{-1}	16.692
F(000)	576
Temperature / K	293(2)
Reflections collected	8909
Independent reflections	931
Reflections with $I > 2\sigma(I)$	710
Observed hkl	$-13 \le h \le 13$, $-22 \le k \le 22$, $-5 \le l \le 5$
Measuring range $\theta_{min/max}$ / °	3.31 / 29.99
Goodness-of-fit on F_0^2	0.956
R_{int} /R_σ	0.0493 / 0.0350
R indices ($F_0^2 \le 2\sigma(F_0^2)$)	$R1$ = 0.0316, $wR2$ = 0.0776
R indices (all data)	$R1$ = 0.0444, $wR2$ = 0.0800
Largest diff. peak and hole / e Å^{-3}	1.54 / −0.90

Table S12: Atom coordinates of $LiGe_3P_3$ at 293 K from single crystal diffraction data.

Atom	**Wyck.**	***x***	***y***	***z***	U_{iso}
Ge1	4g	0.38291(7)	0.14395(4)	0.0000	0.01317(18)
Ge2	4h	0.05728(7)	0.10288(5)	0.5000	0.01850(19)
Ge3	4h	0.14978(7)	0.25307(4)	0.5000	0.01443(18)
P1	4g	0.29966(17)	0.28263(11)	0.0000	0.0143(3)
P2	4h	0.52703(17)	0.11824(11)	0.5000	0.0131(3)
P3	4g	0.19830(18)	0.05331(11)	0.0000	0.0158(4)
Li1	4h	0.7927(15)	0.0699(10)	0.5000	0.040(4)

Table S13: Anisotropic displacement parameters of $LiGe_3P_3$ at 293 K from single crystal diffraction data.

Atom	U_{11}	U_{22}	U_{33}	U_{23}	U_{13}	U_{12}
Ge1	0.0093(3)	0.0192(3)	0.0110(3)	0.000	0.000	−0.0001(2)
Ge2	0.0139(4)	0.0244(4)	0.0172(4)	0.000	0.000	−0.0016(3)
Ge3	0.0131(3)	0.0182(3)	0.0120(3)	0.000	0.000	0.0009(2)
P1	0.0130(8)	0.0177(8)	0.0122(8)	0.000	0.000	−0.0002(6)
P2	0.0096(8)	0.0192(8)	0.0104(8)	0.000	0.000	−0.0003(6)
P3	0.0139(8)	0.0195(8)	0.0141(8)	0.000	0.000	−0.0023(6)
Li1	0.027(8)	0.044(9)	0.048(9)	0.000	0.000	0.009(6)

Table S14: Selected distances and angles in $LiGe_3P_3$ at 293 K from single crystal diffraction data.

Atom 1	**Atom 2**	$d_{1\text{-}2}$ **/ Å**	
Ge1	P3	2.3123(19)	
Ge1	P2	2.3296(11)	2×
Ge1	P1	2.3370(18)	
Ge2	P3	2.4060(13)	2×
Ge2	Ge3	2.5393(10)	
Ge2	Li1	2.655(15)	
Ge2	Li1	3.101(15)	
Ge3	P2	2.3631(18)	
Ge3	P1	2.3757(12)	2×
Ge3	Li1	3.128(16)	
P1	Li1	2.945(13)	2×
P2	Li1	2.723(14)	
P3	Li1	2.653(12)	2×

Atom 1		**Atom 2**		**Atom 3**	**Angle**
P3	–	Ge1	–	P2	111.74(5)
P2	–	Ge1	–	P2	101.43(7)
P3	–	Ge1	–	P1	107.71(7)
P2	–	Ge1	–	P1	112.12(5)
P3	–	Ge2	–	P3	97.08(7)
P3	–	Ge2	–	Ge3	95.56(5)
P2	–	Ge3	–	P1	98.54(5)
P1	–	Ge3	–	P1	98.75(7)
P2	–	Ge3	–	Ge2	128.26(5)
P1	–	Ge3	–	Ge2	113.94(4)
Ge1	–	P1	–	Ge3	91.93(5)
Ge3	–	P1	–	Ge3	98.75(7)
Ge1	–	P2	–	Ge1	101.43(7)
Ge1	–	P2	–	Ge3	99.29(5)
Ge1	–	P3	–	Ge2	104.59(5)
Ge2	–	P3	–	Ge2	97.08(7)

Channels in Li_2GeP_2

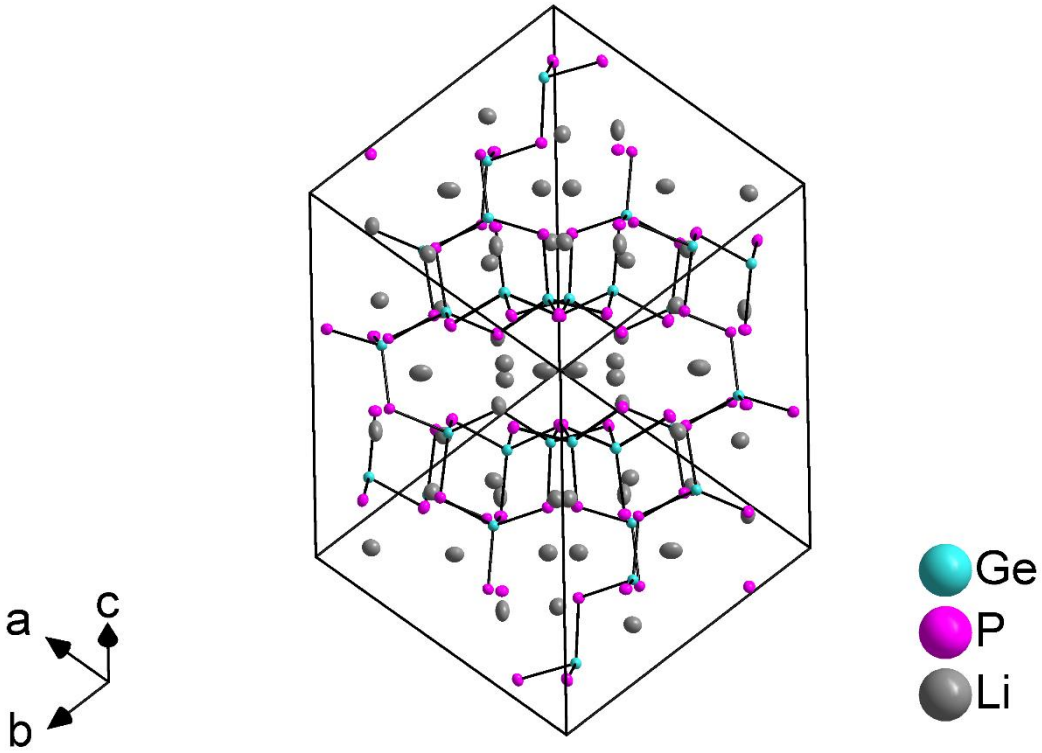

Figure S1: Illustration of the [111] direction of the unit cell of Li_2GeP_2. Ge-P bonds are shown as solid black lines. The Li channel in the center is connected to identical channels parallel to the other space diagonals.

Coordination Polyhedra

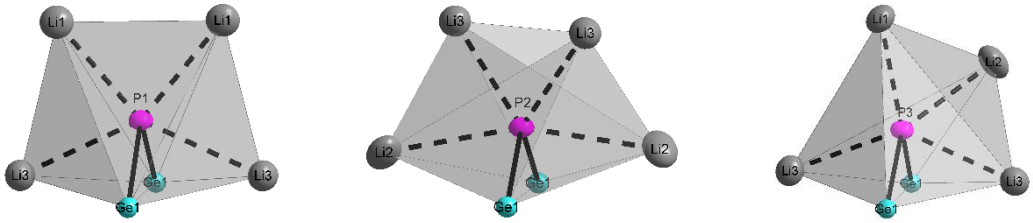

Figure S2: Coordination polyhedra of P in Li_2GeP_2. Each P atom is surrounded by two Ge atoms and four Li atoms.

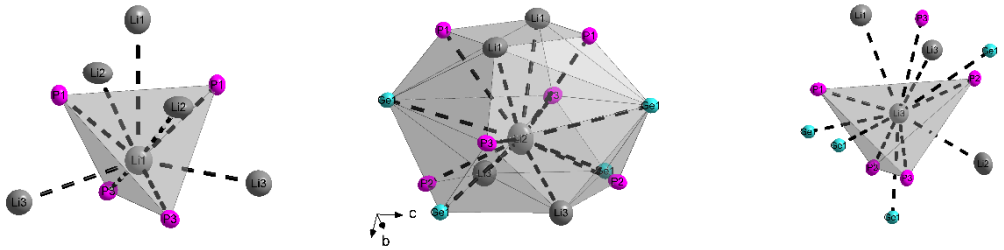

Figure S3: Coordination polyhedra of Li in Li_2GeP_2. Li atoms are located in strongly distorted tetrahedral voids of the *ccp* of P atoms. Additionally, every Li atom shows 3 to 5 short distances to neighboring Li atoms.

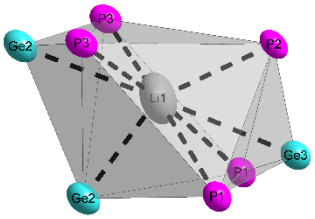

Figure S4: Coordination polyhedron of Li in $LiGe_3P_3$. One Ge2, one P2 and two P3 atoms form the first coordination sphere of a distorted tetrahedron. With the second coordination sphere, containing two P1 and the second Ge2, the polyhedron is supplemented to a two times capped octahedron.

Rietveld Refinements

Table S13: Rietveld refinement data of Li_2GeP_2.

Chemical formula	Li_2GeP_2
Temperature / K	293
Radiation type	Cu $K_{\alpha 1}$
M_r / g mol^{-1}	148.50
Crystal System, space group	Tetragonal, $I4_1/acd$
a, c / Å	12.34823(7), 19.0319(1)
V / Å^3	2901.97(3)
Z	32
ρ_{calcd} / g cm^{-3}	2.72
2θ range	5.03 - 90.31
R_p	5.00%
R_{wp}	8.25%
R_{exp}	5.83%
χ^2	2.00
R_{Bragg}	3.43%
R_f	3.18%

Table S14: Rietveld refinement data of $LiGe_3P_3$.

Chemical formula	$LiGe_3P_3$
Temperature / K	293
Radiation type	Cu $K_{\alpha 1}$
M_r / g mol^{-1}	317.75
Crystal System, space group	Orthorhombic, *Pbam*
a, *b*, *c* / Å	9.8556(2), 15.8586(2), 3.60752(5)
V / Å^3	563.841(1)
Z	4
ρ_{calcd} / g cm^{-3}	3.74
2θ range	5.04 - 90.30
R_p	2.51%
R_{wp}	3.52%
R_{exp}	5.19%
χ^2	0.49
R_{Bragg}	7.41%
R_f	9.03%

Electric Conductivity Measurements

The electric properties are determined by impedance spectroscopy and polarization measurements (Fig. S5). For each compound at least two samples are investigated. The measurement protocol starts with the impedance spectroscopy measurement, followed by the polarization measurement and ends with a second impedance spectroscopy measurement to identify changes in the sample. For Li_2GeP_2 a semicircle at high frequencies and a spike at lower frequencies is observed. By comparison with the polarization measurements, which yields an electronic conductivity of 10^{-8} S cm^{-1}, the origin of the semicircle, fitted with an R/CPE element and fits a conductivity of $1.6(3)\times10^{-7}$ S cm^{-1}, is proven to be mainly ionic conduction. However, separation of the bulk and grain boundary resistance was not possible. The resistance of Li_2GeP_2 does not change during the measurements. From the impedance spectroscopy measurement of $LiGe_3P_3$ only a semicircle, referring to a conductivity of 10^{-4} S cm^{-1}, is observed. Polarization measurements yielded an electronic conduction in the same order of magnitude. The ionic conductivity in $LiGe_3P_3$ can therefore not be determined. During the polarization measurement a slight but clear increase in conductivity is observed, which is also confirmed by the two impedance spectroscopy measurements. However, no structural changes were observed in with PXRD measurements after the electric measurements.

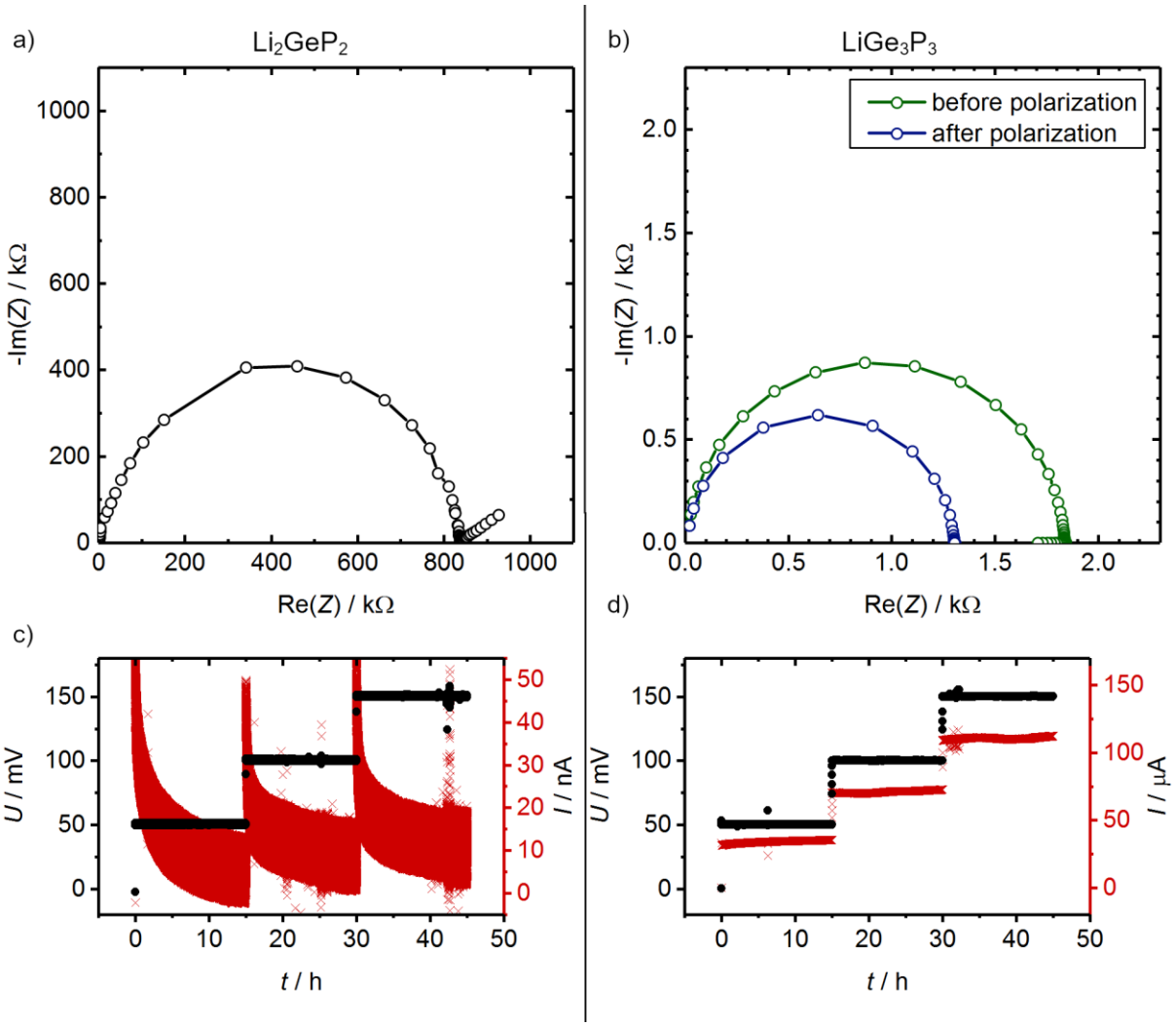

Figure S5: Nyquist plots of Li_2GeP_2 a) and $LiGe_3P_3$ b) and polarization curves of Li_2GeP_2 c) and $LiGe_3P_3$ d). Li_2GeP_2 shows ionic conductivity and only low electronic conductivity and $LiGe_3P_3$ shows only electronic conductivity.

Air and Water Stability Experiments

$LiGe_3P_3$ (50 mg) is ground to a fine powder in a mortar within the glove box. The mortar with the powder is transferred to a fume hood and left there for 24 h at ambient conditions. The condition of the sample is checked by PXRD and no change is observed. Afterwards the mortar is filled with deionized water. After 24 h the water is evaporated, and the sample again checked via PXRD. The ratio of $LiGe_3P_3$ and the side phase Ge stays constant and only slight changes in reflection intensity are observed, indicating no significant change of the structure (Fig. S6).

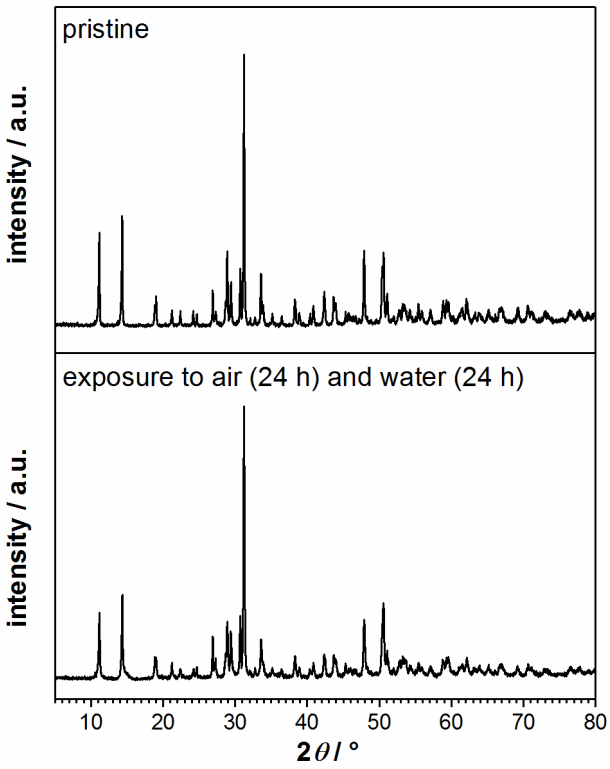

Figure S6: Comparison of $LiGe_3P_3$ PXRD patterns before and after exposure to air and water.

Differential Scanning Calorimetry

Samples of Li_2GeP_2 and $LiGe_3P_3$ investigated with DSC showed distinct signals for melting (Fig. S7). Minor peaks found during heating of $LiGe_3P_3$ could not be assigned to a certain phase transition. During cooling for both samples additional thermal events are observed, which are related to the crystallization of side phases. *Post mortem* PXRD investigations showed a strongly increased amount Ge and other side phases within the samples.

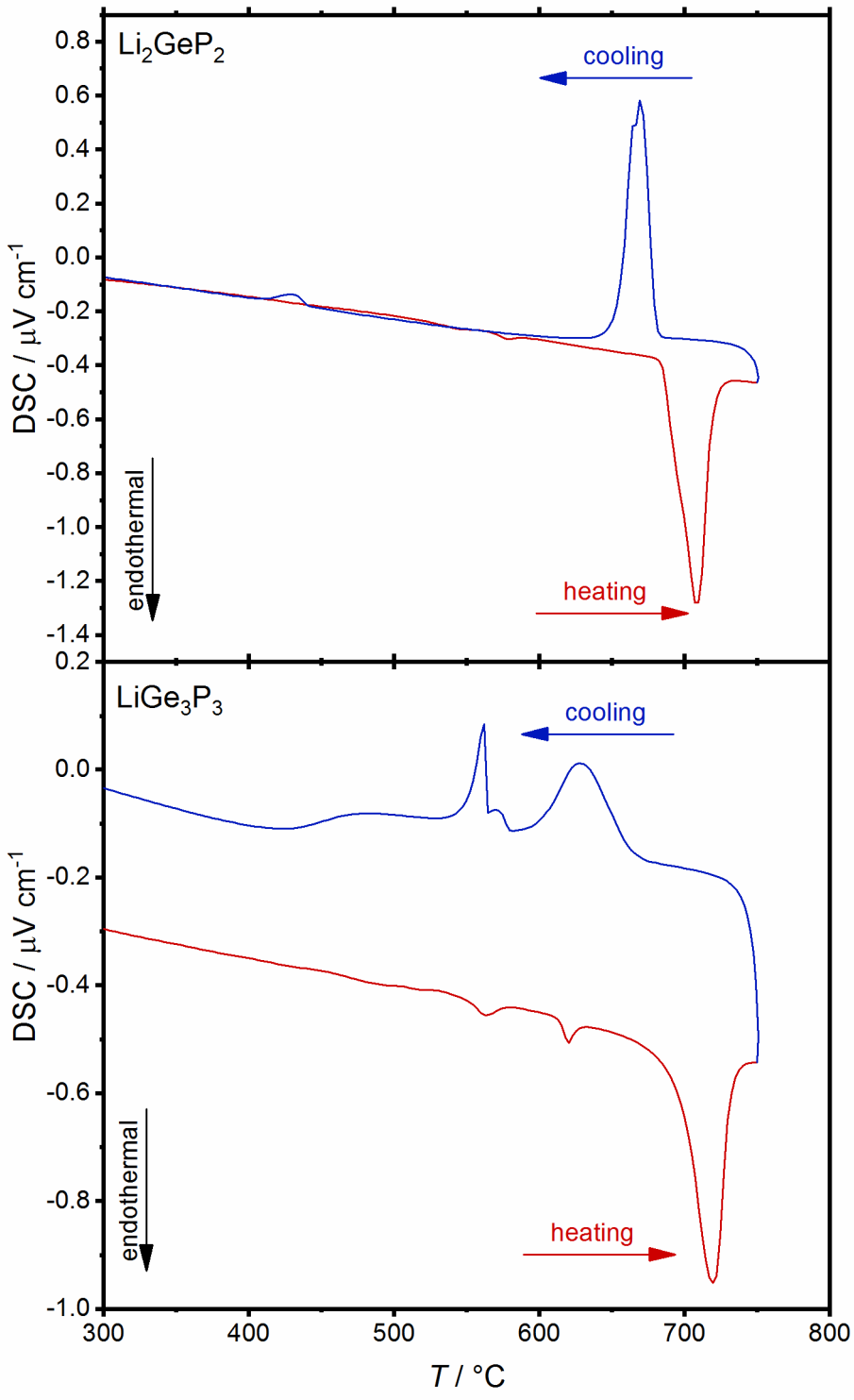

Figure S7: DSC curves of Li_2GeP_2 and $LiGe_3P_3$.

5.5 Planar Tetrelide Pentagons and Isolated Phosphide Anions in Lithium Phosphotetrelides $Li_{10.68(8)}Si_5P$ and $Li_{10.1(2)}Ge_5P$

H. Eickhoff, L. Toffoletti, W. Klein, G. Raudaschl-Sieber, T. F. Fässler

manuscript for publication

Planar Tetrelide Pentagons and Isolated Phosphide Anions in Lithium Phosphotetrelides $Li_{10.68(8)}Si_5P$ and $Li_{10.1(2)}Ge_5P$

Henrik Eickhoff, Wilhelm Klein, Lorenzo Toffoletti, Gabriele Raudaschl-Sieber, Thomas F. Fässler

Department of Chemistry, Technische Universität München,

Lichtenbergstrasse 4, 85747 Garching bei München, Germany

* E-mail: thomas.faessler@lrz.tu-muenchen.de

Abstract

The new phosphotetrelides $Li_{10.68(8)}Si_5P$ and $Li_{10.1(2)}Ge_5P$ are the first ternary compounds in the respective phase system featuring 0-dimensional building blocks which were previously found solely in binary alkaline tetrelides and phosphides. They comprise aromatic Tt_5-pentagons with a mostly ordered Li environment and isolated P^{3-} anions with a mainly disordered Li surrounding. The 5-membered ring subunits are stacked forming $^{1}_{\infty}[Li_6Tt_5]$ (*Tt* = Si, Ge) complex chains. Both compounds crystallize in the space group *Pnma* (63) ($Z = 4$) with cell parameters of $a = 10.2434(3)$ Å, $b = 4.2788(1)$ Å, $c = 23.9767(3)$ Å for $Li_{10.68(8)}Si_5P$ and $a = 10.3599(11)$ Å, $b = 4.3072(2)$ Å, $c = 24.267(2)$ Å for $Li_{10.1(2)}Ge_5P$. Structure determination via X-ray single crystal diffraction is supported by X-ray powder diffraction measurements and solid state MAS NMR of ^{7}Li, ^{29}Si and ^{31}P nuclei on high purity samples.

Introduction

The increasing focus on renewable energy and electromobility are accompanied by the demand for improved battery systems with increased energy and power density. For these systems new materials are crucial.[1-3] While in the past decades silicon and other tetrel elements have been investigated in detail as anode material due to their outstanding theoretic capacity,[4-6] more recently also anodes of binary silicon phosphorus compounds gained interest. Similar to silicon those materials show high theoretic capacities and high capacities on first charging but also a fast fading capacity retention during cycling.[7-10]

For deeper insight into the charging and discharging mechanism of these anode materials the formed phases during lithiation have been investigated and reported. In silicon anodes crystalline $Li_{15}Si_4$, which consists of isolated Si anions, represents the maximum charged species. In between the charged and the discharged state an amorphous phase consisting of Li atoms and isolated Si atoms or Si_2 dumbbells is present.[11,12] During lithiation of SiP_2 various phases have been observed, such as Li_3P, LiP[8] and also ternary lithium phosphidosilicates. The latter occur while charging as $LiSi_2P_3$ to which formally Li_3P is added leading to Li_2SiP_2 and Li_8SiP_4 and finally Li_3P and silicon containing phases.[9]

Despite of the rich structural chemistry of silicides, during lithiation of silicon phosphides negatively charged Si atoms and Si-Si bonds have not been found and are generally scarce in ternary compounds containing silicon and phosphorus. In binary lithium silicide phases various structural motives like isolated Si^{4-} in $Li_{17}Si_4$[13], $Li_{4.11}Si$[14] and $Li_{15}Si_4$[12,15] and Si_2^{6-} dumbbells in Li_7Si_3[16] and $Li_{13}Si_4$[17] as well as three dimensional frameworks in LiSi[18,19] occur. In $Li_{12}Si_7$ exotic silicon building blocks, trigonal planar Si_4^{12-} stars and planar Si_5^{6-} rings, are realized.[20,21] The latter 5-membered rings are aromatic systems,[22] which are also known for the heavy homologues germanium, tin and lead with various alkaline and alkaline earth metal counter ions.[23-25] Li_8MgSi_6[25] and $Li_{11}Ge_6$[26], which *Nesper et al.* suggested to be Li_8MgGe_6, are composed of Tt^{4-} and Tt_5^{6-} anions, of which the latter form multidecker-π-complexes (6π) with magnesium.

In contrast to the structural chemistry of silicides, until now all ternary phases of lithium, silicon and phosphorus are lithium phosphidosilicates, which are built from SiP_4 tetrahedra similar to SiO_4 in "oxido" silicates. In Li_8SiP_4 such tetrahedra are solely isolated, *i. e.* they are surrounded by lithium atoms and are not bonded to other tetrahedra.[27] On the other hand Li_2SiP_2 and $LiSi_2P_3$ form three dimensional frameworks of condensed tetrahedra consisting of T2 or T4 and T5 supertetrahedra, respectively.[27,28] The anionic partial structure of further known compounds, $Li_{10}Si_2P_6$ and $Li_3Si_3P_7$, consist of edge sharing Si_2P_6 double tetrahedra, or Si_3P_7 bilayers of

tetrahedra connected via P-P bonds, respectively.[29] By exchanging lithium with transition or alkaline earth metals the successful synthesis of compounds containing homoatomic Si bonds have been reported as silicon phosphides or phosphosilicides. While these compounds comprise Si-Si bonds they still show tetrahedral and trigonal pyramidal coordination for Si and P, respectively.[30-32]

In this work we present the first lithium phosphosilicide $Li_{10.68(8)}Si_5P$ and lithium phosphogermanide $Li_{10.1(2)}Ge_5P$, which are built solely from 0-dimensional anionic units, namely 5-membered tetrelide rings and isolated phosphide ions.

Experimental

Synthesis

As a precursor Li_3P was synthesized by reaction of 1.206 g Li (Rockwood Lithium, 99%) and 1.794 g P (Sigma Aldrich, 97%) via ball milling (Retsch PM100 planetary ball mill) in a 50 mL steel jar and three balls with 15 mm diameter at 250 rpm for 12 h. The intermediate product was filled in a steel autoclave and heated for to 400 °C for 12 h. Powder X-ray diffraction was used to confirm the crystallographically pure product.

Single crystals of $Li_{10.68(8)}Si_5P$ were obtained from a reaction with the nominal composition of "$Li_{10.5}Si_5P$" of 106 mg Li_3P, 107 mg Li and 287 mg Si (Wacker, 99.9%) and the bulk material with the same composition was synthesized from 149 mg Li, 287 mg Si and 63 mg P in a tantalum ampoule. Both samples were heated to 700 °C for 24 h and cooled with 1 °C min^{-1} to room temperature.

$Li_{10.1(2)}Ge_5P$ single crystals were found in a sample prepared from 78 mg Li, 388 mg Ge (Evochem, 99.999%) and 33 mg P. It was treated in a tantalum ampoule for 24 h at 680 °C. The bulk material was synthesized from 81.1 mg Li, 385.9 mg Ge and 32.9 P resembling a composition of "$Li_{11}Ge_5P$" in a Ta ampoule at 600 °C for 24 h. To reduce the amount of LiGe the ampoule was opened, the intermediate product ground, sealed in a Ta ampoule and reheated to 500 °C for 72 h. All three heating steps were cooled with a rate of 1 °C min^{-1}.

Powder X-Ray Diffraction

Powder X-ray diffraction data was collected on a Stoe Stadi P diffractometer at room temperature in Debye-Scherrer geometry. It was equipped with a Cu $K_{\alpha 1}$ radiation source (λ = 0.154056 Å), a Ge(111) monochromator and a Dectris Mythen 1 K detector. Samples were sealed in capillaries with 0.3 mm diameter, data were processed with WinX-POW software[33] and for Rietveld refinement the Fullprof Suite program[34] was used. A free refinement of Li occupancy in $Li_{10.68(8)}Si_5P$ and $Li_{10.1(2)}Ge_5P$ led to 11.1(3) and 11.7(2) Li per formula unit, respectively.

Single Crystal X-Ray Diffraction

Single crystal X-ray diffraction was performed with an Xcalibur 3 (Oxford Diffraction) equipped with a fine focused Mo-K_α radiation source (λ = 0.71073 Å), a graphite monochromator and a Sapphire 3 CCD detector. The data were processed with the program package ShelX-2014[35]. Refinement was possible in space groups $P2_1/m$, *Pnma* and *Cmcm* with similar good residuals but no further splitting of Li atoms was observed when reducing the symmetry from *Pnma* to $P2_1/m$. In $Li_{10.1(2)}Ge_5P$ the positions Li2 and Li10 to Li14 were refined with isotropic displacement parameters leading to mostly reasonable occupancies. Only the S.O.F of Li14 in $Li_{10.68(8)}Si_5P$ and $Li_{10.1(2)}Ge_5P$ was set to 0.5.

Magic Angle Spinning Nuclear Magnetic Resonance Spectroscopy

Magic angle spinning nuclear magnetic resonance (MAS NMR) spectra were recorded with a Bruker Avance 300 operating at 7.04 T. Due to its metallic appearance the sample of $Li_{10.68(8)}Si_5P$ diluted in a 1:2 ratio with GeO_2. Resonance frequencies of 116.6, 59.6, and 121.5 MHz and pulse width of 13, 10, and 1.33 µs were applied for ^{7}Li, ^{29}Si, and ^{31}P measurements, respectively. Relaxation delays were set to 4, 10, and 60 s for the three elements in $Li_{10.68(8)}Si_5P$ and to 4 and 10 s for Li and P in $Li_{10.1(2)}Ge_5P$. Samples were packed in 4 mm ZrO MAS NMR probes and rotated with frequencies of 15 kHz for ^{7}Li and, 8 kHz for ^{29}Si and 15 kHz and 10 kHz for ^{31}P in $Li_{10.68(8)}Si_5P$ and $Li_{10.1(2)}Ge_5P$, respectively, during the measurements.

Differential scanning calorimetry

Differential scanning calorimetry (DSC) measurements were recorded on a DSC 404 Pegasus (Netzsch). The samples (50 mg to 100 mg) are welded in custom build Nb crucibles and the measurements are carried out with a gas flow of 75 mL min^{-1} and a heating rate of 10 °C min^{-1}.

Electronic conductivity

A pellet of $Li_{10.68(8)}Si_5P$ was pressed (ø = 13 mm), sputtered with Au contacts (ø = 12 mm) and used for chronoamperometry measurements with potential steps of 50 mV, 100 mV and 150 mV applied for 30 s.

Discussion

Crystal structure of $Li_{10.68(8)}Si_5P$ and $Li_{10.1(2)}Ge_5P$

The lithium phophosilicide $Li_{10.68(8)}Si_5P$ crystallizes as grey metallic blocks in the orthorhombic space group *Pnma* (62) with lattice parameters of a = 10.2434(3) Å, b = 4.2788(1) Å, c = 23.9767(3) Å at 130 K (Fig. 1a). In contrast to the lithium phosphidosilicates known so far, this compound is composed of planar 5-membered rings of Si and isolated P atoms surrounded by Li atoms. The Si_5 ring is very similar to the tetrel anions found in related compounds $Li_{11}Ge_6$, Li_8MgSi_6, Na_8BaSn_6, Na_8EuSn_6, Na_8BaPb_6.[23,25,26]

Due to the similar X-ray scattering factors of Si and P, an assignment to structure positions via X-ray diffraction data has to be considered carefully. The crystal structure with the lowest residual values found for homoatomic Si_5-rings and accompanied isolated P anions in single crystals of $Li_{10.68(8)}Si_5P$ is confirmed by chemical shifts in ^{29}Si and ^{31}P MAS NMR spectra. The chemical shifts of ^{29}Si with ~273 ppm, ~294 ppm and ~374 ppm fall in the chemical shift range of anionic silicon moieties but is larger than chemical shifts reported for other 5-membered Si rings as found in $Li_{12}Si_7$ (δ(^{29}Si; Si_5) = 171.1 ppm, 195.7 ppm, 231.5 ppm, 295.7 ppm and 311.5 ppm; δ(^{29}Si; Si_4) = 55.5 ppm, 62.1 ppm, 191.8 ppm, 369.5 ppm,).[36] In the ^{31}P NMR spectrum two distinct signals at −272 ppm and −283 ppm and a shoulder at ~−295 ppm are visible that fit the chemical shift reported for Li_3P [δ(^{31}P) = −278 ppm] hinting for the presence of P^{3-}.[37] Since single crystal analysis shows only one P position is found, the presence of multiple peaks suggest different surroundings for this position. EDX measurements confirm the expected Si:P ratio with 80(4):20(4). In addition the reported stability of Tt_5-rings and the presence of Ge_5-rings in $Li_{10.1(2)}Ge_5P$ support this assignment. Thus, the six different heavy atom positions were assigned as Si1 to Si5 in the pentagonal rings and to P1 as an isolated phosphide anion. These building blocks are coordinated by fourteen different Li positions, of which Li6 to Li8 and Li10 to Li14 are partially occupied, leading to 10.68(8) Li atoms per formula unit.

The pentagonal Si rings are slightly distorted with bond lengths ranging from 2.3511(5) Å to 2.3810(4) Å and internal angles between 106.45(2)° and 109.73(2)°. These findings fit well to reported values in Li_8MgSi_6 (2.346 Å to 2.385 Å)[25] and $Li_{12}Si_7$ (2.356 Å to 2.381 Å),[21] in which the planar rings are described as aromatic systems with a formal charge of −6. In $Li_{10.68(8)}Si_5P$ these units are also stacked along the b axis and sandwich the Li1 position forming infinite $^1_\infty[LiSi_5]$ complexes. Coplanar to Li1 these stacks are surrounded by 5 Li, consisting of the positions Li2, Li3, Li4, Li5 and the split position Li6/Li7, extending the complexes to $^1_\infty[Li_6Si_5]$ (Fig. 1b,c).

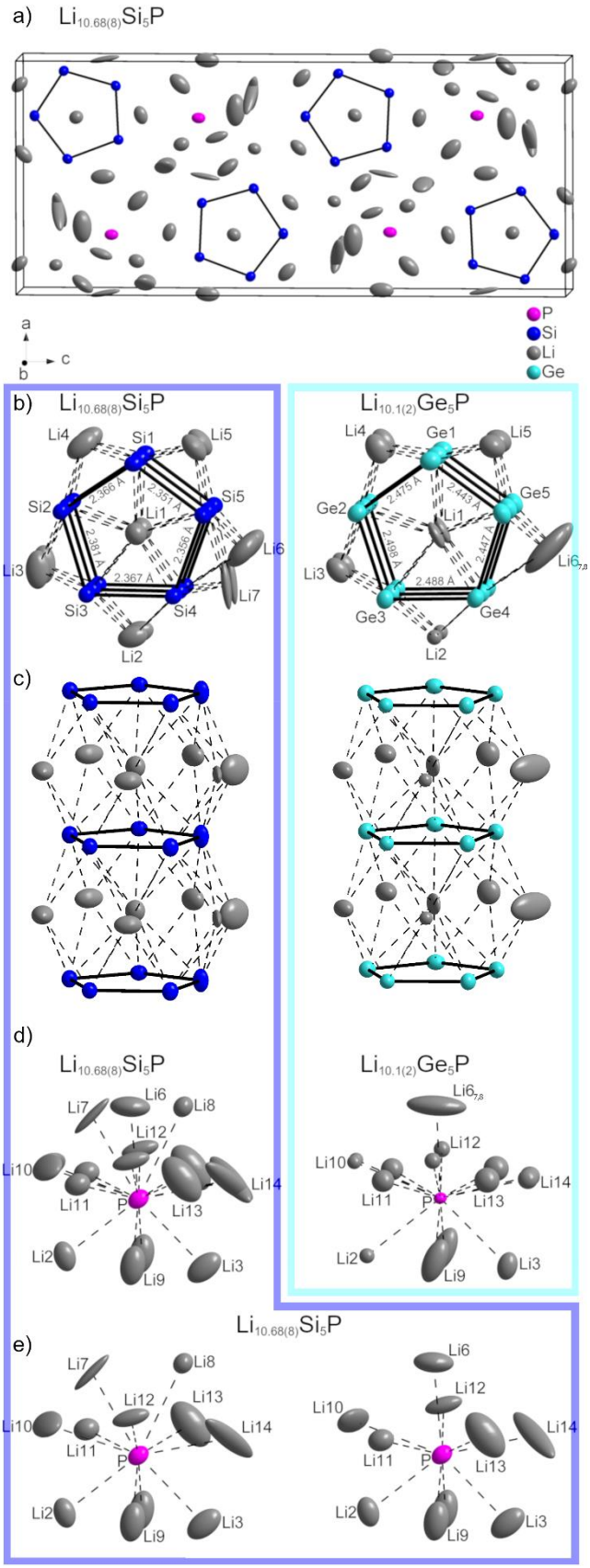

Figure 1: a) Unit cell of $Li_{10.68(8)}Si_5P$ also representing the isotype $Li_{10.1(2)}Ge_5P$; b) Environment of Tt_5 pentagons forming $^1_\infty[Li_6Tt_5]$ chains; c) side view of $^1_\infty[Li_6Tt_5]$ π-stacks; d) Environment of P in both compounds; e) Potential ordered model for two coordination spheres for local Li environment of P in $Li_{10.68(8)}Si_5P$.

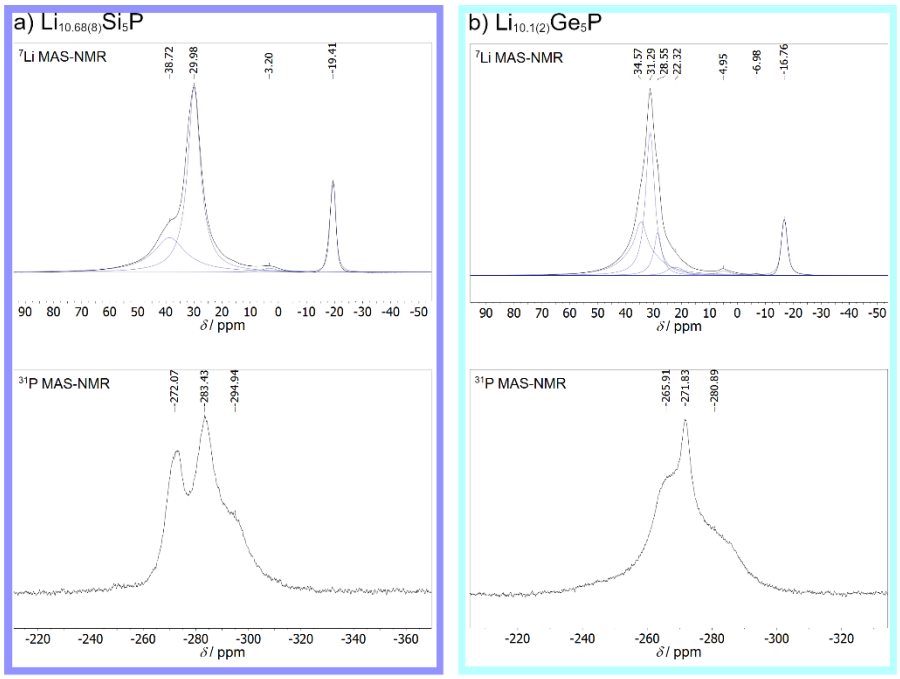

Figure 2: ^{7}Li and ^{31}P MAS NMR spectra of a) $Li_{10.68(8)}Si_5P$ and b) $Li_{10.1(2)}Ge_5P$. Line fits are depicted as blue lines.

Between those sandwich stacks the isolated P atom, which can be regarded as P^{3-}, is placed, separating the Li-Si tubes. A closer inspection reveals a regardably disordered Li environment around this position. It is surrounded by four fully occupied atom sites, Li2, Li3 and two Li9 atoms, and 13 partially occupied sites, Li6, Li7, Li8 and two Li10, Li11, Li12, Li13, Li14 (Fig. 1d). Considering reasonable interatomic Li-Li distances of at least 2 Å and summed occupations of neighboring Li positions of unity or lower, the disordered coordination environment can be split in at least two different discrete coordination spheres containing up to 11 Li atom sites (Fig. 1e). These findings agree with the measured ^{31}P MAS NMR spectrum, which contains two signals and a shoulder indicating the presence of at least three different P environments (Fig. 2). Also, the ^{7}Li MAS NMR spectrum coincides with the distribution of Li. A narrow signal with a chemical shift of −19.4 ppm is assigned to Li1 due to ring currents in the Si_5 units confirming its aromatic character.[20,22,36] The largest signal centered at 30.0 ppm with shoulders at 38.7 ppm and 3.2 ppm could only be fitted with three different signals. This could resemble different coordination environments with Si or P. Compared to the upfield signal with a half width of 281 Hz the much wider constituents of the larger signal show half widths of 1627 Hz, 634 Hz and 861 Hz from downfield to upfield, respectively, indicating a larger disorder in these sites. However, since distinct signals are observable, an exchange of Li atoms between the coordination environments seems unlikely or slow. Comparing the amount of Li we find a sum of 10.68(8) Li atoms per formula unit for single crystal data. This translates to an intensity ratio of 9.7:1 for the observed NMR signals, since Li1 is solely the origin of the downfield signal. The found ratio in NMR varies

from 8.2:1 to 10.0:1 for different samples, representing Li contents of 9.2 to 11.0 per formula unit and includes the value found in the single crystal.

A Li content of 9 atoms per formula unit would counterbalance the anionic units of Si_5^{6-} (representing the Si analogue to an unprotonated cyclopentadienyl anion) and P^{3-} and would lead to a classical Zintl phase. The higher content implies a non-classical Zintl phase, which usually show metallic properties. Indeed, the investigation of the electronic conductivity in $Li_{10.68(8)}Si_5P$ revealed $2(1)\times10^{-2}$ S cm^{-1}, which is more than an order of magnitude higher than conductivities of related ternary phases as Li_8MgSi_6.[25] Li_8MgSi_6 can be described as a classical, electron precise Zintl phase, like other ternary tetrel pentagon containing ternary phases. Contrary to that, all binary lithium silicides are not electron precise, metallic Zintl phases. With $Li_{10.68(8)}Si_5P$ also showing an electron excess it is the first ternary phase containing tetrel pentagons, while being a metallic Zintl phase.

The isotypic compound $Li_{10.1(2)}Ge_5P$ crystallizes with larger cell parameters of a = 10.3599(11) Å, b = 4.3072(2) Å, c = 24.267(2) Å at 120 K. More clearly than for the Si containing compound X-ray data showed the presence of planar Ge_5-rings and isolated P anions. For Li a slightly different distribution is found leading to 12 different Li sites resulting in 10.1(2) Li per formula unit. The Ge pentagons exhibit bond lengths ranging from 2.4432(11) Å to 2.4884(12) Å and show Ge-Ge-Ge angles from 107.33(4)° to 109.13(4)°. The environment of these rings is built from Li1 to $Li6_{7,8}$, of which $Li6_{7,8}$ shows a large anisotropic ellipsoid. This atom position replaces three partially occupied sites (Li6, Li7, Li8) present in $Li_{10.68(8)}Si_5P$, which could not be refined separately in $Li_{10.1(2)}Ge_5P$. In the Ge containing compound the isolated P anion is surrounded by Li2, Li3, $Li6_{7,8}$ and two Li9 to Li12 each. This leads to 15 atom positions in the proximity, two less compared to $Li_{10.68(8)}Si_5P$ since the positions Li6, Li7 and Li8 were merged. ^{31}P MAS NMR spectroscopy shows a single signal at −272 ppm with two shoulders at ~−266 ppm and ~−281 ppm again indicating more than one local environment around the P anion. Differences to the Si-compound might result from the merged $Li6_{7,8}$ position giving less possible arrangements for Li around P. The ^{7}Li MAS NMR spectrum, similar to the one of $Li_{10.68(8)}Si_5P$, contains a downfield signal with a chemical shift of −16.7 ppm representing Li1 centered between the Ge_5 rings and a broad signal centered at a shift of 31.28 ppm, which breaks down into three signals [δ(^{7}Li) = 34.6 ppm, 31.3 ppm, 28.6 ppm] representing the different environment of Li. Additionally, two weak signals at 5.0 ppm and −7.0 ppm are observed. Normalizing the downfield signal to an intensity of 1 Li atom, as Li1 is the only origin, results in a Li content of 10.5 Li per formula unit.

Table 1: Data of single crystal refinement of $Li_{10.68(8)}Si_5P$ and $Li_{10.1(2)}Ge_5P$.

Empiric formula	$Li_{10.68(8)}Si_5P$	$Li_{10.1(2)}Ge_5P$
T / K	130(2)	120(2)
Formula weight / g mol^{-1}	245.51	464.11
Crystal size / mm^3	0.17 × 0.10 × 0.09	0.19 × 0.07 × 0.05
Crystal color	silver, metallic	black
Crystal system	orthorhombic	orthorhombic
Space group	*Pnma* (62)	*Pnma* (62)
Unit cell dimensions / Å	a = 10.2434(3)	a = 10.3599(1)
	b = 4.2788(1)	b = 4.3072(2)
	c = 23.9767(3)	c = 24.267(2)
V / Å^3	1050.89(1)	1082.85(2)
Z	4	4
ρ (calc.) / g cm^{-3}	1.522	2.863
μ / mm^{-1}	0.755	13.791
F(000)	460	826
θ range / deg	3.23 - 37.08	3.195 - 28.938
Index range (*hkl*)	$-15 \leq h \leq 15$	$-12 \leq h \leq 13$
	$-7 \leq k \leq 7$	$-5 \leq k \leq 5$
	$-40 \leq l \leq 40$	$-30 \leq l \leq 32$
Reflections collected	46975	6986
Independent Reflections	2458	1396
R_{int}	0.0400	0.0699
Reflections with $I > 2\sigma(I)$	1700	946
Absorption correction	multi-scan	multi-scan
Data / restraints /parameters	2458 / 0 / 134	1396 / 0 / 98
Goodness-of-fit on F^2	0.940	0.833
R_1, wR_2 (all data)	0.0449, 0.0536	0.0549, 0.0576
R_1, wR_2 ($I > 2\sigma(I)$)	0.0265, 0.0515	0.0303, 0.0543
Largest diff. peak and hole / e Å^{-3}	0.336, −0.647	1.276, −0.974

Table 2: Occupancies of partially occupied Li positions in $Li_{10.68(8)}Si_5P$ and $Li_{10.1(2)}Ge_5P$.

Atom	S.O.F.($Li_{10.68(8)}Si_5P$)	S.O.F.($Li_{10.1(2)}Ge_5P$)
Li6 / $Li6_{7,8}$	0.532(13)	1
Li7	0.425(13)	-
Li8	0.393(10)	-
Li10	0.312(7)	0.35(3)
Li11	0.680(11)	0.47(5)
Li12	0.292(11)	0.38(5)
Li13	0.733(15)	0.55(5)
Li14	0.5	0.5

The compounds $Li_{10.68(8)}Si_5P$ and $Li_{10.1(2)}Ge_5P$ were synthesized in high purity from the elements. For $Li_{10.68(8)}Si_5P$ a reaction temperature of 700 °C was chosen while $Li_{10.1(2)}Ge_5P$ was synthesized at 600 °C due to melting points found in DSC measurements between 682 °C and 732 °C or 582 °C and 633 °C, respectively. $Li_{10.1(2)}Ge_5P$ was ground and reheated to 500 °C to remove the remaining side phase LiGe. After that treatment the sample with the nominal composition of "$Li_{11}Ge_5P$" did not show any remaining side phases in a Rietveld refinement (Fig. 3). In identically treated samples with a slightly lower Li content of "$Li_{10.5}Ge_5P$" and "$Li_{10}Ge_5P$" still LiGe was present.

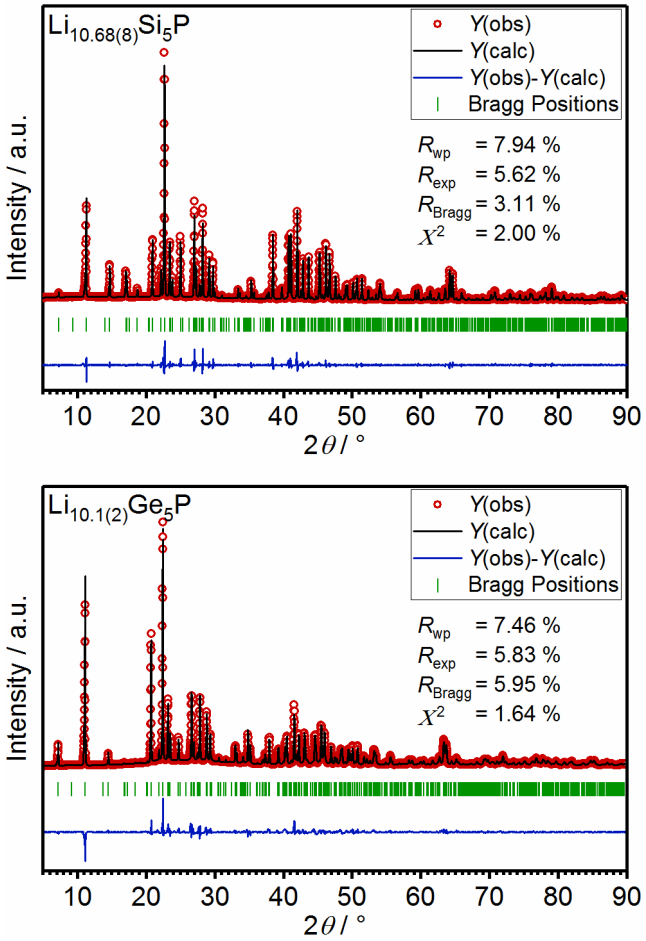

Figure 3: Rietveld refinement plots of $Li_{10.68(8)}Si_5P$ (top) and $Li_{10.1(2)}Ge_5P$ (bottom) with experimental data *Y*(obs) and calculated pattern *Y*(calc). The refinement led to cell parameters of a = 10.26738(5) Å, b = 4.29631(2) Å, c = 23.97193(12) Å and a = 10.42302(8) Å, b = 4.33906(3) Å, c = 24.28783(19) Å, respectively.

Conclusion

The lithium phosphotetrelides $Li_{10.68(8)}Si_5P$ and $Li_{10.1(2)}Ge_5P$ represent the first compounds comprising separated, anionic tetrelide Tt_5^{6-} and phosphide P^{3-} building blocks. These structural features distinguish them significantly from other compounds in the corresponding Li/*Tt*/P phase systems, which are mainly built from TtP_4 tetrahedra. The new compounds show similarities with $Li_{12}Si_7$ and ternary phases from main groups I-II-IV such as Li_8MgSi_6. While in those compounds formally an alkaline metal atom is replaced by an alkaline earth metal atom, providing an additional electron, in the new lithium phosphotetrelides the isolated tetrel atom position is replaced by phosphorus, providing an additional electron. These materials might also shed further light onto the transitions occurring during lithiation of Tt_xP_y based anode materials and could provide a potential explanation for compositional discrepancy for TtP/SiP_2 and phases occurring in their highly lithiated state such as Li_8SiP_4.

References

[1] Croguennec, L.; Palacin, M. R.; Recent Achievements on Inorganic Electrode Materials for Lithium-Ion Batteries, *J. Am. Chem. Soc.* **2015**, *137*, 3140-3456.

[2] Nitta, N.; Wu, F.; Lee, J. T.; Yushin, G.; Li-Ion battery materials: present and future, *Mater. Today* **2015**, *5*, 252-264.

[3] Blomgren, G. E. The Develepment and Future of Lithium Ion Batteries, *J. Electrochem. Soc.* **2017**, *164*, A5019-A5025.

[4] Zuo, X.; Zhu, J.; Müller-Buschbaum, P.; Chen, Y.-J.; Silicon based lithium-ion battery anodes: A chronicle perspective review, *Nano Energy* **2017**, *31*, 113-143.

[5] Zhang, W.-J.; A review of the electrochemical performance of alloy anodes for lithium-ion batteries, *J. Power Sources* **2011**, *196*, 13-24.

[6] McDowell, M. T.; Lee, S. W.; Nix, W. D.; Cui, Y.; 25th Anniversary Article: Understanding the Lithiation of Silicon and Other Alloying Anodes for Lithium-Ion Batteries, *Adv. Mater.* **2013**, *25*, 4966-4985.

[7] Kwon, H.-T.; Lee, C. K.; Jeon, K.-J.; Park, C.-M.; Silicon Diphosphide: A Si-Based Three-Dimensional Crystalline Framework as a High-Performance Li-Ion Battery Anode, *ACS Nano* **2016**, *10*, 5701-5709.

[8] Reinhold, R.; Stoeck, U.; Grafe, H.-J.; Mikhailova, D.; Jaumann, T.; Oswald, S.; Kaskel, S.; Giebeler, L.; Surface and Electrochemical Studies on Silicon Diphosphide as Easy-to-Handle Anode Material for Lithium-Based Batteries-the Phosphorus Path, *ACS Appl. Mater Interfaces*, **2018**, *10(8)*, 7096-7106.

[9] Coquil, G.; Fraisse, B.; Dupré, N.; Monconduit, L.; Versatile Si/P System as Efficient Anode for Lithium and Sodium Batteries: Understanding of an Original Electrochemical Mechanism by a Full XRD-NMR Study, *ACS Appl. Energy Mater.* **2018**, *1(8)*, 3778-3789.

[10] Reinhold, R.; Mikhailova, D.; Gemming, T.; Missyul, A. B.; Nowka, C.; Kaskel, S.; Giebeler, L.; Silicon monophosphide as a possible lithium battery anode material, *J. Mater. Chem. A* **2018**, *6*, 19974-19978.

[11] Key, B.; Bhattacharyya, R.; Morcrette, M.; Seznéc, V.; Rarascon, J.-M.; Grey, C. P. Real-Time NMR Investigations of Structural Changes in Silicon Electrodes for Lithium-Ion Batteries, *J. Am Chem. Soc.* **2009**, *131*, 9239-9249.

[12] Obrovac, M. N.; Christensen, L. Structural Changes in Silicon Anodes during Lithium Insertion/Extraction, *Electrochem. Solid St.* **2004**, *7*, A93-A96.

[13] Zeilinger, M.; Benson, D.; Häussermann, U.; Fässler, T. F.; Single Crystal Growth and Thermodynamic Stability of $Li_{17}Si_4$, *Chem. Mater.* **2013**, *25*, 1960-1967.

[14] Zeilinger, M.; Kurylyshyn, I. M.; Häussermann, U.; Fässler, T. F.; Revision of the Li-Si Phase Diagram: Discovery and Single-Crystal X-ray Structure Determination of the High-Temperature Phase $Li_{4.11}Si$, *Chem. Mater.* **2013**, *25*, 4623-4632.

[15] Hatchard, T. D.; Dahn, J. R.; *In Situ* XRD and Electrochemical Study of the Reaction of Lithium with Amorphous Silicon, *J. Electrochem. Soc.* **2004**, *151*, A838-A842.

[16] von Schnering, H. G.; Nesper, R.; Tebbe, K. F.; Curda, J.; Structure and properties of Li14Si6/Li2.33/Si/, the violet phase in the lithium-silicon, *Z. Metallkd.* **1980**, *71*, 357.

[17] Frank, U.; Müller, W.; Schäfer, H.; Zur Kenntnis der Phase $Li_{13}Si_4$/On the Phase $Li_{13}Si_4$, *Z. Naturforsch.* **1975**, *30b*, 10-13.

[18] Evers, J.; Oehlinger, G.; Sextl, G.; Hochdruck-Synthese von LiSi: Raumnetzstruktur aus dreibindigen Si^--Ionen, *Angew. Chem.* **1993**, *105*, 1532-1533; High-Pressure Synthesis of LiSi: Three-Dimensional Network of Three-Bonded Si^- Ions, *Angew. Chem. Int. Ed. Engl.* **1993**, *32*, 1442-1444.

[19] Tang, W. S.; El Chotard, J.-N.; el Janotz, R.; Synthesis of Single-Phase LiSi by Ball-Milling: Electrochemical Behavior and Hydrogenation Properties, *J. Electrochem. Soc.* **2013**, *160*, A1232-A1240.

[20] Nesper, R.; von Schnering, H. G.; Curda, J.; $Li_{12}Si_7$, eine Verbindung mit trigonal-planaren Si_4-Clustern und isometrischen Si_5-Ringen, *Chem. Ber.* **1986**, *119*, 3576-3590.

[21] von Schnering, H. G.; Nesper, R.; Curda, J.; Tebbe, K. F.; $Li_{12}Si_7$, eine Verbindung mit trigonal-planarem Si_4-Cluster und planaren Si_5-Ringen, *Angew. Chem.* **1980**, *92*, 1070; $Li_{12}Si_7$, a Compound Having a Trigonal Planar Si_4 Cluster and Planar Si_5 Rings, *Angew. Chem. Int. Ed. Engl.* **1980**, *19*, 1033-1034.

[22] Kuhn, A.; Sreeraj, P.; Pöttgen, R.; Wiemhöfer, H.-D.; Wilkening, M.; Heitjans, P.; Li-NMR-Spektroskopie an kristallinem Li12Si7: zur Aromatizität planarer, Cyclopentadienyl-analoger Si_5^{6-}-Ringe, *Angew. Chem.* **2011**, *123*, 12305-12308; Li NMR Spectroscopy on Crystalline $Li_{12}Si_7$: Experimental Evidence for the Aromaticity of the Planar Cyclopentadienyl Analogous Si_5^{6-} Rings, *Angew. Chem. Int. Ed. Engl.* **2011**, *50*, 12099-12102.

[23] Todorov, I.; Sevov, S. C.; Heavy-Metal Aromatic Rings: Cyclopentadienyl Anion Analogues Sn_5^{6-} and Pb_5^{6-} in the Zintl Phases Na_8BaPb_6, Na_8BaSn_6, and Na_8EuSn_6, *Inorg. Chem.* **2004**, *43*, 6490-6494.

[24] Todorov, I.; Sevov, S. C.; Heavy-Metal Aromatic and Conjugated Species: Rings, Oligomers, and Chains of Tin in $Li_{9-x}EuSn_{6+x}$, $Li_{9-x}CaSn_{6+x}$, $Li_5Ca_7Sn_{11}$, $Li_6Eu_5Sn_9$, $LiMgEu_2Sn_3$, and $LiMgSr_2Sn_3$, *Inorg. Chem.* **2005**, *44*, 5361-5369.

[25] Nesper, R.; Curda, J.; von Schnering, H. G.; Li_8MgSi_6, a Novel Zintl Compound Containing Quasi-aromatic Si_5 Rings, *J. Solid State Chem.* **1986**, *62*, 199-206.

[26] Frank, U.; Müller, W.; $Li_{11}Ge_6$ – eine Phase mit isolierten, ebenen Ge-Fünfringen / $Li_{11}Ge_6$ – a Phase with Isolated, Plane, Five-Membered Ge-Rings, *Z. Naturforsch.* **1975**, *30B*, 313-315.

[27] Toffoletti, L.; Kirchhain, H.; Landesfeind, J.; Klein, W.; van wüllen, L.; Gasteiger, H. A.; Fässler, T. F.; Lithium Ion Mobility in Lithium Phosphidosilicates: Crystalstructure, ^7Li, ^{29}Si, and ^{31}P MAS NMR Spectroscopy, and Impedance Spectroscopy of Li_8SiP_4 and Li_2SiP_2, *Chem.-Eur. J.* **2016**, *22*, 17635-17645.

[28] Haffner, A.; Bräuniger, T.; Johrendt, D.; Netzwerke aus Supertetraedern und Lithiumionenbeweglichkeit in Li_2SiP_2 und $LiSi_2P_3$, *Angew. Chem.* **2016**, *128*, 13783-13786; Supertetrahedral Networks and Lithium-Ion Mobility in Li_2SiP_2 and $LiSi_2P_3$, *Angew. Chem. Int. Ed. Engl.* **2016**, *55*, 13585-13588.

[29] Eickhoff, H.; Toffoletti, L.; Klein, W.; Raudaschl-Sieber, G.; Fässler, T. F.; Synthesis and Characterization of the Lihium-Rich Phosphidosilicates $Li_{10}Si_2P_6$ and $Li_3Si_3P_7$, *Inorg. Chem.* **2017**, *56*, 6688-6694.

[30] Kirschen, M.; Vincent, H.; Pierrier, Ch.; Chaudouet, P.; Chenevier, B.; Madar, R.; Synthesis and crystal structure of rhodium and iridium new phosphor-silicides, *Mater. Res. Bull.* **1995**, *30*, 507-513.

[31] Eisenmann, B.; Jordan, H.; Schäfer, H.; $Ba_3Si_4P_6$ eine neue Zintlphase mit vernetzten Si_4P_5-Käfigen, *Z. Naturforsch.* **1984**, *39b*, 864-867.

[32] Zhang, X.; Yu, T.; Li, C.; Wang, S.; Tao, X.; Synthesis and Crystal Structures of the Calcium Silicon Phosphides $Ca_2Si_2P_4$, $Ca_3Si_8P_{14}$ and $Ca_3Si_2P_4$, *Z. Anorg. Allg. Chem.* **2015**, *641*, 1545-1549.

[33] *Win* XPOW *3.0.2.1*, STOE & Cie GmbH, Darmstadt, Germany **2009**.

[34] J. Rodriguez-Carvajal, J. Gonzales-Platas, *FullProf Suite 2.05*, Institute Laue-Langevin Grenoble, France, **2011**.

[35] G. M. Sheldrick, SHELXT – Integrated space-group and crystal-structure determination, *Acta Crystallogr. Sect. A* **2015**, *71*, 3–8.

[36] Dupke, S.; Langer, T.; Pöttgen, R.; Winter, M.; Eckert, H.; Structural and dynamic charaterization of $Li_{12}Si_7$ and $Li_{12}Ge_7$ using solid state NMR, *Solid State Nucl. Mag.* **2012**, *42*, 17-25.

[37] Boyanov, S.; Bernardi, J.; Bekaert, E.; Ménétrier, M.; Doublet, M. L.; Monconduit, L.; P-Redox Mechanism at the Origin of the High Lithium Storage in NiP_2 Based Batteries, *Chem. Mater.* **2009**, *21*, 298-308.

Supporting Information

Planar Tetrelide Pentagons and Isolated Phosphide Anions in Lithium Phosphotetrelides $Li_{10.68(8)}Si_5P$ and $Li_{10.1(2)}Ge_5P$

W. Klein, L. Toffoletti, H. Eickhoff, G. Raudaschl-Sieber, T. F. Fässler

Dr. W. Klein, L. Toffoletti, H. Eickhoff, Dr. G. Raudaschl-Sieber, Prof. Dr. T. F. Fässler
Department of Chemistry, Technische Universität München,
Lichtenbergstrasse 4, 85747 Garching bei München, Germany
* E-mail: thomas.faessler@lrz.tu-muenchen.de

Content:

Table S1: Atom positons, Wyckoff sequence, site occupancy factors (S.O.F) and isotropic displacement parameters of $Li_{10.68(8)}Si_5P$.

Atom	Wyckoff position	S.O.F	*x*	*y*	*z*	*U*eq / Å²
Si1	4c		0.24117(4)	1/4	0.47605(1)	0.00916(7)
Si2	4c		0.05727(4)	1/4	0.41633(1)	0.00951(8)
Si3	4c		0.13975(4)	1/4	0.32349(1)	0.00895(8)
Si4	4c		0.37056(4)	1/4	0.32810(1)	0.00994(8)
Si5	4c		0.43360(4)	1/4	0.42260(1)	0.01231(8)
P	4c		0.24900(4)	1/4	0.67046(1)	0.01153(7)
Li1	4c		0.2520(2)	3/4	0.39322(9)	0.0154(4)
Li2	4c		0.2624(2)	3/4	0.27575(9)	0.0179(5)
Li3	4c		0.0935(3)	3/4	0.4895(1)	0.0212(5)
Li4	4c		0.3912(3)	3/4	0.4960(1)	0.0192(5)
Li5	4c		0.0018(3)	1/4	0.6550(1)	0.0249(6)
Li6	4c	0.532(13)	0.4605(6)	1/4	0.6178(3)	0.032(2)
Li7	4c	0.425(13)	0.4988(6)	1/4	0.6588(4)	0.027(3)
Li8	4c	0.393(10)	0.393(6)	1/4	0.5690(2)	0.014(2)
Li9	4c		0.1205(3)	3/4	0.7113(1)	0.0273(6)
Li10	8d	0.312(7)	0.4558(6)	0.373(1)	0.7317(2)	0.029(2)
Li11	4c	0.680(11)	0.3783(4)	3/4	0.7090(1)	0.017(1)
Li12	4c	0.292(11)	0.3475(8)	3/4	0.6445(4)	0.021(3)
Li13	4c	0.733(15)	0.2315(5)	3/4	0.6101(2)	0.046(2)
Li14	8d	0.5	0.1499(5)	0.334(1)	0.5746(1)	0.069(3)

Table S2: Anisotropic displacement parameters of $Li_{10.68(8)}Si_5P$.

	U_{11}	U_{22}	U_{33}	U_{23}	U_{13}	U_{12}
P	0.00943(17)	0.00970(12)	0.01544(13)	0	-0.00031(12)	0
Si1	0.01056(19)	0.00866(13)	0.00826(12)	0	0.00037(12)	0
Si2	0.00870(19)	0.01082(17)	0.00899(13)	0	0.00092(12)	0
Si3	0.00840(19)	0.00979(17)	0.00867(13)	0	0.00006(11)	0
Si4	0.0092(2)	0.01229(18)	0.00835(13)	0	0.00078(11)	0
Si5	0.0089(2)	0.0195(2)	0.00855(13)	0	−0.00053(12)	0
Li1	0.0142(12)	0.0164(10)	0.0155(9)	0	−0.0011(9)	0
Li2	0.0262(15)	0.0123(9)	0.0151(10)	0	0.0043(9)	0
Li3	0.0172(14)	0.0122(13)	0.0452(15)	0	−0.0019(12)	0
Li4	0.0255(15)	0.0138(12)	0.0243(11)	0	0.0107(10)	0
Li5	0.0198(15)	0.0174(13)	0.0204(10)	0	−0.0083(9)	0
Li6	0.026(4)	0.035(3)	0.034(3)	0	0.017(3)	0
Li7	0.005(3)	0.010(3)	0.067(6)	0	−0.012(3)	0
Li8	0.011(4)	0.017(3)	0.014(3)	0	−0.001(2)	0
Li9	0.0321(16)	0.0173(14)	0.0325(13)	0	−0.0144(11)	0
Li10	0.016(4)	0.041(4)	0.031(3)	−0.007(2)	0.002(2)	−0.018(3)
Li11	0.015(2)	0.0168(19)	0.0196(17)	0	0.0017(13)	0
Li12	0.012(5)	0.012(4)	0.039(5)	0	0.011(4)	0
Li13	0.081(5)	0.027(2)	0.028(2)	0	0.002(2)	0
Li14	0.098(4)	0.094(6)	0.0151(14)	0.0149(19)	0.0171(17)	0.087(4)

Table S3: Si-Si bond length and selected interatomic distances in $Li_{10.68(8)}Si_5P$.

Atom 1	Atom 2		Distance / Å	Atom 1	Atom 2		Distance / Å
Si1	Si2		2.3662(5)	Li1	Li7		2.840(7)
Si1	Si5		2.3512(5)	Li1	Li3		2.845(4)
Si2	Si3		2.3810(4)	Li1	Li5		2.847(3)
Si3	Si4		2.3669(5)	Li2	Li10	2×	2.527(6)
Si4	Si5		2.3560(5)	Li2	Li9	2×	2.898(2)
Si1	Li14	2×	2.567(3)	Li2	Li7		2.907(7)
Si1	Li4	2×	2.6398(16)	Li2	Li10		2.939(6)
Si1	Li8		2.641(5)	Li3	Li14	2×	2.480(5)
Si1	Li5	2×	2.6773(15)	Li3	Li10	2×	2.807(6)
Si2	Li4		2.736(2)	Li3	Li9	2×	2.807(2)
Si2	Li14	2×	2.778(4)	Li4	Li14	2×	2.768(5)
Si2	Li4	2×	2.7911(16)	Li4	Li4	2×	2.916(4)
Si2	Li3	2×	2.8049(18)	Li5	Li8	2×	2.767(4)
Si3	Li3	2×	2.6352(16)	Li5	Li8		2.817(6)
Si3	Li2	2×	2.7323(14)	Li5	Li5	2×	3.095(4)
Si3	Li11		2.752(3)	Li6	Li7		1.059(8)
Si3	Li9		2.794(3)	Li6	Li8		1.433(9)
Si4	Li7	2×	2.543(3)	Li6	Li12	2×	2.516(5)
Si4	Li2	2×	2.7167(15)	Li6	Li10	2×	2.783(8)
Si4	Li11		2.721(4)	Li7	Li10	2×	1.878(10)
Si4	Li10	2×	2.797(6)	Li7	Li8		2.475(10)
Si4	Li9		2.801(3)	Li7	Li12	2×	2.664(6)
Si5	Li6	2×	2.587(3)	Li7	Li11	2×	2.748(5)
Si5	Li5		2.652(2)	Li8	Li14	2×	2.384(8)
Si5	Li12		2.760(8)	Li8	Li13	2×	2.802(5)
Si5	Li5	2×	2.8039(15)	Li8	Li12		2.823(7)
Si5	Li8	2×	2.877(4)	Li9	Li11		2.642(5)
P	Li12	2×	2.446(4)	Li9	Li13		2.682(5)
P	Li6		2.508(5)	Li9	Li10	2×	2.705(6)
P	Li2		2.527(2)	Li9	Li12		2.823(9)
P	Li14	2×	2.538(4)	Li10	Li10		1.050(13)
P	Li3		2.560(3)	Li10	Li11		1.880(7)
P	Li7		2.574(6)	Li10	Li11		2.833(6)
P	Li13	2×	2.590(2)	Li10	Li12		2.864(10)
P	Li10	2×	2.630(6)	Li11	Li12		1.577(10)
P	Li11		2.680(3)	Li11	Li13		2.809(6)
P	Li9	2×	2.696(2)	Li12	Li13		1.447(10)
P	Li8		2.777(5)	Li13	Li14	2×	2.141(7)
Li1	Li2		2.819(3)	Li13	Li14	2×	2.770(6)
Li1	Li4		2.822(3)	Li14	Li14		0.721(12)

Table S4: Bond angles of the Si_5 pentagons in $Li_{10.68(8)}Si_5P$.

Atom	Angle / °
Si1	109.732(16)
Si2	106.452(19)
Si3	108.111(17)
Si4	108.582(18)
Si5	107.123(19)

Table S5: Atom positons, Wyckoff sequence, site occupancy factors (S.O.F) and isotropic displacement parameters of $Li_{10.1(2)}Ge_5P$.

Atom	Wyckoff position	S.O.F	*x*	*y*	*z*	*U*eq / Å²
Ge1	4c		0.23553(8)	1/4	0.47948(3)	0.01142(18)
Ge2	4c		0.05061(8)	1/4	0.41488(3)	0.0107(2)
Ge3	4c		0.14007(8)	1/4	0.31928(3)	0.0096(2)
Ge4	4c		0.37951(8)	1/4	0.32723(3)	0.0105(2)
Ge5	4c		0.43433(7)	1/4	0.42532(3)	0.0114(2)
P	4c		0.24434(18)	1/4	0.67226(7)	0.0058(3)
Li1	4c		0.2572(13)	3/4	0.3928(5)	0.016(3)
Li2	4c		0.2297(11)	3/4	0.7769(4)	0.007(2)
Li3	4c		-0.0024(12)	3/4	0.6545(5)	0.016(3)
Li4	4c		0.0860(13)	3/4	0.4862(5)	0.020(3)
Li5	4c		0.3894(13)	1/4	0.4977(5)	0.021(3)
$Li6_{7,8}$	4c		0.4494(18)	1/4	0.6160(8)	0.050(5)
Li9	4c		0.1229(15)	3/4	0.7097(7)	0.032(4)
Li10	8d	0.35(3)	0.452(2)	0.355(4)	0.7264(8)	0.006(7)
Li11	4c	0.47(5)	0.373(3)	3/4	0.7059(10)	0.015(10)
Li12	4c	0.38(5)	0.342(3)	3/4	0.6472(12)	0.008(11)
Li13	4c	0.55(5)	0.219(2)	3/4	0.6099(9)	0.019(9)
Li14	8d	0.5	0.1560(16)	0.366(4)	0.5778(6)	0.012(4)

Table S6: Anisotropic displacement parameters of $Li_{10.1(2)}Ge_5P$.

	U_{11}	U_{22}	U_{33}	U_{23}	U_{13}	U_{12}
Ge1	0.0135(4)	0.0096(4)	0.0112(4)	0	0.0004(3)	0
Ge2	0.0107(4)	0.0108(5)	0.0107(4)	0	0.0015(3)	0
Ge3	0.0088(4)	0.0085(5)	0.0115(4)	0	0.0003(3)	0
Ge4	0.0090(4)	0.0113(5)	0.0111(4)	0	0.0010(3)	0
Ge5	0.0104(4)	0.0106(5)	0.0131(4)	0	−0.0024(3)	0
P	0.0042(8)	0.0077(8)	0.0055(8)	0	0.0005(7)	0
Li1	0.010(6)	0.018(6)	0.020(6)	0	−0.010(6)	0
Li3	0.017(7)	0.012(7)	0.019(7)	0	−0.006(6)	0
Li4	0.019(7)	0.014(7)	0.027(7)	0	−0.006(6)	0
Li5	0.022(8)	0.025(8)	0.017(6)	0	−0.002(6)	0
$Li6_{7,8}$	0.049(12)	0.031(10)	0.070(12)	0	0.046(10)	0
Li9	0.029(8)	0.018(8)	0.049(9)	0	−0.021(8)	0

Table S7: Ge-Ge bond length and selected interatomic distances in $Li_{10.68(8)}Si_5P$

Atom 1	Atom 2		Distance / Å	Atom 1	Atom 2		Distance / Å
Ge1	Ge2		2.4754(12)	Li2	Li1		2.816(15)
Ge1	Ge5		2.4433(12)	Li3	Li14	2×	2.53(2)
Ge2	Ge3		2.4980(11)	Li3	Li9	2×	2.848(12)
Ge3	Ge4		2.4880(11)	Li3	Li1		2.878(18)
Ge4	Ge5		2.4472(11)	Li4	Li14	2×	2.862(19)
Ge1	Li14		2.573(15)	Li1	Li3		2.879(18)
Ge1	Li4	2×	2.658(8)	Li1	Li5		2.891(18)
Ge1	Li5	2×	2.716(8)	Li1	$Li6_{7,8}$		3.05(2)
Ge2	Li14	2×	2.710(16)	Li2	Li10	2×	2.65(2)
Ge2	Li3	2×	2.779(8)	Li3	Li14	2×	2.53(2)
Ge2	Li4		2.787(13)	Li4	Li4	2×	2.874(19)
Ge2	Li4	2×	2.787(8)	Li5	Li5	2×	3.15(2)
Ge2	Li13		2.86(2)	Li5	$Li6_{7,8}$		3.22(2)
Ge3	Li3	2×	2.660(8)	Li5	Li13		3.24(3)
Ge3	Li2	2×	2.742(7)	Li5	Li14		3.52(2)
Ge3	Li11		2.76(2)	$Li6_{7,8}$	Li12	2×	2.539(18)
Ge3	Li9		2.813(15)	$Li6_{7,8}$	Li10	2×	2.72(3)
Ge4	Li11		2.69(3)	Li9	Li11		2.59(3)
Ge4	Li2	2×	2.722(7)	Li9	Li13		2.62(3)
Ge4	Li10	2×	2.76(2)	Li9	Li12		2.73(3)
Ge4	Li9		2.853(16)	Li9	Li10	2×	2.90(2)
Ge5	Li5		2.613(13)	Li10	Li10		0.91(4)
Ge5	$Li6_{7,8}$	2×	2.663(9)	Li10	Li11		1.95(2)
Ge5	Li5	2×	2.817(8)	Li10	Li11		2.78(2)
P	Li12	2×	2.456(15)	Li10	Li12		2.81(3)
P	Li14	2×	2.520(16)	Li11	Li12		1.46(4)
P	$Li6_{7,8}$		2.526(16)	Li11	Li10		1.95(2)
P	Li2		2.543(10)	Li11	Li13		2.82(3)
P	Li10	2×	2.56(2)	Li12	Li13		1.56(4)
P	Li3		2.592(13)	Li13	Li14	2×	1.94(2)
P	Li13	2×	2.645(13)	Li13	Li14	2×	2.844(18)
P	Li9		2.654(10)	Li14	Li14		1.00(3)
Li1	Li2		2.816(15)	Li14	Li14		3.30(3)
Li1	Li4		2.878(19)				

Table S8: Bond angles of the Ge_5 pentagons in $Li_{10.68(8)}Si_5P$

Atom	Angle / °
Ge1	108.16(4)
Ge2	107.52(4)
Ge3	107.33(4)
Ge4	107.86(4)
Ge5	109.13(4)

Table S9: Refinement parameters of the Rietveld analysis of $Li_{10.68(8)}Si_5P$.

empirical formula	$Li_{10.68(8)}Si_5P$
T / K	293
formula weight / g mol^{-1}	245.51
space group	*Pnma* (62)
unit cell parameters / Å	a = 10.26738(5) b = 4.29631(2) c = 23.97193(12)
Z	4
V / Å^3	1057.445(9)
$\rho_{calc.}$ / g cm^{-3}	1.542
2θ range / °	5.019 - 90.414
R_p	0.0536
R_{wp}	0.0794
R_{exp}	0.0562
X^2	2.00
R_{Bragg}	0.0311
R_f	0.0229

Table S10: Refinement parameters of the Rietveld analysis of $Li_{10.1(2)}Ge_5P$.

empirical formula	$Li_{10.1(2)}Ge_5P$
T / K	293
formula weight / g mol^{-1}	464.11
space group	*Pnma* (62)
unit cell parameters / Å	a = 10.42302(8) b = 4.33906(3) c = 24.28783(19)
Z	4
V / Å^3	1098.445(14)
$\rho_{calc.}$ / g cm^{-3}	2.806
2θ range / °	5.003 - 99.713
R_p	0.0539
R_{wp}	0.0746
R_{exp}	0.0583
X^2	1.64
R_{Bragg}	0.0595
R_f	0.0318

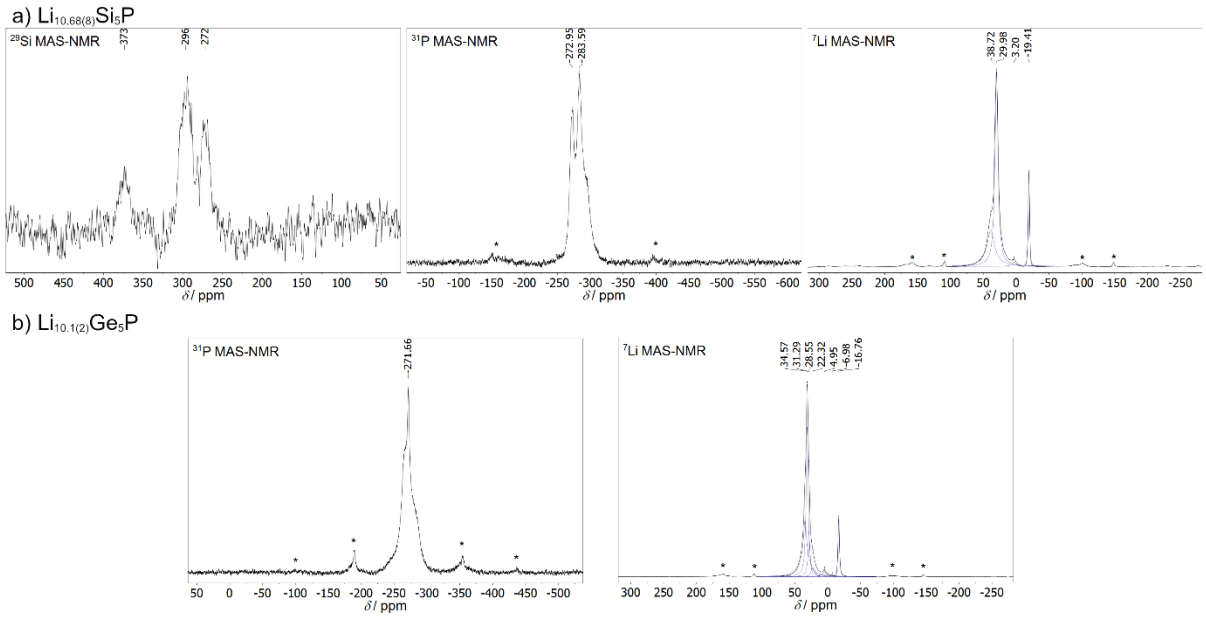

Figure S1: MAS NMR spectra of a) $Li_{10.68(8)}Si_5P$ and b) $Li_{10.1(2)}Ge_5P$ on the nuclei ^{29}Si, ^{31}P and ^{7}Li. Blue lines depict the line fits.

5.6 On the Structure and Conductivity of Na_3P

H. Eickhoff, C. Dietrich, W. Klein, W. G. Zeier, T. F. Fässler

manuscript for publication

On the Crystal Structure and Conductivity of Na_3P

Henrik Eickhoff[a], Christian Dietrich[b], Wilhelm Klein[a], Wolfgang. G. Zeier[b] and Thomas F. Fässler[a]*

[a]Department of Chemistry, Technische Universität München,
Lichtenberstrasse 4, München, 85747, Germany
[b]Institute of Physical Chemistry, Justus-Liebig-University,
Heinrich-Buff-Ring 17, Gießen, 35392, Germany
* E-mail: Thomas.Faessler@lrz.tu-muenchen.de

Abstract

As a potential material for Na-ion battery systems and on the basis of a structural discussion of compounds formerly believed to crystallize in the so-called Na_3As type the structure of Na_3P has been reinvestigated. Na_3P is found to crystallize in the Cu_3P type, analogous to Na_3As and is described by a three times larger unit cell ($P6_3cm$, a = 8.61224(10) Å and c = 8.81949(10) Å) in which the sodium atoms are slightly distorted compared to the former model ($P6_3/mmc$, a = 4.9512(5) Å and c = 8.7874(13) Å). The high purity of the material further enables the determination of its properties, showing mainly semiconducting behavior with a conductivity of 12 S cm^{-1} at room temperature.

Introduction

The ambition for renewable energy sources and the accompanied demand for affordable electrochemical energy storage systems encourages the research on available sodium-based batteries.[1-3] For these systems novel compounds are needed, including new synthesis approaches as well as the reevaluation of known materials. In this context, ternary sodium phosphides like $NaSi_2P_3$ have been shown to exhibit Na ion conductivities of up to 0.4 mS cm^{-1}.[4] Even the binary lithium phosphide Li_3P was reported to exhibit high ionic conductivities up to 0.1 mS cm^{-1}.[5] Li_3P and Na_3P chemically represent the lithiated or sodiated state, respectively, in high capacity phosphorous anodes[6-8] and hence are interesting for battery applications. In addition, Na_3P has shown to be a decomposition product in solid state batteries at the sodium metal anode[9] and is often used as simple starting material in syntheses of ternary phosphides.

During our investigations we found significant discrepancies in the powder X-ray diffraction patterns, subsequently confirmed by X-ray single crystal diffraction measurements, with respect to the previous structure reports.[10,11] The structure is described to adopt the formerly so called Na_3As type with planar sheets of hexagons of alternating Na-P stacked alternatingly with corrugated sheets formed exclusively by Na atoms (grey As-like). A hexagonal unit cell with lattice parameters of a = 4.9512(5) Å and c = 8.7874(13) Å and space group $P6_3/mmc$ is proposed. At this time additional unassigned reflections have already been reported, that could not be removed by increased experimental accuracy.[10] This led to a discussion about the certainty of the assumed structures of various A_3B compounds including the Na_3As type.[12.13] However, Dong & DiSalvo confirmed the structural model of Na_3P containing large prolate ellipsoids for certain Na positions.[11]

To match the experimentally observed additional reflections in the X-ray powder pattern of Cu_3P, a three times larger supercell with anti-LaF_3 structure (space group: $P\bar{3}c1$) was suggested[12] and this was applied to various compounds with A_3B composition, such as Na_3As and Na_3P (a = 8.626 Å, c = 8.797 Å). According to this structure type 2/3 of the Cu atoms are displaced from the formerly planar Cu-P sheet, while 1/3 of the Cu atoms remain coplanar to the P atoms. Later Hafner & Range revisited Na_3As on the basis of single crystal data and suggested the space group $P6_3cm$ leading to a displacement of all Na atoms from the Na-As sheet, resulting in less prolate ellipsoids.[13] They also recommended this space group and structure for related alkaline-pnictide systems, however no additional experimental evidence was provided. In this work, we use a combination of powder and single crystal X-ray diffraction techniques to solve the crystal structure type of Na_3P and investigate the electronic transport properties.

Experimental

Synthesis

Na_3P was synthesized as black crystalline powder from stoichiometric mixtures of Na (960 mg, 99%, Chempur) and P (310 mg, 97%, Sigma-Aldrich) in Ta ampoules. The sample was heated to 700 °C for 1 h, cooled to 500 °C, annealed for 24 h, reground and reheated to 400 °C for 36 h. Temperature rates were 4 °C min^{-1} for heating and 1 °C min^{-1} for cooling. Samples were synthesized and prepared under an inert argon atmosphere inside a glovebox.

Differential Scanning Calorimetry

Phase transitions were investigated using two different DSC devices. Low temperature DSC measurements were conducted with a Netzsch DSC 200 F3 Maia in the temperature range −150 °C to 300 °C. The samples (ca. 10 mg) were filled in aluminum crucibles and closed via cold welding. For DSC measurements from 200 °C to 750 °C a Netzsch DSC 404 Pegasus was used, for which the samples (ca. 50 mg) were filled into a niobium crucible and sealed by arc welding.

Single Crystal X-Ray Diffraction

A black crystal was isolated and sealed in a fused silica capillary (diameter 0.3 mm). Data were collected on a single-crystal X-ray diffractometer equipped with a FR591 rotating anode with Mo K_α radiation (λ = 0.71073 Å), a Montel optic, a APEX II, κ-CCD detector and the *APEX 2* software package.[14] The structure was solved via direct methods with ShelXS97.[15] For structure refinement the program package SHELX-2014[16] was used. Details on crystal data, data collection and structure refinement are summarized in Table 1. During the refinements in $P6_3cm$ and $P3c1$ the *z* parameter of the P atom has been restrained to $^1/_4$, and in $P1$ additionally the *x* and *y* parameters to 0, to ensure optimal comparability between the structure parameters in the different space groups. In the final refinement cycles they were released to obtain e.s.d.'s.

X-Ray Powder Diffraction

The sample was sealed in a fused silica capillary (diameter 0.3 mm). Data collection was performed in Debye-Scherrer geometry on a STOE Stadi P diffractometer (Ge(111)) monochromator, Cu $K_{\alpha1}$ radiation, λ = 1.54056 Å) with a Dectris MYTHEN 1K detector. Raw data were processed with the WinXPOW software package[17] and for Rietveld refinements the FullProf software package was used.[18]

Conductivity measurements

Prior to impedance spectroscopy measurements the sample was densified within a hot press setup at 150 °C and 2 tons (ø 12 mm).[19] Within the setup electronic impedance spectroscopy was performed at different temperatures between 25 °C and 300 °C using a frequency response analyzer (BioLogic SP-150) with a frequency range of 1 MHz to 10 Hz and an amplitude of 20 mV. The pellet height was extrapolated at room temperature after hot pressing.

Discussion

Upon synthesizing Na_3P, additional reflections are found in the X-ray powder diffraction pattern, which do not correspond to the structural model established by Brauer & Zintl ($P6_3/mmc$, a = 4.9512(5) Å and c = 8.7874(13) Å).[10] Similar to their previous observations the relative intensities of these reflections did not alter with the synthesis conditions such as reaction temperature and time or an added excess of Na or P. Different from the early results the indexing of these additional reflections succeeded, leading to a three times larger unit cell (a = 8.61224(10) Å and c = 8.81949(10) Å; Fig. 1), similar to results as proposed formerly.[12,13] These findings were confirmed by X-ray single crystal measurements, in which the super structure reflections were clearly detected. Moreover, a structure refinement from single crystal data using the small unit cell and deliberately ignoring the super structure reflections lead to large U_{33} parameters for Na in the planar Na-P sheet, which can also be seen in structure refinements of Na_3P prior to this work.[11] Attempts to identify a possible phase transition via differential scanning calorimetry in the temperature range of −150 °C to 750 °C measurements showed a weak reversible, endothermal signal during heating at ca. 665 °C. However, the high temperature phase could not be isolated or characterized and may originate from a transformation into a higher symmetric space group.

As a reflection condition $hh\bar{0}l : l = 2n$ is observed in our single crystal data, in the hexagonal crystal system a set of space groups consisting of $P6_3/mcm$, $P\bar{6}c2$ and $P6_3cm$ is obtained. Additionally, the trigonal space groups $P\bar{3}c1$, as found for the (anti-)LaF_3 type, and $P3c1$ were considered and finally the results were compared to a refinement in $P1$ to eliminate any possible restrictions from symmetry. In all investigated space groups the structure solution resulted roughly in the same structure model, which is identical with the atomic arrangement proposed by Brauer and Zintl: more or less planar graphite-, or better boron nitride-like sheets of P and Na atoms separated by corrugated layers of Na atoms, as shown in Fig. 2.b,c. The shortest interatomic contacts are found between the phosphorous atom and five sodium atoms which form a trigonal

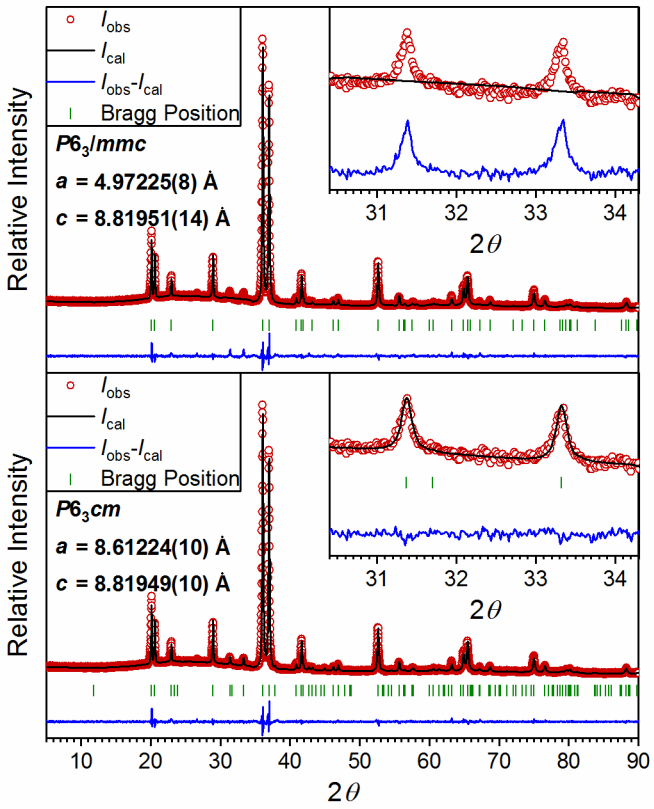

Figure 1: Rietveld refinement of Na_3P. Top: cell parameters a = 4.97225(8) Å, c = 8.81951(14) Å ($P6_3/mmc$, R_{wp} = 3.81%, R_{exp} = 3.70 %, R_{Bragg} = 2.66 %, GOF = 1.92) and bottom: cell parameters a = 8.61224(10) Å, c = 8.81949(10) Å ($P6_3cm$, R_{wp} = 3.23%, R_{exp} = 3.69 %, R_{Bragg} = 1.79 %, GOF = 1.39). I_{obs} and I_{cal} represent the observed and calculated intensity, respectively. The most intense reflections determining the unit cell are depicted as inset.

bipyramid, so alternatively the crystal structure can be described as built from ($PNa_2Na_{3/3}$) polyhedra which are connected via common corners to form layers (Fig. 2.f). Taking into account the slightly extended second coordination sphere around the P atom, all six faces of each bipyramid are capped by further Na atoms forming the apices of neighboring bipyramids, so each P atom is surrounded by eleven Na atoms (Fig. 2.g). Although the structure model is roughly the same after the refinements in all space groups, the residual factors differ considerably owing to several features of the crystal structure. Most strikingly, the quality factors of the refinements correlate with the planarity of the P/Na layers. While in $P6_3/mcm$ and in $P\bar{6}c2$, similar to the Brauer/Zintl model in $P6_3/mmc$, the P and Na atoms within these layers are restrained by symmetry to the same value for the z parameter and the residuals are outrageously high (Tab. 1), in $P6_3cm$ and $P3c1$ the relevant atoms may be displaced from exact planarity resulting in considerably lower R-values. In $P\bar{3}c1$ with two third of the relevant Na atoms having a free z parameter intermediate R values are obtained. The obvious inadequacies of the correct structure description are compensated by particularly large U_{33} parameters for the concerning Na atoms in $P6_3/mcm$ and in $P\bar{6}c2$ which are considerably larger than those with free z parameters in $P6_3cm$ and $P3c1$. As another feature the

main axis of the trigonal PNa_5 bipyramid is slightly tilted with respect to the *c* axis which is not possible to constitute in $P6_3/mcm$ and in $P\bar{6}c2$ nor in $P6_3/mmc$ of the Brauer/Zintl model. Again, this *lack* is indicated by ellipsoids of Na atoms as those of atoms within the corrugated layers are elongated and strangely skewed ($P6_3/mcm$, $P\bar{6}c2$) or strongly flattened ($P6_3/mmc$) with respect to the c axis. After these considerations for the correct space group of Na_3P the higher symmetric groups ($P6_3/mcm$, $P\bar{6}c2$, $P\bar{3}c1$) can be closed out while applying lower symmetries no significant differences appear between $P6_3cm$, $P3c1$ and $P1$, and space group $P6_3cm$ is the clearly preferred choice (Tab. 1 and 2). Additionally, after refinements in all acentric space groups the Flack parameter was close to zero, therefore centrosymmetric groups should be less probable.

Table 1: Comparison of the structure refinement results of single crystal data in different space groups, illustrated by selected significant structure parameters. The reported and new structural model are highlighted in bold and suspicious parameters are colored in red.

	P6$_3$/mmc	$P6_3/mcm$	$P\bar{6}c2$	***P6$_3$cm***	$P\bar{3}c1$	$P3c1$	$P1$
wR_2(all)	**0.0667**	0.7367	0.5497	**0.0653**	0.0880	0.0640	0.0793
z(P)	**¼**	¼	¼	**0.2500(6)**	¼	0.2500(5)	0.2500(1)
$z(Na_{eq1})$	**¼**	¼	¼	**0.2225(7)**	¼	0.2375(6)	0.2213(3)
$z(Na_{eq2})$		¼	¼	**0.2646(8)**	0.2271(2)	0.2373(6)	0.2653(4)
$z(Na_{eq3})$			¼			0.2794(6)	0.2653(4)
$U_{33}(Na_{eq1})$	**0.0960**	0.0390	0.4600	**0.0530**	0.0940	0.0644	0.0526
$U_{33}(Na_{eq2})$		0.3000	0.1120	**0.0626**	0.0509	0.0633	0.0596
$U_{33}(Na_{eq3})$			0.0420			0.0518	0.0615
$U_{11}(Na_{cap1})$	**0.0625**	0.0570	0.0700	**0.0399**	0.0441	0.0369	0.0386
$U_{22}(Na_{cap1})$	**0.0625**	0.0570	0.0670	**0.0339**	0.0550	0.0481	0.0376
$U_{33}(Na_{cap1})$	**0.0239**	0.0610	0.0820	**0.0235**	0.0239	0.0236	0.0242

Na-P-Na angle sum of 360.00(8)°. The closest interatomic distances are nearly not affected by the changes in symmetry, and the P-Na distances within the PNa_5 bipyramid (2.8701(13) Å - 2.928(7) Å) are almost identical with the latest values presented by Dong & DiSalvo (2.874 Å - 2.920 Å).[11] This polyhedron is just slightly distorted, indicated by the linear main Na1-P-Na2 axis (179.58(9)°) and the equatorial PNa_3 plane mentioned above, the axis direction deviates from the plane normal by 8.48°. The polyhedron is slightly tilted with respect to the unit cell, e.g. the angle between the main axis of the polyhedron and the crystallographic *c* axis is 3.53°, that between the equatorial plane and the *ab* plane is 4.94°. The P-Na distances within the second coordination sphere are not changed in average but are more irregular (3.094(4) Å - 3.418(3) Å, comp. to 6 × 3.239 Å in $P6_3mmc$). As a consequence, the Na1 and Na2 atoms which are surrounded by distorted tetrahedra of P atoms, are situated closer to a tetrahedron face (Na2) and a tetrahedron edge (Na1) in $P6_3cm$, respectively. The closest Na-Na distances, which are found between two apices of bipyramids belonging neighboring layers, are only slightly affected by the symmetry change (3.0136(12) Å in $P6_3cm$ vs. 2.988 Å in $P6_3/mmc$).

Table 2: Data collection and refinement parameters of a single crystal structure determination of Na_3P.

	***P*6$_3$*cm* (No. 185)**
Crystal data	
Chemical formula	Na_3P
M_r	99.94
Crystal system, space group	Hexagonal, *P*6$_3$*cm*
Temperature (K)	293
a, *b*, *c* (Å)	8.6216 (1), 8.6216 (1), 8.8285 (2)
α, *β*, *γ* (°)	90, 90, 120
V (Å^3)	568.32 (2)
Z	6
Radiation type	Mo K_α
μ (mm^{-1})	0.80
Crystal size (mm)	0.17 × 0.16 × 0.12
Data collection	
Diffractometer	Bruker *APEX2*
Absorption correction	Multi-scan *SADABS*, Bruker AXS Inc., 2001
T_{min}, T_{max}	0.622, 0.747
No. of measured, independent and observed [$I > 2\sigma(I)$] reflections	31731, 619, 582
R_{int}	0.046
$(\sin \theta/\lambda)_{max}$ (Å^{-1})	0.702
Refinement	
$R[F^2 > 2\sigma(F^2)]$, $wR(F^2)$, S	0.020, 0.065, 1.15
No. of reflections	619
No. of parameters	25
No. of restraints	1
$\Delta\rho_{max}$, $\Delta\rho_{min}$ (e Å^{-3})	0.17, −0.27
Absolute structure parameter	0.1 (3)

The main structural indications for an incorrect symmetry in this compound are several large anisotropic displacement parameters of Na atoms, i. e. particularly the U_{33} of the equatorial Na and those parallel to *ab* of the apex atoms (Tab. 3). These directions may be expected due to their orthogonality to the strongest Na-P interactions and are indeed observed in all the structure refinements in different symmetries, however, in the new structure model in *P*6$_3$*cm* they are considerably smaller than in the Brauer/Zintl model.

Table 3:Wyckoff sequence, atom coordinates, isotropic and anisotropic displacement parameters of atoms in the refinement in $P6_3cm$.

	Wyck.	*x*	*y*	*z*	U_{iso}	
P	6*c*	0.33171(13)	0	0.2500(6)	0.0164(2)	
Na1	6*c*	0.3539(2)	0.3539(2)	0.0810(2)	0.0384(6)	
Na2	6*c*	0.3121(2)	0.3121(2)	0.4199(2)	0.0375(6)	
Na3	4*b*	2/3	1/3	0.2646(8)	0.0344(7)	
Na4	2*a*	0	0	0.2225(7)	0.0315(9)	
	U_{11}	U_{22}	U_{33}	U_{23}	U_{13}	U_{12}
P	0.0160(3)	0.0162(4)	0.0170(3)	0	0.00058(14)	0.0081(2)
Na1	0.0399(7)	0.0579(11)	0.0235(12)	-0.0023(9)	-0.0023(9)	0.0110(6)
Na2	0.0489(9)	0.0489(9)	0.0224(12)	-0.0022(10)	-0.0022(10)	0.0304(8)
Na3	0.0204(4)	0.0204(4)	0.063(2)	0	0	0.0102(2)
Na4	0.0205(5)	0.0205(5)	0.053(3)	0	0	0.0103(3)

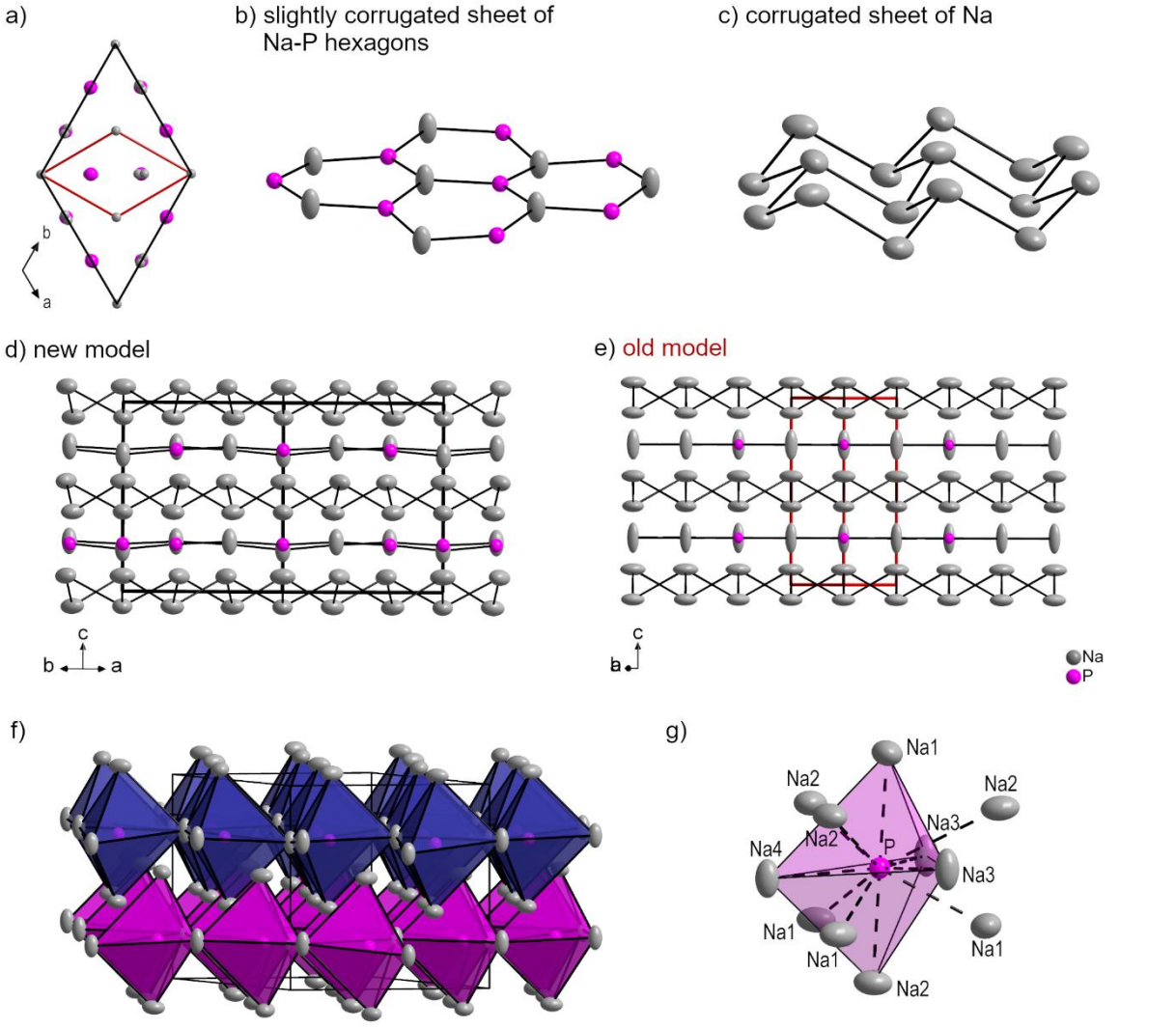

Figure 2: Illustration of the crystal structure of Na_3P. a) Relative cell edges *a* and *b* of the new (black) and reported model (red) with view along the [001] direction. b) and c) Illustration of the different layers occurring in the structure. Comparison of the projection of the extended unit cell along the [110] direction of the new model d) with the reported model e). Some Na-P bonds are drawn to indicate the corrugated NaP sheets. f) Polyhedral representation of Na_3P emphasizing two layers of corner-connected trigonal PNa_5 bipyramids. g) Coordination polyhedron of phosphorus, a distorted six times capped trigonal bipyramid.

Conductivity measurements

Since the material is interesting for application in sodium-ion batteries and has been shown as a decomposition product at the anode in all solid state batteries,[9] we investigated its electrical conductivity. Therefore, impedance spectra were recorded in a temperature range of 25 °C to 350 °C. A total conductivity of σ = 12 S cm^{-1} at room temperature was found to be mainly electronic of nature and we were not able to resolve the partial ionic conductivity. A slight increase of the conductivity with temperature up to 350 °C (Fig. 3a) corresponds to the calculated activation energy E_A = 0.11 eV (Fig. 3b) showing semiconducting behavior.

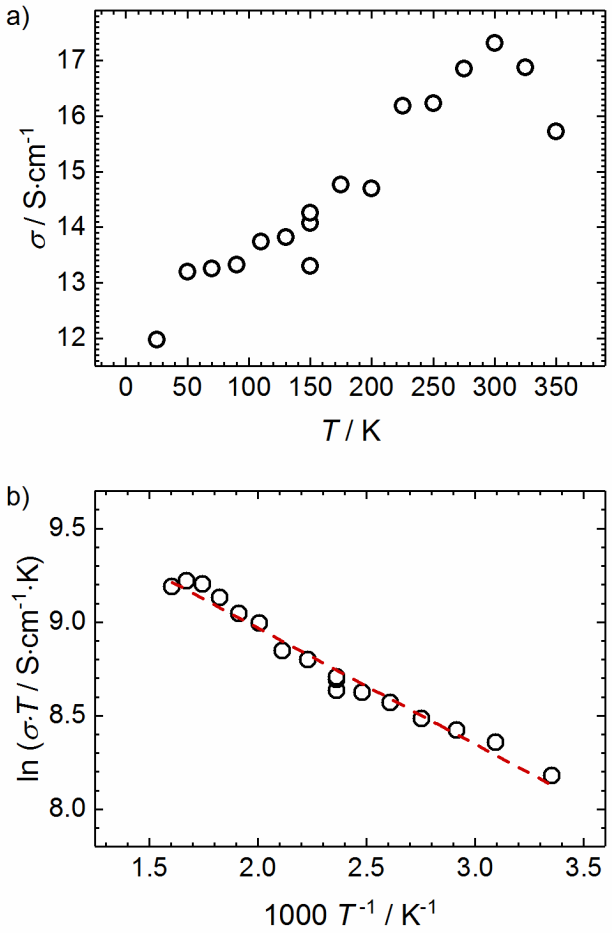

Figure 3: a) Total electrical conductivity in the temperature range from 25 °C to 350 °C derived from impedance spectroscopy measurements and b) the corresponding Arrhenius plot to determine the activation energy barrier.

Conclusion

A close inspection of powder and especially single crystal X-ray diffraction data of Na_3P revealed several superstructure reflections which lead to a three times larger unit cell (a = 8.61224(10) Å and c = 8.81949(10) Å) compared of the formerly reported one (a = 4.9512(5) Å, c = 8.7874(13) Å). Na_3P crystallizes in space group $P6_3cm$ and differs slightly from the reported model by additional degrees of freedom for some refinement parameters lead to allow an increased shortest distance between neighboring cations and decreased anisotropic displacement parameters. The higher reliability of the new structure model as compared to the hitherto accepted model of Braun & Zintl[10] was shown by comparison of some relevant structure parameters resulting from refinements in different space groups. With the presented structure model and symmetry, Na_3P is isotypic to Na_3As (which underwent a similar transformation of its generally accepted crystal structure)[13] as well as Cu_3P,[20] and support the assumption of Hafner & Range that more trialkaline pnictides crystallize within this structure type. These authors also provided the hypothesis of ternary compounds crystallizing with the small unit cell and the higher symmetric space group $P6_3/mmc$. This might explain the earlier findings of Dong & DiSalvo[11] whose Na_3P crystals were isolated from a reacted mixture of NaN_3, TiN, P and KI and, thus, could contain impurities stabilizing the higher symmetry. The conductivity of Na_3P was found to be mainly semiconducting of nature, with a total electrical conductivity of σ = 12 S cm^{-1}.

References

[1] J. Deng, W.-B. Luo, S.-L. Chou, H.-K. Liu, S.-X., *Adv. Energ. Mater.* **2017**, 8, 1701428.
[2] J. Peters, D. Buchholz, S. Passerini, M. Weil, *Energy Environ Sci.* **2016**, 9, 1744-1751.
[3] M. D. Slater, D. Kim, E. Lee, C. S. Johnson, *Adv. Funct. Mater.* **2012**, 23, 947-958.
[4] A. Haffner, A.-K. Hatz, I. Moudrakovski, B. V. Lotsch, D. Johrendt, *Angew. Chem.* **2018**, 130, 6263-6268; *Angew. Chem. Int. Ed.* **2018**, 57, 6155-6160.
[5] G. Nazri, *Solid State Ionics* **1989**, 34, 97-102.
[6] L.-Q. Sun, M.-J. Li, K. Sun, S.-H. Yu, R.-S. Wang, H.-M. Xie, *J. Phys. Chem. C* **2012**, 116, 14772-14779.
[7] Y. Kim, Y. Park, A. Choi, N.-S. Choi, J. Kim, J. Lee, J. H. Ryu, S. M. Oh, K. T. Lee, *Adv. Mater.* **2013**, 22, 3045-3049.
[8] T. Ramireddy, T. Xing, M. M. Rahman, Y. Chen, Q. Dutercq, D. Gunzelmann, A. M. Glushenkov, *J. Mater. Chem. A* **2015**, 3, 5572-5584.
[9] S. Wenzel, T. Leichtweiss, D. A. Weber, J. Sann, W. G. Zeier, J. Janek, *ACS Appl. Mater. Interfaces* F, 8, 28216-28224.
[10] G. Brauer, E. Zintl, *Z. Phys. Chem. Abt. B* **1937**, 37, 323-352.
[11] Y. Dong, F. J. DiSalvo, *Acta Crystallogr. E* **2005**, 61, i223-i224.
[12] M. Mansmann, *Z. Kristallogr.* **1965**, 122, 399-406.
[13] P. Hafner, K.-J. Range, *J. Alloy. Compd.* **1994**, 216, 7-10.
[14] Bruker AXS Inc. *APEX 2: APEX suite of crystallographic software*, version 2008.4., **2012**.
[15] G. M. Sheldrick, *Acta Crystallogr., Sect. A: Found. Cystallogr.* **2008**, 64, 112-122.
[16] G. M. Sheldrick, *Acta Crystallogr., Sect. C: Struct. Chem.* **2015**, 71, 3-8.
[17] *WinXPOW V3.0.2.1.*, 3.0.2.1.; STOE & Cie GmbH: Darmstadt, Germany, **2011**.
[18] J. Rodriguez-Carvajal, J. Gonzales-Platas, *FullProf Suite 2. 05*, Institute Laue-Langevin Grenoble: France, **2011**.
[19] M. R. Busche, D. A. Weber, Y. Scheider, C. Dietrich, S. Wenzel, T. Leichtweiss, D. Schröder, W. Zhang, H. Weigand, D. Walter, S. J. Sedlmaier, D. Houtarde, L. F. Nazar, J. Janek, *Chem. Mater.* **2016**, 28, 6152-6165.
[20] O. Olofsson, *Acta Chem. Scand.* **1972**, 26, 2777-2787.

Supporting information

On the Crystal Structure and Conductivity of Na_3P

Henrik Eickhoff[a], Christian Dietrich[b], Wilhelm Klein[a], Wolfgang. G. Zeier[b] and Thomas F. Fässler[a]*

[a]Department of Chemistry, Technische Universität München, Lichtenberstrasse 4, München, 85747, Germany

[b]Institute of Physical Chemistry, Justus-Liebig-University, Heinrich-Buff-Ring 17, Gießen, 35392, Germany

Correspondence email: Thomas.Faessler@lrz.tu-muenchen.de

Rietveld Refinement of Na_3P

Table S1: Parameters of Rietveld refinement of Na_3P (space group $P6_3cm$).

Chemical formula	Na_3P
Temperature / K	293
Radiation type	Cu $K_{\alpha 1}$
M_r / g mol^{-1}	99.94
Crystal System, space group	Hexagonal, $P6_3cm$
a, c / Å	8.61224(10), 8.81949(10)
V / Å^3	566.508(11)
Z	6
ρ_{calcd} / g cm^{-3}	1.76
2θ range	5.09 - 90.125
R_p	3.23%
R_{wp}	4.22%
R_{exp}	3.69%
χ^2	1.30
GOF	1.39
R_{Bragg}	1.79%
R_f	2.13%

Single crystal structure details

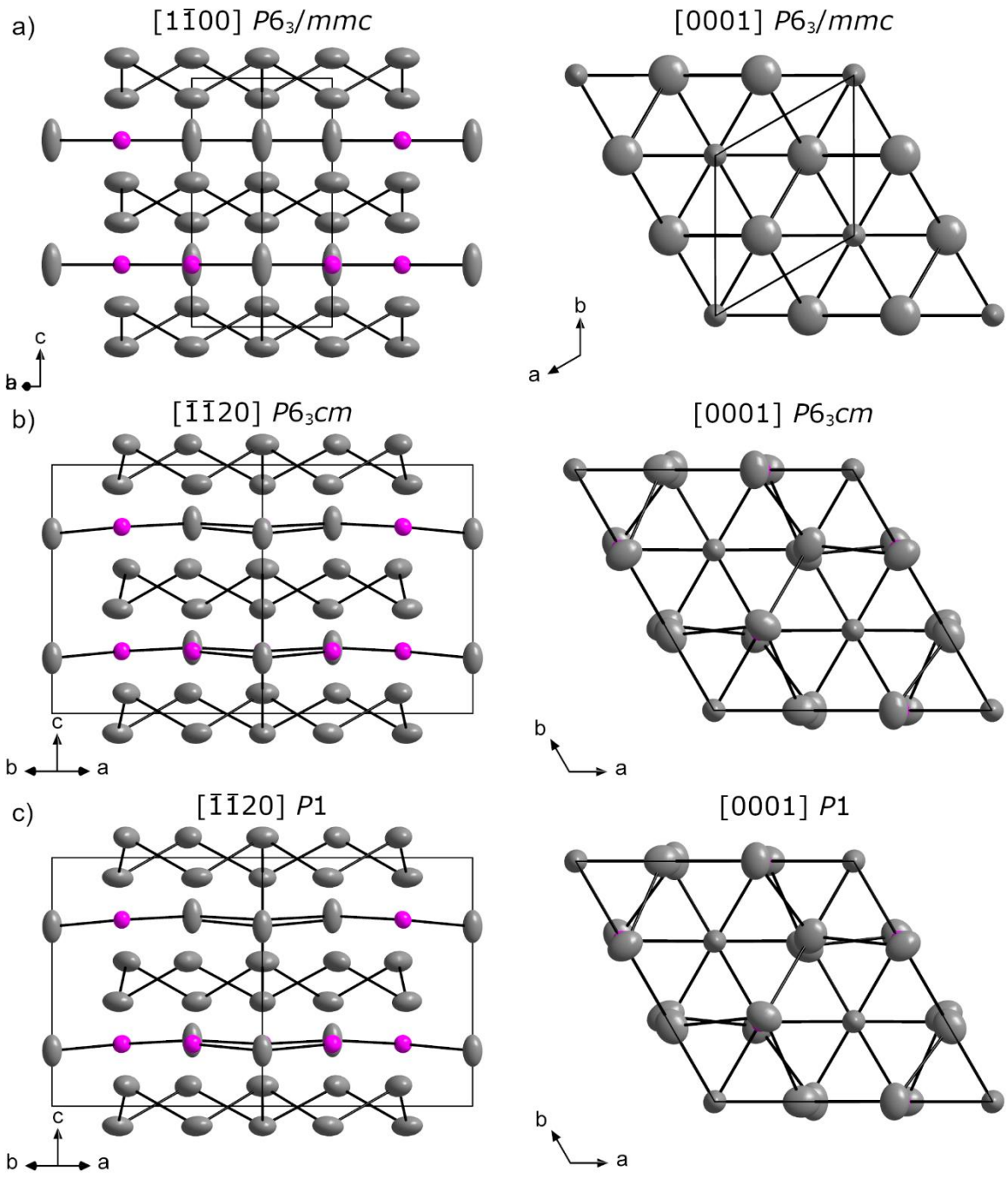

Figure S1: Comparison of the crystal structure of Na_3P after refinements in a) $P6_3/mmc$, b) $P6_3cm$ and c) $P1$.

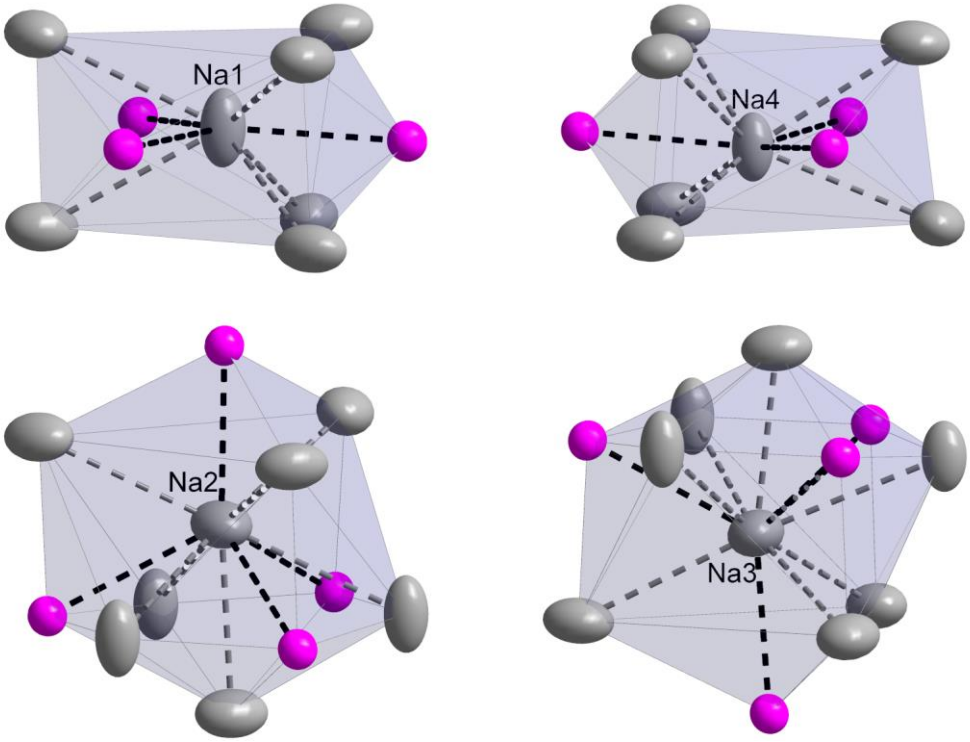

Figure S2: Coordination polyhedra of Na in Na_3P (space group $P6_3cm$).

Symmetry Reduction

Na_3P : $P6_3/mmc$ (194) → $P6_3/mcm$ (193) → $P6_3cm$ (185) → $P3c1$ (158)

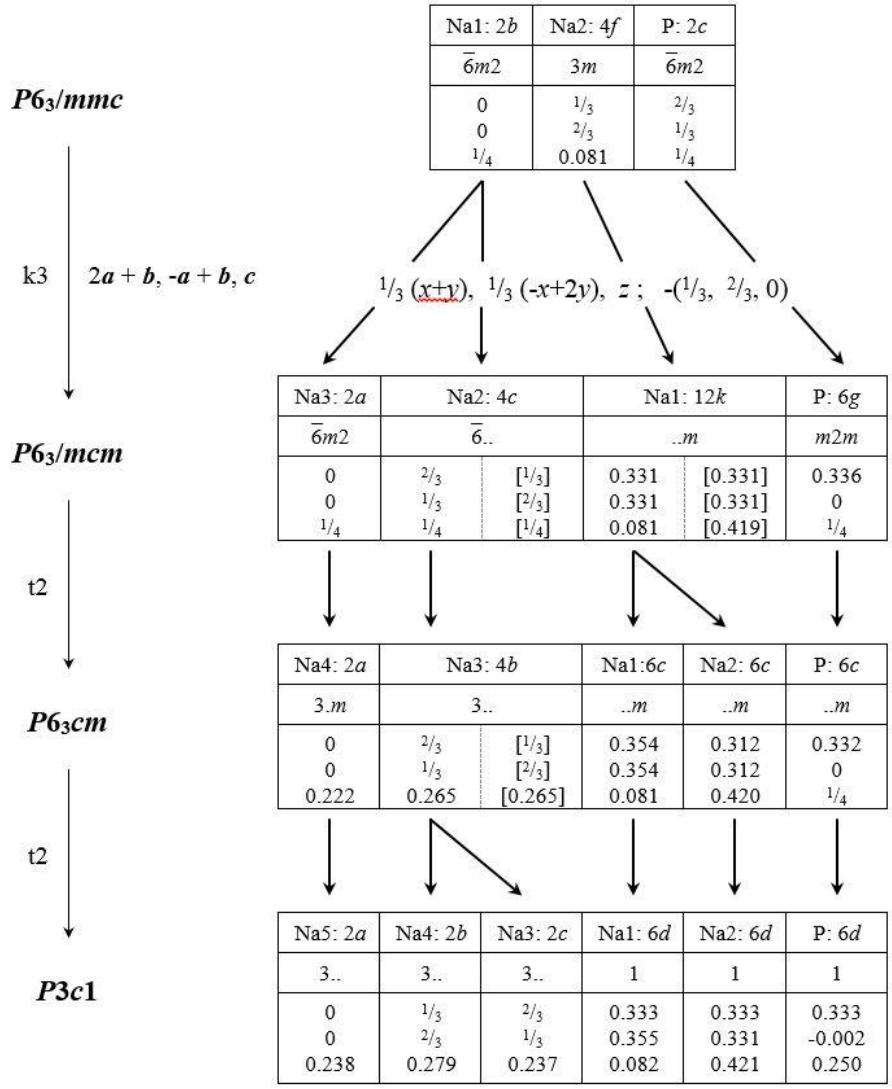

Na_3P : $P6_3/mmc$ (194) → $P6_3/mcm$ (193) → $P\bar{6}c2$ (188) → $P3c1$ (158)

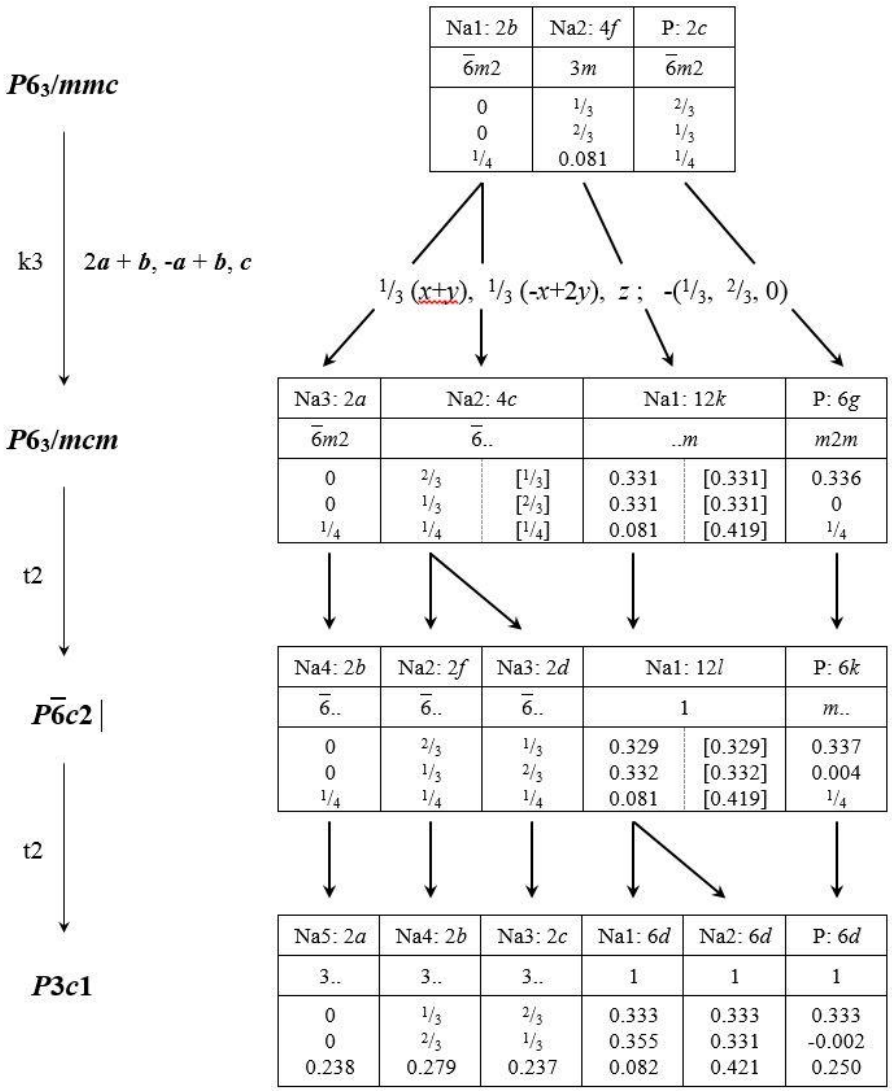

Na_3P : $P6_3/mmc$ (194) → $P6_3/mcm$ (193) → $P\bar{3}c1$ (165) → $P3c1$ (158)

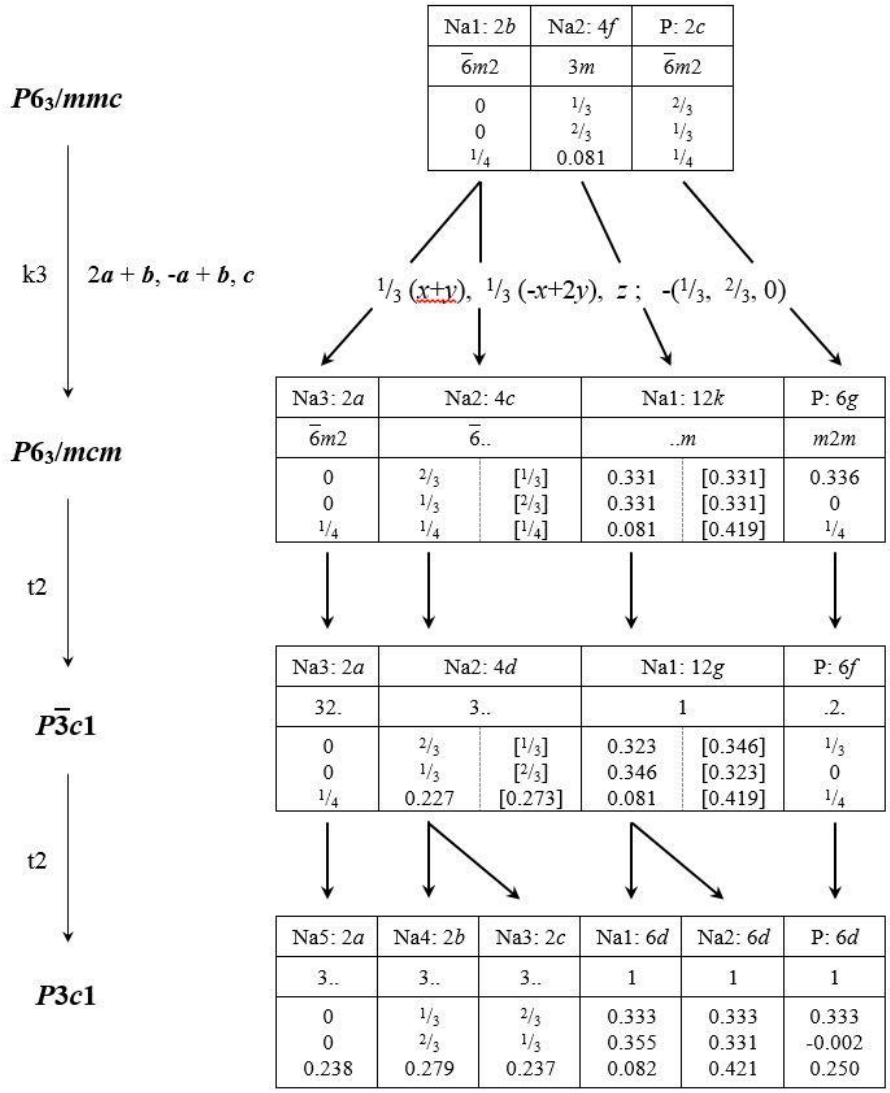

Single crystal X-ray refinements of Na_3P

Table S2: Comparison of the structure refinement results in different space groups, illustrated by residuals, atom coordinates and anisotropic displacement parameters. The reported and new model are highlighted bold.

	$P6_3/mmc$	$P6_3/mcm$	$P\bar{6}c2$	**$P6_3cm$**	$P\bar{3}c1$	$P3c1$	$P1$
R_{int}	**0.0441**	0.0461	0.0455	**0.0458**	0.462	0.0452	0.0317
$R_1(I>2\sigma)$	**0.0292**	0.1902	0.1622	**0.0200**	0.423	0.0213	0.0291
$wR_2(I>2\sigma)$	**0.0655**	0.7314	0.5288	**0.0627**	0.0866	0.0615	0.0879
R_1(all)	**0.0308**	0.1920	0.1661	**0.0219**	0.447	0.0241	0.0418
wR_2(all)	**0.0667**	0.7367	0.5497	**0.0653**	0.0880	0.0640	0.0793
GoF	**1.250**	4.901	3.028	**1.147**	1.131	1.141	1.044
x(P)	**$^2/_3$**	0.3360(3)	0.3371(3)	**0.3317(1)**	0.3335(1)	0.3333(1)	0.3324(3)
y(P)	**$^1/_3$**	0	0.0039(3)	**0**	0	-0.0015(1)	0.0004(3)
z(P)	**$^1/_4$**	$^1/_4$	$^1/_4$	**0.2500(6)**	$^1/_4$	0.2500(5)	0.2500(1)
$x(Na_{eq1})$	**0**	0	0	**0**	0	0	0.0000(3)
$y(Na_{eq1})$	**0**	0	0	**0**	0	0	0.0000(3)
$z(Na_{eq1})$	**$^1/_4$**	$^1/_4$	$^1/_4$	**0.2225(7)**	$^1/_4$	0.2375(6)	0.2213(3)
$x(Na_{eq2})$		$^2/_3$	$^2/_3$	**$^2/_3$**	$^2/_3$	$^2/_3$	0.6668(3)
$y(Na_{eq2})$		$^1/_3$	$^1/_3$	**$^1/_3$**	$^1/_3$	$^1/_3$	0.3334(3)
$z(Na_{eq2})$		$^1/_4$	$^1/_4$	**0.2646(8)**	0.2271(2)	0.2373(6)	0.2653(4)
$y(Na_{eq3})$			$^1/_3$			$^1/_3$	0.3333(3)
$y(Na_{eq3})$			$^2/_3$			$^2/_3$	0.6668(3)
$z(Na_{eq3})$			$^1/_4$			0.2794(6)	0.2653(4)
$x(Na_{ax1})$	**$^1/_3$**	0.3307(4)	0.3289(4)	**0.3539(2)**	0.3229(1)	0.3333(3)	0.3548(6)
$y(Na_{ax1})$	**$^2/_3$**	0.3307(4)	0.3325(5)	**0.3539(2)**	0.3463(2)	0.3546(2)	0.3541(6)
$z(Na_{ax1})$	**0.0808(2)**	0.0810(8)	0.0811(8)	**0.0810(2)**	0.0807(1)	0.0819(6)	0.0810(4)
$x(Na_{ax2})$				**0.3121(2)**		0.3334(3)	0.3139(6)
$y(Na_{ax2})$				**0.3121(2)**		0.3128(2)	0.3130(6)
$z(Na_{ax2})$				**0.4199(2)**		0.4207(6)	0.4202(4)
U_{11}(P)	**0.0166**	0.0210	0.0250	**0.0160**	0.0155	0.0161	0.0167
U_{22}(P)	**0.0166**	0.0250	0.0240	**0.0162**	0.0187	0.0160	0.0152
U_{33}(P)	**0.0176**	0.0340	0.0340	**0.0170**	0.0173	0.0169	0.0170
$U_{11}(Na_{eq1})$	**0.0206**	0.0220	0.0260	**0.0205**	0.0209	0.0202	0.0223
$U_{22}(Na_{eq1})$	**0.0206**	0.0220	0.0260	**0.0205**	0.0209	0.0202	0.0215
$U_{33}(Na_{eq1})$	**0.0960**	0.0390	0.4600	**0.0530**	0.0940	0.0644	0.0526
$U_{11}(Na_{eq2})$		0.0220	0.0260	**0.0204**	0.0204	0.0203	0.0216
$U_{22}(Na_{eq2})$		0.0220	0.0260	**0.0204**	0.0204	0.0203	0.0211
$U_{33}(Na_{eq2})$		0.3000	0.1120	**0.0626**	0.0509	0.0633	0.0596
$U_{11}(Na_{eq3})$			0.0240			0.0205	0.0217
$U_{22}(Na_{eq3})$			0.0240			0.0205	0.0209
$U_{33}(Na_{eq3})$			0.0420			0.0518	0.0615
$U_{11}(Na_{cap1})$	**0.0625**	0.0570	0.0700	**0.0399**	0.0441	0.0369	0.0386
$U_{22}(Na_{cap1})$	**0.0625**	0.0570	0.0670	**0.0339**	0.0550	0.0481	0.0376
$U_{33}(Na_{cap1})$	**0.0239**	0.0610	0.0820	**0.0235**	0.0239	0.0236	0.0242
$U_{11}(Na_{cap2})$				**0.0489**		0.0572	0.0490
$U_{22}(Na_{cap2})$				**0.0489**		0.0402	0.0476
$U_{33}(Na_{cap2})$				**0.0224**		0.0220	0.0221

Table S3: Selected bond lengths and distances for investigated space groups given in Å. The reported and new model are highlighted in bold.

	P*6$_3$/*mmc	*P*6$_3$/*mcm*	*P*$\bar{6}$*c*2	***P*6$_3$*cm***	*P*$\bar{3}$*c*1	*P*3*c*1	*P*1
P-Na_{eq1}	**2.874**	2.897	2.890	**2.870**	2.875	2.882	
P-Na_{eq2}	**2.874**	2.862	2.841	**2.884**	2.880	2.872	
P-Na_{eq3}	**2.874**	2.862	2.892	**2.884**	2.880	2.883	
P-Na_{ax1}	**2.920**	2.923	2.924	**2.920**	2.925	2.914	
P-Na_{ax2}	**2.920**	2.923	2.924	**2.928**	2.925	2.935	
P-Na_{cap1}	**3.239**	3.237	3.233	**3.315**	3.381	3.411	
P-Na_{cap2}	**3.239**	3.239	3.245	**3.094**	3.232	3.151	
P-Na_{cap3}	**3.239**	3.239	3.236	**3.315**	3.113	3.150	
P-Na_{cap4}	**3.239**	3.237	3.233	**3.158**	3.113	3.101	
P-Na_{cap5}	**3.239**	3.239	3.245	**3.418**	3.232	3.222	
P-Na_{cap6}	**3.239**	3.239	3.236	**3.158**	3.381	3.322	
Na_{cap1}-P_{bas}	**3.239**	3.239	3.233	**3.315**	3.381	3.411	
Na_{cap1}-P_{bas2}	**3.239**	3.239	3.236	**3.315**	3.232	3.151	
Na_{cap1}-P_{bas3}	**3.239**	3.237	3.245	**3.094**	3.113	3.150	
Na_{cap1}-P_{ap}	**2.920**	2.923	2.924	**2.928**	2.925	2.935	
Na_{cap1}-Na_{cap4}	**2.988**	2.984	2.982	**3.014**	3.010	3.012	
Na_{cap1}-Na_{cap7}	**3.208**	3.190	3.252	**3.219**	3.222	3.213	
Na_{cap1}-Na_{cap8}	**3.208**	3.190	3.233	**3.219**	3.222	3.220	
Na_{cap1}-Na_{cap9}	**3.208**	3.250	3.149	**3.212**	3.207	3.219	
Na_{cap1}-Na_{eq1}	**3.239**	3.218	3.217	**3.297**	3.286	3.272	
Na_{cap1}-Na_{eq2}	**3.239**	3.248	3.269	**3.227**	3.254	3.272	
Na_{cap1}-Na_{eq3}	**3.239**	3.248	3.227	**3.227**	3.207	3.206	
Na_{cap4}-P_{bas}				**3.158**		3.101	
Na_{cap4}-P_{bas2}				**3.158**		3.322	
Na_{cap4}-P_{bas3}				**3.418**		3.322	
Na_{cap4}-P_{ap}				**2.920**		2.914	
Na_{cap4}-Na_{cap1}				**3.014**		3.012	
Na_{cap4}-Na_{eq1}				**3.206**		3.225	
Na_{cap4}-Na_{eq2}				**3.271**		3.226	
Na_{cap4}-Na_{eq3}				**3.271**		3.296	
Na_{cap4}-Na_{cap10}				**3.219**		3.213	
Na_{cap4}-Na_{cap11}				**3.212**		3.220	
Na_{cap4}-Na_{cap12}				**3.219**		3.219	
Na_{eq2}-P_{eq}		2.862	2.841	**2.884**	2.880	2.883	
Na_{eq2}-P_{eq2}		2.862	2.841	**2.884**	2.880	2.883	
Na_{eq2}-P_{eq3}		2.862	2.841	**2.884**	2.880	2.883	
Na_{eq2}-Na_{cap1}		3.248	3.269	**3.227**	3.286	3.272	
Na_{eq2}-Na_{cap2}		3.248	3.269	**3.227**	3.286	3.272	
Na_{eq2}-Na_{cap13}		3.248	3.269	**3.227**	3.286	3.272	
Na_{eq2}-Na_{cap4}		3.248	3.269	**3.271**	3.205	3.226	
Na_{eq2}-Na_{cap5}		3.248	3.269	**3.271**	3.205	3.226	
Na_{eq2}-Na_{cap14}		3.248	3.269	**3.271**	3.205	3.226	
Na_{eq3}-P_{eq}			2.892	**2.884**		2.872	
Na_{eq3}-P_{eq5}			2.892	**2.884**		2.872	
Na_{eq3}-P_{eq6}			2.892	**2.884**		2.872	
Na_{eq3}-Na_{cap3}			3.227	**3.227**		3.206	
Na_{eq3}-Na_{cap2}			3.227	**3.227**		3.206	
Na_{eq3}-Na_{cap15}			3.227	**3.227**		3.206	
Na_{eq3}-Na_{cap6}			3.227	**3.271**		3.296	
Na_{eq3}-Na_{cap5}			3.227	**3.271**		3.296	
Na_{eq3}-Na_{cap16}			3.227	**3.271**		3.296	
Na_{eq1}-P_{eq}	**2.874**	2.897	2.890	**2.870**	2.875	2.882	
Na_{eq1}-P_{eq7}	**2.874**	2.897	2.890	**2.870**	2.875	2.882	
Na_{eq1}-P_{eq8}	**2.874**	2.897	2.890	**2.870**	2.875	2.882	
Na_{eq1}-Na_{cap1}	**3.239**	3.218	3.217	**3.297**	3.254	3.272	

Na_{eq1}-Na_{cap3}	**3.239**	3.218	3.217	**3.297**	3.254	3.272	
Na_{eq1}-Na_{cap17}	**3.239**	3.218	3.217	**3.297**	3.254	3.272	
Na_{eq1}-Na_{cap4}	**3.239**	3.218	3.217	**3.206**	3.254	3.225	
Na_{eq1}-Na_{cap2}	**3.239**	3.218	3.217	**3.206**	3.254	3.225	
Na_{eq1}-Na_{cap18}	**3.239**	3.218	3.217	**3.206**	3.254	3.225	

5.7 $Na_2Ge_3P_3$ & $Na_5Ge_7P_5$: Flexible Systems Built from 1-Dimensional Modular Units

H. Eickhoff, V. Hlukhyy, T. F. Fässler

manuscript for publication

$Na_2Ge_3P_3$ & $Na_5Ge_7P_5$: Flexible Systems Built from 1-Dimensional Modular Units

Henrik Eickhoff, Viktor Hlukhyy, Thomas F. Fässler

Department of Chemistry, Technische Universität München,
Lichtenbergstrasse 4, 85747 Garching bei München, Germany
* E-mail: Thomas.Faessler@lrz.tu-muenchen.de

Abstract

The compounds $Na_2Ge_3P_3$ and $Na_5Ge_7P_5$ crystallize both in the monoclinic space group *C*2/*m* with the unit cell parameters a = 17.639(4) Å, b = 3.6176(7) Å, c = 11.354(2) Å, β = 92.74(3)° and a = 16.168(5) Å, b = 3.6776(7) Å, c = 12.924(4) Å, β = 91.30(3)°, respectively. Both compounds are built from linear condensed cages of 9 atoms with 4 Ge and 5 P or 5 Ge and 4 P atoms, respectively. These cages contain Ge-Ge bonds and are connected by sharing three atoms to 1-dimensional tubes. The parallel tubes are connected to pairs forming further Ge-Ge bonds resulting in Ge_4 and larger Ge_n units, which are covalently connected. The comparison with further compounds from the corresponding phase system such as $NaGe_3P_3$ and GeP reveals recurring structural motives with a broad variety of connection patterns.

Introduction

An increasing interest in further evolved battery systems for various applications promotes the research on new materials. For stationary devices Na based systems show a great potential. In these, compared to Li, the lower gravimetric power and energy density plays a minor role in contrast to the high abundance and affordability of Na.[1,2]

Recently, a new class of materials, sodium phosphidosilicates, has been shown to exhibit high mobilities for Na ions of up to 4×10^{-4} S cm^{-1}.[3] The compounds $Na_{19}Si_{13}P_{25}$, $Na_{23}Si_{19}P_{33}$, $Na_{23}Si_{28}P_{45}$, $Na_{23}Si_{37}P_{57}$, *LT*-$NaSi_2P_3$ and *HT*-$NaSi_2P_3$ consist of supertetrahedra of SiP_4 units, which form three dimensional channels for ion migration.[3] For related Li based materials also fast ion conduction is reported, which could be further increased by substitution of Si by Ge.[4,5] Additionally, for the heavier homologues of Si (*Tt* = Ge, Sn) a broader variety of connection patterns are reported enabling the formation of *Tt*-*Tt* bonds and formally negatively charged *Tt* atoms as found in $NaGe_3P_3$.[6-9] These structures can provide alternative physical properties caused by the different bonding situation. Moreover, when comparing structural motives of binary *A*/*Tt* (*A* = Li, Na; *Tt* = Si, Ge) compounds, a significantly increased tendency to the formation of low dimensional building blocks is observed for the Na/Ge system. This is illustrated by the cluster containing compounds Na_4Ge_4 and $Na_{12}Ge_{17}$,[10,11] which are not reported for Li containing systems. Such units result in a denser framework of short Na-Na distances, which are usually seen as beneficial for ion hopping.

Following these ideas, the new compounds $Na_2Ge_3P_3$ and $Na_5Ge_7P_5$ are prepared and presented.

Experimental Section

All syntheses are carried out under Ar atmosphere in Gloveboxes (MBraun, 200B) with moisture and oxygen level below 1 ppm or in containers, which were sealed under Ar atmosphere.

Synthesis

All compounds are synthesized from the elements, Na (ChemPur, 99%), Ge (EVOCHEM GmbH, 99.999%) and red P (Sigma-Aldrich, 97%), in Tantalum ampoules. The ampoules are 10 mm in diameter and 3 cm long and are closed within the glove box via arc welding. The closed Ta ampoules are sealed in evacuated silica glass vessels and heated in muffle furnaces. As heating and cooling rates 4 °C min^{-1} and 1 °C min^{-1} are set, respectively.

Single crystals of and bulk material of $Na_2Ge_3P_3$ are prepared with the nominal composition of "$Na_2Ge_2P_3$" with 161.9 mg (7.04 mmol) Na, 512.3 mg (7.04 mmol) Ge and 327.4 mg (10.56 mmol) P. The sample is heated to 700 °C for 72 h.

$Na_5Ge_7P_5$ single crystals are isolated from a sample with the nominal composition "$Na_2Ge_5P_2$", 29.3 mg (1.27 mmol) Na, 231.3 mg (3.18 mmol) Ge and 39.5 mg (1.27 mmol) P heated to 700 °C for 120 h. Bulk material is prepared with the nominal composition of "NaGeP", 36.3 mg (1.58 mmol) Na, 114.7 mg (1.58 mmol) Ge and 48.9 mg (1.58 mmol) P heated to 700 °C for 24 h.
A sample with the nominal composition of "Na_2GeP_2" (76.4 mg, 3.32 mmol Na, 120.7 mg, 1.66 mmol Ge, 102.9 mg, 3.32 mmol P) heated to 700 °C yielded crystals, which could be refined to the composition of "NaGeP".

Powder X-ray diffraction

Data are collected at room temperature on a STOE Stadi P diffractometer equipped with a Cu $K_{\alpha 1}$ radiation source (λ = 1.54056 Å), a Ge(111) monochromator and a Dectris MYTHEN 1K detector in Debye-Scherrer geometry. Samples are sealed in glass capillaries (Ø 0.3 mm) for measurement. Raw data were processed with WinXPOW[12] software.

Single crystal X-ray data collection

Single crystals are isolated and sealed in glass capillaries (0.3 mm). For diffraction data collection, the capillary is mounted on a STOE StadiVari (Mo K_α radiation, λ = 0.71073) diffractometer equipped with a DECTRIS PILATUS 300 K detector and a nitrogen jet cooling system for measurements at 120 K. Structures are solved by Direct Methods (SHELXS-2014) and refined by full-matrix least-squares calculations against F^2 (SHELXL-2014).[13]

Differential scanning calorimetry (DSC)

For investigation of the thermal behavior of the compounds a Netzsch DSC 404 Pegasus device is used. Niobium crucibles are filled with 50 mg to 100 mg sample and sealed by arc-welding. Empty, sealed crucibles served as reference. Measurements are performed under an Ar flow of 75 ml min^{-1} and a heating/cooling rate of 10 °C min^{-1} up to a temperature of 750 °C. Data collection and handling was carried out with the Proteus Thermal Analysis program.[14]

Results and Discussion

Synthesis

The compounds $Na_2Ge_3P_3$ and $Na_5Ge_7P_5$ are synthesized from elements with various compositions close to exact composition at 700 °C. The highest purity is obtained from samples with the nominal composition of "$Na_2Ge_2P_3$" and "NaGeP". Thermal analysis also showed reversible phase transitions at 520 °C ($Na_2Ge_3P_3$) and 572 °C ($Na_5Ge_7P_5$). While in $Na_2Ge_3P_3$ this effect was

contributed to a decomposition or melting, in $Na_5Ge_7P_5$ a solid to solid phase transition to an unknown phase is observed in PXRD measurements after fast cooling. In both cases single crystals of the corresponding compound form during cooling. Thus for preparation of large single crystals a slow cooling rate beneficial, which is confirmed by the circumstance that all crystals are found in samples cooled with a rate of 1 °C min^{-1}.

Crystal structure of $Na_2Ge_3P_3$

The compound $Na_2Ge_3P_3$ crystallizes as black needles in the monoclinic space group *C*2/*m* with unit cell parameters of a = 17.639(4) Å, b = 3.6176(7) Å, c = 11.354(2) Å and β = 92.74(3)° (Fig. 1, left). The crystal structure consists of eight crystallographically independent positions, two Na, three Ge and three P sites. Ge and P atoms form covalently bound $^1_\infty[Ge_3P_3]^{2-}$ subunits separated by Na^+. The 1-dimensional units are built of two parallel tubes. Each tube consists of 9 atom cages of Ge_4P_5 composed by 5- and 6-membered rings. These cages are connected by sharing three atoms (Ge1, P2, P3). The tube pairs are formed via bonds between Ge2 atoms of the two tubes, forming Ge_4 chains. Following this connection pattern the tubes can also be described as a chain of condensed GeP_4 and Ge(P_2Ge_2)tetrahedra. The GeP_4 tetrahedra are formed by Ge1 surrounded by two P1, one P2 and one P3 atom and are connected via P1 to chains. The Ge(P_2Ge_2) tetrahedra (Ge2 surrounded by two P2, Ge2, Ge3) are connected to the GeP_4 by sharing P3 atoms and by forming bonds between Ge2 and P2. The connection between the tubes results from interpenetrating Ge(P_2Ge_2) tetrahedra. Within the chain pairs two different Ge-Ge distances are found. Between the tubes (Ge2-Ge2) the bond length of 2.4631(14) Å is similar to the ones found in elemental Ge (2.450 Å).[16] The bond within the tubes (Ge2-Ge3) is with 2.5574(14) Å significantly longer than the first, but shorter than the Ge-Ge bond found in $NaGe_3P_3$ (2.626 Å), which consists similar structural motives.[7] Further, the Ge-P bond length in the slightly distorted GeP_4 tetrahedra are in a range of (2.323(2) Å to 2.368(3) Å are in good agreement with Ge-P bonds found in GeP, $NaGe_3P_3$ and α-, β-Li_8GeP_4.[5] The bond angles of 102.262(6)° to 113.302(13)° deviate from the ideal tetrahedron angle of 109.47°, most likely due to tensions within the tubes. This can be induced by different connectivity patterns of the atoms. As already mentioned, Ge1 is coordinated by four P atoms, similar to Ge2, which is coordinated by three P atoms and one Ge atom. Contrary, Ge3 has only three neighbors (two P3 and one Ge2). Similar differences are found for the P atoms. P2 and P3 are each coordinated by three Ge atoms, while P1 is only bond to two Ge atoms. Regarding the connectivity of the atoms of two 4b-Ge, one 3b-Ge, two 3b-P and one 2b-P atoms the negative charges, according to the 8-N rule, are formally situated at the 3b-Ge

(Ge3) and 2b-P (P1) atoms. These charges are counterbalanced by two Na^+, which is placed in distorted octahedral voids (P_5Ge) between the paired tubes.

Crystal structures comprising similar tubes are known from various compounds in alkaline-tetrel-pnictide system. For the most prominent composition ATt_3Pn_3, such as $NaGe_3P_3$, these building blocks are connected to slabs,[7] but also in binary compounds like GeP similar motives occur.[15]

Crystal structure of $Na_5Ge_7P_5$

$Na_5Ge_7P_5$ crystallizes as black needles in the monoclinic space group *C*2/*m* with unit cell parameters of *a* = 16.168(5) Å, *b* = 3.6776(7) Å, *c* = 12.924(4) Å and β = 91.30(3)° (Fig. 1, right). The similarity to $Na_2Ge_3P_3$, which is already indicated by the unit cell dimensions and space group, is confirmed by the presence of covalently bound tube pairs with identical atom connectivity. However, differences are found in the number of atom positions. For $Na_5Ge_7P_5$ one additional Na site occurs and the P2 site is mixed and partially occupied by Ge4, leading to a total of nine independent sites, three Na, three Ge, two P and one Ge/P site. The occupation of Ge4 and P2 on the mixed position is 0.44 and 0.56, respectively, closely fitting the ideal ratio of 0.5. The ratio of 0.5 leads to the anion description $^1_\infty[Ge_7P_5]^{5-}$. If on a certain position the mixed position is occupied with P, the building blocks found are identical to $Na_2Ge_3P_3$, GeP_4 tetrahedra with bond length and angles of 2.3429(4) Å to 2.4885(8) Å and 103.41(2)° to 113.662(13)° and Ge2-Ge3 bonds with a length of 2.4807(8) Å. The bond of the two Ge2 atoms between the two tubes of a pair are 2.4288(7) Å. If the split position is occupied by a Ge atom, the tetrahedra become $Ge(P_3Ge)$ and $Ge(PGe_3)$ or $Ge(Ge_4)$ units. The Ge atom also connects the 4 atom chains to form Ge_{10} units, a 7 atom chain with additional Ge atom branches at chain atom position 3, 4 and 5. Since more Ge atoms on split positions bound to that chain are highly probable, longer chains and rings will occur. To conserve charge neutrality the additional, formally negatively charged Ge atoms are counterbalanced by Na3. This is situated in a distorted octahedral void (P_6) in the center of the unit cell, formed by a rotation of the anionic units compared to $Na_2Ge_3P_3$. The angle of the Ge2-Ge2 to the c axis is reduced from 37.56(3)° ($Na_2Ge_3P_3$) to 23.91(6)° ($Na_5Ge_7P_5$), explaining the shortened *a*, but enlarged *c* parameter. These changes also affect the remaining Na^+. While Na1 is coordinated octahedrally by $P_{4-x}Ge_{2+x}$ ($0 \leq x \leq 3$), due to three neighboring split positions, Na2 is surrounded by a rectangular pyramid of P_5.

A general formula of $Na_{5-x}Ge_{7-x}P_{5+x}$, describing both compounds, can be formulated indicating the presence of compounds with intermediate composition.

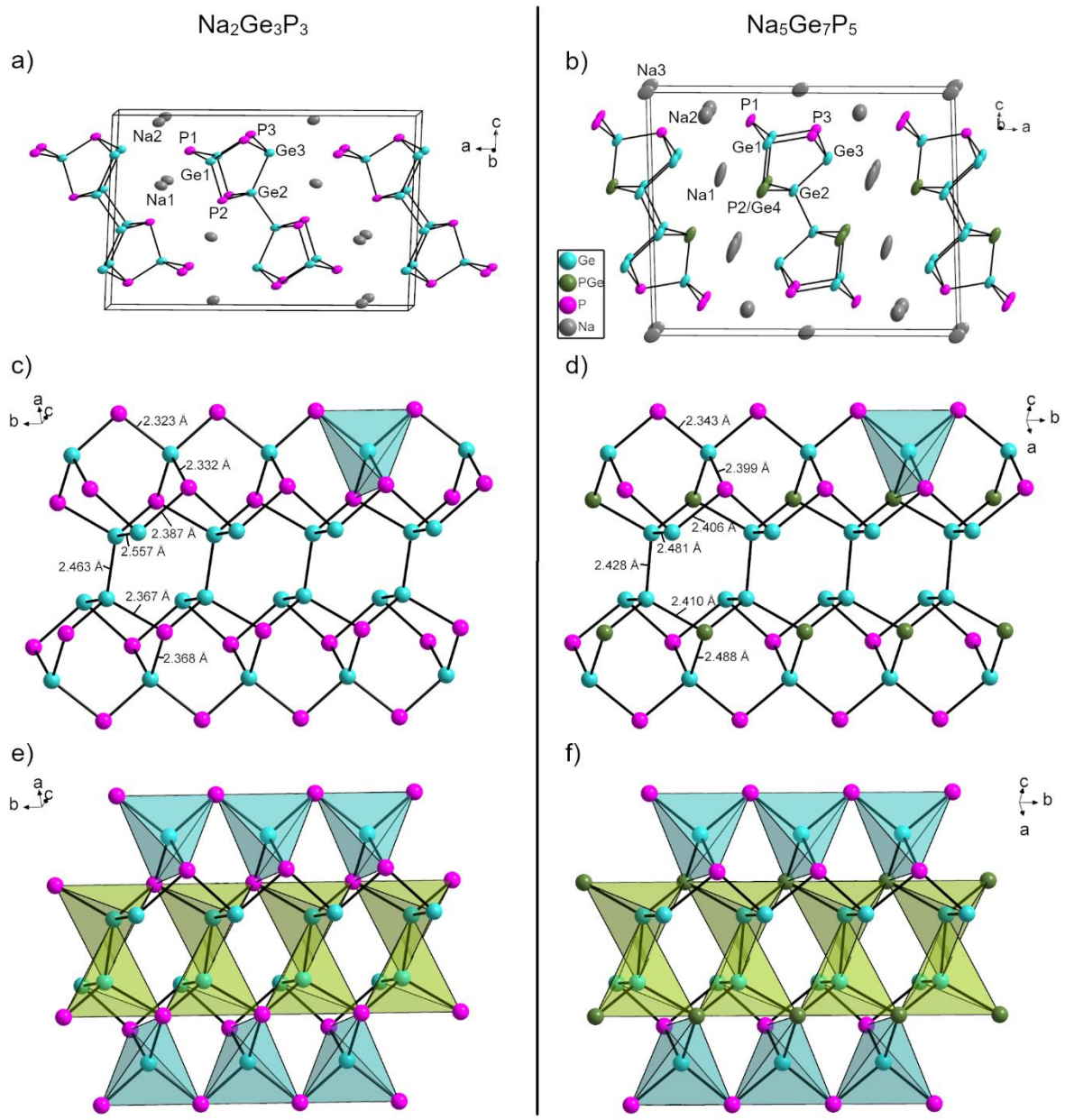

Figure 1: Structural motives of $Na_2Ge_3P_3$ (left) and $Na_5Ge_7P_5$ (right). a) and b) unit cells with atom names. c) and d) enlarged anionic building blocks with bond length. A GeP_4/GeP_3Ge tetrahedron is highlighted in light blue. e) and f) connectivity of tetrahedral building blocks. Tetrahedra around Ge1 are highlighted in light blue, tetrahedra around Ge2 are highlighted in green. Within one tube one Ge1 and two Ge2 tetrahedra share a P2(/Ge4) vertex and are connected via two Ge3-P3 bonds each. The Ge2 tetrahedra of connected tubes are interpenetrating each other.

Table 1: Refinement data of the single crystal diffraction data of $Na_2Ge_3P_3$ and $Na_5Ge_7P_5$ at 293 K.

Sum formula	$Na_2Ge_3P_3$	$Na_5Ge_7P_5$
Molar mass / g mol^{-1}	356.72	778.07
Crystal system	monoclinic	monoclinic
Space group	*C*2/*m* (12)	*C*2/*m* (12)
Radiation λ / Å	0.71073 (Mo K_α)	0.71073 (Mo K_α)
Crystal size / mm^3	2.0 × 0.10 × 0.10	1.5 × 0.03 × 0.03
Crystal color, shape	black, needle	black, needle
Cell parameters / Å	*a* = 17.639(4)	*a* = 16.168(5)
	b = 3.6176(7)	*b* = 3.6776(7)
	c = 11.354(2)	*c* = 12.924(4)
	β = 92.74(3)	β = 91.30(3)
Cell volume / Å^3	723.7(2)	768.2(2)
Z	4	2
ρ (calc.) / g cm^{-3}	3.274	3.343
μ / mm^{-1}	13.046	13.934
F(000)	652	704
Temperature / K	293(2)	293(2)
Reflections collected	4260	6185
Independent reflections	747	931
Reflections with $I > 2\sigma(I)$	671	683
Observed *hkl*	$-20 \le h \le 20$,	$-20 \le h \le 17$,
	$-4 \le k \le 4$,	$-4 \le k \le 4$,
	$-13 \le l \le 13$	$-16 \le l \le 16$
Measuring range $\theta_{min/max}$ / °	3.00 / 24.99	2.94 / 26.50
Goodness-of-fit on F_0^2	1.166	1.096
R_{int} /R_σ	0.0536 / 0.0242	0.1176 / 0.0731
R indices ($F_0^2 \le 2\sigma(F_0^2)$)	*R*1 = 0.0361, *wR*2 = 0.0903	*R*1 = 0.0886, *wR*2 = 0.2161
R indices (all data)	*R*1 = 0.0427, *wR*2 = 0.0796	*R*1 = 0.1224, *wR*2 = 0.2362
Largest diff. peak/hole / e Å^{-3}	1.242 / −1.105	2.702 / −2.894

Comparison of the new crystal structures with related structures reveals an intriguing relations. Already on the first look, the crystal structure of new compounds remind of the one of fibrous phosphorus,[17] as they consist of two connected parallel tubes with a pentagonal cross sections. On the closer view on single tubes differences are found. In fibrous phosphorus the tubes are built from P_8 and P_9 cages connected via P_2 dumbbells. In the ternary compounds also 9 atom cages of Ge_4P_5 and Ge_5P_4 for $Na_2Ge_3P_3$ and $Na_5Ge_7P_5$, respectively. However, these cages are not connected by P_2 units, but by sharing three atoms (Ge1, P2(/Ge4), P3) with each neighboring cage. Additionally, the connection of the tubes alters. In fibrous phosphorus the tubes are connected via the P atom in the apex of the P_9 cage. The corresponding atom in the ternary compounds (P1) is not connected to another chain but bears a negative charge. Instead a bond between Ge2 atoms, representing atoms from the former backbone of fibrous phosphorus, is formed. This difference is most likely induced by the presence of Ge atoms, which often occur in tetrahedral environments. Therefore tetrahedral centers and additional bonds are added, leading to a denser connection of the cages. The reason for the different connectivity between the tubes can be found in the Ge_2 dumbbell. A connection pattern as found in fibrous phosphorus would lead to two formally negatively charged, adjacent Ge atoms. With the bond between the Ge2 atoms the formal charge of this atom is 0 and instead the P1 atom is charged negatively, spreading the negative charge.

Comparing the compounds with other Ge and P containing compounds with different amounts of Na show an interesting trend. Similar structural motives, polyanionic tubes of Ge and P are a recurring motive. Starting from $Na_2Ge_3P_3$ many of these compounds can be constructed formally. A partial substitution of P with Ge leads to $Na_5Ge_7P_5$. The possibility of an atom exchange is also indicated by related compounds such as SiP_2 and Li_3NaSi_6, which both consist of slabs of the described tubes. However, while in SiP_2 all fourfold coordinated sites are occupied by Si and all threefold coordinated sites by P, the anions in Li_3NaSi_6 solely consist of Si on all sites, independent of the connectivity.

Keeping the Ge:P ratio in $Na_2Ge_3P_3$ constant and reducing the Na content leads to $NaGe_3P_3$.[7] This compound consists of slabs formed by tubes identical to the ones found in $Na_2Ge_3P_3$. Contrary to the latter the slabs are not connected via a Ge_4 chain, but between a Ge dumbbells and the two times bond P atoms. Completely removing Na leads to the binary compound GeP.[15] It consists of tubes condensed to slabs built from Ge atoms surrounded tetrahedrally by one Ge and three P atoms and P atoms surrounded by three Ge atoms. This leads to a different assignment of atoms to the atom positions within the tube, compared to the presented compounds. Additionally, two bonds to the first neighboring tube and one to the second are formed. By breaking selected bonds in

$NaGe_3P_3$, rotating half of the subunits and atom swapping this structure can be formally constructed.

Starting from $Na_2Ge_3P_3$ and increasing the Na content should lead to the cleavage of the Ge2-Ge2 bond and the formation of "NaGeP". First crystals found in a sample with the nominal composition "Na_2GeP_2" showed the isolated tubes surrounded by Na (compare Supporting Information). However, an assignment of P and Ge to certain positions of the polyanion was not possible, due to the quality of the data.

Conclusion

The two new phases $Na_2Ge_3P_3$ and $Na_5Ge_7P_5$ illustrate the flexibility of structures in the Na/Ge/P phase system by retaining basic structural polyanionic units. Both compounds represent the first compounds comprising a new connection mode for a known building block, leading to pairs of parallel, 1-dimensional Ge-P tubes. Additionally, the connection via Ge-Ge bonds leads to the formation of Ge_n chains in $Na_5Ge_7P_5$. The compounds themselves also give a descriptive example for pnictide-tetrel substitution. Substituting P with Ge and adding a corresponding amount of Na forces the rotation of the polyanions to provide space for the added cations. This results in an increasing *c* and decreasing *a* parameter, while conserving the symmetry of the structure.

Comparison with other compounds from that phase system reveal a modular construction pattern. By different connectivities the building blocks can be combined to 1-dimensional units, or more or less condensed 2-dimensional structures in GeP[15] and $NaGe_3P_3$.[7] Furthermore, first experiments hint to the presence of the isolated building block in the compound "NaGeP".

In all prepared compounds 3-dimensional networks of short Na-Na distances are present. Further, the synthesis of material with high purity and subsequent determination of its electric properties are highly desirable.

Acknowledgements

The authors greatly acknowledge Alexander Mutschke and Ludwig Petters for preparative experiments and Tassilo Restle for DSC measurements.

References

[1] Chayambuka, K.; Mulder, G.; Danilov, D. L.; Notten, P. H. L.; Sodium-Ion Battery Materials and Electrochemical Properties Reviewed, *Adv. Energy Mater.* **2018**, *8*, 1800079.

[2] Fang, Y.; Xiao, L.; Chen, Z.; Ai, X.; Cao, Y.; Yang, H.; Recent Advances in Sodium-Ion Battery Materials, *Electrochemical Energy Reviews* **2018**, *1*, 294-323.

[3] Haffner, A.; Hatz, A.-K.; Moudrakovski, I.; Lotsch, B. V.; Johrendt, D.; Fast Sodium-Ion Conductivity in Supertetrahedral Phosphidosilicates, *Angew. Chem.* **2018**, *130*, 6263-6268; *Angew. Chem. Int. Ed.* **2018**, *57*, 6155-6160.

[4] Toffoletti, L.; Kirchhain, H.; Landesfeind, J.; Klein, W.; van wüllen, L.; Gasteiger, H. A.; Fässler, T. F.; Lithium Ion Mobility in Lithium Phosphidosilicates: Crystalstructure, ^{7}Li, ^{29}Si, and ^{31}P MAS NMR Spectroscopy, and Impedance Spectroscopy of Li_8SiP_4 and Li_2SiP_2, *Chem.-Eur. J.* **2016**, *22*, 17635-17645.

[5] Eickhoff, H.; Strangmüller, S.; Klein, W.; Kirchhain, H.; Dietrich, C.; Zeier, W. G.; van Wüllen, L.; Fässler, T. F.; Lithium Phosphidogermanates α- and β-Li8GeP4 – A Novel Coumpound Class with Mixed Li+ Ionic and Electronic Conductivity, Chem. Mater. 2018, 30, 6440-6448.

[6] Klein, J.; Eisenmann, B.; Zintl-phasen mit komplexen anionen: Darstellung und Einkristallstrukturbestimmung von KSnAs und K6Sn3As5, Mater. Res. Bull. 1988, 23, 587-594.

[7] Feng, K.; Yin, W.; He, R.; Lin, Z.; Jin, S.; Yao, J.; Fu, P.; Wu, Y.; NaGe3P3: a new ternary germanium phosphide featuring an unusual [Ge3P7] ring, Dalton Tans. 2012, 41, 484-489.

[8] Mark, J.; Hanrahan, M. P.; Woo, K. E.; Lee, S.; Rossini, A. J.; Kovnir, K.; Chemical and Electrochemical Lithiation of van der Waals Tetrel-Arsenides, Chem. Eur. J. 2019, 25, 6392-6401.

[9] Khatun, M.; Stoyko, S. S.; Mar, A.; Ternary arsenides ATt3As3 (A=K, Rb; Tt=Ge, Sn) with layered structures, J. Solid State Chem. 2016, 238, 229-235.

[10] Bürger, H.; Eujen, R.; Infrarot-Spektren der Tetraeder-Ionen Si_4^{4-} and Ge_4^{4-}, *Z. Anorg. Allg. Chem.* 1**972**, *894*, 19-25.

[11] Carrillo-Cabrera, W.; Cardoso Gil, R.; Somer, M.; Persil, Ö.; von Schnering, H. G.; $Na_{12}Ge_{17}$: A Compound with the Zintl Anions $[Ge_4]^{4-}$ and $[Ge_9]^{4-}$ - Synthesis, Crystal Structure, and Raman Spectrum, *Z. Anorg. Allg. Chem.* **2003**, *629*, 601-608.

[12] *WinXPOW V3.0.2.1.*, 3.0.2.1.; STOE & Cie GmbH: Darmstadt, Germany, 2011.

[13] Sheldrick, G. M. Crystal Structure Refinement with SHELXL. *Acta Crystallogr., Sect. C: Struct. Chem.* **2015**, *71*, 3-8

[14] *Proteus Thermal Analysis V4.8.2*, Netzsch-Gerätebau GmbH: Selb, 2006.

[15] Wadsten, T.; Crystal structures of silicon phosphide, silicon arsenide, and germanium phosphide, *Acta Chem. Scand.* **1967**, *21*, 593-594.

[16] Straumanis, M. E.; Aka, E. Z.; Lattice parameters, coefficients of thermal expansion and weights of purest silicon and germanium, *J. Appl. Phys.* **1952**, *23*, 330-334.

[17] Ruck, M.; Hoppe, D.; Wahl, B.; Simon, P.; Wang, Y.; Seifert, G.; Fibrous Red Phosphorus, *Angew. Chem. Int. Ed.* **2005**, *44*, 7616-7619; Faserförmiger roter Phosphor, *Angew. Chem.* **2005**, *46*, 7788-7792.

Supporting Information

$Na_2Ge_3P_3$ & $Na_5Ge_7P_5$: Flexible Systems Built from 1-Dimensional Modular Units

Henrik Eickhoff, Viktor Hlukhyy, Thomas F. Fässler

Department of Chemistry, Technische Universität München,
Lichtenbergstrasse 4, 85747 Garching bei München, Germany
* E-mail: Thomas.Faessler@lrz.tu-muenchen.de

Bulk Synthesis

Bulk materials of the compounds $Na_2Ge_3P_3$ and $Na_5Ge_7P_5$ are synthesized from elements in samples with a reduced amount of Ge, "$Na_2Ge_2P_3$" and "NaGeP", respectively, at 700 °C (Fig. S1). The content of Ge is reduced since in most samples elemental Ge in found in the product despite the high temperature applied for synthesis. Also prolonged reaction times do not reduce the portion of Ge.

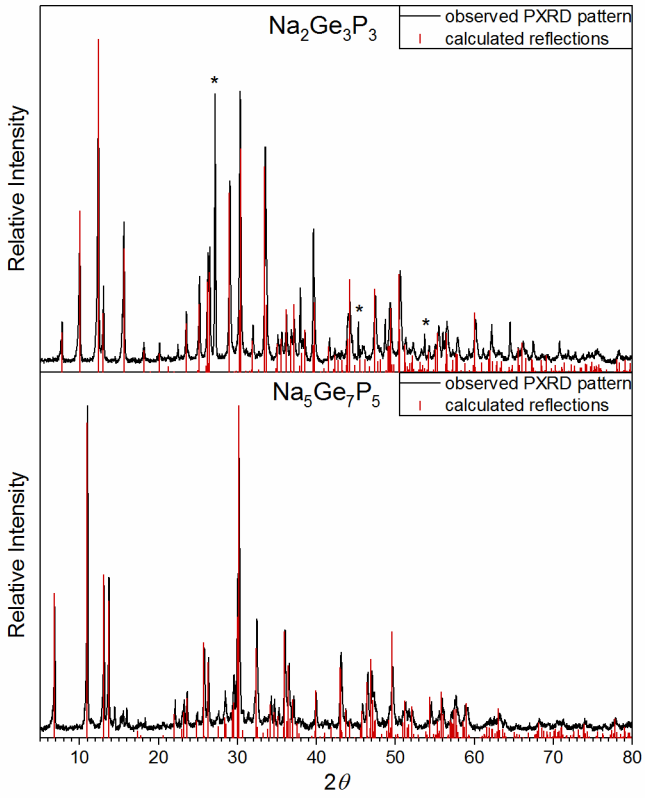

Figure S1: Powder X-ray diffraction pattern of $Na_2Ge_3P_3$ (top) and $Na_5Ge_7P_5$ (bottom). Red lines represent calculated peaks from the single crystal structure and the Ge side phase is indicated with asterisks.

Differential Scanning Calorimetry

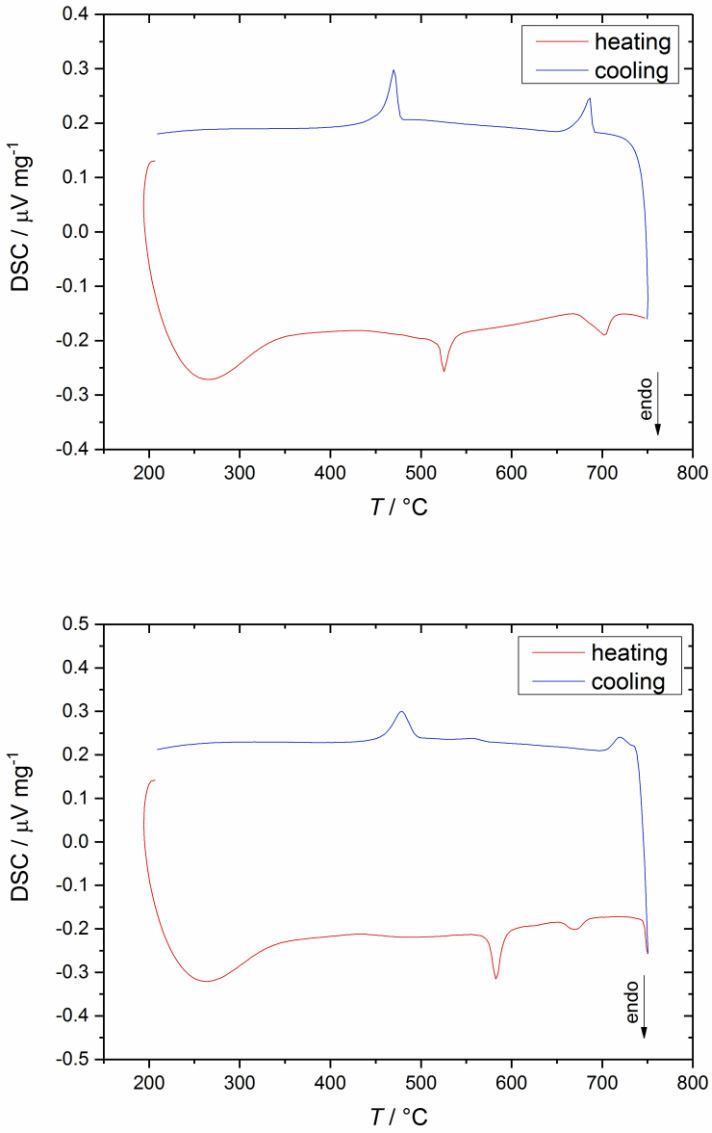

Figure S2: DSC curves of $Na_2Ge_3P_3$ (top) and $Na_5Ge_7P_5$ (bottom).

Single Crystal Data of $Na_2Ge_3P_3$

Refinement parameters and description are found in the discussion part of the main article.

Table S1: Atom coordinates of $Na_2Ge_3P_3$ at 293 K from single crystal diffraction data.

Atom	**Wyck.**	***x***	***y***	***z***	U_{iso}
Ge1	4i	0.32927(8)	0.0000	0.23656(11)	0.0122(3)
Ge2	4i	0.01171(8)	0.0000	0.20584(12)	0.0123(3)
Ge3	4i	0.04259(8)	0.0000	0.58909(11)	0.0136(3)
P1	4i	0.3733(2)	0.0000	0.4368(3)	0.0129(5)
P2	4i	0.7492(2)	0.0000	0.1961(3)	0.0124(5)
P3	4i	0.4369(2)	0.0000	0.1260(3)	0.0130(5)
Na1	4i	0.1691(4)	0.0000	0.3619(5)	0.0233(9)
Na2	4i	0.1533(3)	0.0000	0.0365(5)	0.0204(9)

Table S2: Anisotropic displacement parameters of $Na_2Ge_3P_3$ at 293 K from single crystal diffraction data.

Atom	U_{11}	U_{22}	U_{33}	U_{23}	U_{13}	U_{12}
Ge1	0.0147(5)	0.0118(6)	0.0100(5)	0.0000	0.0004(3)	0.0000
Ge2	0.0159(5)	0.0119(6)	0.0088(5)	0.0000	−0.0006(4)	0.0000
Ge3	0.0154(5)	0.0136(6)	0.0117(5)	0.0000	0.0009(4)	0.0000
P1	0.0136(11)	0.0110(12)	0.0140(11)	0.0000	−0.0009(9)	0.0000
P2	0.0163(11)	0.0109(12)	0.0101(11)	0.0000	−0.0004(9)	0.0000
P3	0.0174(12)	0.0121(12)	0.0097(11)	0.0000	0.0015(9)	0.0000
Na1	0.031(2)	0.019(2)	0.021(2)	0.0000	0.009(2)	0.0000
Na2	0.028(2)	0.018(2)	0.015(2)	0.0000	−0.004(2)	0.0000

Table S3: Selected distances and angles in $Na_2Ge_3P_3$ at 293 K from single crystal diffraction data.

Atom 1	**Atom 2**	***d*$_{1\text{-}2}$ / Å**		**Atom 1**		**Atom 2**		**Atom 3**	**Angle**
Ge1	P1	2.3232(16)	2×	P1	–	Ge1	–	P1	102.26(10)
Ge1	P3	2.332(3)		P1	–	Ge1	–	P3	113.30(7)
Ge1	P2	2.368(2)		P1	–	Ge1	–	P2	111.11(7)
Ge1	Na1	3.221(4)		P3	–	Ge1	–	P2	105.91(9)
Ge2	P2	2.3666(16)	2×	P2	–	Ge2	–	P2	99.69(9)
Ge2	Ge2	2.4632(19)		P2	–	Ge2	–	Ge2	105.04(7)
Ge2	Ge3	2.5573(14)		P2	–	Ge2	–	Ge3	112.15(6)
Ge2	Na1	3.491(4)		Ge2	–	Ge2	–	Ge3	120.49(6)
Ge3	P3	2.3869(17)	2×	P3	–	Ge3	–	P3	98.54(9)
Ge3	Na1	3.218(5)		P3	–	Ge3	–	Ge2	97.00(6)
Ge3	Na2	3.240(4)		Ge2	–	P2	–	Ge2	99.68(9)
P2	Na1	3.038(4)	2×	Ge2	–	P2	–	Ge1	93.48(7)
P1	Na2	3.014(4)	2×	Ge1	–	P1	–	Ge1	102.26(10)
P1	Na1	3.016(4)	2×	Ge1	–	P3	–	Ge3	104.24(7)
P1	Na2	3.202(5)		Ge3	–	P3	–	Ge3	98.54(9)
P3	Na2	2.999(4)	2×						
Na1	Na1	3.6176(7)	2×						
Na1	Na2	3.692(6)							
Na2	Na2	3.6176(7)	2×						
Na2	Na2	3.956(7)	2×						

Single Crystal Data of $Na_5Ge_7P_5$

Refinement parameters and description are found in the discussion part of the main article.

Table S4: Atom coordinates of $Na_5Ge_7P_5$ at 293 K from single crystal diffraction data.

Atom	**Wyck.**	***x***	***y***	***z***	U_{iso}	***Occ.***
Ge1	4i	0.60557(2)	0.0000	0.20967(2)	0.01391(1)	
Ge2	4i	0.03044(2)	0.0000	0.41496(2)	0.01367(1)	
Ge3	4i	0.08405(2)	0.0000	0.71613(2)	0.01568(1)	
Ge4	4i	0.37407(2)	0.0000	0.59888(2)	0.02014(2)	0.44452(14)
P1	4i	0.16572(2)	0.0000	0.12795(2)	0.01510(2)	
P2	4i	0.37407(2)	0.0000	0.59888(2)	0.02014(3)	0.55548(14)
P3	4i	0.45883(2)	0.0000	0.17769(2)	0.01206(1)	
Na1	4i	0.26937(2)	0.0000	0.35089(2)	0.03761(4)	
Na2	4i	0.80735(2)	0.0000	0.09451(2)	0.03348(3)	
Na3	2d	0.0000	0.0000	0.0000	0.02049(4)	

Table S5: Anisotropic displacement parameters of $Na_5Ge_7P_5$ at 293 K from single crystal diffraction data. The split position of P2 and Ge4 was refined isotropically.

Atom	U_{11}	U_{22}	U_{33}	U_{23}	U_{13}	U_{12}
Ge1	0.01362(1)	0.00877(1)	0.01965(1)	0.0000	0.00698(1)	0.0000
Ge2	0.01221(1)	0.00880(1)	0.02031(1)	0.0000	0.00700(1)	0.0000
Ge3	0.01148(1)	0.01342(1)	0.02239(1)	0.0000	0.00596(1)	0.0000
Ge4	0.01778(3)	0.01210(3)	0.03105(3)	0.0000	0.01167(2)	0.0000
P1	0.01284(3)	0.01095(3)	0.02191(3)	0.0000	0.00898(2)	0.0000
P2	0.01778(5)	0.01210(5)	0.03105(6)	0.0000	0.01167(5)	0.0000
P3	0.01428(3)	0.00790(2)	0.01404(3)	0.0000	0.00153(2)	0.0000
Na1	0.01803(5)	0.02307(6)	0.07264(8)	0.0000	0.02129(5)	0.0000
Na2	0.02601(5)	0.03872(7)	0.03589(6)	0.0000	0.00478(5)	0.0000
Na3	0.03326(7)	0.00389(6)	0.02465(7)	0.0000	0.00812(6)	0.0000

Table S6: Selected distances and angles in $Na_5Ge_7P_5$ at 293 K from single crystal diffraction data.

Atom 1	**Atom 2**	$d_{1\text{-}2}$ **/ Å**		**Atom 1**		**Atom 2**		**Atom 3**	**Angle**
Ge1	P1	2.3429(4)	2×	P1	–	Ge1	–	P1	103.41(2)
Ge1	P3	2.3990(8)		P1	–	Ge1	–	P3	109.958(14)
Ge1	Ge4/P2	2.4885(8)	2×	P1	–	Ge1	–	P2	113.662(13)
Ge2	Ge4/P2	2.4103(4)	2×	P3	–	Ge1	–	P2	106.21(2)
Ge2	Ge2	2.4288(7)		P1	–	Ge1	–	Ge4	113.662(13)
Ge2	Ge3	2.4807(8)		P3	–	Ge1	–	Ge4	106.21(2)
Ge3	P3	2.4059(4)	2×	P2	–	Ge2	–	P2	99.44(2)
Ge3	Na2	2.9794(9)		Ge4	–	Ge2	–	P2	99.44(2)
Ge3	Na1	3.1370(7)	2×	P2	–	Ge2	–	Ge4	99.44(2)
Ge4/P2	Na1	3.0414(6)	2×	Ge4	–	Ge2	–	Ge4	99.44(2)
P1	Na2	2.9175(9)		P2	–	Ge2	–	Ge2	109.913(15)
P1	Na2	2.9759(6)	2×	Ge4	–	Ge2	–	Ge2	109.913(15)
P1	Na3	3.1164(10)		P2	–	Ge2	–	Ge3	114.748(14)
P1	Na1	3.3000(10)		Ge4	–	Ge2	–	Ge3	114.748(14)
P3	Na3	3.0277(6)	2×	Ge2	–	Ge2	–	Ge3	107.86(2)
P3	Na2	3.2274(7)	2×	P3	–	Ge3	–	P3	99.69(2)
Na1	Na1	3.6776(7)	2×	P3	–	Ge3	–	Ge2	99.745(15)
Na1	Na2	3.8507(9)	2×	Ge2	–	Ge4	–	Ge2	99.44(2)
Na2	Na3	3.3716(10)		Ge2	–	Ge4	–	Ge1	90.189(16)
Na2	Na2	3.5470(9)	2×	Ge1	–	P1	–	Ge1	103.41(2)
Na2	Na2	3.6776(7)	2×	Ge2	–	P2	–	Ge2	99.44(2)
Na3	Na3	3.6776(7)	2×	Ge2	–	P2	–	Ge1	90.189(17)
				Ge1	–	P3	–	Ge3	101.447(15)
				Ge3	–	P3	–	Ge3	99.69(2)

Crystal Structure and Refinement Parameters of „NaGeP”

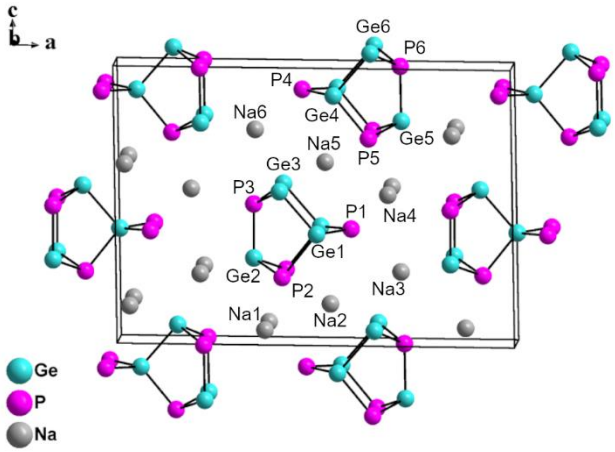

Figure S3: Crystal structure of “NaGeP”. A clear assignemt of Ge and P to certain crystallographic positions of the polyanion was not possible. All atoms a.d.p. are refined isotropially.

Table S7: Refinement data of the single crystal diffraction data of "NaGeP" at 293 K.

Sum formula	"NaGeP"
Molar mass / g mol^{-1}	126.60
Crystal system	monoclinic
Space group	*Cm* (8)
Radiation λ / Å	0.71073 (Mo K_α)
Crystal size / mm^3	0.50 × 0.02 × 0.02
Crystal color, shape	black, needle
Cell parameters / Å	a = 17.943(4)
	b = 3.6528(7)
	c = 12.527(3)
	β = 91.31(3)
Cell volume / Å^3	820.8(3)
Z	12
ρ (calc.) / g cm^{-3}	3.072
μ / mm^{-1}	11.558
F(000)	696
Temperature / K	293(2)
Reflections collected	10243
Independent reflections	5579
Reflections with $I > 2\sigma(I)$	2399
Observed *hkl*	$-34 \le h \le 34$,
	$-4 \le k \le 6$,
	$-23 \le l \le 23$
Measuring range $\theta_{min/max}$ / °	2.76 / 43.090
Goodness-of-fit on F_0^2	2.360
R_{int} /R_σ	0.3306 / 0.2150
R indices ($F_0^2 \le 2\sigma(F_0^2)$)	$R1$ = 0.2496, $wR2$ = 0.4814
R indices (all data)	$R1$ = 0.3632, $wR2$ = 0.5306
Flack	0.49(7)
Largest diff. peak/hole / e Å^{-3}	1.262 / −7.613

Table S8: Atom coordinates of "NaGeP" at 293 K from single crystal diffraction data. All atoms a.d.p. are refined isotropically.

Atom	**Wyck.**	***x***	***y***	***z***	U_{iso}
Ge1	2a	0.5062(3)	0.0000	0.4049(4)	0.0255(12)
Ge2	2a	0.3423(4)	0.5000	0.2942(5)	0.0308(14)
Ge3	2a	0.4137(5)	0.0000	0.5495(6)	0.041(2)
Ge4	2a	0.0537(3)	0.5000	0.9061(4)	0.0247(11)
Ge5	2a	0.2183(3)	0.0000	0.7963(5)	0.0274(13)
Ge6	2a	0.1487(5)	0.5000	0.0532(6)	0.041(2)
P1	2a	0.5888(8)	0.5000	0.4082(12)	0.022(2)
P2	2a	0.4181(6)	0.0000	0.2431(9)	0.014(2)
P3	2a	0.3434(5)	0.5000	0.4908(7)	0.0056(13)
P4	2a	-0.0295(9)	0.0000	0.9099(13)	0.030(3)
P5	2a	0.1379(9)	0.5000	0.7503(13)	0.029(3)
P6	2a	0.2184(6)	0.0000	-0.0100(8)	0.010(2)
Na1	2a	0.370(2)	0.0000	0.046(3)	0.060(8)
Na2	2a	0.536(2)	0.5000	0.150(3)	0.044(5)
Na3	2a	0.2116(12)	0.0000	0.257(2)	0.025(4)
Na4	2a	0.1859(13)	0.5000	0.547(2)	0.028(4)
Na5	2a	0.0199(12)	0.0000	0.655(2)	0.024(4)
Na6	2a	0.8450(2)	0.0000	0.757(3)	0.049(7)

6 List of Publications and Manuscripts

See Chapter 5.1	Synthesis and Characterization of the Lithium-Rich Phosphidosilicates $Li_{10}Si_2P_6$ and $Li_3Si_3P_7$ H. Eickhoff, L. Toffoletti, W. Klein, G. Raudaschl-Sieber, T. F. Fässler, *Inorg. Chem.* 2017, 56, 6688-6694.
See Chapter 5.2	Fast Ionic Conductivity in the Lithium-Rich Phosphidosilicate $Li_{14}SiP_6$ S. Strangmüller, H. Eickhoff, D. Müller, W. Klein, G. Raudaschl-Sieber, H. Kirchhain, C. Sedlmeier, V. Baran, A. Senyshyn, V. L. Deringer, L. van Wüllen, H. A. Gasteiger, T. F. Fässler, manuscript for publication.
See Chapter 5.3	Lithium Phosphidogermanates α- and β-Li_8GeP_4 - A Novel Compound Class with Mixed Li^+ Ionic and Electronic Conductivity H. Eickhoff, S. Strangmüller, W. Klein, H. Kirchhain, C. Dietrich, W. G. Zeier, L. van Wüllen, T. F. Fässler, *Chem. Mater.* 2018, 30, 6440-6448.
See Chapter 5.4	Polyanionic Frameworks in the Lithium Phosphidogermanates Li_2GeP_2 and $LiGe_3P_3$ H. Eickhoff, C. Sedlmeier, W. Klein, G. Raudaschl-Sieber, H. A. Gasteiger, T. F. Fässler, manuscript for publication
See Chapter 5.5	Planar Tetrelide Pentagons and Isolated Phosphide Anions in Lithium Phosphotetrelides $Li_{10.68(8)}Si_5P$ and $Li_{10.1(2)}Ge_5P$ H. Eickhoff, L. Toffoletti, W. Klein, G. Raudaschl-Sieber, T. F. Fässler, manuscript for publication
See Chapter 5.6	On the Structure and Conductivity of Na_3P H. Eickhoff, C. Dietrich, W. Klein, W. G. Zeier, T. F. Fässler, manuscript for publication
See Chapter 5.7	$Na_2Ge_3P_3$ & $Na_5Ge_7P_5$: Flexible Systems Built from 1-Dimensional Modular Units H. Eickhoff, V. Hlukhyy, T. F. Fässler, manuscript for publication